Development of an *in-situ* monitoring technique for hydrogen uptake evaluation from lubricated tribo-contacts

by

Erfan Abedi Esfahani

Submitted in accordance with the requirements for the degree of

Doctor of Philosophy

The University of Leeds

School of Mechanical Engineering

Leeds, UK

September, 2017

The candidate confirms that the work submitted is his own, except where work which has formed part of jointly-authored publications has been included. The contribution of the candidate and the other authors to this work has been explicitly indicated below. The candidate confirms that appropriate credit has been given within the thesis where reference has been made to the work of others.

In the paper contributing to this thesis, the candidate (first author) carried out all the experiments, analysis and preparation of the manuscript. All other authors contributed by proof reading and providing insight on the discussions.

Paper contributing to this thesis:

- Esfahani, E.A., A. Morina, B. Han, I. Nedelcu, M.C. van Eijk, and A. Neville, *Development of a novel in-situ technique for hydrogen uptake evaluation from a lubricated tribocontact.* Tribology International, 2017. **113**: p. 433-442.

This copy has been supplied on the understanding that it is copyright material and that no quotation from the thesis may be published without proper acknowledgement.

Acknowledgments

To My Family

Abstract

The majority of rolling bearings are made from steel due to its suitable mechanical properties. It has been demonstrated that hydrogen evolution from lubricated contacts significantly shortens the steel fatigue life. Significant efforts have been made so far to understand the mechanism of hydrogen-induced failure. However, the failure mechanism is complex and a conclusive theory has remained unknown.

The main aim of this study is to develop a novel method, based on the modified Devanathan-Stachurski technique, to experimentally assess hydrogen intrusion into the steel. This new technique enables the study of the hydrogen source in a lubricated contact and the rate of its permeation into the steel. The hydrogen intrusion from various lubricants has been evaluated at both room temperature and high temperature. The effect of water contamination, anti-wear and friction modifier additives in poly-alpha-olefin base oil on tribologically-induced hydrogen uptake were investigated.

The results suggest a significant influence of water on hydrogen intrusion. The ZDDP anti-wear and MoDTC friction modifier could reduce hydrogen uptake by forming a uniform tribofilm. On the other hand, the hydrogen permeation is promoted by ZDDP additive when the tribofilm is patchy. This is speculated to be due to the ZDDP decomposition products acting as poisonous agents for recombination of hydrogen atoms. The results indicate that water contamination is more detrimental in presence of ZDDP additive in the lubricant. The study shows that hydrogen is liberated from decomposition of hydrocarbon molecules. The liberation of hydrogen is tied to the rubbing process. The surface rubbing forms a nascent steel surface with active sites by removing contaminants and surface oxide layer. This fresh metal surface catalyses the lubricant decomposition process. It also reveals that hydrogen permeation rate is higher when the load and sliding speed are higher mainly due to the higher wear rate.

Table of Contents

List of Figures

List of Tables

Nomenclature

AW	Anti-Wear additive
EP	Extreme Pressure additive
EHL	Elastohydrodynamic Lubrication regime
ZDDP	Zinc Dialkyl DithioPhosphate
PAO	Poly Alpha Olefin
BO	Base Oil
MoDTC	Molybdenum DialkyldiThioCarbamate
PFPE	Perfluoropolyether
TOP	Trioctylphosphate
DS technique	Devanathan-Stachurski technique
Q-MS	Quadrupole Mass Spectrometer
OCP	Open Circuit Potential
EIS	Electrochemical Impedance Spectroscopy
SEM	Scanning Electron Microscopy
SRET	Scanning Reference Electrode Technique
TEM	Transmission Electron Microscopy
XPS	X-ray Photoelectron Spectroscopy
EDX	Energy Dispersive X-ray analysis
WLI	White Light Interferometry
FTIR	Fourier Transform InfraRed Spectroscopy
RE	Reference Electrode
WE	Working Electrode
CE	Counter Electrode
SCE	Saturated Calomel Electrode
SHE	Standard Hydrogen Electrode
DP	Diamond Powder
$|z|$	Absolute magnitude of the impedance

Z_{real}	Real component of the impedance
Z_{img}	Imaginary component of the impedance
i	Hydrogen oxidation current density
J	Hydrogen flux
D_{eff}	Effective Diffusivity
F	Faraday's Constant
θ_H	hydrogen atoms coverage
H_{ads}	Adsorbed hydrogen
H_{abs}	Absorbed hydrogen
$t_{1/2}$	Half-life decay time
P_{max}	Maximum Hertzian Contact Pressure
P	Partial pressure
C_e	Hydrogen solubility
S	Solubility coefficient
U	Entrainment speed
σ_{rms}	Mean surface roughness
λ	Lambda ratio
h_{min}	Minimum lubricant film thickness
η_0	Lubricant's viscosity at atmospheric pressure
E'	Reduced elastic modulus
R'	Reduced radius of curvature
α	Pressure viscosity coefficient
f	Friction force
μ	Friction coefficient
W	Normal force
τ	Shear stress
T	Torque
t_b	Breakthrough time

t_{lag}	Time lag
L	Thickness of the membrane
S_H	Hydrogen solubility in BCC iron
I_m	Moment of inertia for a hydrogen molecule
K_{eff}	Equivalent spring constant
x	Displacement of the spring
RCF	Rolling Contact Fatigue
SCC	Stress Corrosion Cracking
HE	Hydrogen Embrittlement
WSF	White Structure Flaking
WEA	White Etching Area
WEC	White Etching Crack
ATR	Attenuated Total Reflectance

Chapter 1 Introduction

Bearings are often categorized among the most important machine elements. They are widely utilised in diverse industrial sectors ranging from automobiles, aerospace to household appliances. The global rolling bearing market's size in 2016 has been forecast around US$40 billion by SKF. The bearing market is estimated to reach US$83 billion by 2020. The industrial heavy machinery and automotive sectors constitute the largest markets for bearings [1].

The majority of bearings are made from steel by virtue of its suitable mechanical properties [2]. However, hydrogen has been proved to have many deleterious effects on durability and strength characteristics of steel. Steel alloys are susceptible to "hydrogen embrittlement" or "delayed fracture" which decreases steel ductility and consequently leads to premature failure.

Hydrogen atoms, unlike hydrogen molecules, could easily penetrate into the steel due to their extremely small size. The reducing character of hydrogen atoms modifies the chemical structure of the steel. As a result, damage of steel due to hydrogen is prevalent and cannot be easily detected which makes it even more catastrophic [3]. Hydrogen-induced failure could either happen due to the generation of internal cracks which is called hydrogen induced cracking or generation of surface cracks which is called hydrogen stress cracking [4].

It has been widely stated that hydrogen uptake happens in mechanical elements with lubricated contacts due to the generation and entry of atomic hydrogen via tribochemical reactions and lubricant decomposition during surface-rubbing [5-15]. Lubricants in bearings tend to degrade with heat and shear stress [12]. Lubricant degradation not only decreases a lubricant's lubricity but can also promote hydrogen uptake into the steel [9, 13]. Therefore, it is important to follow up the hydrogen generation and its diffusion through the steel in order to predict the safe functioning of the machine element.

Controlling diffusion of hydrogen into the steel can effectively decrease hydrogen embrittlement and provide longer component life leading to huge cost saving. Special efforts have been made to understand the mechanism of hydrogen evolution and its entry into the steel from a lubricated tribo-contact. So far these studies have been mainly done using *ex-situ* techniques by employing mass spectrometry and ion beam measurement methods [5, 12-14, 16]. However, *ex-situ* analyses are subject to error due to the variability of hydrogen content measurement as a result of de-gassing between experiment and detection process. The sample preparation for the detection technique

causes hydrogen escape. In addition, the measurement values show the total hydrogen in the steel including the amount of hydrogen remained in the steel from the manufacturing process and the amount of hydrogen diffused in the metal during surface-rubbing.

Considering the limitations of the *ex-situ* techniques, an *in-situ* measurement method is considered to be employed in the current study to understand the mechanism of Hydrogen Embrittlement (HE) as a result of tribochemistry. *In-situ* monitoring of tribological hydrogen evolution has already been carried out by other investigators [9, 11, 12, 17]. Those investigations have mainly been performed in a high vacuum or controlled gaseous atmosphere. The gaseous products of tribochemical decomposition of the lubricant were monitored using a quadrupole mass spectrometer [9, 11, 12]. However, the results of these experiments in such controlled atmospheres often miss some critical aspects of hydrogen generation and permeation when used to study the HE phenomenon. Firstly, these techniques only detect desorbed hydrogen from the contact which is harmless for the steel. However, tribological contacts can introduce hydrogen into the contacting bodies leading to premature hydrogen induced fatigue failure. Secondly, oxidative decomposition of the lubricant is considered as one of the sources of hydrogen. This is believed to be attributed to the fresh metal surface catalytic effect on lubricant decomposition rate [9, 11]. However, running the experiment in a vacuum chamber delays the oxidation of fresh surface and varies the hydrogen generation rate compared to real working conditions [12].

Based on the aforementioned discussion, this research has been motivated by the necessity of a robust monitoring technique for tribological hydrogen permeation *in-situ* measurement. This is vitally important for any further studies of tribological hydrogen evolution. The main contributing factors to hydrogen generation from a lubricated contact can be studied using this technique. Development of an in-situ robust monitoring technique will help to understand the mechanism of tribological hydrogen evolution. The mechanism of failure is complex and a conclusive theory is yet to be established. This enables assessing the risks, predicting the failure and providing a protective solution.

Modifying the Devanathan-Stachurski (DS) technique has been chosen in order to monitor tribological hydrogen uptake. The high sensitivity of electrochemical measurement in this technique allows very detailed real-time measurements to be taken; any slight changes of the hydrogen evolution rate on entry side can be reflected in the hydrogen permeation current. This new

technique is employed in this study to reveal some of the complexity of interplay between lubricant composition and hydrogen generation on the one hand and between the tribological parameters and hydrogen entry into the steel on the other hand. The results from this technique is also used to give insights into the effect of water contamination and temperature on hydrogen uptake.

1.1 Thesis outline

- Chapter One: The topic of this study is introduced and the motivation of that is discussed.

- Chapter Two: Fundamental theory relevant to this study and major failure mechanisms in bearings are presented.

- Chapter Three: The idea of hydrogen being present in lubricated tribological contacts is discussed. The interplay between hydrogen and failure mechanisms of steel is described.

- Chapter Four: A summary of various electrochemical techniques and a review of devices and methods that are capable of detecting hydrogen in metals are presented.

- Chapter Five: The prototype set-up and its results are presented in this chapter. The limitations of this method are described and the design history of the new rig enabling *in-situ* hydrogen permeation measurement from a lubricated contact is summarized.

- Chapter Six: Materials, preparation procedure and experimental techniques used in this study are presented.

- Chapter Seven: The hydrogen uptake measurements from lubricated tribo-contact were carried out at room temperature. The effect of water contamination, lubricant additives and contact pressure are investigated.

- Chapter Eight: The hydrogen uptake results from lubricated tribo-contact at high temperature are presented. The effect of water contamination, contact pressure, sliding speed and lubricant additives are investigated.

- Chapter Nine: The application of AC impedance measurement in lubricant, a high resistance media, is studied. This is explained how

such measurements could help further development of the current hydrogen uptake rig.

- Chapter Ten: Discussion on results obtained from Chapter Five to Chapter Nine is presented and recommendations for future studies are outlined. The influence of chemical composition of the lubricant and the effect of tribological parameters on the mechanism of hydrogen generation are discussed based on hydrogen uptake measurement results and surface analysis techniques.

- Chapter Eleven: Main conclusions from this study are detailed.

Chapter 2 Lubricated contacts in bearings

2.1 Introduction

This chapter contains a review of different types of bearings and their manufacturing materials. Fundamentals of tribology and lubrication theories are discussed and major failure mechanisms in bearing are briefly mentioned. An introduction of lubricants and additives that may have importance for hydrogen-generation in rubbing contacts is also given.

2.2 Introduction to bearings

Bearings are machine elements which are designed to facilitate relative motion between moving parts. The relative motion can be either linear or rotational. The main aim of the bearings is to keep friction as low as possible between two moving parts of the machine [2]. Reducing friction is crucial in order to improve efficiency and decrease wear. It also facilitates higher speeds and prevents overheating leading to higher efficiency and lower energy consumption [18].

There are different types of bearings such as plain bearings, rolling-element bearings and magnetic bearings. However, in this thesis, the phrase bearing refers to 'rolling element bearing'. Rolling-element bearings are extensively used in a wide range of industries ranging from aerospace, gear boxes and wheel bearings in automobiles, wind turbines, bicycle wheel hubs and dental drills [19]. Rolling element bearings are used to locate rotating shafts in order to decrease the friction. This is mainly due to the fact that rolling requires less effort than sliding motion and consequently lower energy will be consumed. Rolling element bearings are more efficient than plain bearings in decreasing friction since balls and cylinders have much lower coefficient of friction than if two flat surfaces slide against each other [18].

In rolling element bearings, balls or cylinders keep the raceways apart. Rollers are held in a cage preventing contact between them and maintaining the correct angular spacing (Figure 2-1). The reliability and integrity of operational bearings, as a crucial part of bigger machines, are important to reduce the danger of failure and break down of the whole machine. Therefore, monitoring the working conditions to determine bearing life is significantly important as it could save unforeseen expenses by reducing unexpected maintenance time or failure.
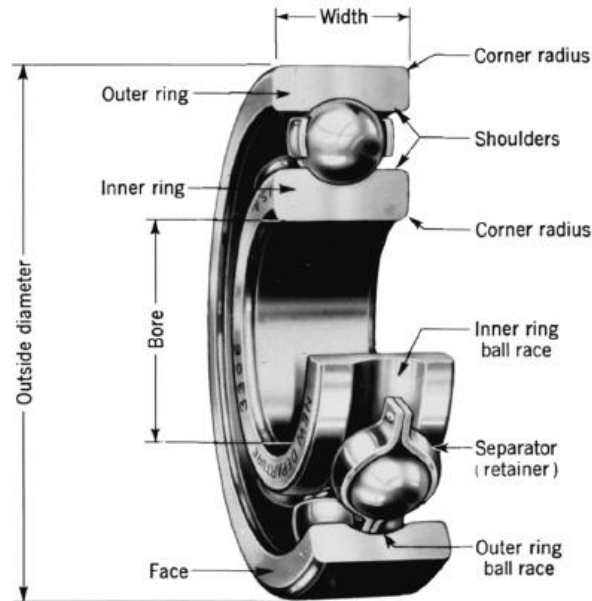
Figure 2-1: Cutaway view of rolling element bearings (image courtesy of Timken Co.)

2.3 Types of bearings

There are different types of bearings based on their shapes, materials and lubrications each suited for specific applications dealing with wide range of radial and thrust pressures. Different types of bearings can handle different speeds [20]. The main focus of this project is on rolling element bearings. So, different types of this category of bearings are briefly discussed here. The contacts between the rollers and raceways are usually subject to very high pressures, typically around 1-2 GPa in this type of bearings. A selection of rolling element bearings is as follows (Figure 2-2) [20].

a) Angular contact ball bearings are designed with a capability to carry combined radial and axial pressures at a high speed with an outstanding precision. Contact angle is the angle between the line which connects the contact points of the ball and the raceways in the radial plane and a perpendicular line to the bearing axis. The axial pressure capacity is directly proportional to the contact angle.

b) Deep groove bearings in which balls fit into the deep grooves. These bearings can bear both radial and thrust pressures.

c) Tapered roller bearings in which the raceways and rollers are made tapered to increase the contact area and handle greater radial pressures while being able to transmit thrust greater forces

d) Self-aligning ball bearings in which two rows of balls slide on a pair of grooves on the inner race; outer raceway has a concave surface. This type of bearing allows some misalignment of the shaft.

e) Needle roller bearings in which rollers are made with large length-to-diameter ratio. This type of bearings are especially suitable for places that need very small bearings because of limited space.

a

b

c

d

e
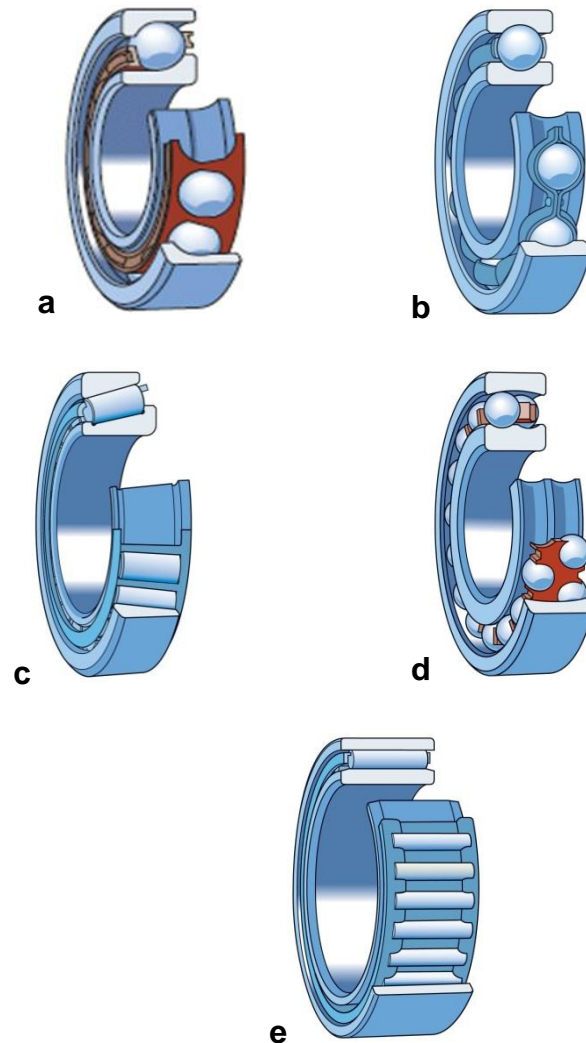
Figure 2-2: Illustrations of: a) angular contact single row, b) deep groove bearing, c) tapered roller bearing, d) self-aligning bearing and e) needle roller bearing [21]

2.4 Materials for bearings

Bearings usually operate under very high contact pressure and high speed conditions making them more exposed and hence more susceptible to degradation. The pressure should always be kept in the elastic region since applying a very high pressure, above yield stress, leads to plastic deformation

of bearing components, either balls or raceway. This is crucial to ensure that bearings work reliably under severe static and cyclic loads.

Increasing the bearing load capacity has been the aim of numerous studies in the last century. The use of different materials for manufacturing bearings has been extensively investigated. Some of the important characteristics of bearing materials are shown in Figure 2-3 [2].

Fatigue: rolling contact, axial loading, crack growth	Hardness Strength	Toughness
		Ductility
Ability to manufacture: machining, forming, forging, grinding, heat-treatments, dimensional control, tolerance to variations	Hydrogen resistance	Cleanliness
		Hardenability
	Corrosion resistance	Through life cost
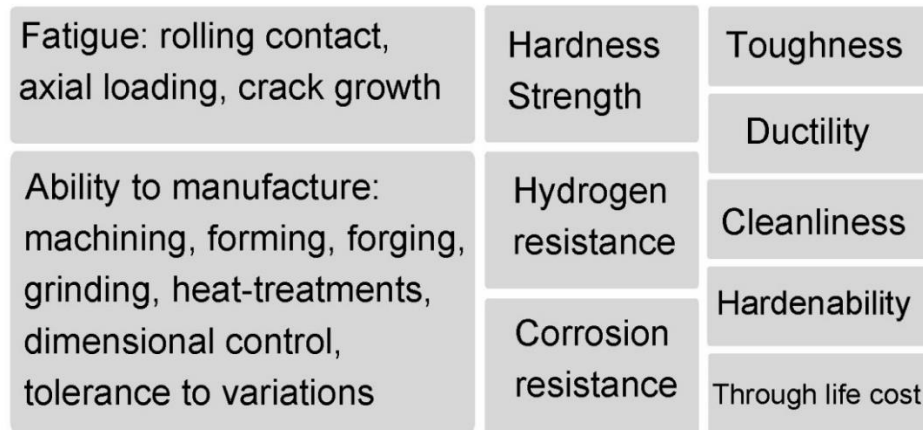
Figure 2-3: Some of the essential features for bearing steels [2]

Steel alloys are the most popular materials for bearings manufacturing. Steels with 0.8-1.1 wt% carbon concentration and 3 wt% substitutional solute content have been conventionally used for bearings manufacturing. It has been revealed that two types of steels are appropriate in the majority of bearings. Firstly, through hardened steels with martensitic or bainitic structure which are hardened throughout the section. Secondly, case hardened steels which have soft cores but hard surface layers. This hard layer is formed using processes such as carburizing, and induction hardening. Surface treatments, to produce case-hardened steel, are usually more expensive and more complex than through-hardening procedures.

AISI 52100 steel with chemical composition shown in Table 2-1 is extensively used for bearings production. The microstructure is usually tempered martensite for through-hardened bearings [2]. The same material is used for both rolling elements and raceways. In Figure 2-4, hardenability of 52100 steel in Jominy test is shown [2].

Table 2-1: Chemical composition of AISI 52100 steel in wt% [2]

C	Mn	Cu	S	Si	Cr	Fe
0.95-1.10	0.20-0.50	≤ 0.025	≤ 0.025	≤ 0.35	1.30-1.60	Balance
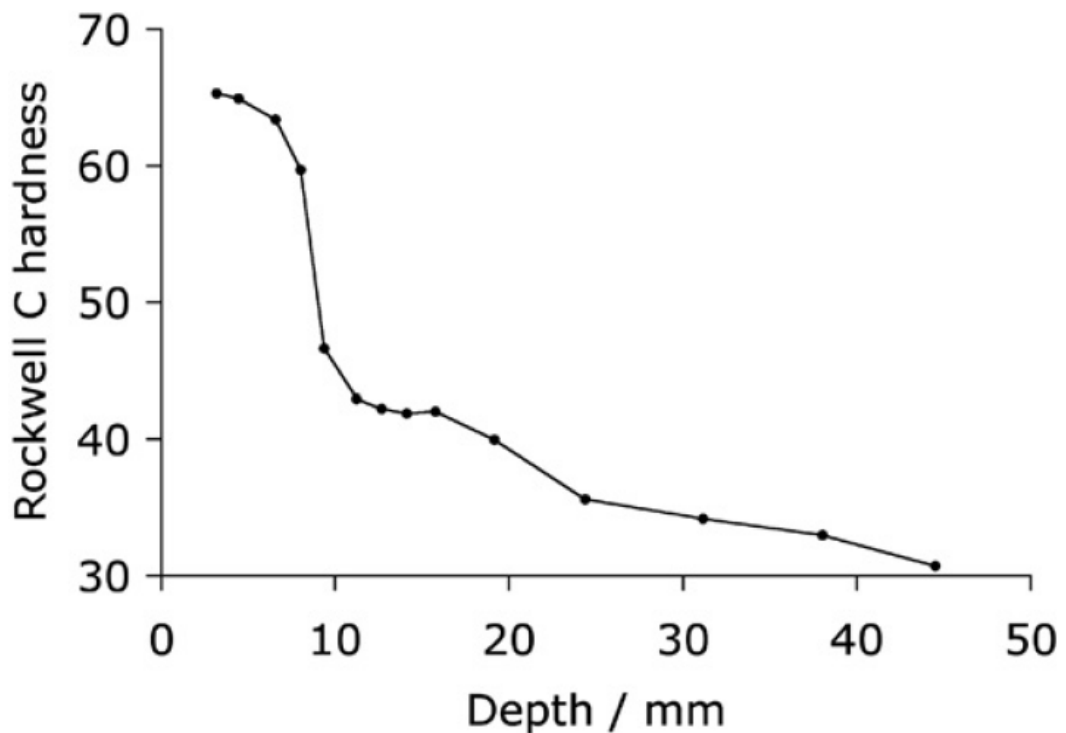
Figure 2-4: Hardenability of 52100 steel austenitised at 845°C [2]

Surface engineering processes are employed to modify the steel surface of case hardened steels for bearings applications. The depth of hardening is usually less than 1 mm. Using lasers is one of the techniques used to increase the hardness of bearing steel [22]. Ion implantation is another surface treatment to improve surface hardness of the 52100 steel [23]. There are also some surface engineering processes to improve the surface hardness of steel by changing the chemical composition locally. Carburising, nitriding and carbonitriding are some of the common techniques to increase surface hardness by changing the surface composition. More details on surface hardening methods can be found in [24].

2.5 Principles of tribology

Tribology refers to the science of investigation on friction, wear and lubrication of two rubbing surfaces. Tribology is an important science since the loss of energy and material have a huge negative impact on the economy of industries annually [25]. Tribology is a significant concern in many engineering components today such as bearings, gears, clutches, brakes, cams, wheels and tires, pumps, turbines, pistons, and internal combustion engines. Studies by Holmberg et al. [26] showed that about 33% of fuel energy in passenger vehicles is lost due to friction loss (Figure 2-5). Tribology is also an important environmental issue due to its impact on fuel consumption and faster material

degradation. Furthermore, unwanted friction generates heat and causes noise in mechanical components.
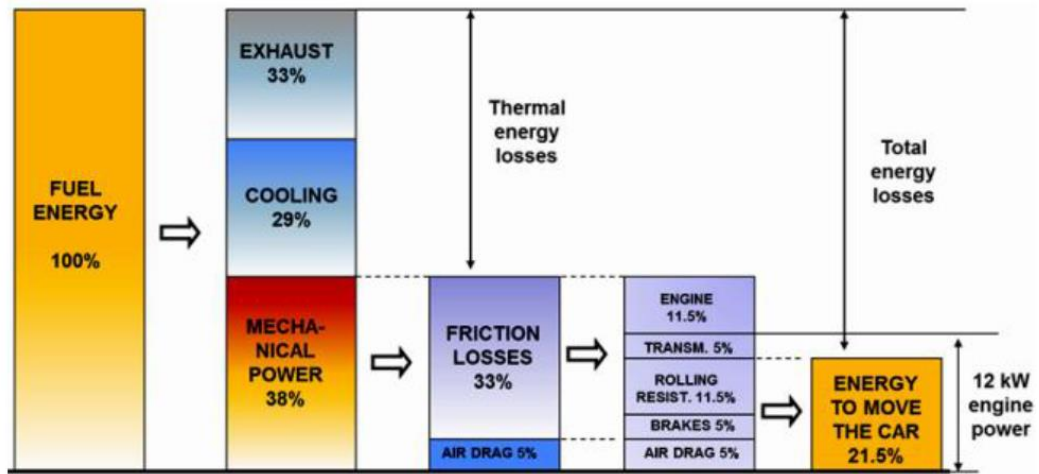
Figure 2-5: Energy losses in passenger cars [26]

Tribochemistry is the science of investigation of the chemical reactions in a tribological contact. This is used to study the mechanism of tribofilms formation and their composition. Tribochemistry includes wide range of sciences such as chemical, physical, mechanics, and material sciences. Tribochemical studies proved that tribological parameters and chemical reactions are strongly interconnected mutually affecting each other. Chemical reaction by-products form on the surface affect friction and therefore influence kinetics of reactions [27].

2.5.1 Friction

Resistance against tangential motion between two rubbing surfaces is known as friction. Frictional instability leads to motion disruption and generating energy which can affect tribochemical reactions in the system. Friction is dependent on many factors such as normal load, velocities of moving parts, surface roughness and lubricant [28]. Friction force is used to calculate coefficient of friction (μ) by equation (2-1):

$$\mu = \frac{f}{W} \qquad (2-1)$$

Where f is friction force and W is applied load.

Four main laws of friction under dry sliding have been developed by da Vinci and Amontons [25]:

- Maximum tangential force before sliding proportionally relates to the normal force when a static body is subjected to increasing tangential load
- Tangential friction force is proportional to the normal force
- Apparent contact area does not affect friction force
- Friction force only slightly depends on the sliding speed

2.5.2 Wear

Wear refers to the progressive material loss on surfaces of components as a result of relative motion between two adjacent bodies [29]. Wear usually increases with increasing sliding distance and contact pressure. Higher surface hardness usually decreases wear.

There are five common wear mechanisms:
- **Adhesive wear** is a very severe mechanism of wear. This happens when two bodies are in direct contact via asperities. The lubrication regime is either mixed or boundary when this type of wear occurs. Transfer of weaker material to the stronger one happens due to cold welding as shown in Figure 2-6. The friction coefficient is unstable in this type of wear [25]. The main failure mechanism in cam and cam follower contacts is attributed to adhesive wear [30].
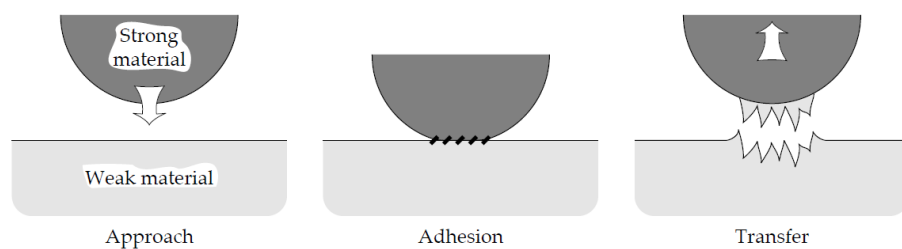
Figure 2-6: Mechanism of adhesive wear [25]

- **Abrasive wear** happens when a solid object is moved against another one with equal or greater hardness. The softer material is ploughed out leaving some scratches and furrows on the metal surface. Abrasive wear happens when the lubrication is not sufficient or the surface roughness is high. Different mechanisms have been presented for abrasive wear which are illustrated schematically in Figure 2-7 [25].

11
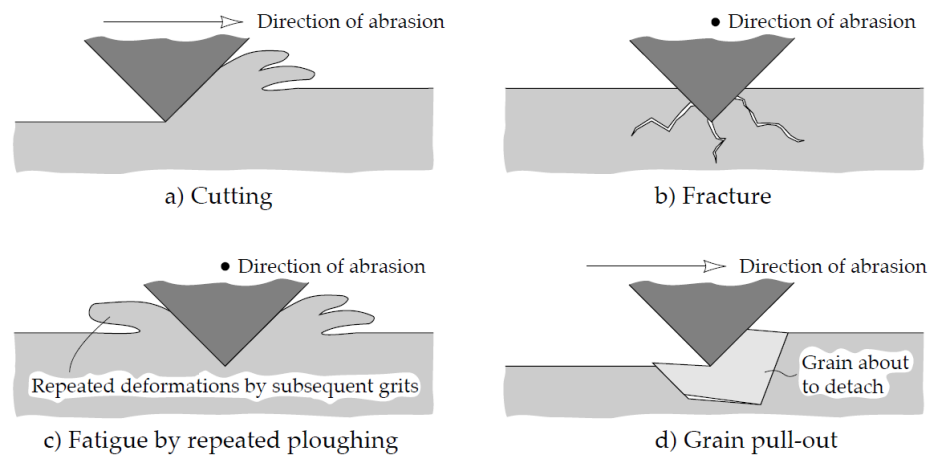
Figure 2-7: Mechanisms of abrasive wear [25]

- **Erosive wear** happens when suspended particles in fluid or gas impact a solid surface and remove the material. It usually happens in a high flow rate liquids that gasses or solid particles are entrained in.

- **Fatigue wear** occurs when contact between asperities with very high local stress repeats many times. Wear particles generate by fatigue propagated cracks in this failure mechanism [31]. Failure by fatigue wear usually happens during a long period of time and could even happen without any direct contact between two surfaces. This type of failure even happens in well-lubricated bearings. Fatigue wear is very typical in rolling element bearing and will be discussed in more details later in this chapter.

- **Corrosive wear** also known as tribocorrosion, oxidative wear, and wear accelerated corrosion. Tribocorrosion is the loss of material due to synergic effect of chemical/electrochemical reactions and mechanical wear. In the absence of rubbing between two surfaces, corrosion products accumulate on the surface of metal preventing further corrosion. However, rubbing removes corrosion products exposing fresh metal to the corrosive media. Many different models are presented for material loss under corrosive wear systems. Some of them are shown schematically in Figure 2-8 [32]. Tribocorrosion is considered as one of the major problems in bearings. In some corrosive media, such as food process industries and aircraft, stainless steel is used to prevent severe corrosion. In stainless steel, the corrosion rate is greatly decreased due to the formation of a thin passive layer

12

covering the fresh metal preventing further degradation. Chromium has a major role in formation of this thin, dense, and coherent layer. The protective passive layer is adhesive to the substrate and is electrically insulated. Nitrogen and molybdenum can improve pitting resistivity of passive layer in stainless steels.
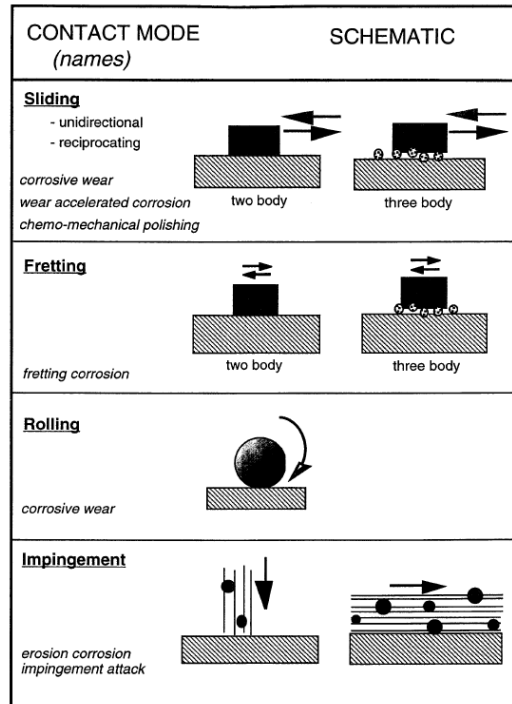
Figure 2-8: Different types of tribocorrosion systems (simultaneous effect of mechanical and chemical phenomena) [32]

One of the effects of corrosion reactions happening on the surface is hydrogen generation which penetrates into the steel. Monitoring hydrogen permeation rate into the steel is the main interest of the current research.

2.5.3 Lubrication

Lubrication is essential for reducing wear and friction between two interacting surfaces leading to higher energy efficiency [25]. Lubricant forms a thin film on the moving metal surfaces protecting the steel parts from wear by preventing solid-solid contact. Both friction and wear dramatically decrease when a liquid lubricant film forms between two surfaces. There are some more advantages for using lubricants such as heat transfer and removing debris from contacting surfaces. In this study, we are focusing on the effect of tribochemical and tribocorrosion reactions occurring in lubricated interface leading to hydrogen evolution [33].

The lubricant viscosity is defined as resistance to shear in a fluid. Viscosity is not constant and changes with temperature and pressure. The viscosity of Newtonian fluids follows equation (2-2) [30].

$$\tau = \eta \frac{\delta u}{\delta y} \qquad (2\text{-}2)$$

Where τ is shear stress, η is dynamic viscosity and $\frac{u}{y}$ is the gradient of the velocity profile.

2.6 Lubricant formulation

Lubricant participates in tribochemical reactions within the contact and plays a major role in the lifetime achieved. The properties of the lubricant change while chemical reactions occur. Lubricant oxidation increases its viscosity makes it difficult for lubricant to enter the contact. On the other hand, lubricant may break into smaller molecules with lower viscosity under shear stress leading to thinner lubricant film [30].

Lubricants consist of base oil and some specific chemical additives to improve their performance in harsh environments. There are two different base oils; mineral and synthetic base oils. Synthetic oils are more thermally and oxidative stable with better film formation ability. Synthetic oils are widely used throughout industry although they are more expensive [34]. Amongst the synthetic oils, poly-alpha-olefins (PAOs) are the most common base oil used [25].

However, base oils alone do not satisfy the lubrication needs of modern equipment. The need to improve the limitations of base oils pushed towards using a wide range of additives to enhance the physical and chemical stability of the lubricants for a long-term performance. Additives are used in lubricants for different purposes such as cleaning the surfaces, preventing solid-solid contact, maintaining the oil properties, preventing lubricant oxidation and minimising the contamination effects on lubricant behaviour. The mechanism by which the additives work is very complex. Additives can be either chemically active or chemically inert. The chemically active additives such as anit-wear and extreme-pressure additives, organic corrosion and oxidation inhibitors and dispersants mostly have unsaturated chemical bonds and functional groups or molecules (from group V and VI in periodic table: nitrogen, sulphur, phosphor, and oxygen). Viscosity index improvers which are chemically inert are used to minimize the viscosity changes in different temperatures. A lubricant can contain any number of additives with different

concentrations depending upon the application. The most widely used additives are as follows:

Detergents are usually metal (calcium, magnesium, barium, and zinc) based compounds that prevent insoluble deposits form on the surface. Detergents form microemulsion of insoluble contaminations on the surface. Metal sulfonates, metal phenates, metal salicylates and metal thiophosphonates are recognised as common detergents. Overbased detergents i.e. calcium carbonate, is added to the lubricants in order to neutralize acidic contaminants formed for oxidation of the lubricant [35]. Overbased detergents have a configuration similar to Figure 2-9. The core is composed of metal carbonate while the shell consists a surfactant layer.
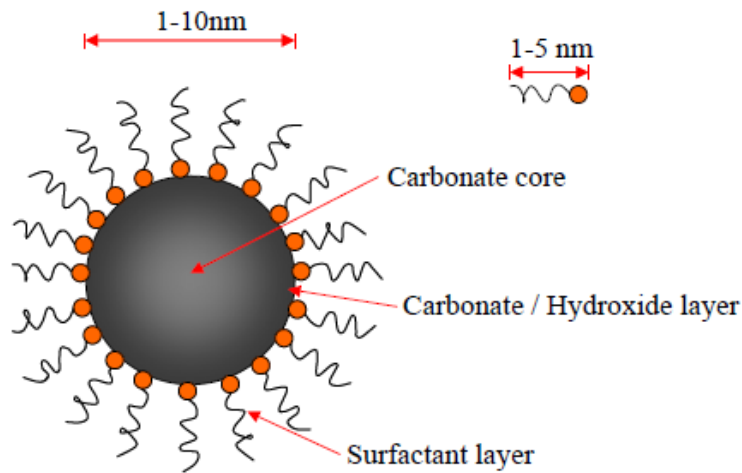
Figure 2-9: Core-shell configuration of metal carbonate detergents [36]

Dispersants do not contain metals in their structure (ashless). They can suspend the insoluble oxidised products and contaminants at low temperatures (below 100°C). There are two common types of the dispersants: Mannich base (amino carbonyl compounds) and Succinimide (cyclic imide). Pour point depressants are utilised to lower the pour point of the lubricant improving the lubricant performance at lower temperatures.

Antioxidants are mainly used to protect the lubricant from thermal degradation and the oxidation process [27]. Amines, hindered phenols, sulphur and phosphorus compounds are recognised as the most common antioxidants [37].

Viscosity Index (VI) improvers are polymers with molecular weights of more than 100,000. The most common VI improvers are polymethacrylates, polyisobutenes, olefins and styrene/dienecopolymers. The concentration and

15

molecular weight of the polymer are important as the backbone chain of the polymer breaks down in high shear rates leading to shear thinning. 5-10% of VI improver significantly improves VI [37].

Extreme Pressure additives (EP) are a group of additives that are designed to prevent adhesive wear under sliding motion. Adhesive wear is specifically an issue in extreme pressure contacts such as in bearings and gear transmissions particularly if sliding occurs. EPs mainly contain sulphur or chlorine organic molecules that break down under extreme pressure solid-solid contact conditions. Iron sulphide (FeS) forms on the steel surface as a product of extreme pressure additive decomposition. Iron sulphide remains on the surface due to its very high melting point protecting metal by preventing solid-solid contact [38]. However, hydrogen is generated as a by-product of extreme pressure additives decomposition. This hydrogen could diffuse into the steel increasing sub-surface concentration of hydrogen and accelerating crack propagation.

Corrosion inhibitors are utilised to form a chemically or physically surface film to reduce the cathodic and/or anodic chemical reaction rates on the surface. Rust inhibitors such as alkyl thioacetic acids, imidazolines, amine phosphates and acid phosphate esters are another type of the corrosion inhibitors that can mitigate rust formation [37].

Among all different additives that are used in industrial lubrication, two groups, friction modifiers and anti-wear additives, are examined in this research due to their academic and industrial importance. There are ex-situ measurement studies that have shown the effect of anti-wear additives on hydrogen intrusion into the steel [39]. Friction modifiers have also the potential effect to reduce hydrogen evolution by forming a tribofilm and reducing the friction.

2.6.1 Friction modifier additive

Friction modifiers such as molybdenum bis-diethylhexyl dithio-carbamate (MoDTC) generate a film on the surface alleviating friction up to 30%. Recent studies [40, 41] try to synthesize and implement nanoparticles of molybdenum disulphide (MoS_2) and tungsten disulphide (WS_2) and finely dissolved graphite as potential effective friction modifiers. Friction modifiers are especially important in boundary regime. The molecular structure of MoDTC compounds depend on the synthesis process. The varying MoDTC structures are shown in Figure 2-10 [42].
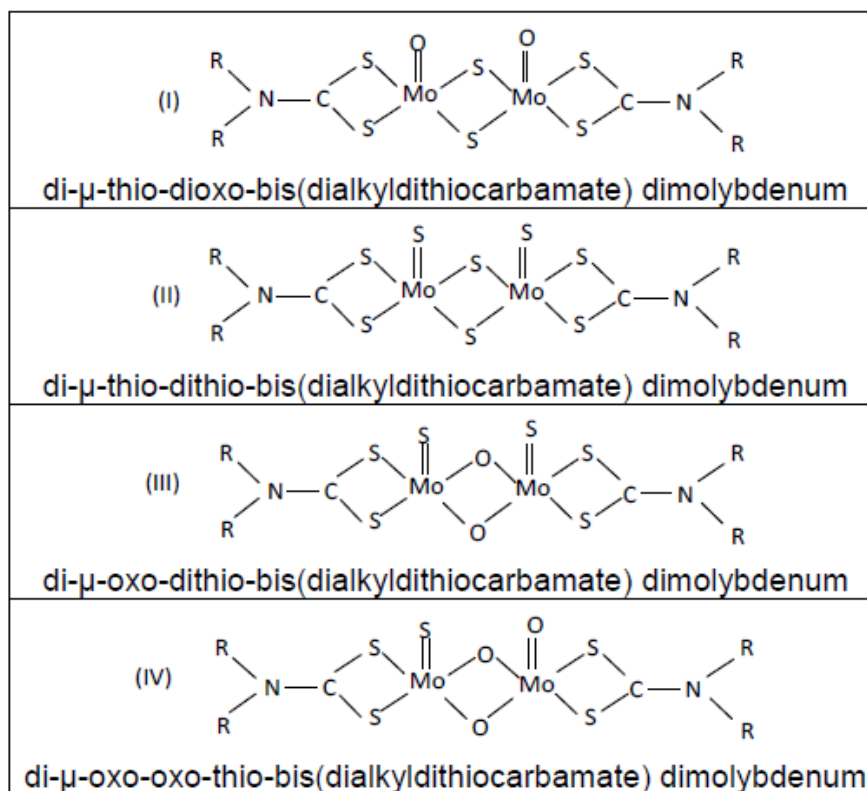
Figure 2-10: Molecular structures of MoDTC [42]

2.6.2 Anti-wear additives (AW)

Anti-wear additives are utilised to supress wear particularly by forming a tribofilm on the surface. The main surface protector additive is ZDDP [43]. The film is composed of a thin layer of iron sulphide with a phosphate glass layer on top. The presence of zinc cation stabilizes this glass structure [44]. ZDDP has either neutral or basic molecular structure as illustrated in Figure 2-11 [45]. Depending on the number of carbon atoms which can attached to the carbon atom of the alkyl (R) group, new categories are defined as primary, secondary and tertiary ZDDPs [27]. The protective film can also be formed by decomposition of ZDDP under heating or high pressure without rubbing [46, 47]. It has been reported that ZDDP tribofilm has excellent thermal and mechanical stability once it is formed. Bancroft et al. [48] replaced the base oil containing ZDDP with oil without ZDDP after the formation of ZDDP tribofilm and continued the tribo-test for extended periods up to 24 hours. Their results showed that the tribofilm remained on the surface without being completely removed by rubbing. Similar behaviour was reported by Fuller et al. [49].

17
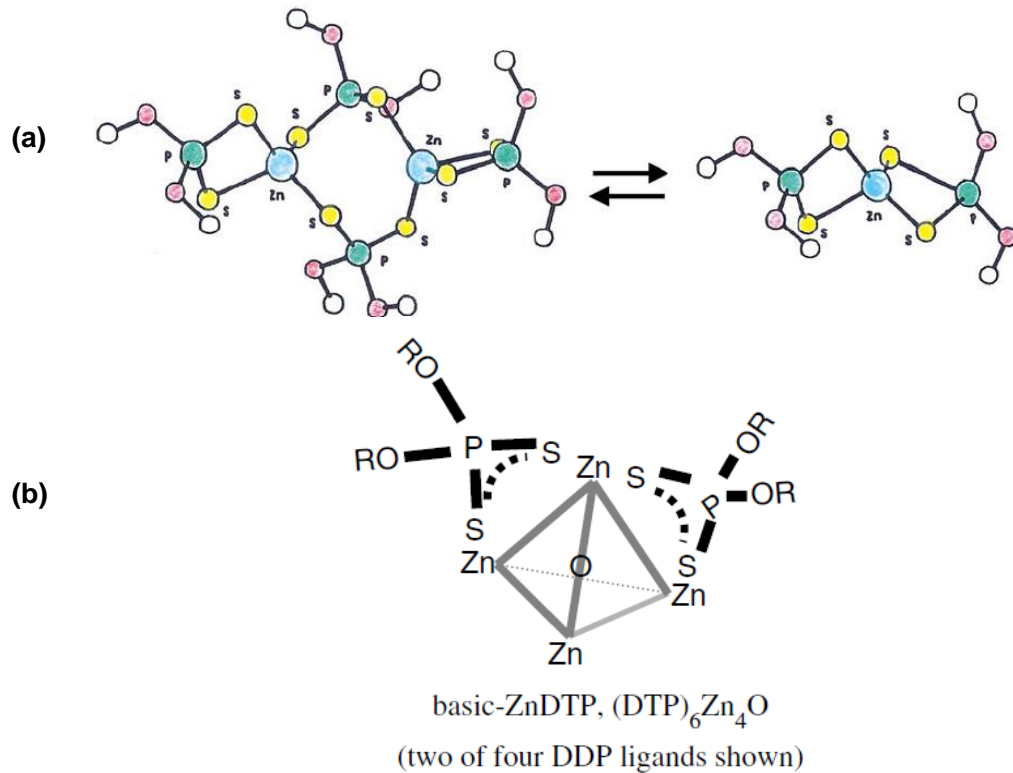
Figure 2-11: (a) Equilibrium between dimeric and monomeric neutral ZDDP, (b) basic ZDDP [45]

There are some adverse reports on the effect of anti-wear additives on steel failure. In particular, Laine et al. [50] and Benyajati et al. [51] showed that micropitting is more severe in presence of the anti-wear additive, ZDDP, compared to a simple base stock. Spikes et al. [52] reported a nearly inverse relation between micropitting damage and the wear in sliding contacts for lubricants containing secondary ZDDP for various concentrations between 0-1.3 wt%. On the other hand, another investigation by Laine et al. [53] showed that the presence of friction modifier additive (MoDTC) in a formulation consisting of a mineral base stock and ZDDP significantly decreases micropit formation compared to the lubricant consisting of ZDDP alone.

2.7 Regimes of lubrication

Lubrication regimes help to predict overall performance of the tribological interface. Lubrication regime is usually determined by lambda ratio, equation (2-3). Stribeck diagram (Figure 2-12) is used to analyse friction in different regimes.

$$\lambda = \frac{h_{min}}{\sigma_{rms}} = \frac{h_{min}}{\sqrt{R_{q1}^2 + R_{q2}^2}} \tag{2-3}$$

Where h_{min} is the minimum film thickness and σ_{rms} is mean square surface roughness. h_{min} is considerably important as it governs the lubrication regime. h_{min} is numerically defined in equation 2-4 [25, 54]

$$\frac{h_{min}}{R'} = 3.63 \left(\frac{U\eta_0}{E'R'}\right)^{0.68} (\alpha E')^{0.49} \left(\frac{W}{E'R'^2}\right)^{-0.073} (1 - e^{-0.68k}) \quad (2\text{-}4)$$

Where U is the entrainment speed and defined as $U = \frac{U_A + U_B}{2}$. U_A and U_B refer to the velocities of bodies A and B. η_0 is the viscosity at atmospheric pressure of the lubricant. E' is the reduced elastic modulus and R' is the reduced radius of curvature of the contact. α is defined as the pressure viscosity coefficient and W is the contact load. K is ellipticity parameter; for point contact $K=1$. There are mainly four lubrication regimes based on film thickness.
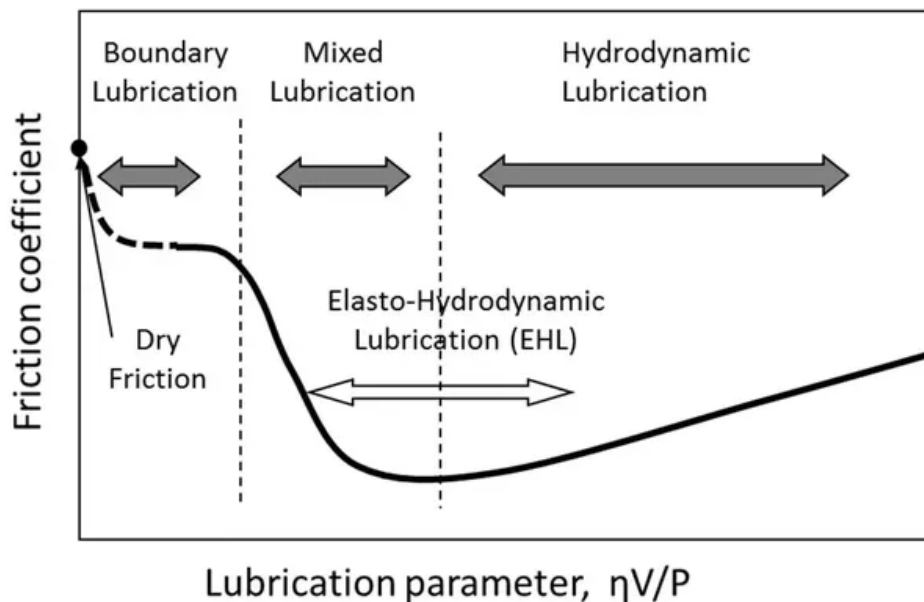
Figure 2-12: Stribeck curve and lubrication regimes [55]

2.7.1 Hydrodynamic lubrication regime

Lubricant film is much thicker than surface roughness in this regime and there is no solid-solid contact between asperities. Friction coefficient is low in this regime and load is taken by the oil film. Elastic deformation is not expected due to the low pressure contact. As seen in Stribeck curve, increasing specific film thickness leads to increase in coefficient of friction in this regime.

2.7.2 Elastohydrodynamic lubrication regime

Two surfaces are fully separated similar to hydrodynamic lubrication. The specific film thickness is higher than 4 or 5 and the lowest coefficient of friction is achieved under this lubrication regime. Elastic deformation occurs in this

regime due to the high pressure. Fatigue failure due to the crack propagation is reported under this lubrication regime. However, a very low wear rate has been observed for elastohydrodynamic lubrication regime (EHL). This regime is very common in rolling element bearings.

2.7.3 Mixed lubrication regime

In mixed lubrication regime, coefficient of friction is inversely proportional to specific film thickness. Fluid film is not continuous in mixed regime and partial solid-solid contact is observed in this type of lubrication. Both elastic and plastic deformation is expected. The specific film thickness in this regime is between 1 and 4.

2.7.4 Boundary lubrication regime

The specific film thickness in this regime is less than 1 and thickness of lubricant is not enough to keep the distance between rubbing surfaces. Thus, asperity contact occurs in large extent and severe wear is expected in this regime. The highest coefficient of friction is seen in this lubrication regime and the load is fully carried by the contacting asperities. Physical and chemical characteristics of the metal surface play the most important role in this lubrication regime.

2.8 Major failure mechanisms in bearings

In the following subsections, a review will be provided on the major failure mechanisms in bearings. This will shed some light on the most important mechanisms that needs to be understood concerning the failures in lubricated contacts.

2.8.1 Fatigue

Fatigue failure occurs under repeatedly applied loads at lower stresses than the actual material strength. Cyclic loads, which are very common in bearings, form microcracks and these cracks propagate until they reach the critical size and cause failure in the material. The susceptibility of the steel to fatigue depends on its microstructure. The effect of tempering and austenitisation temperatures on crack growth rate of AISI 52100 steel is shown in Figure 2-13. As it is seen, crack growth rate is faster at higher austenitisation temperature and lower tempering temperature. This is attributed to the fact that the amount of carbon in solid solution is affecting the martensite structure properties and it changes by both tempering and austenitisation temperatures [2].

2.8.2 Rolling contact fatigue

Rolling Contact Fatigue (RCF) is the main failure mode reported in components with rolling/sliding contact such as rolling element bearings. This type of failure is likely to happen even if bearings are properly loaded, lubricated and kept free from any contamination. There are some differences between RCF and classical fatigue [56]:

- RCF happens in a small dimension (less than 1000 µm)
- RCF is a multiaxial fatigue mechanism in contrast to classical fatigue
- The loading history is nonproportional at a point below the surface in rolling contact fatigue
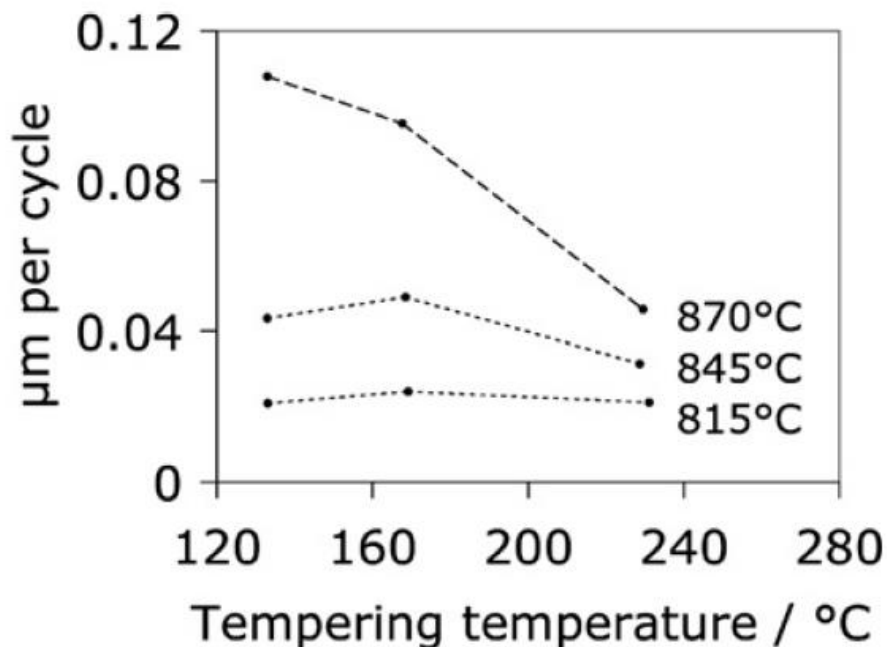
Figure 2-13: AISI 52100 steel crack growth per cycle at ΔK=10 MPam$^{1/2}$ at different austenitised temperatures [2]

In the process of RCF, cracks are formed by the action of cyclic stress. Cracks initiate either from subsurface origins such as inclusion in the steel or from stress risers on the surface such as surface defects. The initiated cracks from material inclusion can branch towards the surface, remove the material and cause outer surface spall. This mechanism is shown in Figure 2-14 and this is the main reason of failure in bearings with a smooth surface working under EHL regime [56]. These cracks can also branch towards the center of material and eventually lead to complete failure of the component.
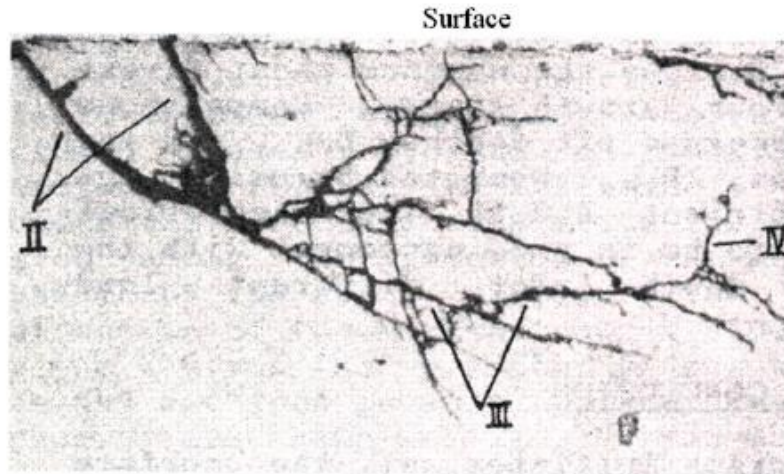
Figure 2-14: Sub-surface cracks due to the RCF [56]

On the other hand, surface defects such as dents, grinding furrows and scratches locally increase stress concentration causing crack formation. Cracks initiated from surface defects propagate at a shallow angle (15-30 deg) towards sub-surface. When these cracks reach a critical size, they branch towards the surface and remove a piece of surface forming pitting (Figure 2-15). This mechanism of failure accelerates when the lubricant and/or corrosive contaminants squeeze into the crack and increase crack propagation rate [56].
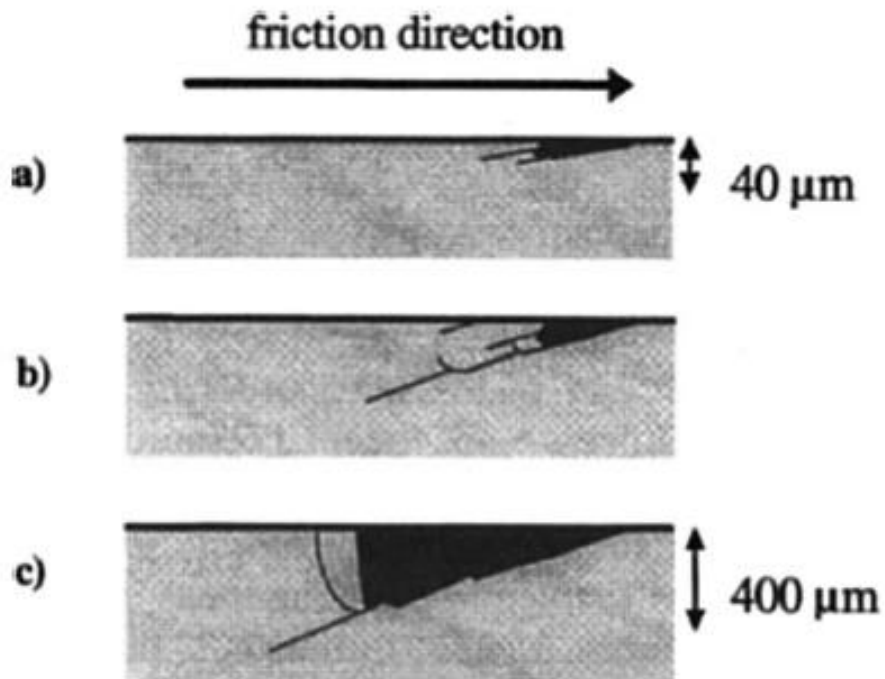
Figure 2-15: Surface originated pitting mechanism [56]

The effect of lubricant on crack appearance is schematically shown in Figure 2-17. The spalls which form in absence of lubricant pressure have a well-defined edge. However, the shape and edge of the spalls that form in presence of lubricant pressure are not significant [2].

2.8.3 Micropitting

Micropitting is currently recognized as a significant failure mechanism in mechanical elements such as gears and bearings. Generally, micropitting is a form of wear process associated with tangential shear cycles of stress at asperity level. It is categorized as a type of RCF at asperity level. The contact fatigue is not only related to metal-metal asperity contact, but also to pressures transmitted by the fluid film between two surfaces. In the early stages of micropitting, numerous microcracks initiate at or very close to the surface. These shallowly inclined cracks propagate into the material in the direction opposed to that of the surface traction and eventually rupture occurs to form shallow micropits. Plastic deformation and fatigue cracking were seen during this type of failure. Spikes et al. [52] reported plastic deformation and fatigue cracking during failure process. They reported a nearly inverse relation between micropitting damage and the wear in sliding contact for lubricant contains secondary ZDDP for various concentrations between 0-1.3 wt%.

Based on the previous studies, micropitting is promoted due to some or all of the following:
- Low lambda ratio (thin film thickness compare to the surface roughness) [50, 52]
- Small slide-to-roll ratio [52]
- Difference in hardness between two rubbing surfaces, the softer surface is more susceptible to micropitting [52]
- Higher temperature [57]
- Some additives in the lubricant promote micropitting [50, 51]

Many works and efforts have been made in recent years to bring more understanding about the influential parameters on micropitting [50-52, 57, 58]. The main influential parameters on micropitting are believed to be roughness, pressure, hardness, sliding speed, temperature and lubricant [50, 57]. Oila et al. [57] evaluated the effect of these parameters on micropitting and showed that at very high contact pressure (P_0=2.2 GPa), micropitting initiation is almost independent of other factors. They also observed that increasing

temperature from 60°C to 100°C decreased the critical number of cycles N_0 for micropitting initiation from 17000 to 4000. It has also been found that the effects of speed and slide-to-roll ratio are much higher than the other parameters. It was also reported that micropitting progression rate is significantly higher when phase transformation of the material or martensite decay happens. The plastic deformation of asperities leads to considerable heat generation which is the main driving force for martensite decay and eventually micropitting.

Hoeprich [58] believed that hydrogen could also increase the rate of microcrack/pit development. He concluded that dark etching effect in gears is happening due to the diffusion of hydrogen from the lubricant into the steel as a result of tribological reactions in asperity contacts. Therefore, the role of lubricants, additives, contaminants and flash temperature take on another dimension. In another piece of research, Nedelcu et al. [59] revealed the role of water concentration in oil on micropit density on metal surfaces as shown in Figure 2-16.
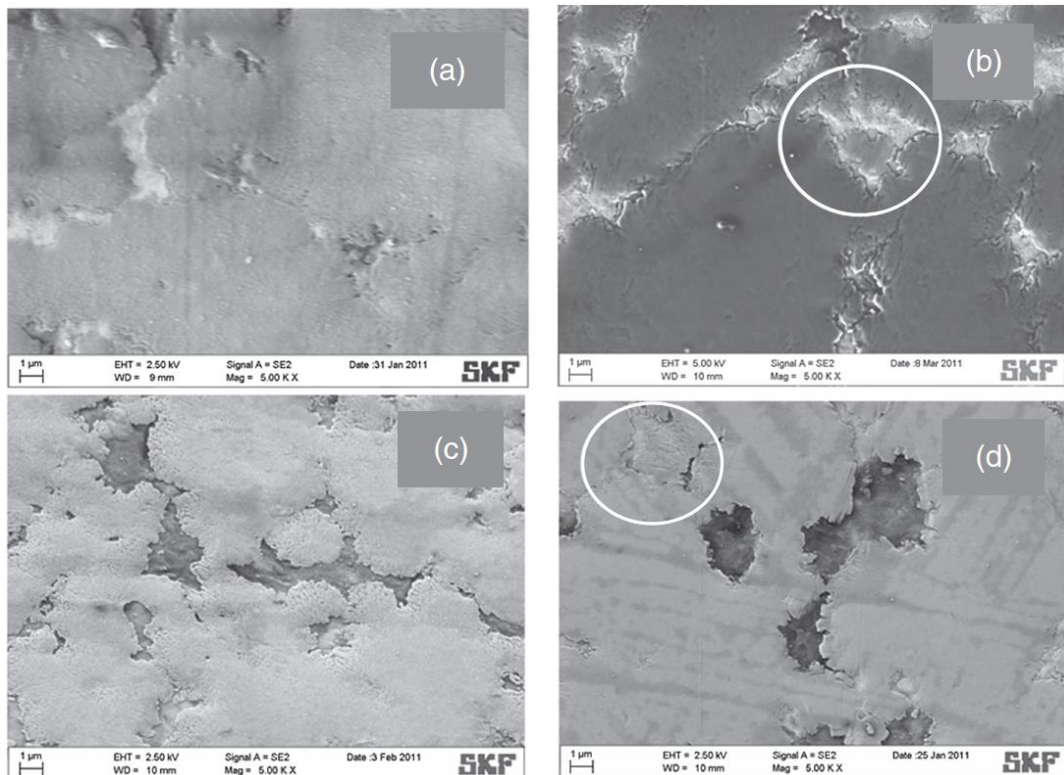
Figure 2-16: SEM micrographs of 52100 metal surface after 24 hours four-ball tribology test in PAO lubricant containing ZDDP and different amount of waters (a) 0% (b) 0.5% (c) 1% (d) 2% [59]

2.8.4 Fretting wear

Vibration causes fretting and influences the quality of bearings. When the movement between the surfaces has the approximate size of few micrometers, fatigue cracks can nucleate and propagate. Fretting wear can also produce debris and cause three-body wear. The problem becomes more severe when debris retains in the affected area. Another observation in fretting wear is removal of the material and its transfer to the opposite surface.
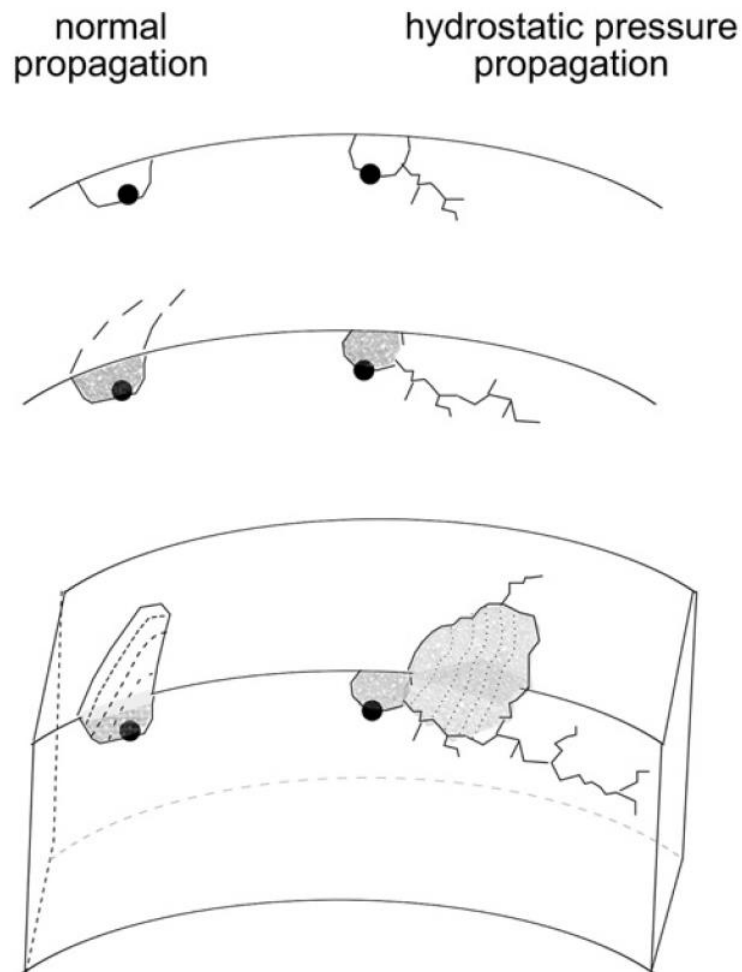
Figure 2-17: The influence of lubricant hydrostatic pressure on the appearance of spall [2]

2.8.5 Stress corrosion cracking

The failure evidence of HE and Stress Cossion Cracking (SCC) is very similar. However, SCC accelerates by anodic polarization and HE becomes faster under cathodic polarization. Crack propagation in SCC promotes by anodic dissolution at the crack tip. However, HE promotes by hydrogen generation due to cathodic polarization.

2.8.6 Hydrogen effects

Hydrogen can significantly accelerate fatigue failure by damaging the mechanical properties of the steel. The effect of hydrogen on bearing failure as well as the suggested mechanisms will be discussed in detail in section 3.5.

2.8.7 Moisture corrosion

Corrosion reactions are usually involved with water and oxygen. This makes water an important subject of study for the failures in corrosive environments. The effect of water on bearing failure will be discussed in detail in section 3.7.

2.9 Summary

Fundamentals of tribology including lubrication theories, friction and wear were discussed in this chapter. The type of steel used for manufacturing of bearings and the major failure mechanisms of bearings were mentioned briefly. Chapter 3 will focus on the sources of hydrogen in steel and the effects of hydrogen on steel behaviour. The effect of hydrogen on failure mechanisms of lubricated contacts will be discussed in details.

Chapter 3 Hydrogen in lubricated contacts

3.1 Introduction

This chapter reviews the effect of hydrogen on fatigue failure. The behaviour of hydrogen in metals with the focus on iron base alloys, especially those employed in bearings, is described. Moreover, the published works that support the idea of hydrogen being present in lubricated tribological contacts are discussed. This is shown that hydrogen uptake from lubricated contacts could be a plausible reason behind many of mechanisms attempting to justify the chemical effect of lubricant on bearing failures.

3.2 Hydrogen solubility in iron

Hydrogen, carbon, nitrogen and oxygen are particular non-metal materials that interstitially dissolve in metals. Atomic hydrogen has a remarkable ability to diffuse within many metals due to its small size. The diffusion rate of hydrogen is 10^{12} times higher than that of carbon at 293 K [60]. Hydrogen is capable of reacting with strongly electropositive alkali and alkaline earth metals similar to halogen gases. Hydrogen acts as anions, within these metals, and produce metallic ionic hydrides. It is not very likely for hydrogen to interact with less electropositive transition metals and formation of metallic hydrides. However, hydrogen molecules can dissociate on the metal surface and generate atomic hydrogen. Hydrogen atoms are small enough to diffuse into the metal and sit in interstitial holes in the metal crystal lattice forming interstitial compounds. Overall solubility of hydrogen in BCC iron metal can be estimated using equations (3-1) and (3-2) developed by Fukai [61]:

$$S_H = \sqrt{\frac{P}{P_0}}\, e^{-6} e^{\frac{-0.25}{kT}} \tag{3-1}$$

$$P_0(T) = \frac{(4\pi kT)^{\frac{7}{2}} m^{\frac{3}{2}} I_m}{2h^5} \tag{3-2}$$

where S_H is hydrogen solubility (H atoms/Fe atoms), I_m is the moment of inertia for a hydrogen molecule, m is the mass of hydrogen atom, T is temperature and h is the partial enthalpy. The lattice defects and impurities in iron increase hydrogen solubility compared to the value measured by equations (3-1) and (3-2). The solubility of hydrogen has been estimated to be around one atom per 10^7-10^8 iron atoms in a perfect iron crystal bulk in equilibrium with hydrogen gas at 300 K [62]. Figure 3-1 illustrates the hydrogen solubility limits in iron as a function of temperature and pressure. Hydrogen solubility significantly increases at higher temperature and higher pressure [3].
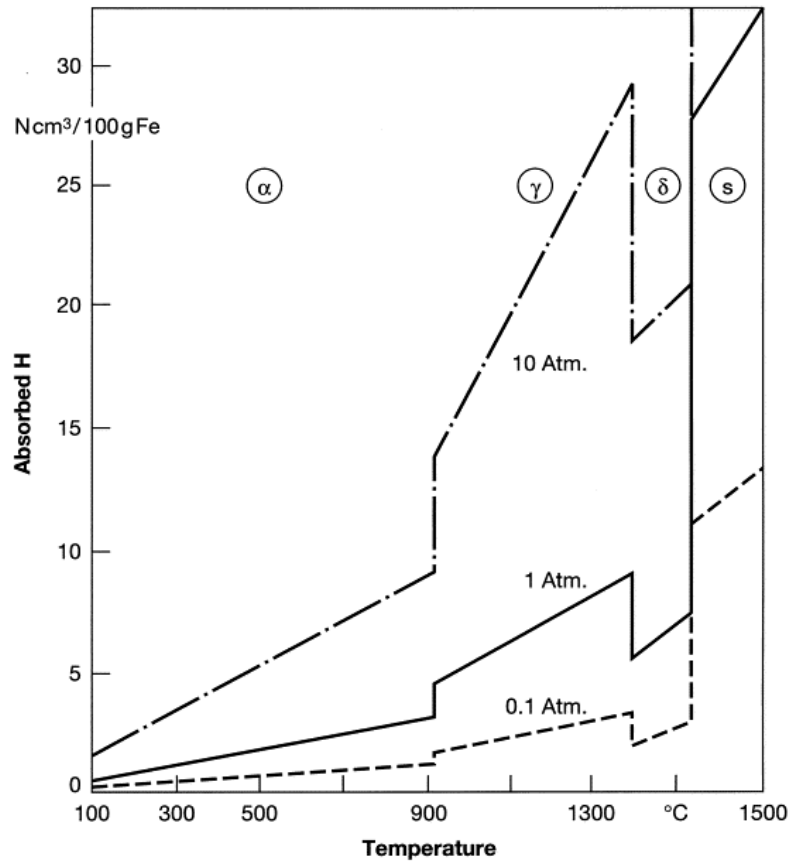
Figure 3-1: The effect of temperature and pressure on hydrogen solubility in iron [3]

3.3 Hydrogen trapping

Hydrogen diffusion rate into the steel depends on the temperature, material composition, microstructure, heat treatment and stress history. Figure 3-2 shows the dependence of diffusion coefficient of hydrogen and the steel microstructure [3]. Diffusion of hydrogen into steel also depends on plastic and elastic deformation. Deformation not only accentuates hydrogen diffusion into steel but also directs it toward the area which tensile stresses concentrate [63].

Hydrogen can be sustained within irregularities in the steel beyond its solubility limit (~ 1 ppm) [64]. The likelihood of this occurrence depends on the density of traps and concentration of hydrogen. Vacancies, grain boundaries, alloying elements, inclusions, dislocations, micro-voids, and interfaces are identified as possible hydrogen trapping sites in steel [64]. Hydrogen in steel can exist in two forms; as non-mobile or mobile/diffusible. Diffusible hydrogen which is trapped in weak reversible traps can maintain their mobility, whereas non-mobile hydrogen refer to hydrogen atoms which are trapped at irreversible traps.

28
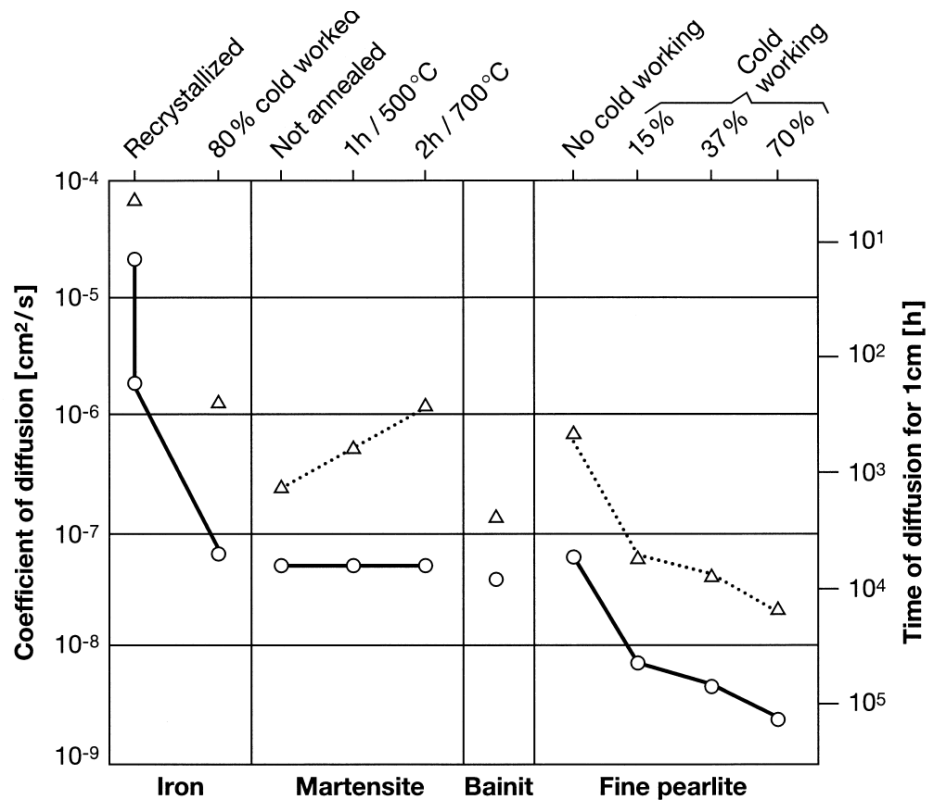
Figure 3-2: Hydrogen diffusion (solid line) and effusion (dotted line) coefficient in different microstructures [3]

Trap density is dependent on steel purity, manufacturing processes, heat treatment and cold working history. Some of the traps such as grain boundaries are saturable as they have a finite capacity for hydrogen atoms. On the other hand, nonsaturable traps can accommodate the large volume of space for hydrogen storage and tend to expand under increasing hydrogen pressure. Void is an example of nonsaturable trap since the amount of hydrogen in the void is increasing in higher hydrogen lattice concentrations. If traps fully filled up with hydrogen, the bulk of hydrogen diffuse through the steel with no more interaction with the traps giving higher diffusion rate similar to that in the flawless lattice. Dislocations have a tendency to move along grain boundaries and the trapped hydrogen in dislocations can be swept along leading to higher rate of hydrogen transport compared to its movement by lattice diffusion mechanism. Huang et al. [65] studied the hydrogen induced cracking susceptibility of high strength low alloy steels in a H_2S environment. Their investigation showed that hydrogen atoms diffuse to some areas that contain defects such as inclusions and segregation regions and become entrapped. The hydrogen pressure increases in these zones and when it reaches a critical value, the crack will be initiated. They reported that a larger amount of the inclusions make steels more susceptible to hydrogen cracking.

29

The results demonstrate that increasing the volume fraction of the inclusions in the steel from 1.23% to 4.13% will increase the hydrogen induced crack sensitivity ratio from 0.10% to 8.06%. On the other hand, the hydrogen diffusion is lower in the steel with larger amount of inclusion mainly due to the more hydrogen entrapment [65].

3.4 Hydrogen embrittlement mechanism

The hydrogen damage in steel is mostly irreversible. Numerous studies attempted to propose a hypothesis to explain the mechanism of HE in steels [66-69]. However, there is still no consensus on one single theory. The most popular one relates the reduced fatigue life of steel to enhancement of dislocation plasticity. This happens as a result of reducing barriers to dislocation motion. Some of the proposed mechanisms for HE are discussed below [64].

a) Precipitation at internal defects theory suggests that hydrogen atoms accumulate in voids. The atomic hydrogens in the void recombine and form molecular hydrogen gas. Consequently, an internal gas pressure adds to the external load on the sample increasing the likelihood of premature fracture.

b) De-cohesion model suggests that dissolved hydrogen weakens atomic bonding in steel. Therefore, less energy is required for rupture to occur.

c) Hydrogen accumulation at the crack tip leads to lower surface energy. As a result, crack growth will be easier and more feasible.

d) The dissolved hydrogen produces methane gas molecules (CH_4) in reaction with carbon in the steel. This causes loss of material strength due to internal decarburisation of the steel. Moreover, methane molecules are insoluble in the steel and accumulate along grain boundaries creating voids.

e) Association with dislocations theory suggests that hydrogen in steel forms cottrell atmosphere around dislocations. This reduces plastic deformation and hardens the metal. Plastic deformation is required to blunt the crack tips. As a result, crack propagation promotes in presence of hydrogen. The TEM observations showing the interaction between dislocations and hydrogen have shown that yield stress decreases as a function of hydrogen pressure [70].

3.5 Negative effects of hydrogen on steel performance

Hydrogen makes bearing steel more susceptible to fatigue cracks and decreases ductility, elongation and toughness [71-73]. All the studies confirm that steel fatigue life significantly shortens in presence of hydrogen [12-14, 71, 74]. Many works have been made in recent years, due to its industrial importance, to bring more understanding about the role of hydrogen in steels. It has been seen that the risk of HE depends on different factors such as steel microstructure, grain size, temperature, load, the presence of alloying elements, etc. [65, 75, 76]. The total hydrogen content in bearing steels following their manufacture is as large as 8 mass-ppm which is not acceptable in the final bearings. So, a variety of processes such as vacuum induction melting are employed to reduce the hydrogen concentration to less than 1 mass-ppm [2]. Hirth [77] summarized the effect of hydrogen on iron and steel as follows:

- Hydrogen does not affect material's yield stress. On the other hand, it reduces ductility and the critical stress intensity factor for crack propagation
- Hydrogen lowers plastic zone size as well as plasticity
- Fractography analysis showed brittle cleavage in presence of hydrogen

Nanninga et al. [78] found that steel hardness has a stronger influence on HE compared to the steel microstructure or the chemical composition. It has been revealed that the effect of hydrogen on high strength martensitic structures is much more detrimental than steels with lower hardness such as the ones with ferritic or austenitic microstructures [79].

Sojka et al. [80] have investigated the behaviour of high strength multiphase steels in presence of hydrogen. Their results showed that HE manifested itself mainly by loss of plasticity and transgranular cleavage fracture. Tiwari et al. [64] investigation revealed that hydrogen charging not only lowered the ductility of the steel but also influence the fracture surface and the size of dimples.

Figure 3-3 illustrates the effect of hydrogen on fatigue crack growth mechanism. It shows that the crack tip is sharper in presence of hydrogen [81]. This is in line with other reports where it was shown cracks are thinner and their tips are sharper in presence of hydrogen [64, 73]. This is mainly due to the fact that hydrogen atoms diffuse and concentrate near a crack tip. The accumulation of hydrogen near the crack tip enhances further crack opening

by slip and crack growth continues without the plastic zone becoming large at the crack tip [81].
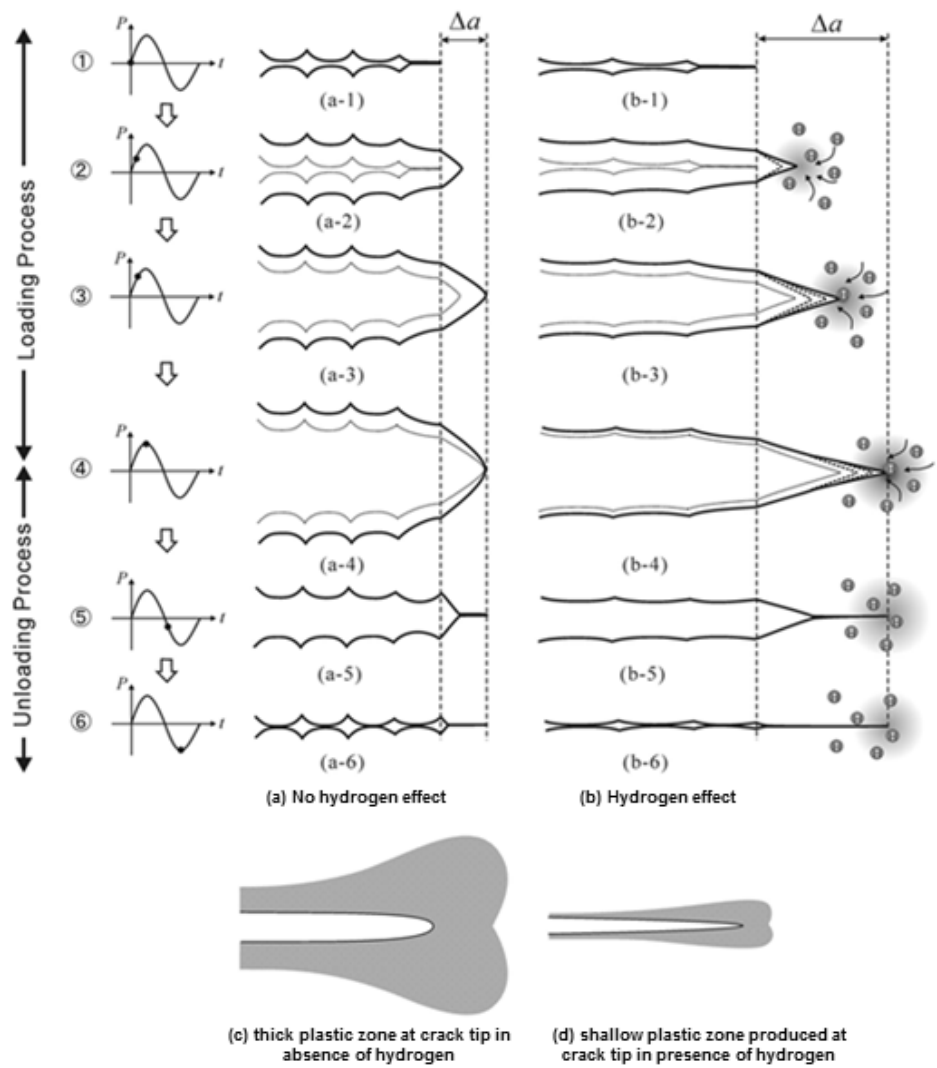
Figure 3-3: Fatigue crack growth mechanism in presence and absence of hydrogen [81]

It has been proven that a critical quantity of hydrogen in the steel is required to see the adverse effects on mechanical properties. These negative effects lead to permanent damage to the steel; these properties never recover even after removal of hydrogen from steel. The critical concentration of hydrogen which causes HE in steel is reported to be around 0.2 ppm [5] while the critical hydrogen content for premature fatigue failure has been reported around 0.4 ppm by Murakami et al. [81]. Hydrogen impact on mechanical properties of the steel depends on two processes. Firstly, the diffusion rate of hydrogen in the steel. Secondly, hydrogen interaction with the trapping sites within the matrix. A tensile test result shown in Figure 3-4 illustrates the negative effect of hydrogen on steel [2].
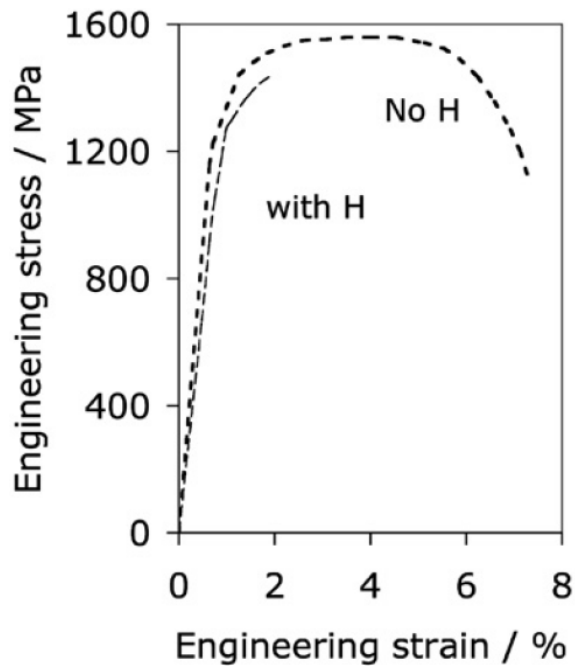
Figure 3-4: The effect of hydrogen charging on the tensile test of martensitic steel (strain rate = 8 x $10^{-5}s^{-1}$) [2]

Figure 3-5 shows that bearing fatigue life will dramatically decrease with an increase in the concentration of hydrogen in steel. Longer fatigue life of 440C is related to lower hydrogen solubility in 440C compared to AISI 52100 [2]. In Figure 3-6, the effect of hydrogen charging and fatigue test frequency on the crack growth rate are shown. It can be seen that *da/dN* (crack growth rate as a function of number of cycles) increases in hydrogen charged sample and it decreases in higher frequencies since hydrogen does no have enough time to concentrate at crack tips. To validate this hypothesis, an experiment was conducted on austenitic stainless steels where the diffusivity of hydrogen is slower than its diffusivity in ferrite. Results of the experiments suggested that hydrogen can only influence the fatigue life of austenitic steel when the test is carried out at a very low frequency (0.0015 Hz) so that hydrogen has enough time to diffuse towards crack tip [64, 73].

Uyama et al. [14] and Ciruna et al. [71] observed that hydrogen content in the AISI 52100 bearing steel is one of the prime reasons for reduced bearing life. They found that fatigue life of AISI 52100 bearing steel ball is inversely proportional to the hydrogen content in the steel. They correlated the reduction of fatigue life of the bearing steel (from 10^6 to 10^3 revolutions) with the diffusion of 4 ppm hydrogen into the steel as a result of 50 min electrolytic and chemical hydrogen charging. Uyama et al. [14] proved that increasing hydrogen content in the steel from 0.03 mass-ppm to 1.2 mass-ppm, decreases steel fatigue life

33

more than one order of magnitude. They pointed out that the shorter life of hydrogen-charged samples is due to accelerating the localised microstructural changes under RCF test.
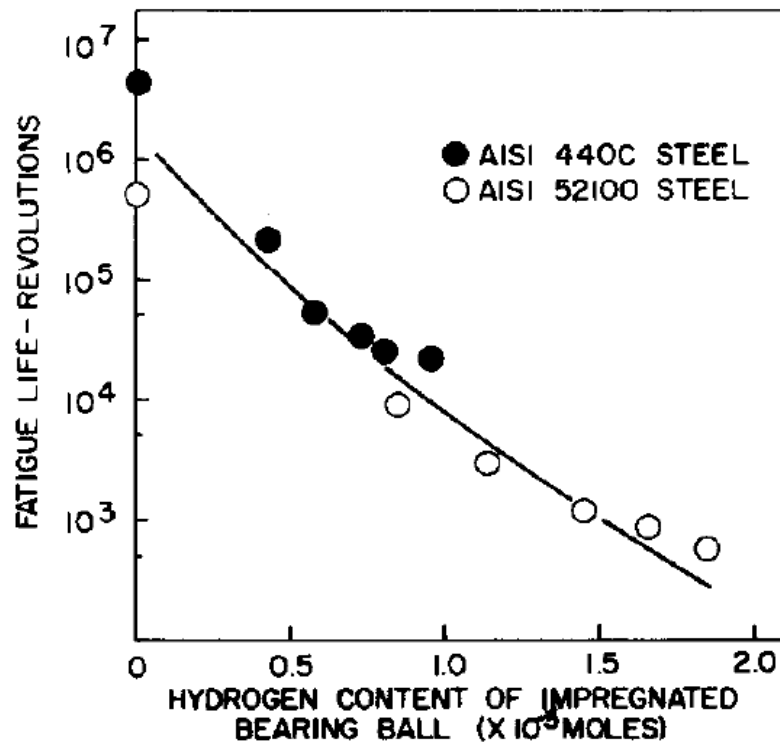
Figure 3-5: Fatigue life of two different steels with different hydrogen concentrations in steel [2]
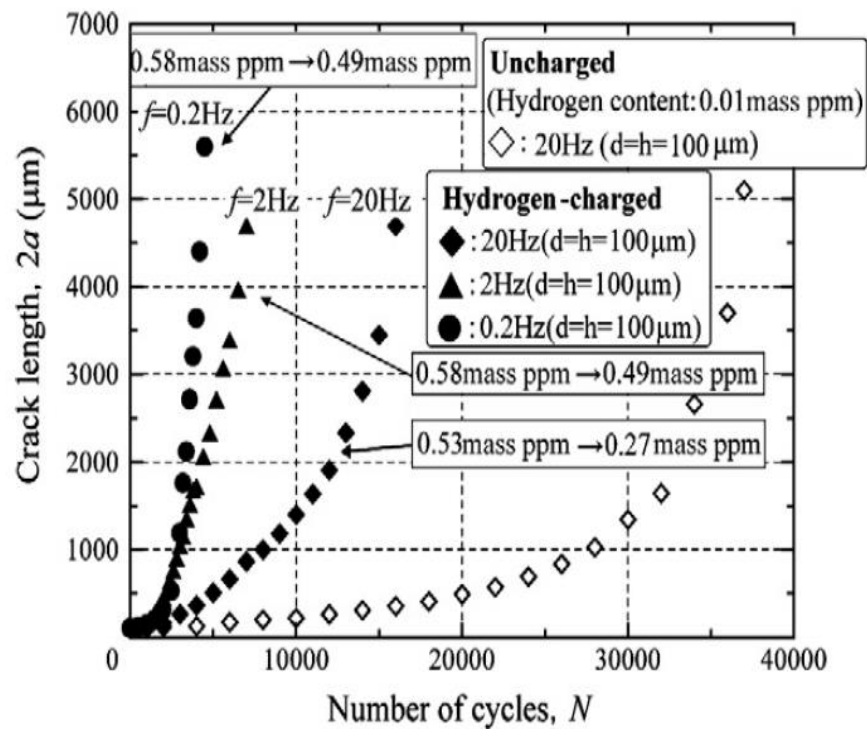
Figure 3-6: Effect of hydrogen and frequency on crack length [73]

Similarly, the shorter fatigue life has been reported as a result of the generation of hydrogen because of decomposition of grease [6]. The effect of grease lubrication on hydrogen induced failure of bearings was investigated by Tamada et al. [6]. A drastic failure due to brittle flaking was reported for tested bearings. Hydrogen was mentioned as the main reason for promoting brittle flaking in these bearings. The mechanism of failure was discussed and it was concluded that an elevated hydrogen concentration leads to microstructure change in steel which is called "black needle" structure. This type of microstructure is prevalent in RCF failure in presence of interstitial hydrogen [82].

In addition to the effects of hydrogen on mechanical properties of steel, tribological parameters can also change when hydrogen adsorbs on the surfaces of two rubbing component. It has been reported that coefficient of friction reduces in presence of hydrogen on the surface [16].

3.6 The sources of hydrogen

Hydrogen contamination can enter the steel component in various stages of its life. There are numerous reports on steel components experiencing premature failure due to the adsorption of hydrogen from hydrogen-containing environments such as pressurised hydrogen gas and sour gas (H_2S) containing fluids. Results presented in Figure 3-7 show that H_2S contamination in oil significantly reduces the fatigue life of AISI 52100 steel [71]. Hydrogen uptake is also promoted due to the corrosion/chemical reactions, electroplating, and applying cathodic protection. Hydrogen could also have been entrapped in the steel lattice during metallurgical processing or fabrication of steel and cause embrittlement later [3, 64].

Hydrogen-induced failures have also been reported in hydrocarbon lubricated contacts. Hydrogen-evolution from lubricated contacts and its absorption into the material is a serious threat to industrial components such as bearings. Entering water into lubricants, running RCF tests in hydrogen gas atmospheres, applying electrical currents across contacting surfaces and using special lubricants that increase hydrogen release are some of the most common ways for promoting hydrogen generation in tribo-contacts. Many physical and chemical interactions occur in lubricated contacts making them very complex. Localised high temperature makes the situation even worse. Variables such as lubricant viscosity and contaminations further complicate understanding of the contact area. Therefore, it is crucial to understand the

role of individual parameters as well as their synergic effect in presence of other factors. Studies showed that hydrocarbon lubricants decompose and generate hydrogen under repeated stress in rolling contacts due to the frictional heat and shear stress [12].
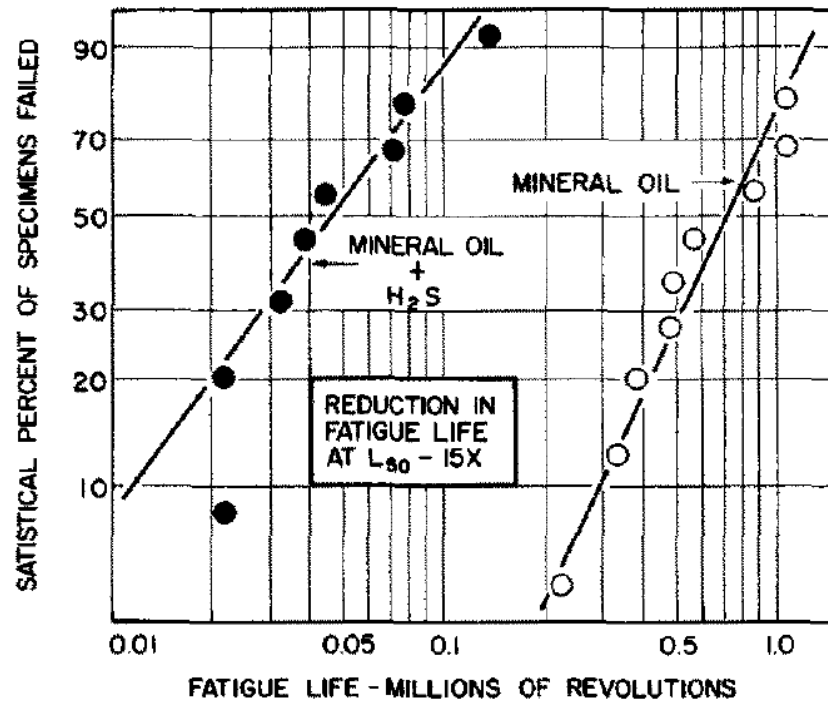
Figure 3-7: The effect of H₂S on the fatigue life of 52100 steel [71]

Hydrogen uptake into the steel is tremendously affected by the concentration of hydrogen on the steel surface. The concentration of hydrogen on the steel surface in lubricated tribo-contact changes when hydrogen is produced due to decomposition of lubricant, water contamination in oil, corrosion reactions or other tribochemical reactions [5, 9, 11]. Tribological parameters influence lubricant decomposition rate and hydrogen generation on the metal surface. It has been revealed that lubricant decomposition rate is directly proportional to sliding velocity and the applied load; a critical minimum load is also needed to activate lubricant decomposition reactions [8, 9, 11]. The increased number of subsurface cracks in presence of certain lubricants or additives may point to either more asperity contact or embrittlement of the material.

Atomic hydrogens, generated on the surface, interact with steel material to induce subcritical crack growth under the action of stresses leading to HE and materials ductility diminution. It has also been seen that hydrogen atoms generated on the metal surface diffuse into steel and tend to collect at some sensitive metallurgical areas called traps; once the hydrogen content exceeds a critical level, hydrogen embrittlement-induced flaking happens [13]. It has

also been shown that if a lubricant film is subjected to shearing between two sliding surfaces, both hydrogen diffusion and hydrogen adsorption on the metal surfaces will increase. The higher sliding velocity results in higher hydrogen adsorption on the metal surface [7].

3.7 The effect of water contamination in lubricant on fatigue failure

Water is considered as one of the sources of contamination in bearing's lubricant which usually enters from the existing humidity in environment [83, 84]. A linear relationship was observed between diffused water in the lubricant and the relative humidity of the air. Water can also contaminate the lubricant due to the leakage of heat exchangers or during cleaning and washing the machine or as a by-product of combustion, oxidation and other chemical/tribochemical reactions. Water has negative effects on both lubricant and the component being lubricated. It can change the lubricant properties by oxidation and also affect the contacting surfaces by corrosion and HE. It was also found that water in lubricant accelerates the fatigue failure in the steel [85]. The condensation of water in micro-cracks might be the reason for promoting this type of failure.

There is a finite solubility degree for water in oil depending on temperature (Figure 3-8), pressure [86], and the additive types [79]. It is seen from Figure 3-8 that higher temperature leads to higher water saturation level in turbine oil. The water solubility degree in the lubricant also depends on the composition of the lubricant. Higher concentration of water dissolves in ester based lubricants due to the polar functional groups in its structure. These groups interact with water through hydrogen bonding. It has been shown that formulated polyolester and formulated dibasic acid ester oils dissolve 10 times higher equilibrium dissolved water contents at a relative humidity of 41% compared to formulated mineral oils [87]. Water appears as free water in the lubricant above its solubility limit. Free water accelerates oxidation of oil and negatively affects performance of antioxidant and ZDDP anti-wear additives [59, 88]. Water accelerates decomposition of ZDDP in lubricant [89]. Surface corrosion is also promoted in presence of water in the oil and material loss is accelerated as a result of the oxidative chemical reaction of metal due to the water contamination.
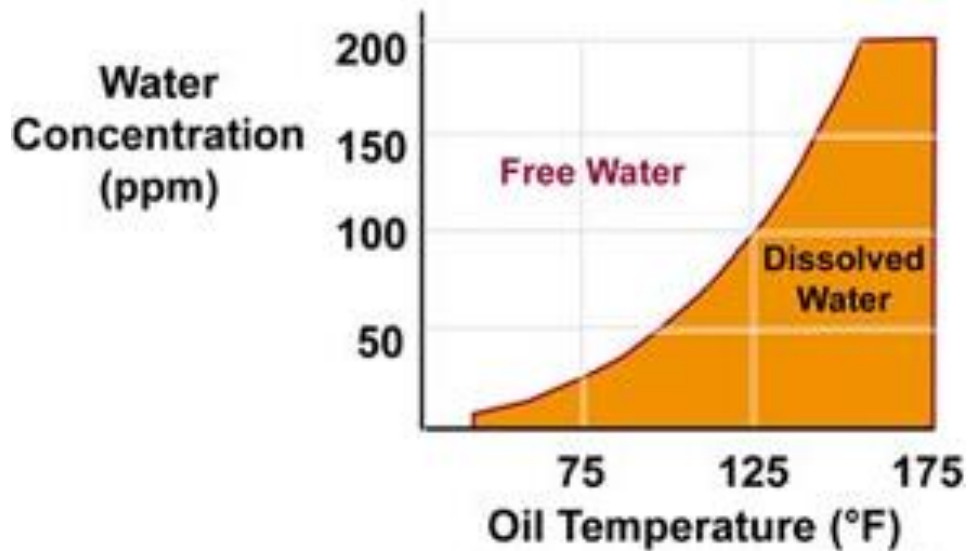
Figure 3-8: The influence of temperature on saturation level of water in lubricant [90]

Water also decreases additive functionality by interfering their adsorption on the surface. Meanwhile, water is attacking rust inhibitors and viscosity improvers. Water in oil also deteriorates the thin protective tribofilm in rolling element bearings promoting metal-metal asperities contact [84]. Liu et al. [91] reported that thickness of EHL film tends to decrease when water added to the base oil (Figure 3-9). Water not only affects the rate of oxidation but also changes types of oxides formed [79].

It has been demonstrated by several investigators that water contamination accelerates failure in lubricated tribological contacts by increasing hydrogen generation and its participation in accelerating crack propagation [5, 84]. Water also promotes failure by affecting tribofilm formation [92]. Lancaster [79] suggested that water can affect lubricant behaviour in lubricated interfaces in several ways:

- In the boundary lubrication regime, the adsorption behaviour of long chain organic compounds is influenced by water. The polyphosphate chain length formed by ZDDP additive in the lubricant is reduced in presence of water [88, 93].

- The protective film that forms on the surface is changed by water contamination in lubricant. Both the film thickness and composition is changed by water.
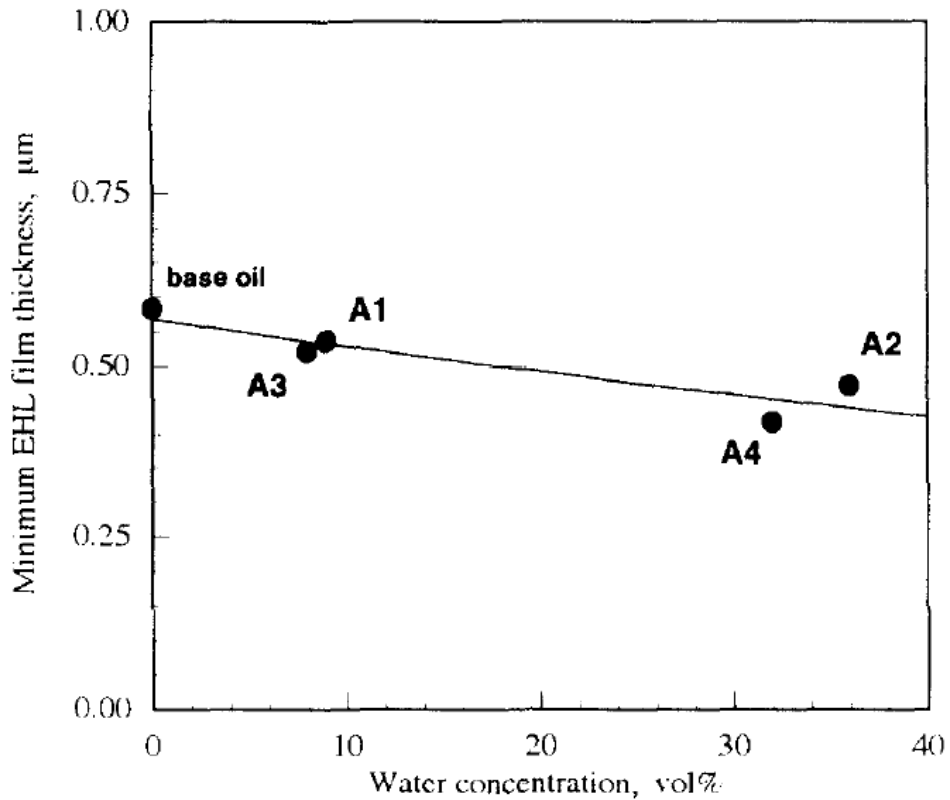
Figure 3-9: Effect of water on minimum EHL film thickness [91]

Cen et. al. [94] used ball-on-disc tribometer to investigate the tribofilm formation in presence of water when a 52100 steel ball is sliding on an AISI 1050 steel disc. The results showed that chemical composition of the tribofilm changes in presence of water when PAO+(2 wt%) ZDDP is used as lubricant. The XPS analyses (Figure 3-10) indicated shorter chains in phosphate tribofilms when water is present. This is due to the depolymerisation of longer phosphate chains. Two mechanisms have been proposed for shorter chain phosphate formation. The first mechanism is the initial formation of longer chain phosphate and then breaking into shorter chains due to the hydrolysis [95]. Another proposed mechanism is the direct formation of shorter chain phosphate in presence of water [88, 94]. Faut et al. [92] reported the same mechanism for tricresyl phosphate additive. Nedelcu et al. [59] also revealed that water contamination in lubricant causes lower tribofilm thickness and reduced length of polyphosphate chains [59]. The equations (3-3) and (3-4) have been suggested for the mechanism [93].

$$7\text{Zn}(\text{PO}_3)_2 + 6\text{H}_2\text{O} \rightarrow \text{Zn}_7(\text{P}_5\text{O}_{16})_2 + 4\text{H}_3\text{PO}_4 \qquad (3\text{-}3)$$

$$Zn(PO_3)_2 + 3H_2O \rightarrow Zn_2P_2O_7 + 2H_3PO_4 \qquad (3\text{-}4)$$
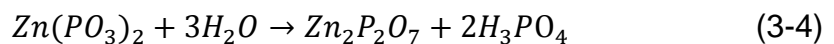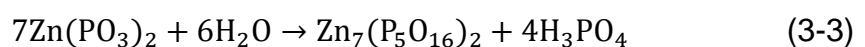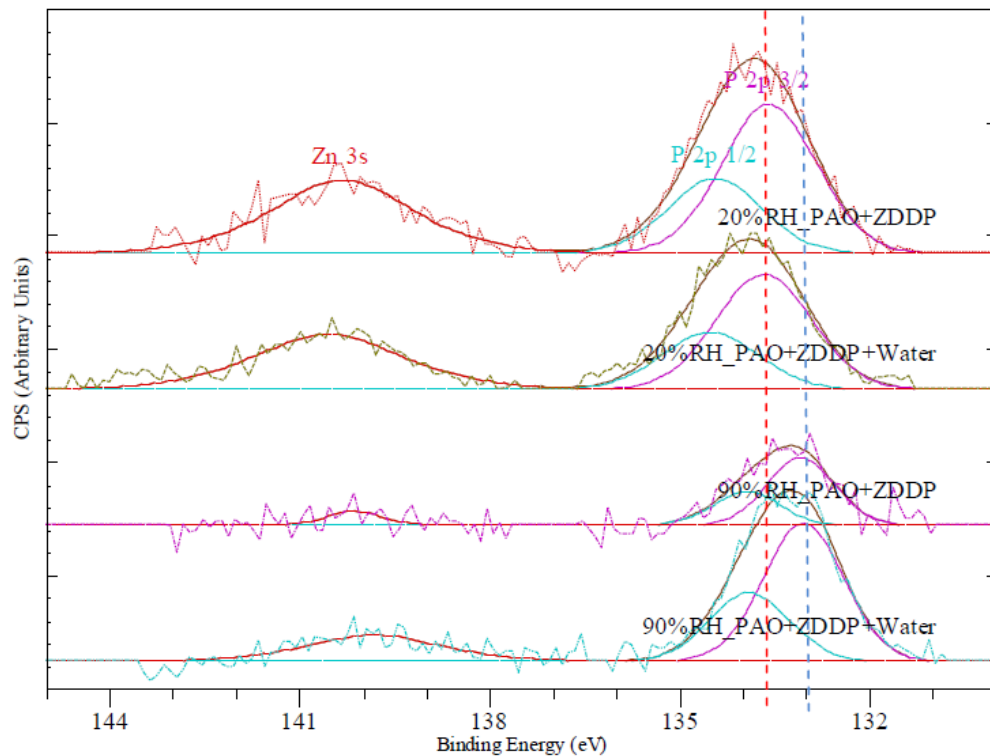
Figure 3-10: XPS spectra comparison of phosphorus element scan on ball wear scar for PAO+ZDDP in different relative humidity and water concentrations [94]

Water contamination in lubricant accelerates RCF [96] leading to acceleration of pitting and shorter bearing life. As presented in Figure 3-11, even very small concentration of water can accelerate bearings failure [71, 79]. Grunberg and Scott [97] showed that 0.002 percent water content reduced the surface fatigue life of steel to 48 percent. Schatzberg and Felsen [98, 99] have concluded that increasing water content from less than 10 ppm to 100 ppm in lubricant causes 43 percent reduction in fatigue life at 9 GPa stress level. Similarly, for the same variation in water content, 48 percent reduction in fatigue life was reported at 7.6 GPa cyclic stresses. The reduced RCF life of steel in presence of water in the lubricant is also reported by Grundberg et al. [100]. They suggested that higher hydrogen uptake from the lubricated contact in presence of water leads to premature failure. Richardson et al. [101] suggested that hydrogen permeation occurs through nascent surface during RCF testing.

Water contamination is considered as one of the main sources of hydrogen in bearings [5, 71, 79]. It is assumed that as soon as the water comes into contact with the fresh metal surface of the fissure formed on the metal surface, it breaks down and generates atomic hydrogen through oxidation process [84]. The generated hydrogen promotes crack propagation by HE through the

40

mechanism described in Figure 3-3. Mizuhara et al. [5] showed that the fatigue life of balls under rolling four ball tests have reduced at low temperature and using butane lubrication. Their research suggested that hydrogen generation on fresh steel surface due to the reactions of butane and water is the main reason for the failure. The generated hydrogen absorbs by steel and causes HE leading to RCF. Grunberg et al. [100] also tested the effect of water contaminated lubricant on fatigue failure of steel in a rolling four-ball machine. The results showed that RCF life of the balls tested under water contaminated lubricant significantly reduced and the hydrogen content of the balls was higher than unused balls. Thermal conductivity measurement of the gas extracted from the samples was examined using hot extraction method in order to quantify hydrogen content of the balls.
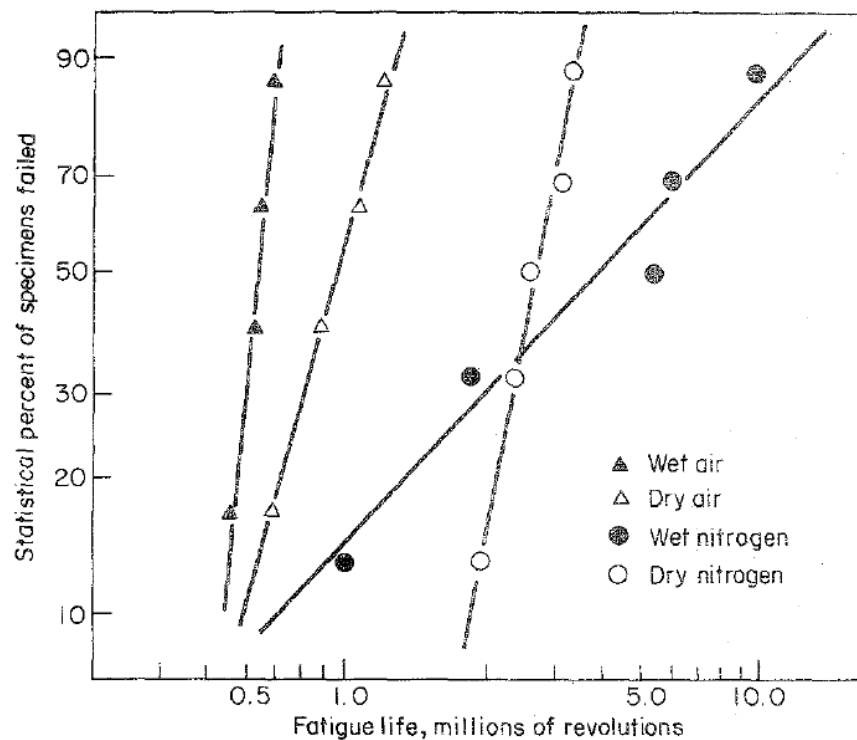
Figure 3-11: Influence of humidity on bearing life [71]

The influence of water in lubricant is more than generating hydrogen. Water can affect additives behaviour by hydrolysis. For instance, simplified reactions of ZDDP (*RO-P*) in presence of water is described in equations (3-5) and (3-6) [46].

$$RO - P - \ + H_2O \rightarrow ROH + \ H^{+-}O - P \qquad (3\text{-}5)$$

$$ROH \xrightarrow{H^+} R' = CH_2 + H_2O \qquad (3\text{-}6)$$

41
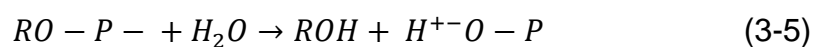
The sum of these two reactions reveals that H_2O acts as a catalyst for the overall reaction (3-7). As presented in equation (3-7), acid is produced as a by-product of ZDDP breakdown in presence of water [46]. The acidity environment is another reason for failure acceleration in presence of water contamination.

$$RO - P - \xrightarrow{H_2O} R' = CH_2 + H^+ {}^-O - P \qquad (3\text{-}7)$$
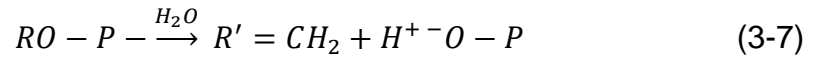
Tribological behaviour of the contact (friction and wear) is also affected in presence of water in the oil [79]. Cen et al. [88] showed that increasing humidity in the environment changes friction and wear coefficient of steel/steel lubricated contact. The results (Figure 3-12) showed that wear is higher in the presence of higher relative humidity. It was also found that the wear rate is always higher in the case of having water contamination in PAO+ZDDP lubricant [88]. The width of wear scar is also increasing in higher relative humidity [88].
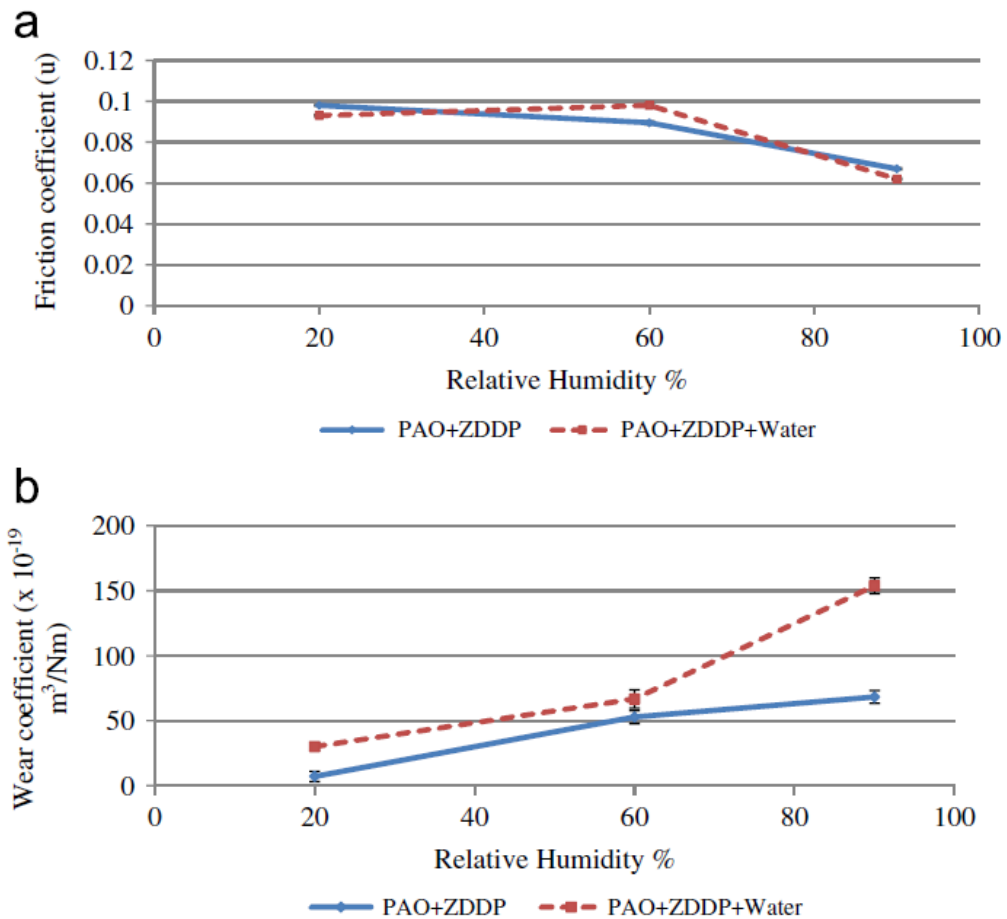
Figure 3-12: Effect of relative humidity on (a) friction and (b) wear [88]

3.8 White etching cracks

White Etching Cracks (WEC) or White Structure Flaking (WSF) in rolling element bearings is another premature failure mode that is linked to a combination of factors including hydrogen diffusion into the bearing steel coming from the lubricated contact [33, 102-104]. WEC causes failure in wind turbine gearbox bearings in as little as 6-24 months of operation which is much shorter than RCF L_{10} life [104]. This phenomenon occurs in the ~1 mm zone beneath the contact surface in a number of applications including wind turbine gearbox bearings and bearings for automotive electrical instruments. The mechanism of this failure is still unknown, particularly due to the difficulties in simulating WEA/WECs in laboratory experiments [103].

Serial sectioning technique and metallographic examination have been used to investigate the initiation and propagation mechanism [33, 103, 104]. It is suggested that WECs propagated from inclusions either from a butterfly or micro-cracking with associated WEA microstructural changes [103].

It was seen that the lubricant, particularly lubricant additives, strongly control WSF formation [105]. WEC and WFS occur under low contact pressure and smaller number of rolling cycles in presence of diffusible hydrogen into the steel. Evans et al. [103] have suggested that an inter-related influence exists between diffusible hydrogen, contact pressure and rolling cycles on the formation of WECs. The results from serial sectioning technique showed that the threshold for WEC formation is a combination of a 1 ppm concentration of diffusible hydrogen, rolling cycle number of $> 10 \times 10^6$ and maximum contact pressure of 1.2 GPa [103]. Altered microstructure was observed in WSF area; this microstructure is appeared white after being etched by Nital solution gives WEA its name.

3.9 Summary

Throughout this chapter, an overview of the effect of water contamination and hydrogen on contacting surfaces, lubricants behaviour, tribological performance and failure mechanism was presented. Based on the aforementioned discussion, it is clear that our understanding of the failure mechanisms that are linked to the tribological hydrogen is incomplete and incapable of suggesting a comprehensive mechanism. The complex interplay between lubricant additives, water contamination, temperature, contact pressure and sliding speed has not been fully understood yet. Therefore, an in-depth study needs to be done to give essential information about the source

and role of hydrogen in these failures. Therefore, various methods that have been used to quantify trapped hydrogen in steel will be discussed in Chapter 4 in order to analyse the possibility of using them to study hydrogen generation from lubricated contacts.

Chapter 4 Detection of hydrogen

4.1 Introduction

This chapter contains a review of several techniques that have been used to measure hydrogen diffusion rate and hydrogen content in the steel. At first a summary of various electrochemical techniques is provided due to their importance in the current study. Then, a review of devices and techniques that are capable of detecting the content of hydrogen in materials is presented.

4.2 Electrochemical techniques

Electrochemical methods have been extensively used to quantify the kinetics of corrosion/electrochemical reactions in aqueous tribocorrosion systems. Measuring the anodic current in electrolyte permits the user to determine the amount of material removed by oxidation compared to mechanical wear in presence of friction. Electrochemical techniques are able to reproduce the real environmental corrosive conditions in an electrochemical cell. As a result, they can be employed to study hydrogen evolution in a corrosive environment. The combination of electrochemical and tribological techniques is a way to study lubricant-surface interactions. In the current study, the electrochemical techniques that were mainly developed for corrosion measurements will be used to evaluate hydrogen generation from a lubricated contact. Therefore, a review of electrochemical techniques is presented in this chapter.

The corrosive environment is simulated by imposing potential on the metal surface in electrochemical measurements. The imposed potential controls metal surface reactivity. In a real situation, actual potential of a metal depends on different parameters such as kinetics of reactions, ion transport condition, temperature, electrolyte, oxide layer formation and external currents [106]. The potential of a metal surface is a relative quantity that needs to be monitored versus a reference point which is called Reference Electrode (RE). The potential of the Standard Hydrogen Electrode (SHE) has been chosen as zero potential point. There are several other REs, mostly work based on the reaction between a metal and a salt solution, that have been developed with a certain offset from zero potential point (SHE). The Saturated Calomel Electrode (SCE) and silver/silver chloride electrode (Ag/AgCl) are two common used REs; the latter is used in this study.

The electron transfer during electrochemical reactions occurs on the metal-electrolyte interface. Therefore, the reactants and products of the reactions

diffuse through the media towards/away from the interface which means both the mass transportation and electron transfer kinetics control the reactions rate on the metal surface. The metal surface always has electric charge when it comes to contact with an electrolyte. This perturbs the distribution of charged species in the electrolyte in adjacent of the metal surface. This phenomenon is called double layer and the metal-electrolyte interface acts like a capacitor in this situation.

The rate of electrochemical reactions can be calculated by measuring the current flow (*I*) and using Faraday's law when the potential is applied between RE and WE:

$$Reaction\ rate = \frac{I}{nF}\ (mol\ s^{-1})\qquad\qquad (4\text{-}1)$$

Where *F* is Faraday constant and *n* is the charge number of the electrochemical reaction.

There are numerous electrochemical methods to monitor and change electrochemical conditions of a metal in electrolyte during friction. The most popular methods are described here.

4.2.1 Open circuit potential

Metal electrodes in an electrolyte reach a stable potential if they are given enough time so that the surface reactions reach equilibrium with the surrounding electrolyte. In Open Circuit Potential (OCP), the potential difference between Working Electrode (WE) and a RE is recorded continuously. The RE is connected in series with a potentiometer and WE to monitor the potential of the metal surface. The RE is usually placed inside a fine capillary filled with electrolyte in order to bring it as close as possible to the metal surface. This technique is very simple and gives useful information about surface state; but, it does not give any information about corrosion reaction rate. This technique is widely used in field applications because of its simplicity. Although this method does not provide any information on corrosion kinetics, it is a very useful method for the qualitative monitoring [106].

Surface potential significantly changes during rubbing when the metal tends to form protective passive layer on its surface. As shown in Figure 4-1, the corrosion potential falls once rubbing is started. However, the potential does not change much with rubbing in active metals. Micro-electrodes and Scanning Reference Electrode Technique (SRET) are employed to measure localized corrosion potential of the wear track and its surrounding [107, 108].
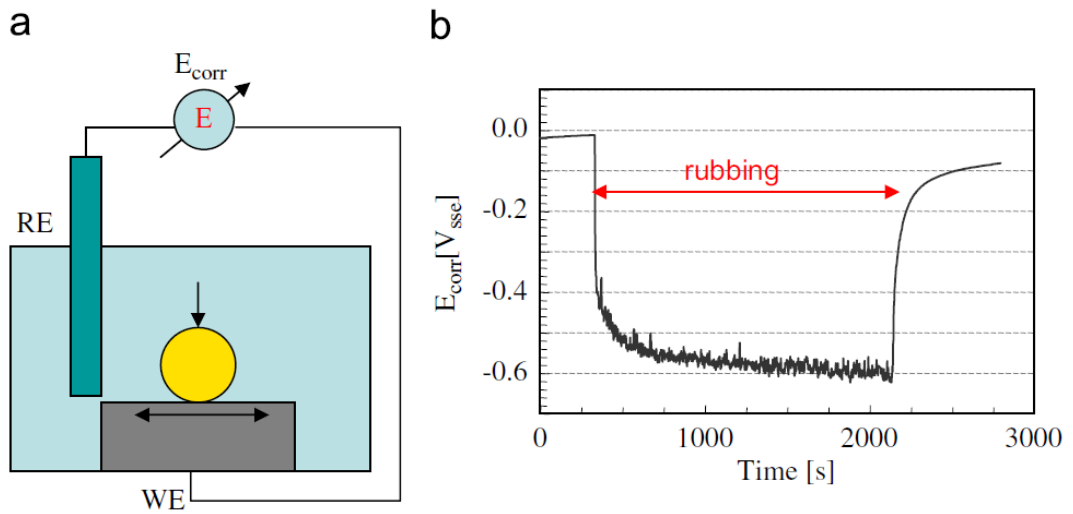
Figure 4-1: (a) Schematic illustration of potential measurement during rubbing (b) corrosion potential of Ti6Al4V alloy in 0.9% NaCl solution rubbing against alumina ball [106]

4.2.2 Potentiostatic test

The equilibrium potential of a metal electrode can be shifted by imposing potential. A three electrode electrochemical set-up (Figure 4-2) is used in this technique to impose a potential to the WE. A third electrode, called auxiliary electrode or Counter Electrode (CE), is needed to control the potential of WE. The CE is made of an inert metal as it should not dissolve or participate in reactions. Platinum has been used in the current study as counter electrode. The three electrodes are used in connection with the potentiostat as shown in Figure 4-2.

The potentiostat keeps the potential constant between RE and WE by passing current through CE and WE. In this method, current is recorded as a function of time identifying the kinetics of the reactions. Figure 4-2 shows that once rubbing started, a significantly higher current is needed to maintain the constant potential between WE and RE. The current oxidises the fresh metal surface after passive layer removal by abrasion. The oxidation current returns to its original value after the rubbing stops and the metal surface becomes passive again. The measured current can be used to calculate the metal's mass loss by corrosion using equation 4-2.

$$m = \frac{I \times M \times t}{n \times F} \qquad (4\text{-}2)$$

Where *m* is the metal mass loss during time *t*, *n* is oxidation valence, *I* is anodic current, *M* is the atomic mass of the metal, and *F* is Faraday's constant [106].
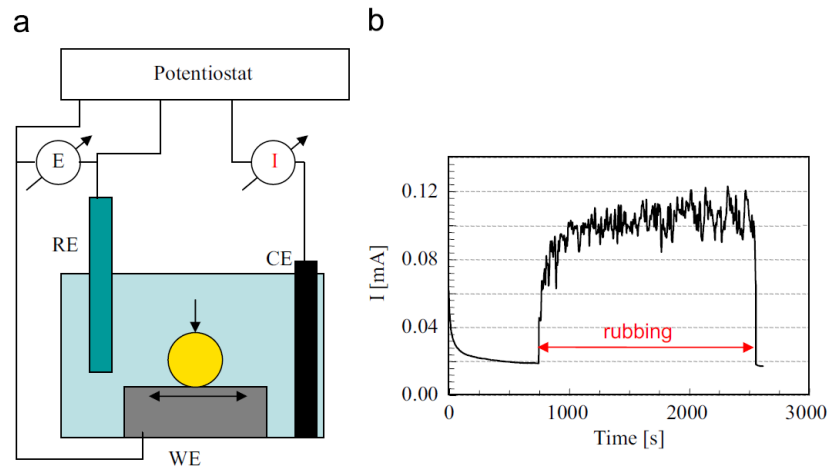
Figure 4-2: (a) Schematic illustration of potentiostatic test during rubbing (b) current increase of Ti6Al4V alloy during rubbing against alumina ball in 0.9% NaCl at potential 0.3 V$_{SSE}$ [106]

4.2.3 Galvanic cell

In this technique, the same material plate (CE) is connected to the WE through an ammeter. Once rubbing starts on WE, corrosion potential of the WE shifts towards more negative values (see Figure 4-1). Therefore, electric current flow initiates between the CE and WE (Figure 4-3(b)) due to the formation of galvanic cell. Once rubbing stopped, the worn area is repassivated and the current flow becomes dim. This galvanic current is considered as rubbing-induced corrosion. The main source of error in this method is the current flow between the worn and unworn area on the WE surface [106].
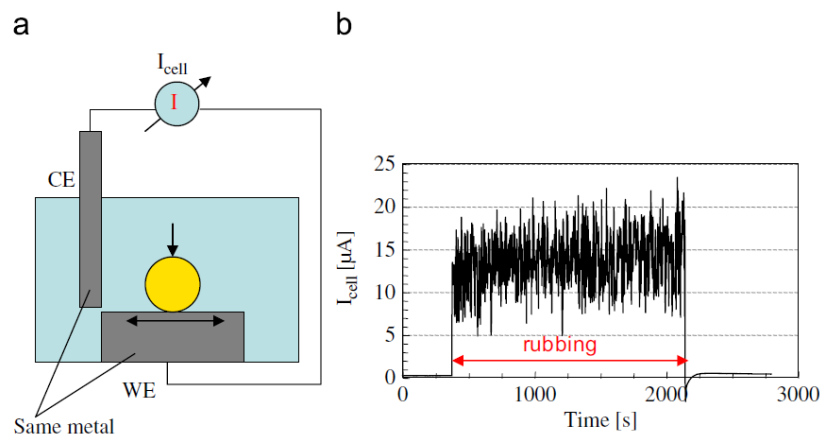
Figure 4-3: (a) Schematic illustration of a galvanic cell and rubbing simultaneously (b) measuring galvanic current of a Ti6Al4V alloy in 0.9% NaCl solution rubbing against alumina ball [106]

48

4.2.4 Potentiodynamic test

In this technique, the potential is swept at a constant rate and current is recorded continuously. Current rises up to a maximum value with increasing the overpotential. At this point, the reactions rates are very high that they are limited by diffusion of species towards/away from the metal-electrolyte interface. Therefore, further overpotential of the surface does not affect the reactions rate. The current density could even drop off at this stage due to the lack of the reactants on the surface.

This method can be employed in a tribocorrosion system in order to study the effect of friction on different electrochemical reactions happening at different potentials. It has been observed by this technique that the active-passive transition will not happen in presence of rubbing and rubbing has no effect on cathodic reactions [106].

4.2.5 Electrochemical impedance spectroscopy

Electrochemical Impedance Spectroscopy (EIS) is a non-destructive electrochemical method in which a small amplitude AC signal is applied to the system with different frequencies and the current is recorded during the test. Simple electric circuit models are usually used to interpret EIS results [109, 110]. This method is mostly used for studying reactions kinetics, their mechanisms, and the passive layer properties. The results of the EIS experiment are shown in different ways, the most common way is called Nyquist diagram. Nyquist diagrams for a stainless steel immersed in 0.5 M sulphuric acid and rubbed against a corundum ball are illustrated in Figure 4-4 for four different stages of the experiment as follows:

- Experiment 1: at the very early stage of immersion before applying the load when the passive layer was not formed yet
- Experiment 2: after passivation of the metal surface but before applying the load
- Experiment 3: when the load was applied and the surface was locally depassivated by friction
- Experiment 4: after unloading and when the surface was re-passivated

Comparing the diameter of semicircle (R_{pol}) in diagram 1 which belongs to the active surface with diagram 2 which belongs to the passive state of that surface shows that it is several orders bigger in the passive state. The

49

corrosion current can be calculated from the diameter of the semicircle (R_{pol}) using equation (4-3) [109].

$$I_c = \frac{B}{R_{pol}} \tag{4-3}$$

Where *B* is a constant coefficient related to the corrosion or passivation mechanism and polarization resistance (R_{pol}) can be extracted from the experimental diagrams.
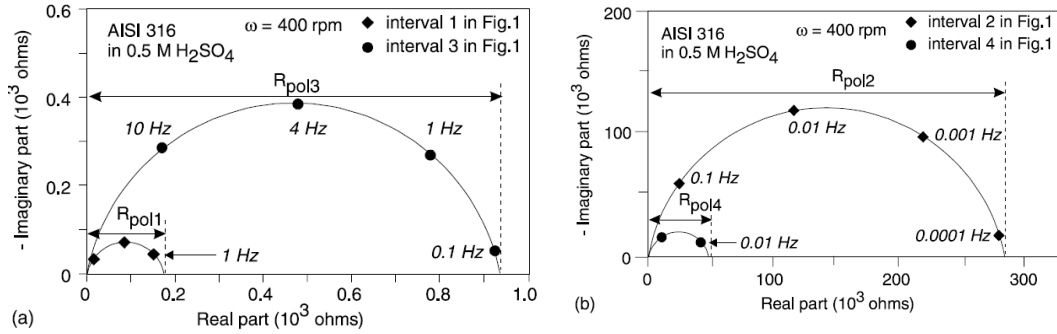
Figure 4-4: Nyquist diagrams for stainless steel immersed in H₂SO₄ solution rubbing against corundum ball in open circuit potential [109]

There is a huge difference between diagram 1 and 4 (for complete and local active surface) in terms of the size of impedance. However, it is not possible to see this difference in some other electrochemical techniques such as measurement of the OCP. Even though the OCP measurement shows similar potential for experiments 2 and 3 described above, the sizes of impedance are showing that kinetics of the reactions are hugely different.

4.3 Hydrogen detection methods

Hydrogen can be detected either in gas phase or dissolved in steel using different techniques. So far, *ex-situ* techniques such as elastic recoil detection [16], melting sample [16] and thermal desorption [111] were mainly used to measure hydrogen content in steel. However, *ex-situ* analyses are subject to error due to the variability of de-gassing between experiment and detection. The usual practice is to use dry ice to chill the samples and reduce hydrogen mobility in the metal [112]. The sample preparation for the detection technique also causes hydrogen escape. The measurement values show the total hydrogen in the steel including the amount of hydrogen remained in the steel from the manufacturing process and also diffused in the metal during rubbing. Electrochemical hydrogen permeation and hydrogen microprint [113] are also some popular techniques developed to measure trapped/diffused hydrogen in

the steel. Special attention in this study has been given to the methods with possible potential to be employed in monitoring hydrogen evolution from lubricated tribological contacts. Hydrogen measurement techniques from lubricated contacts can be categorized into four groups:

- Methods that measure total amount of hydrogen trapped in the metal specimen
- Methods based on measurement of the hydrogen desorption rate from the tribo-contact
- Methods based on monitoring the hydrogen flux diffusing through metal
- Methods based on the measurement of the metal properties in presence of hydrogen

4.3.1 Gas chromatography

The process of hydrogen absorption by metal is reversible depending on the partial pressure in the gas phase. The absorbed hydrogen could be released by vacuum heating or vacuum fusion. The temperature does not exceed metal's melting point in vacuum heating. The effusing gas is analysed by using gas chromatography device. The released gas mainly consists of hydrogen up to 800°C due to its higher diffusion rate compared to nitrogen and oxygen [15].

The basic principle of gas chromatography technique relies on the fact that gas effusion rate is related to the inverse square root of molecular mass. In this method, the tested gas is mixed with an inert gas and passed through a packed column. Different components of the gas are moving at different velocities through the column due to the various degree of interaction with stationary non-volatile phase leading to separation of gas into its constituent components. The separated components are detected by a sensor that monitors changes in the gas properties. Various properties of the gas could be measured such as thermal conductivity or ionisation spectra. The precision of the measurement depends on different factors such as the difference in the properties of the tested gas compared to the carrier gas and also the degree of separation. The column size and the type of the carrier gas are the main influential parameters on the sensitivity of this detection method.

4.3.2 Mass spectrometry

The main working principal of mass spectrometers is separation and detection of ionic species. Ionization of the sample will be done as the first step using an electron gun. The produced positive ions are accelerated and filtered by a mass filter. The filter separates the ions based on their weight and detector only receives ions of calculable mass. Mass spectrometers are categorized based on their mass filtering method, ions detection method, and the energy uses for ionization of the gas.

The ion beam is separated first forming a spectrum. Then the ions with a range of similar mass/charge ratio (m/e) are focused back together to hit the detector. Time of flight analysis is a way of ion filtering that works based on the fact that the flight duration between ion source and detector is different for various groups of ions with different velocities. The ion particles are separated based on their m/e ratio if they release from the ion source with an identical energy level. The resolution of detection directly depends on this energy distribution.

Quadrupole mass filters are also among popular ways of filtering employs in mass spectrometers. In this technique, pairs of rods are used and DC and AC voltages are applied creating a radio frequency field. This radio frequency field leads to oscillation of the ions in a plane orthogonal to the rods placed to coincide with the ion beam injection path. Stable oscillation under certain field only achieves for the ions with a particular m/e and all others collide with the rods. Different ions can be separated using this technique by either changing the radio frequency or the voltage. The main advantage of this technique over time of flight technique is that a simple ion source can be used. This is due to the fact that the filtration process is independent of the energy distribution of the ion beam. This improves the precision of the measurement as the ions in the ion beam better reflecting their concentration in the initial sample.

Mass spectrometry is a common technique in measuring hydrogen extraction from metals in hot vacuum extraction device. Hydrogen has been driven off the metal in high temperature using an induction furnace. The hydrogen content of the metal sample is measured by analysing the produced gas by mass spectrometry. One of the limitations of the vacuum heating/vacuum fusion is the fact that these techniques measure the hydrogen in the steel no matter where it came from while there is always hydrogen in the metal from the manufacturing process which had not diffused into the material from lubricated contact.

Quadrupole mass spectrometer was employed in several studies for *in-situ* monitoring of tribological hydrogen evolution. Those measurements have been done in a high vacuum or controlled gaseous atmosphere using an apparatus similar to the schematic in Figure 4-5 [9, 11, 12]. A ball-on-disc tribometer was installed in a vacuum chamber and the samples were coated by the lubricant. During the sliding, the reaction products were analysed by a quadrupole mass spectrometer (Q-MS) showing the production rate of hydrogen.
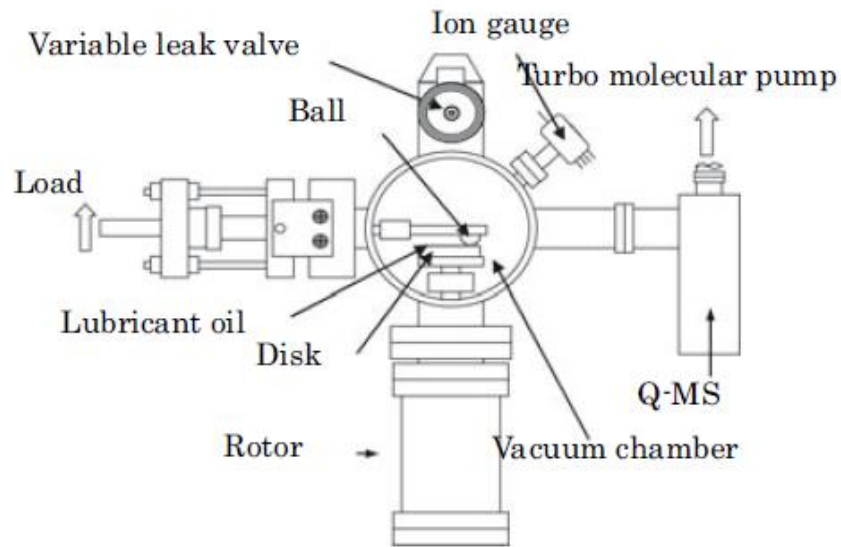
Figure 4-5: Schematic diagram of the test apparatus using the combination of mass spectrometer and tribometer [11]

The influence of mechanical conditions on hydrogen evolution rate was evaluated by this apparatus [11]. The results illustrated in Figure 4-6 depicted that desorption amount of hydrogen from a rubbing contact depends proportionally to sliding velocity and load.
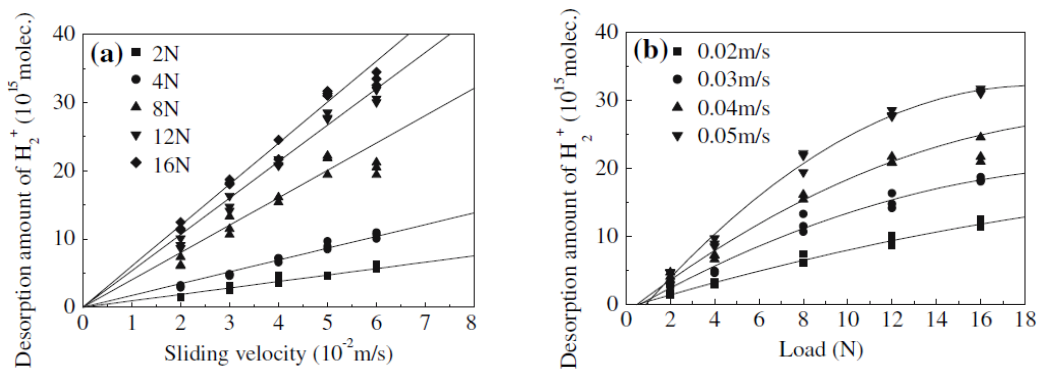
Figure 4-6: Dependence of hydrogen evolution on mechanical conditions (a) sliding velocity, (b) load

Lu et al. [9] investigated the effect of different additives on oil decomposition and hydrogen evolution under friction condition. They have shown that phosphate-containing ionic liquid additives act more efficient in preventing lubricant decomposition in comparison with sulphur, nitrogen, and phosphorus-containing additives. Moreover, the study showed that phosphate-containing ionic liquid additive is more effective in increasing the critical load for hydrogen generation compared to other mentioned additives due to the higher durability of the tribofilm that generated from the oil with this additive.

4.3.3 Palladium sensors

The physical properties of palladium can predictably change in presence of hydrogen. Pd-SiC Schottky diode can be used to sense hydrogen at high temperatures (300-500°C) by measuring its current-voltage response. Hydrogen changes the thermionic characteristic of the diode when adsorbed by palladium [114].

Palladium coating has also been used as cathode layer in electro-luminescent device by Okuyama et al. [115]. Normally, palladium has a high electron work function (5.1 eV) which drops in presence of hydrogen. Therefore, larger amount of light is expected as a result of being in contact with hydrogen. 0.2 cdm^{-2} increase in luminance has been reported due to the exposure to 200 Pa hydrogen gas.

4.3.4 Localised hydrogen detection

Probe methods are employed in order to measure surface distribution of hydrogen over the sliding friction surface. Electron beam or laser is used in these methods to locally fuse the metal surface. Then, the evolved gas from the melted spot is analysed to measure hydrogen content.

Surface analysis techniques such as X-ray diffraction and secondary ion mass spectrometry can also be employed to detect localised hydrogen. X-ray diffraction method can be carried out to look at metal surface up to 10 μm depth [116]. Induced lattice strain due to the hydrogen saturation of the steel is examined using X-ray diffraction ability to measure interatomic distances within the lattice. The secondary ion mass spectrometry can also be used in order to measure the hydrogen content of the surface layer [117]. In this technique, the material is removed from the surface in form of ions by bombarding surface with Cs^+. The resulting ions are analysed by the time of flight analyser to measure hydrogen content.

Hydrogen microprint is another technique which is capable of detecting hydrogen. In this technique, the surface is coated with a photographic emulsion containing silver bromide. Silver bromide reduces to metallic silver once being in contact with released hydrogen atoms from the surface according to reaction (4-4). Finally, the silver bromide crystals are removed from the surface by using fixing solution and the hydrogen exit areas are visualized as metallic silver particles [118].

$$AgBr_{(aq)} + H_{(ads)} = Ag_{(s)} + HBr_{(aq)} \tag{4-4}$$

4.3.5 Hydrogen measurement based on the metal properties

Measurement of changes in metal properties is another approach to determining the degree of hydrogen uptake. Changes in microhardness, plasticity, ultimate strength, fatigue life and electrical conductivity of the metal before and after hydrogen charging give an estimation of hydrogen content. Determination of the number of bends of the metal sample before failure and comparing the necking or elongation of the steel sample in a tensile test are some of the ways to estimate the degree of HE. However, these methods only provide quantitative measurement of hydrogen content and they are poorly reproducible.

4.3.6 Hydrogen permeation method

Devanathan and Stachurski employed this technique in 1962 to measure hydrogen permeation through a palladium membrane [119]. The configuration of the set-up used for this technique is made of two compartments. Hydrogen is generated on one part and detected on the other part. These two parts are connected together by a thin metal membrane. Hydrogen diffusion is driven by concentration gradient on two sides of the membrane. Diffusion of hydrogen is also driven by stress, potential and thermal gradients. This method has been widely used to study the effect of hydrogen recombination poisons on hydrogen permeation rate into the steel. Studies showed that sodium sulphide poisonous effect on hydrogen permeation rate is maximum at certain concentration and pH [120].

There are multiple different ways to introduce and detect hydrogen on two sides of the metal membrane:

- Hydrogen partial pressure is used on the input side of gas driven permeation rig. This is applicable over a wide range of temperature.

The subsurface concentration of hydrogen in this technique is estimated using Sievert's law:

$$C_e = S\sqrt{P}$$ (4-5)

where C_e (H atoms/m^3) is hydrogen solubility, P is the partial pressure and S is the solubility coefficient.

- In electrochemical driven hydrogen permeation technique, hydrogen is introduced into the membrane by placing the input side of the metal membrane in a three electrode electrochemical cell; the membrane acting as WE. Hydrogen is generated on the surface of the metal by applying cathodic potential. Hydrogen entry condition can be changed rapidly and accurately in this technique.

- Gas chromatography or mass spectrometry can be used on detection side of the membrane to monitor effusing flux of hydrogen. However, these techniques work in vacuum condition and it could cause deformation of the membrane, especially if the membrane is very thin or a high input pressure of hydrogen is employed on the input side of gas driven permeation method.

- Electrochemical measurement techniques can also be used to detect effusing flux of hydrogen. In this method, emerging hydrogen is oxidised and the oxidation current is measured continuously. This technique is very accurate as electrochemical techniques are very sensitive allowing detailed real-time measurement.

Electrochemical charging of hydrogen is more popular for investigation of environmental hydrogen induced cracking [121] due to the possibility of reproducing the environment in electrochemical cell. However, the researchers who work on the internal transportation of hydrogen prefer to use hydrogen gas at the input side to minimise the surface effects. The results from experiments done in acidic charging media are unreliable due to the formation of internal voids in material causing non-steady state oxidation current measurement.

This technique can also be used to measure hydrogen content of the metal membrane by observing the decay transient curve. This hydrogen could have been absorbed by the metal in the process of steel manufacturing, welding or being exposed to the hydrogen containing environment.

Many types of modified hydrogen permeation cells have been employed so far to investigate hydrogen diffusion rate through the steel with different hydrogen entry conditions. Turnbull et al. [122] reported that addition of H_2S and decreasing pH in entry electrolyte would increase the hydrogen permeation rate. Tsuru et al. [123] modified the set-up to study the mechanism of hydrogen generation from the atmospheric corrosion process occurring on the steel. Figure 4-7 illustrates the cell which is used for wet and dry corrosion cycles. The hydrogen entry side is exposed to the atmosphere and a pH measurement electrode was installed just above the electrode surface. A solution droplet is placed onto the exposed surface and the hydrogen permeation current is measured on the detection side of the membrane until the droplet totally dried up. This set-up was also used to investigate the effect of steel passive layer and surface pH on hydrogen permeation rate [123].
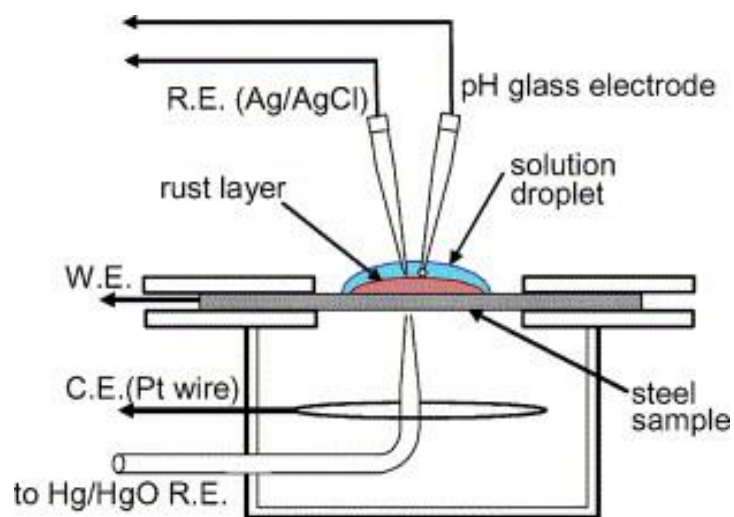
Figure 4-7: Schematic diagram of the modified hydrogen permeation cell for atmospheric corrosion [123]

Ootsuka et al. [124] later used the developed technique by Tsuru et al. [123] in order to do online monitoring of hydrogen permeation into steel parts of a vehicle while it is moving. The results in Figure 4-8 reveals that when it was sunny on the 11th day, the hydrogen permeation keeps very low regardless of the moving of the vehicle. However, a sharp increase in hydrogen permeation is recorded when it is rainy on the late 12th day of the testing. On the 15th day of the testing, almost no hydrogen permeation was recorded even though it was snowing and the roads were wet. This was suggested to be attributed to the vehicle being stopped. It can be concluded that hydrogen permeation into steel is promoted by the splash of water droplets over the vehicle parts while it was moving on the wet road surfaces.
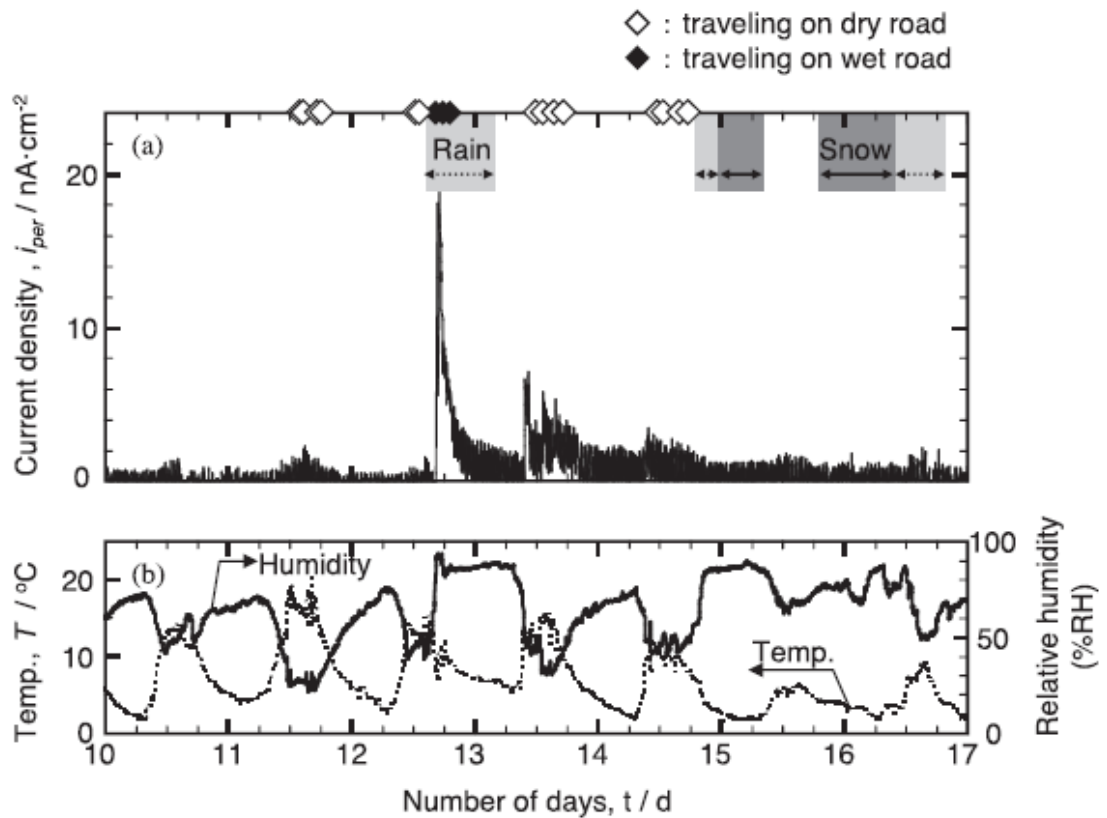
Figure 4-8: (a) Hydrogen permeation current density, (b) temperature and relative humidity, as a function of time from 10th day to 17th day of the on-vehicle monitoring test [124]

Huang et al. [125] also developed a modified set-up to monitor hydrogen permeation rate into the steel under the effect applied load on the membrane. Figure 4-9 shows the variation of steady permeation current with strain under static loading condition. The comparison of the hydrogen permeation current with the stress-strain curve shows that the permeation current (P_∞) increased with the increase of loading.

In the current study, electrochemical measurement is used for hydrogen permeation monitoring; this technique was first developed in 1960's by Devanathan and Stachursci [119]. Electrochemical techniques are very well suited to measure the kinetics of reactions in real time. This is very useful to develop models and collect data to monitor hydrogen permeation in a quantitative way. The details will be discussed in Chapter 5.
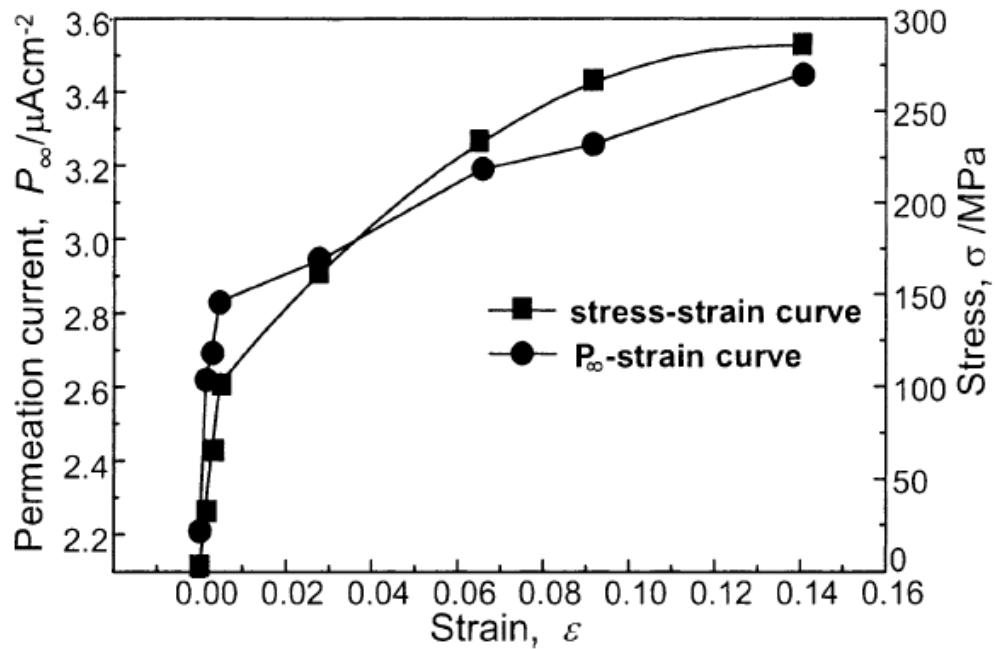
Figure 4-9: The effect stress with static strain on steady state hydrogen permeation current [125]

4.4 Summary of the literature

As discussed in Chapter 3, there are many reports on failures in bearings linked to hydrogen. The strangest unpredicted failures of bearings are often explained as an effect of hydrogen in the steel. This hydrogen is mainly coming from the lubricant accelerating different degradation mechanisms such as RCF. The studies showed that hydrogen damage is due to the changes in mechanical properties of the steel although there is still no agreement on the mechanism.

Despite all investigations into the effect of hydrogen on tribological failures, it still remains unpredictable, difficult to control, and the complete mechanism is not well understood. The detailed process and the influential parameters are also not very much clear. Moreover, the source of hydrogen coming from the lubricant is still unknown. This may come either from the oxidative breakdown of the hydrocarbon molecules or water contamination in the oil. Additives are also considered as a source of hydrogen in the lubricants. Most of the evidence that proves the presence of hydrogen in lubricated contacts is from destructive *ex-situ* measurements. This introduces some uncertainty regarding the source of hydrogen and its background level in the material. Other studies that link hydrogen induced failure to microstructural changes are also not very persuasive. The microstructural change could happen due to other physical or chemical factors.

4.5 Aims and objectives

At this stage suffice to say that there is not enough experimental data on hydrogen evolution from lubricated tribo-contacts mainly due to the lack of monitoring techniques. Therefore, this study aims at filling this gap by developing a reliable, cost-effective, *in-situ* technique to monitor hydrogen uptake from a lubricated tribo-contact. This technique will be used to interrogate the influence of a lubricant's composition and tribological parameters on hydrogen entry into the steel. In Chapter 4, the developed techniques with the potential application of hydrogen permeation monitoring in lubricated tribo-contacts were reviewed. This study will focus on modifying the conventional hydrogen permeation set-up to reach this aim. The next chapter presents the details of the newly developed rig in this study. This new approach tries to capture hydrogen permeation from the dynamic tribo-contact in real time while it is happening. The contact in this test rig is pure sliding which is not a representative of rolling-sliding contacts found in rolling bearings; however this sliding contact provides enough level of shear stress and wear to produce hydrogen within the contact. The repeatability and reliability of the results for different lubricants at different temperatures will be investigated.

The results from this method are expected to provide new insight regarding the effect of both the lubricant's chemical and tribological parameters on hydrogen uptake into steel. At first, the hydrogen generation mechanism and its source will be studied by using this new rig. The effect of water contamination, anti-wear and friction modifier additives on hydrogen permeation rate is studied taking into account different operational conditions including temperature, contact pressure and sliding speed. Finally, surface analysis techniques were employed to answer fundamental questions related to the effect of tribofilm on hydrogen permeation rate. All of these will help to propose a mechanistic understanding of hydrogen induced failures in lubricated contacts and provide data to predict the failure.

Chapter 5 Rig development

5.1 Introduction

In the first chapter of results of this thesis, the development and design history of the hydrogen uptake rig are presented. This chapter explains how the combination of electrochemical techniques, that are usually used in corrosion experiments, with tribology can be harnessed to create a new method to measure tribological hydrogen permeation. Firstly, the hydrogen uptake results from the prototype set-up using the metal-DP sprayed polishing paper contact are presented. Then, the newly developed rig details are described.

5.2 Prototype set-up

5.2.1 Set-up configuration

In the conventional Devanathan-Stachurski (DS) technique [119], the front and back sides of a metal membrane are exposed to two separate environments and employed as hydrogen entry and exit electrodes, respectively. The schematic figure of a conventional DS setup is shown in Figure 5-1. In the hydrogen input side, hydrogen atoms produce and penetrate into the steel membrane by diffusion, while the amount of hydrogen diffused through the specimen is measured by the oxidizing current density on the detection side. The membrane surface on the charging side is often controlled by applying a galvanostatic condition. The hydrogen permeates through the membrane due to the concentration gradient between two sides of the membrane. The hydrogen concentration on the detection side of the membrane is kept zero by polarizing at an anodic potential. The anodic polarization accelerates oxidation of the emergent hydrogen atoms.

Efforts have been put into the standardisation of the hydrogen permeation experimental procedures; thus, the BS EN ISO 17081 (2014) [126], method of measurement of hydrogen permeation and determination of hydrogen uptake and transport in metals by an electrochemical technique, was accepted as the standard method of doing the experiment.

The conventional DS set-up can be modified to develop a new technique to measure tribological hydrogen uptake; the amount of hydrogen that permeates through a steel membrane from an oil-lubricated tribological contact. Figure 5-2 shows a schematic figure of the prototype hydrogen uptake setup developed in SKF Engineering and Research centre, the

Netherlands [127]. The setup was made by replacing the electrochemical charging cell of conventional DS setup by a lubricated rubbing device. However, the rubbing area of the ball rotating on the metal surface was too small and the generated hydrogen was not detectable. Therefore, polishing tape was used in order to both increase the contact area and wear. Using polishing tape helped the removal of the oxide layer on the metal surface.
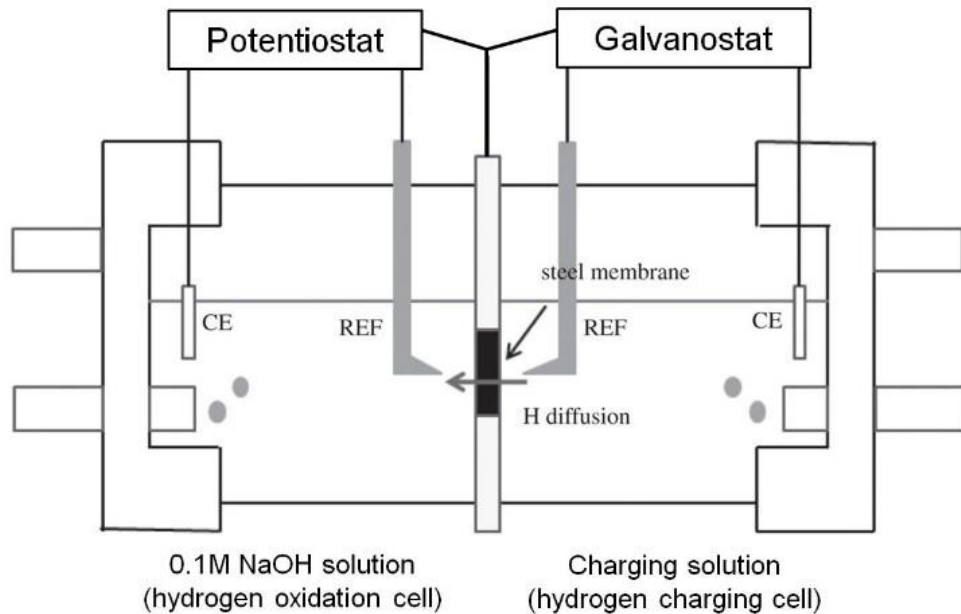
Figure 5-1: Schematic of conventional Devanathan-Stachurski cell, REF – reference electrode [128]
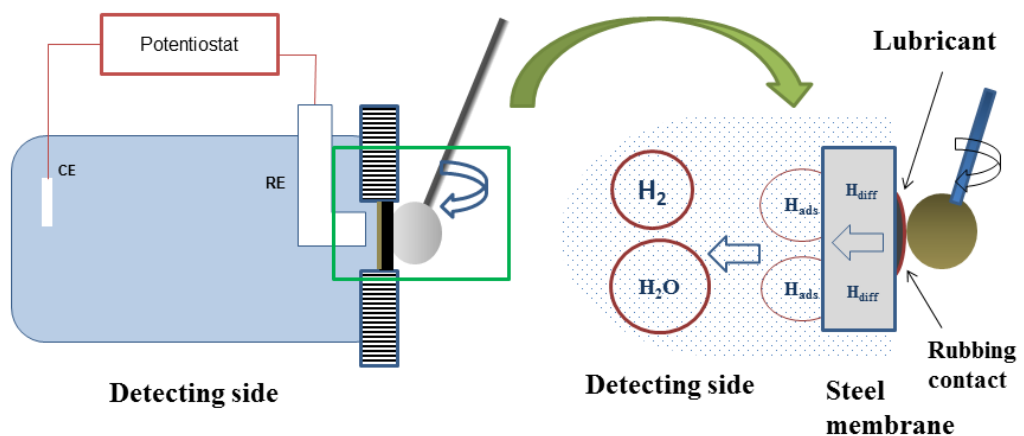
Figure 5-2: Schematic figure of the prototype version of hydrogen uptake set-up [127]

The set-up shown in Figure 5-3, the prototype set-up developed in SKF engineering research centre, was prepared to reproduce some of the old results [127]. In this configuration, the detection cell is a conventional three-electrode electrochemical cell. The cell is filled with 0.1M NaOH electrolyte

which is continuously deaerated using nitrogen flow. A heater was used to heat up the electrolyte and keep the temperature constant at 50°C during the measurement. On the other side of the membrane, tribological hydrogen charging side, a laboratory stirrer was used to rotate a spindle shaft. The spindle shaft is applying both the load and shear stress on the steel membrane. The lubricant is continuously fed into the contact through a capillary tube using a peristaltic pump. The rubbing load was 5~10 N and rubbing speed was 0.12±0.01 m/s. A polishing tape was sprayed with diamond powder (DP-suspension, grain size 1 μm) and used as rubbing counterpart. Although the contact pressure is small in this set-up (~30-60 kPa), the DP was applied to increase the wear leading to efficient removal of the air-formed oxide layer on the surface.
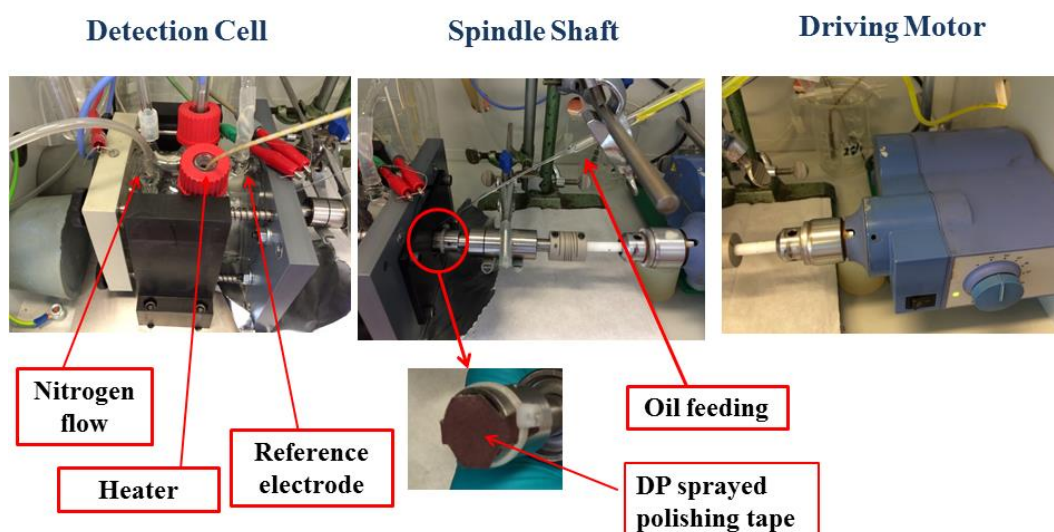
Figure 5-3: Hydrogen uptake prototype set-up

In this set-up, hydrogen was generated on the surface of the membrane from lubricated tribo-contact. Some of this hydrogen, the proportion is unknown, permeated through the steel plate. The permeated hydrogen was monitored on the detection side of the membrane identical to the conventional DS setup. However, there were still some deviations for the system such as contact pressure, contact area, wear volume, rubbing speed, lubricant feeding rate, etc. limiting the repeatability of the results [127]. Another limitation of the system was the fact that hydrogen was produced from abrasive polishing tape rubbing against the metal surface which was a different tribological contact compared to a real metal/metal contact.

5.2.2 Hydrogen uptake results from the prototype set-up

Figure 5-4 shows a hydrogen permeation current curve obtained from the prototype setup when PAO base oil was fed as lubricant into the contact. The curve shows that the hydrogen permeation current increases until a plateau value is achieved. At this point, a steady state hydrogen permeation flux is reached.
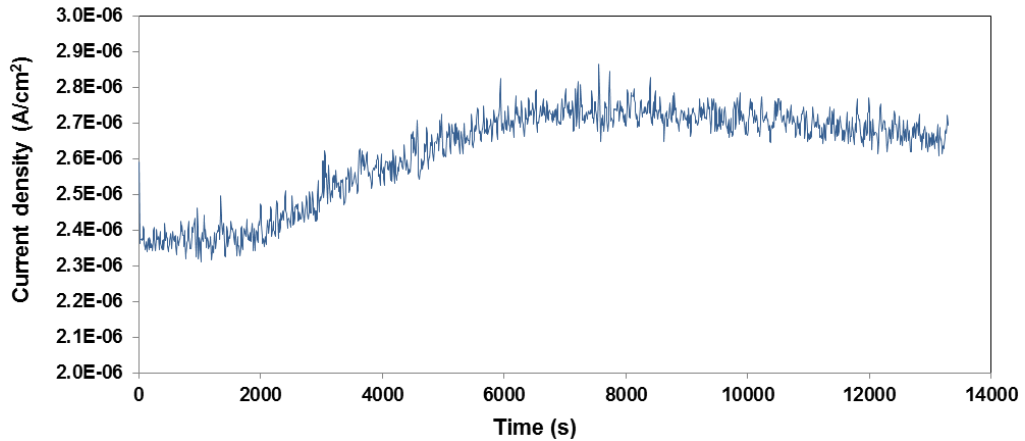
Figure 5-4: Hydrogen permeation current recorded after rubbing and PAO lubricant feed-in

However, there are some deviations in certain system parameters such as wear volume, contact pressure, contact area, and rubbing speed that limit the repeatability of the results from this rig. Therefore, a semi-quantitative approach was defined to compare hydrogen permeation rates:

1) PAO fed continuously into the contact and the oxidation current is recorded until it reaches the steady state. The increase of the oxidation current is considered as ΔI_{PAO}

2) Switch the oil from PAO to the oil of interest. Keep the same load and rubbing speed and record the oxidation current again until it reaches a new steady state. The change in the steady state current value compared to the one recorded for PAO is considered as ΔI_{oil}

3) The ratio shown in equation (5-1) is used to compare the difference in hydrogen uptake rates between the tested oil and PAO. This normalizes system drifts and increases the reliability of hydrogen uptake results.

$$Hydrogen\ uptake\ increase\ ratio = \frac{\Delta I_{oil}}{\Delta I_{PAO}} \qquad (5\text{-}1)$$

As an example, the effect of ZDDP anti-wear additive and water contamination in PAO base oil was investigated using the described method. As shown in

Figure 5-5, hydrogen permeation is promoted in presence of ZDDP in PAO base oil. The hydrogen permeation current increased once PAO+ZDDP lubricant was introduced into the contact instead of PAO.
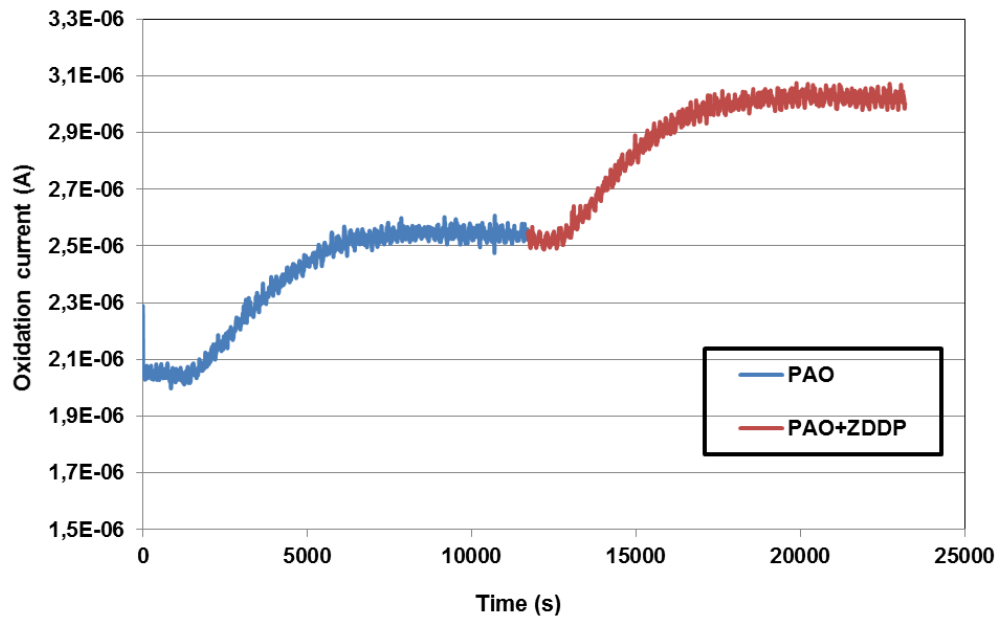
Figure 5-5: Effect of anti-wear additive on promoting hydrogen uptake

The effect of water contamination in PAO base oil was also studied and the results are presented in Figure 5-6. It is seen that introducing contaminated oil into the contact causes higher permeation of the hydrogen. It was also seen that it is a reversible condition; with changing the oil to PAO base oil again, the permeation rate of hydrogen returns to its original value.
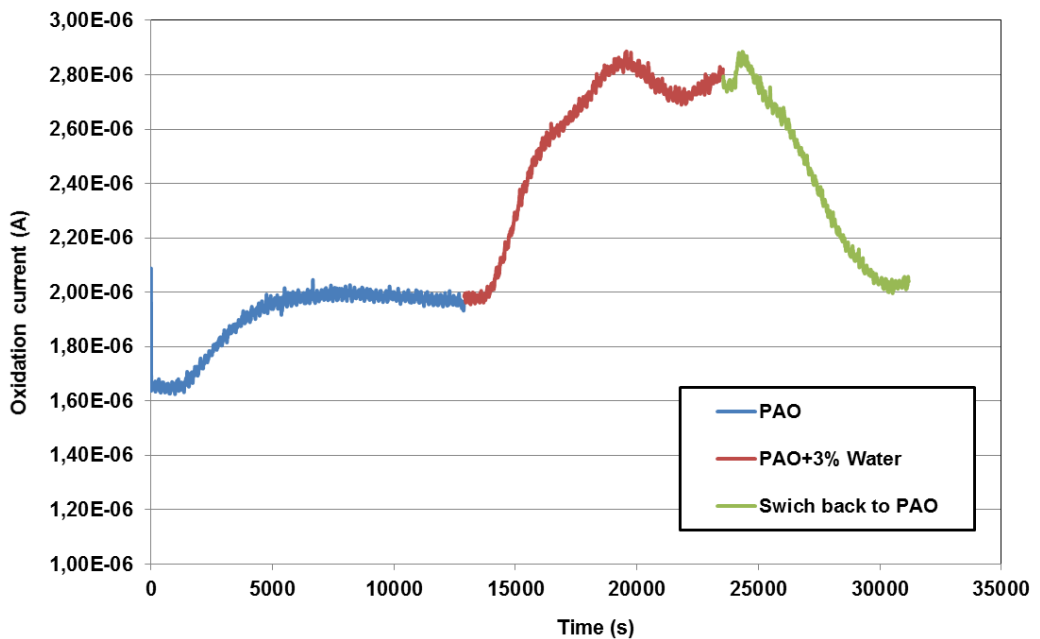
Figure 5-6: The influence of water contamination on promoting hydrogen uptake into steel

65

The hydrogen uptake increase ratio was calculated upon switching from PAO base oil to water contaminated PAO and PAO-ZDDP additive blend. The results are shown in Figure 5-7 and are in line with previous results presented elsewhere [127].
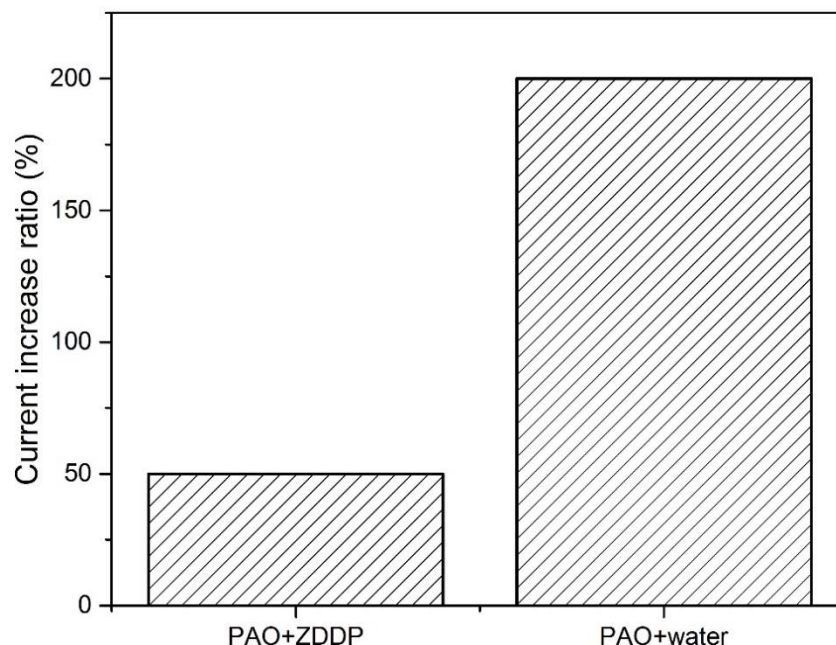
Figure 5-7: Hydrogen uptake increase ratio upon switching from PAO to PAO+water and PAO+ZDDP

This rig successfully monitored hydrogen uptake from a lubricated contact and quantitatively compared the hydrogen permeation rate from different lubricants. However, there are some limitations for this technique:

- There was no control or recording of the tribological parameters such as load, friction and sliding speed
- Oil feed rate was different for different lubricants depending on their viscosity
- There was a limitation for maximum applied load and so the contact pressure
- The heating system was inefficient
- The membrane and the rubbing counterpart were not aligned
- Tests conditions were not repeatable

Considering these limitations, a robust rig was required to be developed in this study. This will enable reliable hydrogen permeation monitoring for different lubricants and rubbing conditions.

In the modified setup developed in this study, the tribo-contact has to impose a highly stable contact pressure and shear stress with low vibration, no

66

misalignment and long-time running accuracy. This is built in order to generate hydrogen on the charging side of the membrane to study the performance of candidate lubricants under different contact pressures and sliding speeds. The load distribution, torque and hydrogen oxidation current are continuously monitored during the rubbing process. Applied load and frequency of oscillatory motion are adjustable in order to evaluate the dependence of hydrogen uptake on the variation of tribo-mechanical action. This technique will provide a new insight into the effect of the lubricant's chemical and tribological parameters on hydrogen uptake into steel. The details of the developed rig will be described in section 5.3.2.

5.3 Hydrogen uptake rig

5.3.1 Development history

In this newly developed rig, the detection cell made of glass works in a similar manner to the conventional DS set-up. However, the hydrogen charging cell is replaced by a lubricated sliding contact. Several different configurations were initially proposed for the set-up and each one of them had its own pros and cons. For the first thing, it was decided to change the DS set-up configuration from horizontal (Figure 5-2) to vertical. It will help to have a better control on the applied load. There were two different approaches to do this; firstly to have the detection cell on the top and applying load from bottom (schematically shown in Figure 5-8). Secondly, to have it the other way around with having the detection cell beneath and applying load from top. There are some advantages for the former configuration such as not having the risk of gas accumulation beneath the membrane and easier connection of the membrane to the wire coming from the potentiostat. There are also some advantages for the latter configuration such as the possibility of having an oil bath which makes it possible to do some other measurements on the oil side during the experiment. Having an oil bath also removes the problem of lubricating the membrane using a pipette tube in case of having the detection cell on the top. The main problem of lubricating with pipette was the fact that different lubricants at different temperatures have different viscosities and lubricating the membrane using pipette tube and peristaltic pump with a consistent flow rate would be difficult.

Although there were some concerns about having the detection cell beneath and applying the load from the top, it has been decided to have the detection cell on the bottom and the oil bath on the top. Further *in-situ* measurements,

such as impedance measurements, can be implemented on the rubbing side of the membrane for future development of the rig. One of the main concerns that needed to be considered in this configuration was the possibility of accumulation of the gas bubbles beneath the membrane during the experiment which could distract the electrochemical permeation current measurement. Moreover, the NaOH electrolyte in detection cell should always be in contact with the membrane during the experiment. The connection of membrane and wire is also a challenge as the membrane will be in contact with lubricant from top and with NaOH electrolyte from bottom in this design.
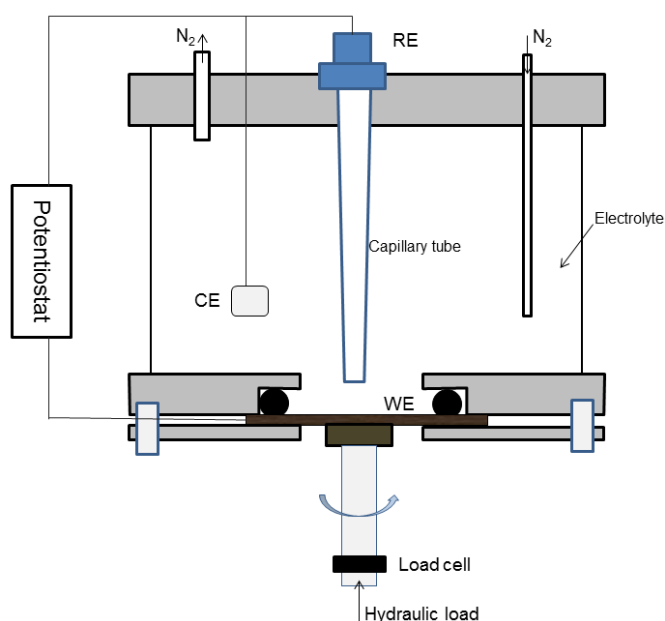
Figure 5-8: The schematic figure of the vertical configuration of hydrogen uptake set-up; load is applied from the bottom

The first design was like the schematic shown in Figure 5-9. It was a spring loaded set-up and the springs were fit between the bottom and middle plate. In this design, the distance between top and middle plate were constant and the distance between the lower and middle plate changed based on the load applied from the top on the membrane. The top and middle plates slide on the pillars. However, this set-up was wobbly and not very stable under the applied load. Some changes needed in order to solve this problem.

Therefore, the middle plate was removed and two stabiliser plates were used between the bottom and top plates. These two stabiliser plates connected the pillars together and the springs were put between the stabilisers and the top plate. This whole set-up will be fixed on an aluminium structure through one of the stabiliser plates and the springs will be compressed by applying load

from the top. The precise calculation of the applied load on the membrane was possible using the Hooke's law (equation 5-2) by measuring the spring's constant and springs displacement.

$$F_{tot} = k_{eff}x \qquad (5\text{-}2)$$

where k_{eff} is the equivalent spring constant (springs are in parallel in this configuration), x is the displacement of the springs and F_{tot} is the applied load.
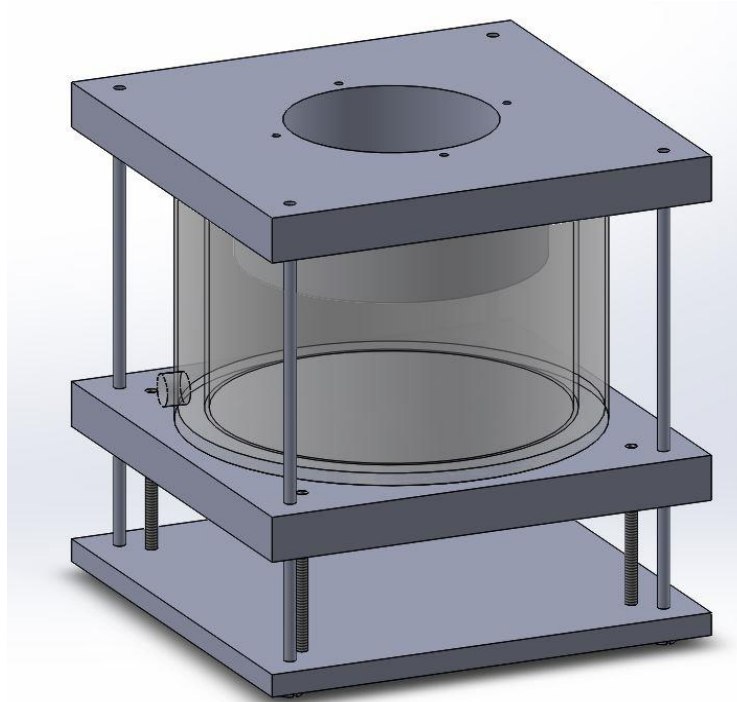
Figure 5-9: The first design for hydrogen uptake set-up

A pillar drill was initially considered to be employed regarding applying the load and rubbing the surface of the membrane. Many different pillar drills with various specifications have been assessed for this application. They were compared based on their size, spindle speed, price, vibration, stability under axial load, long-time running accuracy, etc. However, none of them was able to work several hours continuously and accurately. Therefore, using a more robust apparatus for applying load and spinning the shaft was considered as an alternative. The apparatus needs to be designed for long time running tests with less vibration and better alignment. Instron E1000 ElectroPlus machine is chosen which can apply load on the membrane through a shaft and rotate the shaft with different angles and speeds. It can also be used to apply an oscillating motion between two flat surfaces. The Instron E1000 is equipped with a load cell in order to continuously record thrust load and torque.

Considering the fact that the implemented load cell in this machine can precisely measure the axial load, springs were removed from the design. The height of pillars in the rig was precisely calculated in a way that the applied load on the membrane and top plate bear by the pillars so the glass cell was protected. In this new design, the aluminium structure, the springs, and the stabiliser plates were removed.

5.3.2 The hydrogen uptake rig

In this new rig, a vertical configuration has been designed and built having the detection cell beneath and applying the load from top. A schematic diagram of the test apparatus built in this study is shown in Figure 5-10. In this rig, the load is applied from the top using a shaft held by chuck via a linear motion derived by a pneumatic pump. The rotational motion is also introduced by pneumatic force using an Instron E10000 machine with variable speeds; the entire instrument is computer controlled. The flat metal ring (Figure 5-11) with a rough running surface is fixed on the bottom of the shaft. It permits the oscillatory motion between the ring and the membrane while the shaft is loaded against the membrane. The membrane is fastened and sealed on bottom of the oil bath between a clamp and detection cell. An area of 3.5 cm^2 of the membrane is exposed to the electrolyte inside the detection cell. The applied load and driving torque are continuously recorded during the experiment using a DynacellTM load cell.

The rubbing counterpart for this work is a cylindrically shaped sample drilled with a 7 mm inner diameter hole; the outer diameter is 18 mm, providing 215.9 mm^2 contact area of the bottom flat surface with the membrane (Figure 5-11). The counterpart is made of stainless steel 303. This is not an exact representation of a common tribology regime for rolling contact fatigue evaluation; however this sliding contact provides shear stress and wear which enables study of the hydrogen generation from a lubricated contact.

The contact pressure and shear stress between the membrane surface and the rubbing counterpart were estimated to be high enough to produce wear and remove the surface oxides, decompose the lubricant and produce enough hydrogen to diffuse into the steel membrane. In this technique, hydrogen is produced on the fresh metal surface generated on the oil side of the membrane due to the applied shear stress and friction; some of this hydrogen, the proportion is unknown, permeates within the steel membrane and emerges on detection side.

(a)

SECTION A

DETAIL C
SCALE 1 : 1
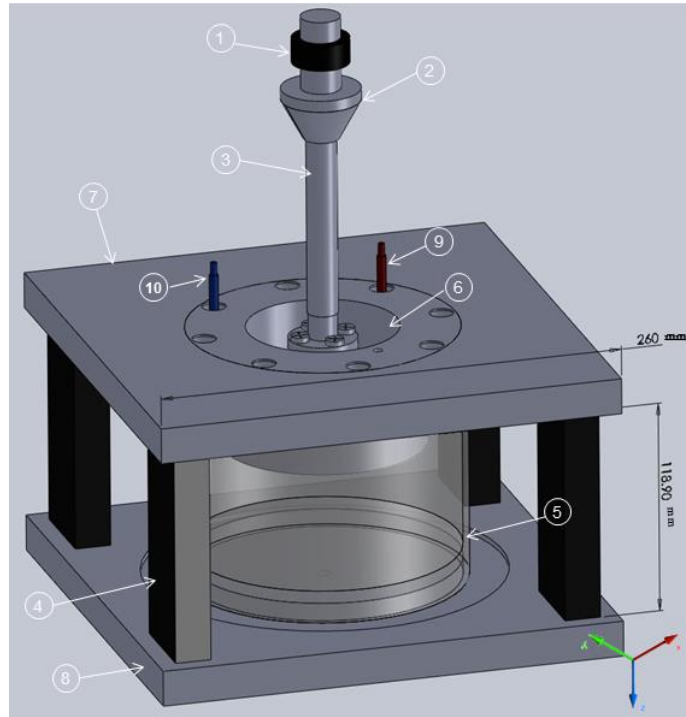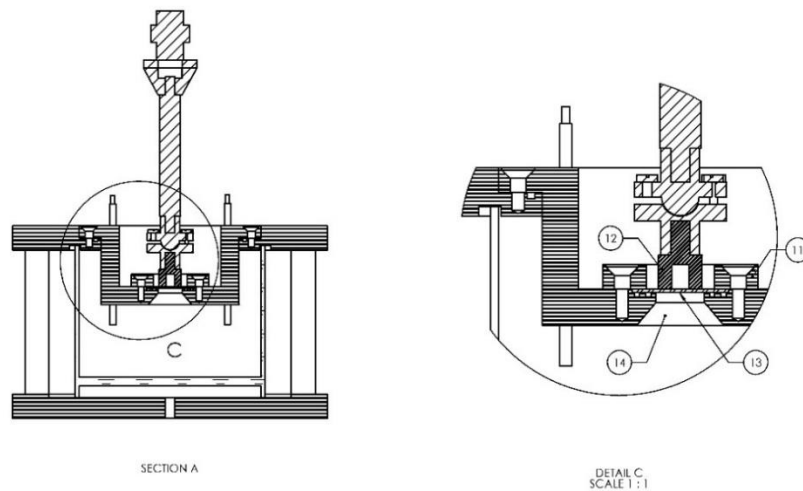
(b)

1. Load cell	6. Oil bath	11. Clamp to fix the membrane
2. Chuck	7. Top plate	12. Rubbing counterpart
3. Shaft	8. Base plate	13. Membrane – Working
4. Pillars to bear the load	9. Counter electrode	electrode
5. Detection cell	10. Reference Electrode	14. Exposure area

Figure 5-10: (a) Isometric schematic view and (b) cross-section view of H-uptake setup

(a)   (b)
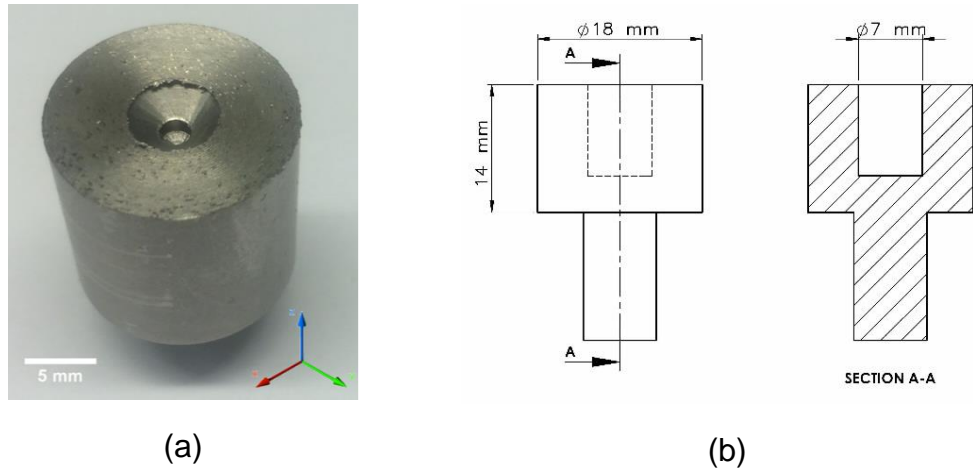
Figure 5-11: (a) The flat ring used as rubbing counterpart; (b) 2D drawing of the rubbing counterpart and dimensions

A self-aligning mechanism is implemented in the shaft in order to keep the rubbing counterpart aligned with the membrane surface during rotation. As shown in Figure 5-12, a hemisphere between two plates and loose pins with springs correct the misalignment between the running surface of the rubbing counterpart and the membrane; this is important as it assures to have a uniform load distribution in rubbing area. Moreover, this flexible joint is able to transfer both load and torque from the shaft to the rubbing counterpart.
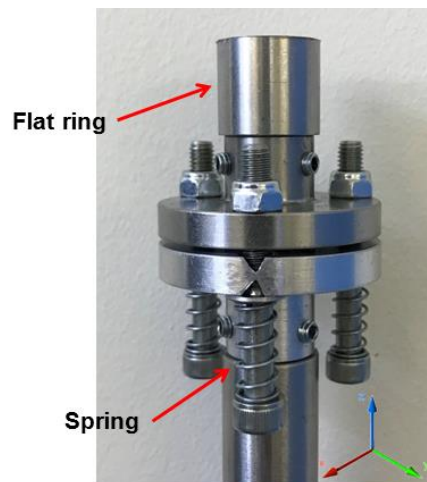
Figure 5-12: Self-aligning mechanism

Nitrogen is flushing into the sodium hydroxide electrolyte for 2 hours before the experiment; it removes the oxygen from the electrolyte. The problem of gas accumulation beneath the membrane would minimize by stopping the nitrogen flush during the experiment. Instead, the flow of nitrogen was used to cover and protect the electrolyte from air dissolution by purging the air in the space above the electrolyte. In addition, an inclined surface is used for the

bottom of the oil bath as shown in Figure 5-13 to decrease the risk of accumulation of gas beneath the membrane.

Sloping surface
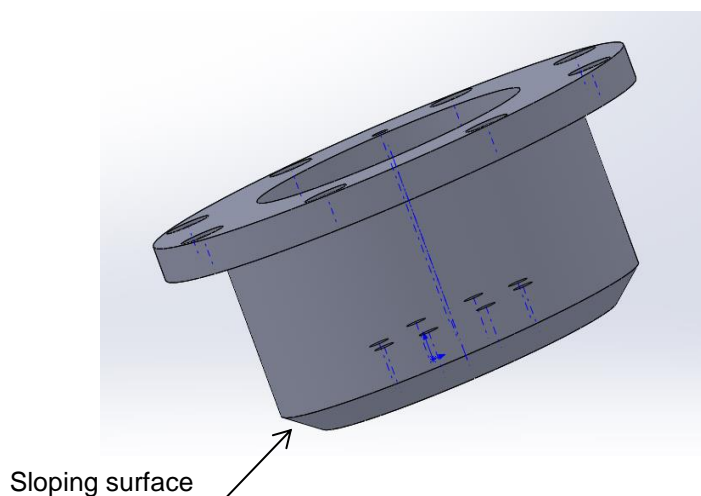
Figure 5-13: Inclined bottom surface to prevent gas accumulation

The engineering drawings of different parts (electrochemical cell, oil bath, mount/base plates, clamp, rear/front stabiliser plates) including dimensions and other details are presented in annex. The processes of manufacture and assembly were done based on these drawings prepared using Solidworks software.

5.3.3 Materials used for rig manufacturing

Different materials were used to build different parts of the rig depending on their application. The oil bath, clamp and top plate were made from Nylon plastic plates. Nylon was chosen due to its strong resistance against hydrocarbons, lubricants, cleaning agents, water and salt water which are used in this study. Moreover, it can work at high temperature up to 185°C which is higher than the working temperatures in this study. The machinability of Nylon was also acceptable considering the geometry of the parts.

The electrochemical cell was a jacketed glass beaker particularly built for this application as there was not any available commercial product with sizes needed for this rig. The wall thickness of the electrochemical cell is 5 mm. The jacket has serrated 3/8" hose connections for circulating hot water around the cell providing a uniform temperature in the electrochemical cell. The design meets requirements in ASTM E960 specifications. The dimensions and details of the cell are provided in annex.

The bottom plate was made from aluminium and the pillars were made from Nylon plastic. Pillars bear the load in order to protect the glass cell under high pressure applied from top.

The shaft was made of three different parts as shown in Figure 5-12. The shaft itself is made from steel, however the joint plates and hemisphere used for alignment system are made of aluminium due to the better machinability of aluminium. Grub screws were used to lock the parts together.

5.4 **Summary**

- The hydrogen uptake prototype set-up was described and some of the measurement results were presented
- The advantages and limitations of the prototype set-up were discussed. This was explained why a more robust rig is crucial to monitor tribological hydrogen permeation into steel
- The details and working mechanism of the newly developed hydrogen uptake rig were described; the drawings are presented in the annex

Chapter 6 Experimental methodology

6.1 Introduction

This chapter outlines details of the main experimental procedure undertaken in this project. Details are given on the lubricants, materials, and preparation procedures in the subsequent sections. This chapter also describes the operating parameters of the hydrogen uptake experiment, EIS measurement technique and the surface analysis techniques employed to establish the tribochemical reactions and the interaction between additives and contaminants. The repeatability and reliability of the results that are obtained from the newly developed hydrogen uptake rig is also discussed.

6.2 Sample preparation and materials

In this project, the hydrogen uptake behaviour of the AISI 52100 steel was investigated using the new modified DS rig described in section 5.3.2. The chemical composition of the steel membrane is shown in Table 6-1. The specimens were discs of about 0.8 mm thickness and 40 mm diameter and hardness of 60 HRC. Both sides of the specimens were ground up to 1200 grit paper with the final surface roughness of R_a=110±10 nm. The specimens were cleaned and then dried in oven. The cleaning process was done by ultrasonic immersion of the specimens in ethanol for about five minutes. Then, the detection sides of the membranes were coated with a 40 nm thick palladium coating applied by K650X sputter coating method. The palladium targets used for the coating were 99.99% pure.

Table 6-1: Chemical composition of AISI 52100 steel in wt%

C	Mn	P	S	Si	Cr	Fe
0.95-1.10	0.25-0.45	0.025	0.025	0.15-0.35	1.35-1.65	Balance

All the hydrogen atoms leaving the steel membrane to the detection side need to be oxidised. However, some of these atoms could recombine to hydrogen molecules before their oxidation. This amount of hydrogen escapes and is not measured by the oxidation current recorded on the detection side. Partial oxidation of hydrogen atoms could compromise the reliability of the method. The palladium layer on the detection side significantly reduces this unmeasured fraction of hydrogen and ensures high detection efficiency and

minimized noise levels [4, 129-131]. Another advantage of having a thin layer of palladium is that it prevents anodic dissolution of the metal membrane. Otherwise, an oxide layer would form on the metal surface acting as a diffusion barrier for hydrogen [129-132].

The rubbing counterpart (shown in Figure 5-11) is made of stainless steel 303 with the hardness of 20 HRC, the chemical composition is shown in Table 6-2. The running surfaces of the specimens were roughened to an average roughness R_a=12±2 μm. The membrane and the rubbing counterpart were changed after each experiment.

Table 6-2: Chemical composition of stainless steel 303 in wt%

C	Cr	Ni	P	S	Si	Mn	Fe
max 0.15	18	8	max 0.2	max 0.15	max 1	max 2	Balance

6.3 **Electrolytic cell and procedure**

In the current work, the hydrogen detection cell is the same as in a conventional DS cell. It is made up of a three-electrode system with the steel membrane as the WE, platinum wire as the CE and Ag/AgCl as the RE. The cell was filled with a deaerated solution of 0.1 M NaOH. The detection side was polarized at a constant potential of 115 mV versus the RE which is sufficient to oxidise the hydrogen atoms emerging on the output face. This anodic potential is maintained on the detection side and the hydrogen leaving the membrane is removed by oxidation according to equation (6-1) until the current becomes very small.

$$H_{ads} \rightarrow H^+ + e^-$$
(6-1)

Once the background current density was stabilised and it reached under 250 nA/cm^2, which is a low background compared to the measured current density, the oil bath (hydrogen input side) was filled with 75 ml of the oil of interest. Then the load was applied and rubbing started; the metal counterpart is rubbing against the steel membrane surface under oscillatory motion condition. Different experimental parameters were chosen, which are listed in Table 6-3. The apparent pressures are around 325 and 163 kPa when 70 and 30 N loads were applied, respectively, although the real contact pressure is much higher at asperity levels. The sliding speed of the rubbing counterpart is between 0.01-0.03 m/sec depending on the distance from the centre of the

ring, and therefore the sliding distance after 5 h experiment is between 180-540 m.

Table 6-3: Test conditions used during hydrogen uptake experiments

Kinematics	Oscillatory motion
Load	70, 30 N
Angular displacement amplitude	55 deg.
Frequency	1, 0.5 Hz
Test duration	5 h

Different lubricant formulations were tested. Information on the lubricants used in this study is shown in Table 6-4. Low viscosity PAO was used as the base oil in our experiments. The kinematic viscosity of the base oil was 4.0 cSt at 100°C and the dynamic viscosity was 2.85 mPa.s at 90°C. PAO is a synthetic lubricant with hydrocarbon molecules which consist of hydrogen and carbon atoms. ZDDP was added to the base oil as an anti-wear additive with 0.08 wt% phosphorus content in the lubricant formulation. 1 wt% MoDTC friction modifier additive was blended to the PAO+ZDDP using a hot-plate at 60°C for 30 minutes. The lubricants were flushed with dry nitrogen before the experiments to remove the possible contaminations.

Table 6-4: List of lubricants

Lubricant	Description
PAO	Polyalphaolefin high purity, synthetic, non-polar base oil
PAO+water	5% water - emulsified
PAO+salt water	5% salt water (3.5% NaCl) - emulsified
PAO+ZDDP	0.08% P
PAO+ZDDP+MoDTC	Lubricant D + 1 %wt MoDTC
PFPE	Perfluoropolyether

The hydrogen atoms which permeated through the steel membrane during rubbing were oxidized by the applied anodic potential and the oxidation current was continuously measured with data logging every 10 seconds. The hydrogen oxidation current is recorded by using an Ivium potentiostat linked to a computer for data capturing and used to quantify hydrogen permeated through the steel. Experiments were carried out at both room temperature

which was 20±2°C and higher temperature around 85°C. Two different temperatures were chosen as such to evaluate temperature effect on both tribofilm formation and water behaviour in the lubricant, as at higher temperature evaporation of water in oil occurs. All measurements were performed at least two times to assure repeatability. At the end of testing, the specimen was removed, ultrasonically cleaned with heptane to remove excess oil and used for surface analysis.

6.4 **Heating-up the lubricant**

Some of the experiments in this study were conducted at room temperature and some others carried out at high temperature. In order to heat up the lubricant, a closed circulatory system was utilised to circulate the oil from the oil bath through a heat exchanger continuously during the experiment. The schematic set-up is shown in Figure 6-1. The temperature of the heat exchanger was fixed at 99°C and the oil flow rate was 25 ml/min. A peristaltic pump was used to circulate the lubricant. The lubricant temperature was monitored in the oil bath, far from the metal membrane, before starting the rubbing using a digital thermometer (Fluke 54) with the accuracy of 0.05% + 0.3°C. The temperature of the lubricant in the oil bath was measured about 80-85°C. The lubricant was left for 30 min before starting the test to reach a stable temperature.
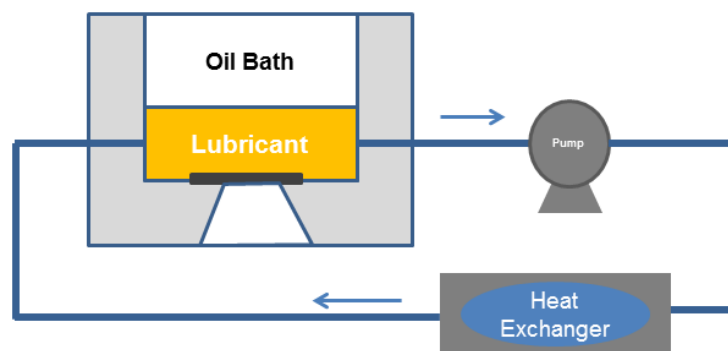
Figure 6-1: Schematic of oil circulation and heating up set-up

6.5 **Oil ageing**

PAO base oil is aged artificially in the lab in accordance with ASTM D4363-99 standard [133]. As shown in Figure 6-2, 200 ml of PAO was placed in a glass container with a three-neck lid. The evaporation of the oil was prevented using a condenser put on top of one of the necks. Air was also blown into the oil, continuously, with the airflow of 10 L/h to provide a source of oxygen. A piece

of metal was also put in the lubricant to provide catalytic reactive surface. One of the necks was allocated to the sampling of the oil and condition monitoring of the system during the ageing process. The beaker containing oil was placed on a hot-plate and its temperature was kept constant at 160°C creating a harsh condition that accelerates degradation of the lubricant.
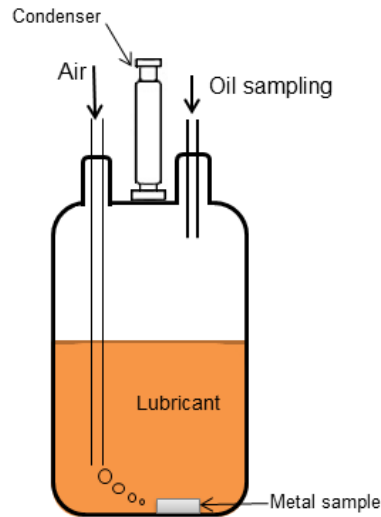
Figure 6-2: Schematic set-up for the artificial oil degradation

6.6 Wear measurement

Optical white light interferometer, NPFLEX from Bruker, was employed to measure the volume loss on the steel membranes allowing assessment of wear after the test. The membranes were rinsed with heptane in an ultrasonic bath after the experiments and then examined by white light interferometry in order to study the profile of the wear track. Basic theory of how this equipment works and how the images are obtained are explained in this section. Interferometers use a single source of light to generate two white beams of light using a beam-splitter. A beam called as reference beam reflects from a reference mirror and another beam, object beam, reflects from the sample being measured. The reflected light of each beam is then recombined. The recombined beams are used to generate bright and dark bands, fringes, that create an interference pattern showing the topography of the object surface. In this study, Vision64 software from Bruker was used to analyse the interference images obtained from NPFLEX.

Two and three-dimensional images were taken from four different areas of the wear track as shown in Figure 6-3 (c) and the average wear width and depth in different areas were used to calculate the wear volume of each sample. The standard deviation equation was used to measure the error bars. Figure 6-3

shows an example of a typical wear measurement image formed on the membrane. The average wear depth was measured by comparing the average heights of points inside and outside of the wear track as shown in Figure 6-3(d). Ethylenediaminetetraacetic acid (EDTA) is the most appropriate solvent for removal of ZDDP tribofilm [134]. However, the samples were cleaned by heptane in this research as the wear depth in these experiments are significantly higher compared to the thickness of the tribofilm.
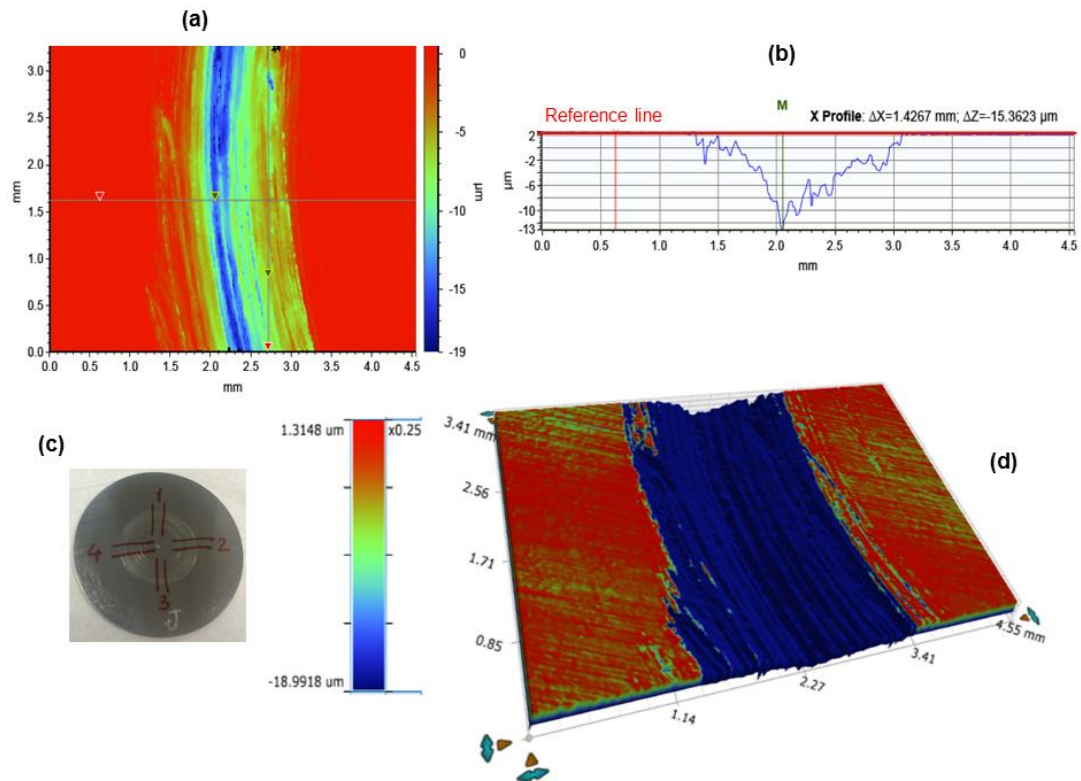
Figure 6-3: (a) Two-dimensional image of the wear track, (b) wear scar profile after the experiment, (c) four different area of wear scars were analysed and (d) three-dimensional images of wear track

6.7 Scanning Electron Microscope (SEM) and Energy Dispersive X-ray analysis (EDX)

In this project, a Carl Zeiss (Oberkochen, Germany) EVO MA15 Scanning Electron Microscope (SEM) was employed in order to take images of the sample surfaces. The microscope was equipped with an Oxford Instruments (Abingdon, UK) XMAX Energy Dispersive X-Ray (EDX) spectrometer enabling chemical analysis of the tribofilm. SEM images and EDX spectra were both recorded at 20 KeV incident beam energy.

The SEM images are produced by scanning a focused beam of high-energy electrons at the surface of the sample. The emitted electrons from the atoms excited by the electron beam, called secondary electrons, are detected and the number of detected electrons depends on specimen topography, among other things. Collecting the secondary electrons produces a high-resolution image of the surface displaying the topography of the surface.

On the other hand, the high-energy electron beam was used to stimulate the emission of characteristic X-rays from the surface of the specimen in EDX analysis. The number and energy of the X-rays emitted from the specimen are measured by an energy-dispersive spectrometer. The energies of the X-rays depend on the energy differences between the electron shells and the atomic structure of the emitting element. Therefore, EDX spectrum allows the elemental identification of the area in question.

In this investigation, SEM and EDX were conducted to study the wear mechanism and surface chemistry of the specimens after tribotests. Both EDX spot and EDX mapping modes were utilised to gather information concerning the chemical composition of different products form on the surface.

6.8 Raman spectroscopy

EDX technique provides information on chemical composition of the surface tribofilm/oxide layer. However, in order to probe the influence of the different products on hydrogen entry, one needs to know not only the elements of the surface layers, but also the compounds structure. Therefore, Raman spectroscopy was performed on the surface of the samples to determine the tribofilm/oxide film structure. The hydrogen entry rate will be correlated with the properties of the surface film. A Renishaw InVia spectrometer (UK) was used in this study to carry out Raman analysis on the steel samples after hydrogen uptake experiments. The spectral resolution and lateral resolution of the spectrometer are 1 cm^{-1} and 800 nm, respectively. This Raman spectrometer is equipped with 5x, 20x and 50x short distance objectives as well as a 50x long distance objective. The Raman equipment has a 488 nm and a 785 nm-wavelength lasers operating at a maximum laser power of 10 mW and 220 mW at the source, respectively. The radius of laser spots were 400 nm and 640 nm for 488 nm and 785 nm laser, respectively. The 488 nm wavelength laser at room temperature was utilised in this study to obtain the spectra. A calibration was performed before the experiments using Si(100) target to check the Si peak at 520 cm^{-1}. A PC is connected to the Raman

equipment to collect spectral data during the analysis using the Renishaw WiRE software.

The samples are placed on the stage and they can be viewed through the eye piece or on the PC. The surface of the samples are analysed with lasers focused through the objective lenses. Single spot analysing method was employed in this study to obtain the Raman spectra. Different regions of the sample, within the wear scar and out of the wear scar, are analysed to ensure the uniformity of the chemical composition. The acquisition range was in the 150-1670 cm^{-1} region where all films tested in this study showed relevant features in the obtained spectra. Assignments to the obtained peaks were done based on the literature.

6.9 Fourier Transform InfraRed Spectroscopy (FTIR)

FTIR method works with the infrared region of the electromagnetic spectrum. FTIR is equipped with a horizontal Attenuated Total Reflectance (ATR) zinc selenide (ZnSe) sample cell accessory. Different chemical bonds of samples can be identified using this technique by measuring the absorption of various infrared light wavelengths [135]. In this analytical technique, the sample is radiated with a broad-band source of light in the infrared region. This technique was employed in this project in order to identify the chemical composition of the bulk oil after ageing. The Perkin Elmer FTIR spectrometer was reported in this study within the range of 650-4000 cm^{-1} with the resolution of 4 cm^{-1}.

6.10 Electrochemical impedance spectroscopy

In the current study, EIS tests were performed using a Solartron 1280 impedance gain-phase analyser linked to a PC for data capturing. The test cell utilised two identical AISI 52100 steel electrodes with diameter of 35 mm as shown in Figure 6-4. Measurements were carried out at 50°C. Before each EIS measurement, the OCP was allowed to stabilize for 2 hours. An AC voltage was applied at constant amplitude varied about the OCP and the resulting current measured. Measurements were carried out over a range of frequency varied from $2x10^4$ to 1 Hz and the impedance calculated and recorded at each frequency. Since there is a phase shift between current and potential, the impedance values are complex quantities. These results are presented in Chapter 9 in which the impedance measurements in lubricant is discussed in details.
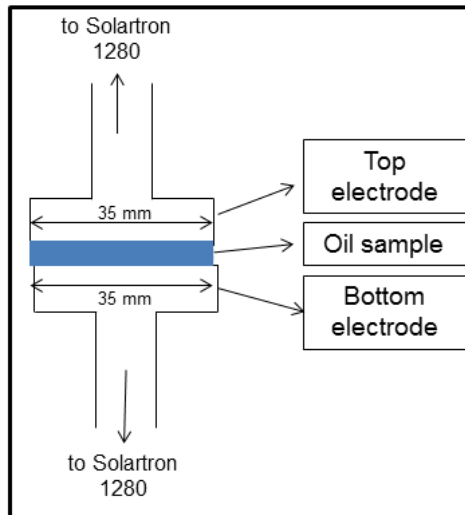
Figure 6-4: The EIS test cell from side view

6.11 Analysis of permeation transient

The primary objective of this study is to define the tribological hydrogen uptake of the steel as a function of environmental variables. When the permeation curve showing the instantaneous rate of hydrogen permeation is obtained, various mathematical analysis can then be used to calculate the hydrogen diffusion rate through the membrane. The most common methods used for analysing the hydrogen permeation curves were derived from Fick's second law [119]. The following equations are considered in this study to analyse the permeation transient curves. Prior to calculating both hydrogen permeation flux and the diffusion coefficient of hydrogen, the background current needs to be subtracted from the measured oxidation current.

➢ Time lag method

The integration of the rising curve gives the quantity of hydrogen which has permeated through the steel. An extrapolation of the plot of quantity against time gives the time lag (t_{lag}). It was shown that the t_{lag} can simply be measured by spotting the time at which the permeation rate is 0.63 times the steady state value (i_{ss}). Equation (6-2) describes the correlation between t_{lag} and diffusion constant:

$$D_{eff} = \frac{L^2}{6t_{lag}} \tag{6-2}$$

L is the thickness of the membrane.

➢ Hydrogen permeation flux

The measured values for current density (i) can be converted to the hydrogen permeation flux (J) using the following equation.

83

$$J = i/nF \qquad (6\text{-}3)$$

where n is the number of electrons transferred and F is the Faraday's constant (96,485 C/mol).

➢ Total hydrogen permeation

The amount of permeated hydrogen through the steel per second (mol/cm^{2}s), can be estimated by integrating hydrogen permeation current density with time by using the following equation [124]:

$$S = \frac{1}{Ft} \int_0^t i \, dt \qquad (6\text{-}4)$$

Where i is hydrogen oxidation current density (A/cm^2), F is Faraday's constant and t is the integration time (s). The equation (6-4) is used as the most accurate way to compare the obtained results from the hydrogen uptake rig in this study. This is showing the total hydrogen permeation through the steel continuously during the rubbing.

6.12 **Repeatability and reliability of the results**

The disadvantages of the prototype set-up were explained in section 5.2.2. The main limitation of using that configuration for hydrogen permeation monitoring from a tribo-contact was the fact that the hydrogen was not generated from a metal-metal contact; it was generated from a polishing paper rubbing the metal membrane surface. The set-up was also not capable of applying repeatable tribological testing parameters such as load, sliding speed, and lubrication.

Therefore, the new set-up described in section 5.3.2 was designed and built in order to improve both the reliability and repeatability of the obtained results. The rubbing counterpart was changed to a metal ring to make the tribo-contact more realistic. A load cell is employed to accurately and continuously monitor the applied load and the sliding speed. These help to have a very good repeatability of the testing parameters improving the reliability of the results.

All measurements in this study were performed at least two times to check repeatability. Generally, the repeated results for the identical experiment conditions were within ±10% of the measured value in the steady state region of the curves for all of the measurements. This is showing very good reliability of the results obtained from the new measurement technique. The repeated experiments for some of the measurements are shown in Figure 6-5 and Figure 6-6. Repeatability of the results was acceptable when precautions were

taken to avoid contamination of surfaces and keep the palladium coating free from mechanical damage.
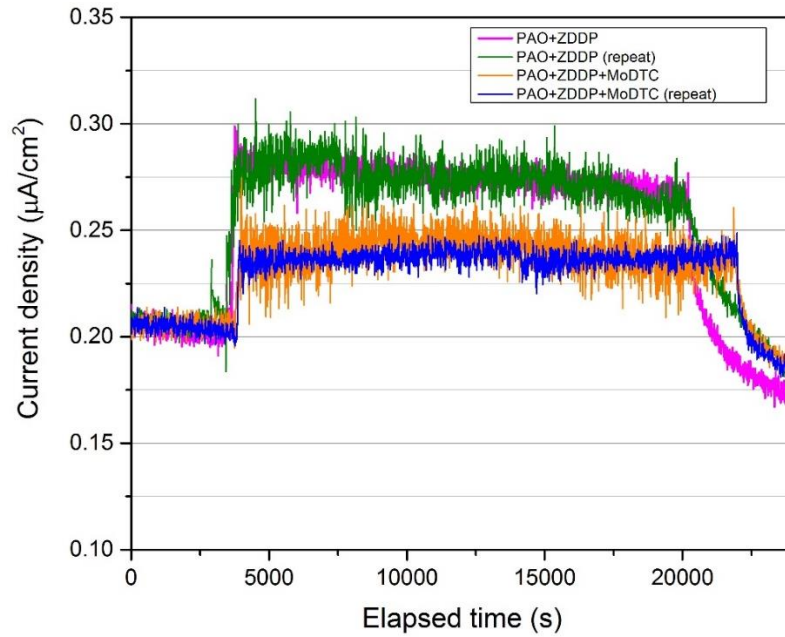
Figure 6-5: Repeatability of the measurements when PAO+ZDDP and PAO+ZDDP+MoDTC were tested
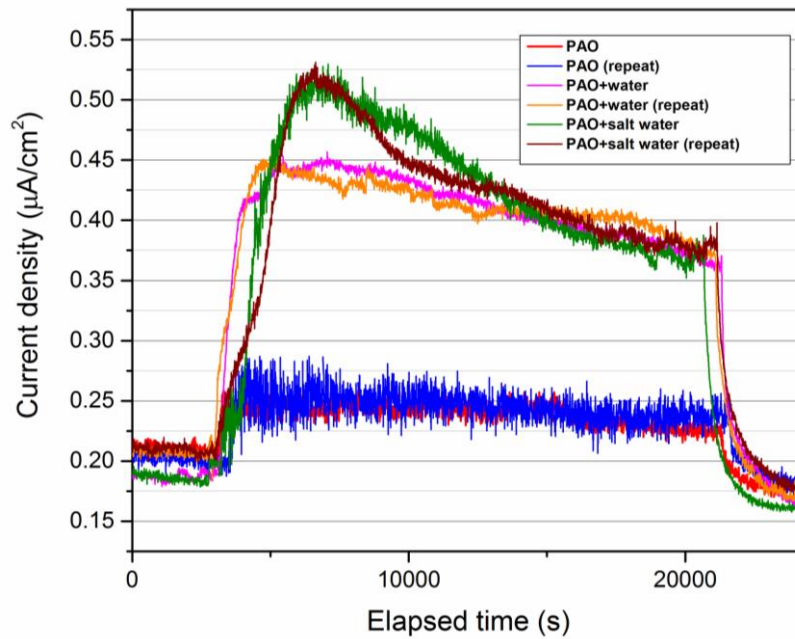
Figure 6-6: Repeatability of the measurements when PAO, PAO + water and PAO + salt water were tested

Chapter 7 Hydrogen uptake results obtained from a lubricated contact at room temperature

7.1 Introduction

Results obtained from the newly developed hydrogen uptake rig for the metal-metal tribo-contact are presented in this chapter. These results help to understand the source of hydrogen in lubricated tribo-contacts and the effect of water contamination, lubricant additives and contact pressure on tribological hydrogen uptake. Various surface analysis techniques such as SEM/EDX, Raman spectroscopy and white light interferometry were employed to verify the mechanism of tribochemical reactions happening on the surface causing hydrogen permeation through the steel.

7.2 Current decay curve – before rubbing

After clamping the sample, a constant anodic potential, 115 $mV_{Ag/AgCl}$, is applied on the detection side of the steel membrane using the three-electrode electrochemical cell. The whole unit is left overnight to reach the steady state without applying the load. However, the oxidation current measurement results were noisy as shown in Figure 7-1. This was due to the increasing of the electrolyte temperature, up to 50°C, within the glass beaker (Figure 7-2) by circulating hot water through the jacket. This is reducing the solubility limit of the dissolved gas, such as CO_2, in the water which was used to prepare sodium hydroxide brine. Consequently, these gases escape the brine in form of bubbles. The bubbles hit the membrane and accumulate beneath the membrane distracting the sensitive electrochemical measurements. The formation and accumulation of the bubbles were visible by the naked eye.
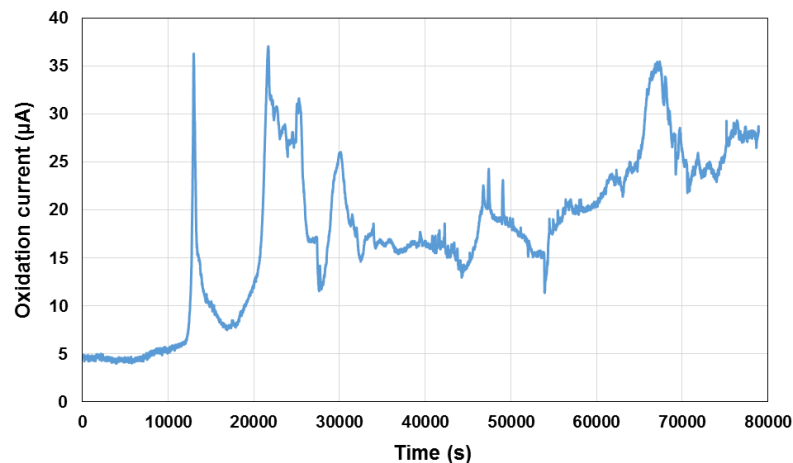
Figure 7-1: Noisy results before applying load

To overcome this challenge, the water was boiled before preparing the brine for 30 minutes in order to remove the dissolved gases. It was noticed that the bubbles would not generate anymore when the temperature increases during the experiment and the decay current curve is produced, as shown in Figure 7-3, indicating that the problem has been solved using this procedure. The brine is protected by the flow of nitrogen on the surface during the experiment. This nitrogen flow covers and protects the electrolyte from air dissolution.
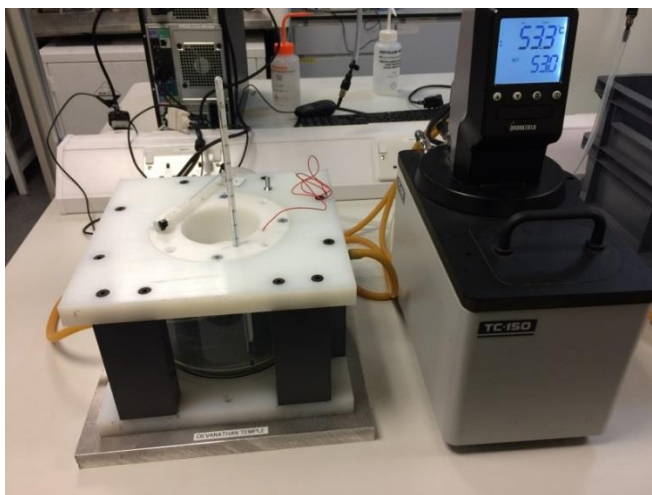
Figure 7-2: Circulating hot water through the jacket

The obtained current decay curves were identical for all experiments before applying the load. The current gradually decays until it reaches a steady state value. This happens as a result of labile hydrogen migrating to the surface. Once the current ramped down and reached below 250 nA/cm^2, the oil bath was filled, the load was applied and rubbing started.
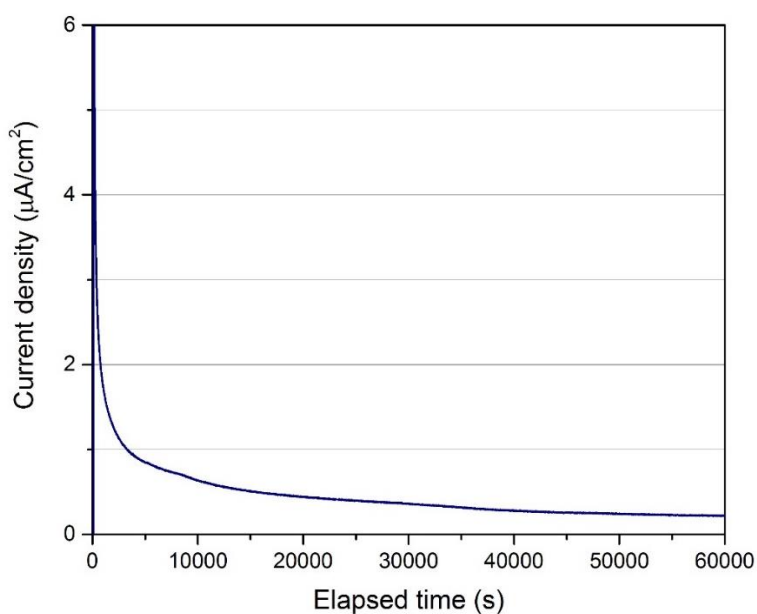
Figure 7-3: Current decay curve

When the rubbing starts, hydrogen is generated from the lubricated contact at the entry side. The diffusion of hydrogen through the steel occurs due to the concentration gradient between the two sides of the membrane. It takes some time, known as the breakthrough time (t_b), for hydrogen to diffuse through the membrane and reach the detection side (t_b is shown in Figure 7-4). Then the oxidation current measured on the detection side will start to increase leading to a build-up permeation transient.

The obtained hydrogen uptake curves in this study are similar to the typical curves from conventional hydrogen permeation experiments [136]. The key components of this plot are shown in Figure 7-4:

I.   A stable and static current in static conditions, before rubbing
II.   An induction time when rubbing starts after which current rises
III. The current remains high either at a steady state or decreasing depending on conditions; this is discussed later
IV.   A decay of current when rubbing stops.

The induction time for hydrogen atoms to emerge on the detection side of the cell depends on the thickness of the membrane. The steady state current value and the time needed to reach steady state depend on the concentration of hydrogen on the rubbing side as well as the steel microstructure which determines hydrogen diffusivity. Generally, hydrogen permeation rate into the membrane depends on the nature of the metal, its metallurgical treatment, composition of the lubricant and the surface state.
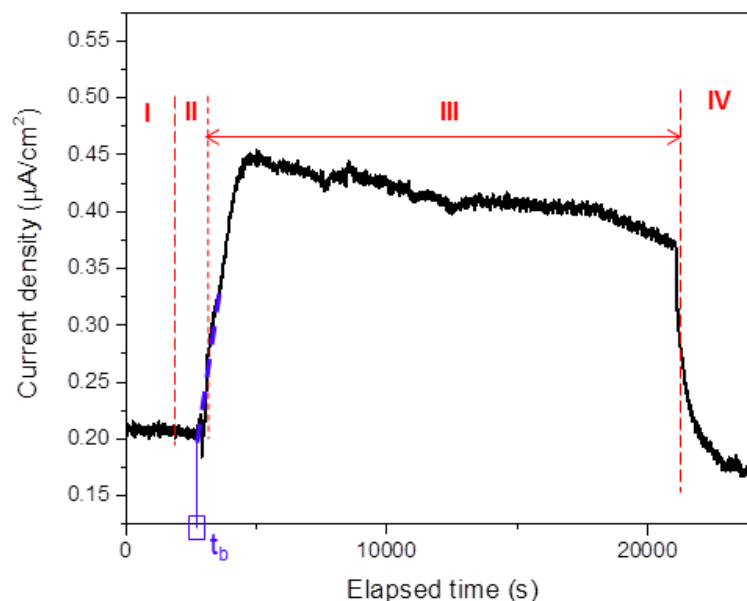
Figure 7-4: The key features and typical shape of the hydrogen permeation charging and de-charging curve

7.3 Diamond powder sprayed polishing paper as rubbing counterpart

Similar to the experiments carried out by the prototype set-up described in section 5.2.2, polishing tape was sprayed with diamond powder (grain size 1 µm) and used as rubbing counterpart for the experiments conducted by the newly developed rig. The results for two different lubricants, PAO and PAO+ZDDP, are shown in Figure 7-5.

The increase in current density shows that hydrogen was generated and detected successfully using the new rig. The permeation current returned to its original value within two hours when the rubbing stopped. This clearly shows that hydrogen generation is linked to the shear stress and friction in tribo-contact. Severe wear marks were observed on the rubbed side of the membrane as shown in Figure 7-6. However, the palladium coating remained intact on detection side of the membrane. The detection side remained intact for all the tested membranes in this study and will not be shown for other experiments.
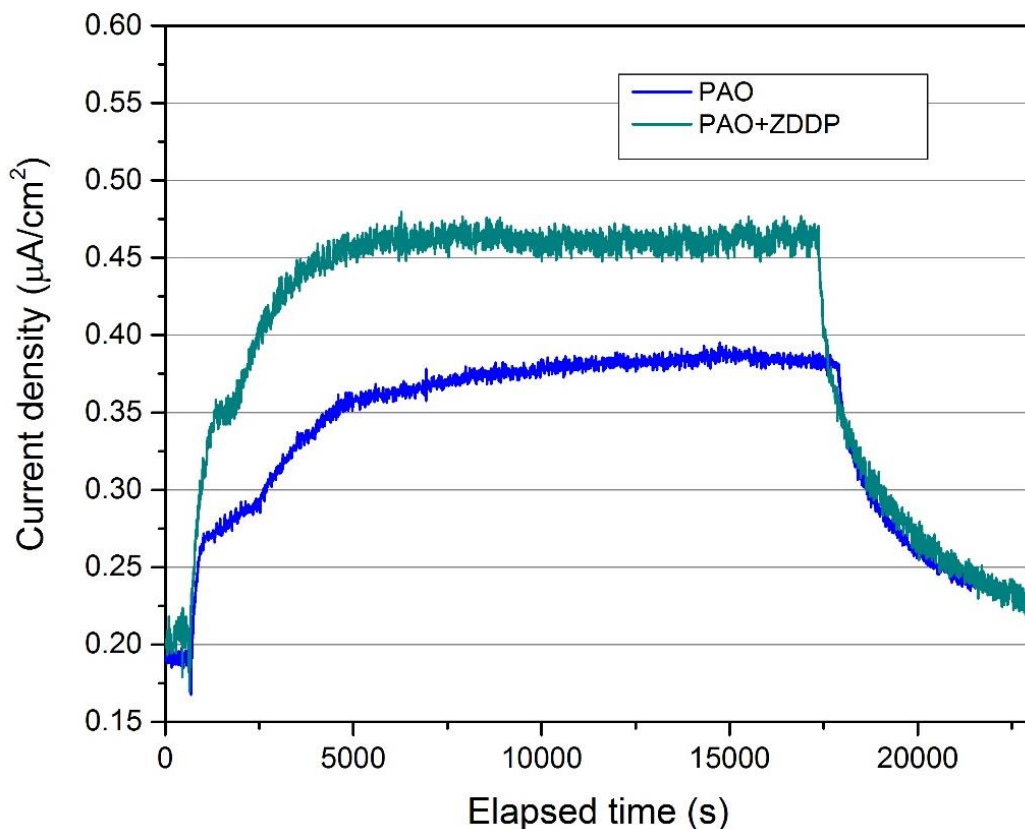
Figure 7-5: Hydrogen uptake curves obtained when DP sprayed polishing paper is used as rubbing counterpart

Rubbed side	Detection side
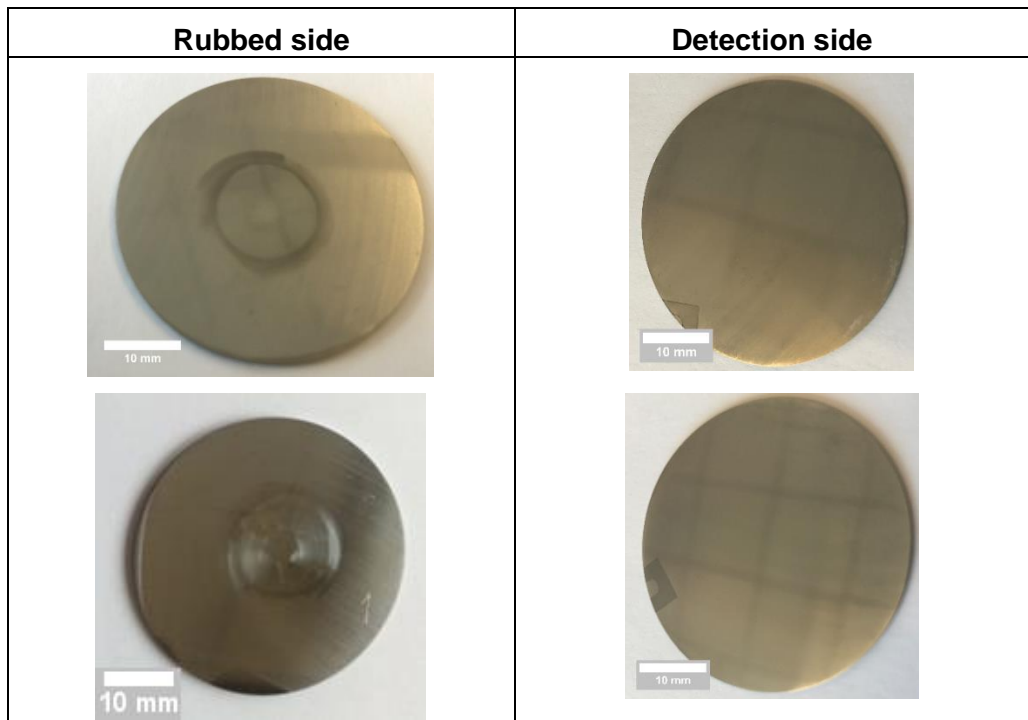
Figure 7-6: Optical photos of the rubbed side and detection side of the membrane

Total wear volume of the membranes after each experiment was measured using the white light interferometry by the procedure described in section 6.6. Comparison of the wear measurement results for different lubricants are presented in Figure 7-7. The wear volume was almost the same for both lubricants.
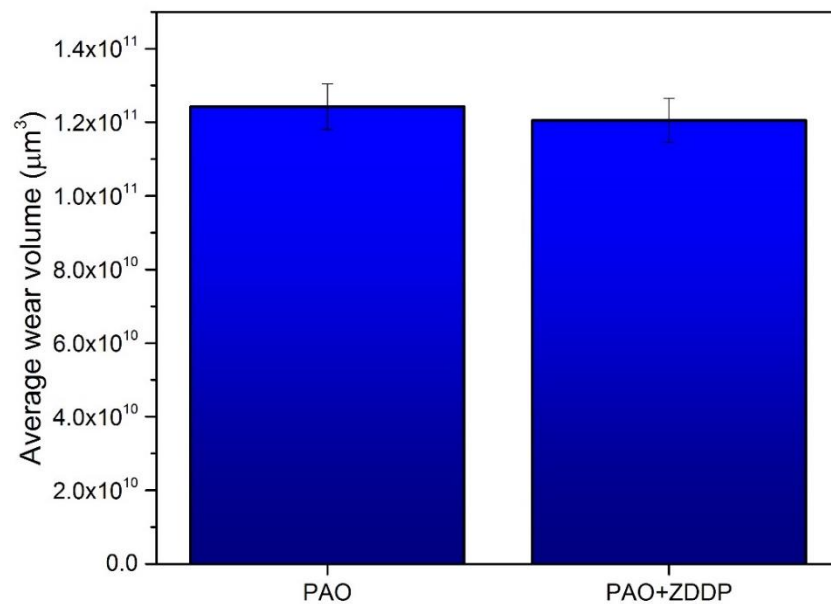
Figure 7-7: The wear volume of the samples tested by PAO and PAO+ZDDP lubricants at room temperature using DP sprayed polishing paper as rubbing counterpart

The total amount of permeated hydrogen through the steel membrane was calculated using equation (6-4) described in section 6.11. The results plotted in Figure 7-8 indicate that hydrogen uptake is promoted in presence of ZDDP additive in PAO base oil. This behaviour is similar to that reported by Bo Han et al. [127].
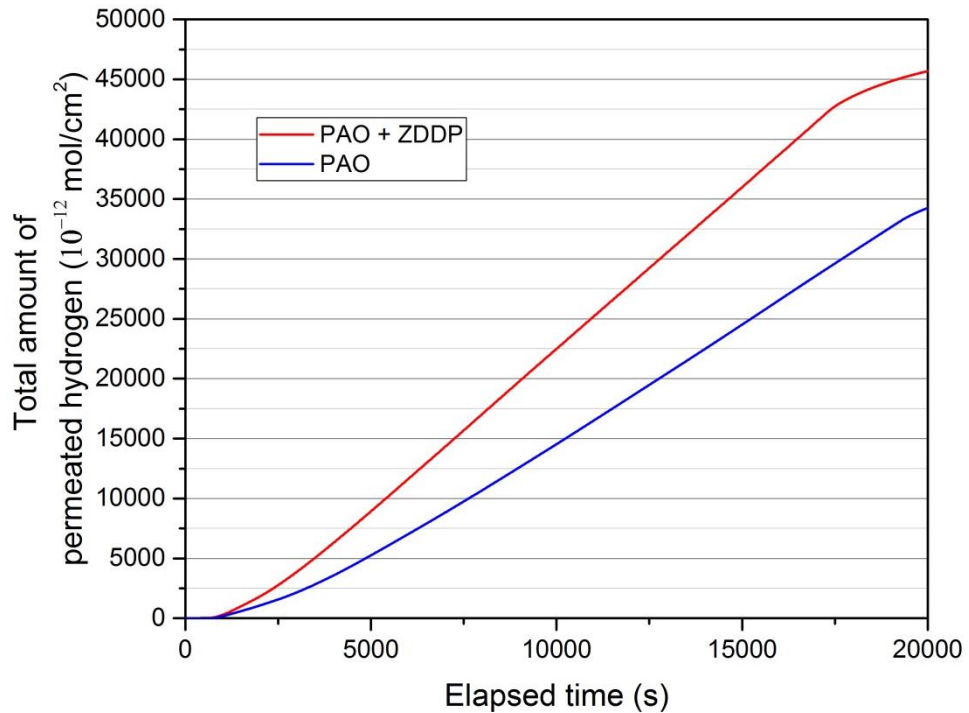
Figure 7-8: Total amount of hydrogen uptake when DP sprayed polishing paper is used as rubbing counterpart

However, one of the main objectives of developing the new rig was to measure hydrogen uptake from a more realistic metal-metal contact. Thus, the DP sprayed polishing paper was replaced by a rough metal surface as described in section 5.3.2. All the rest of results presented in this study were obtained from metal-metal tribo-contact.

7.4 **Source of hydrogen**

Hydrocarbon base oil has been considered as one of the sources of hydrogen in lubricated tribo-contacts. In order to find out if any of hydrogen is coming from the hydrocarbon lubricant, a control test was done by using hydrogen free lubricant, perfluoropolyether known as PFPE. This is a type of fluorinated oil that does not contain hydrogen in its structure unlike hydrocarbon lubricants such as PAO base oil. PAO that is used in this study is a polymer formed by polymerizing alpha-olefin with formula presented in Figure 7-9 [25].

$$(—CH_2—CH_2—CH_2—CH_2—)_n \cdots CH_2—CH_2—CH=CH_2$$
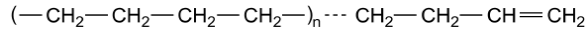
Figure 7-9: Structure of PAO [25]

The hydrogen permeation current for PFPE is measured and compared with PAO lubricant in Figure 7-10. As it is seen in Figure 7-10, when rubbing starts with PFPE fluid as lubricant no hydrogen permeation current is observed apart from an offset in decay baseline. The curve shape is different for hydrogen permeation current from PAO lubricant that gradually increases and reaches a steady state.
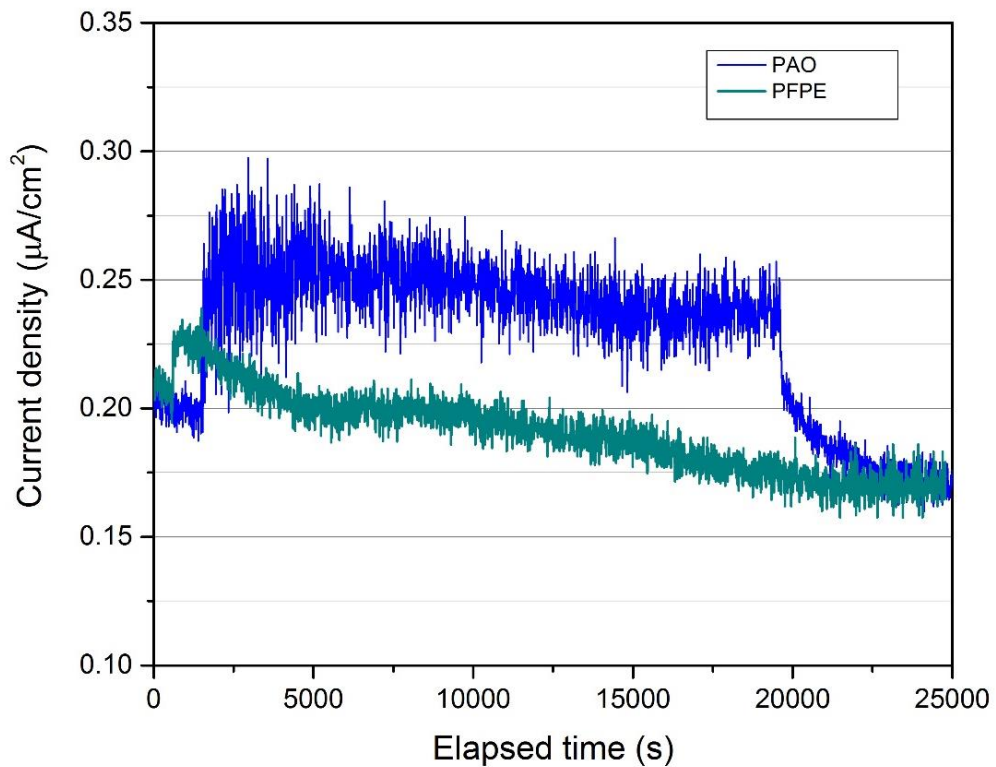
Figure 7-10: Hydrogen uptake measurement when PAO and PFPE were used as lubricant

The friction torque is also measured continuously during the surface-rubbing and the results for PAO lubricant during 2 minutes and 5 seconds of the experiment are separately shown in Figure 7-11. The friction torque shows a sinusoidal behaviour due to the oscillating motion. However, to have a better comparison for different lubricants, only the maximum and minimum values of the torque measurement, as marked by circles, are used to calculate the friction coefficient in this study.
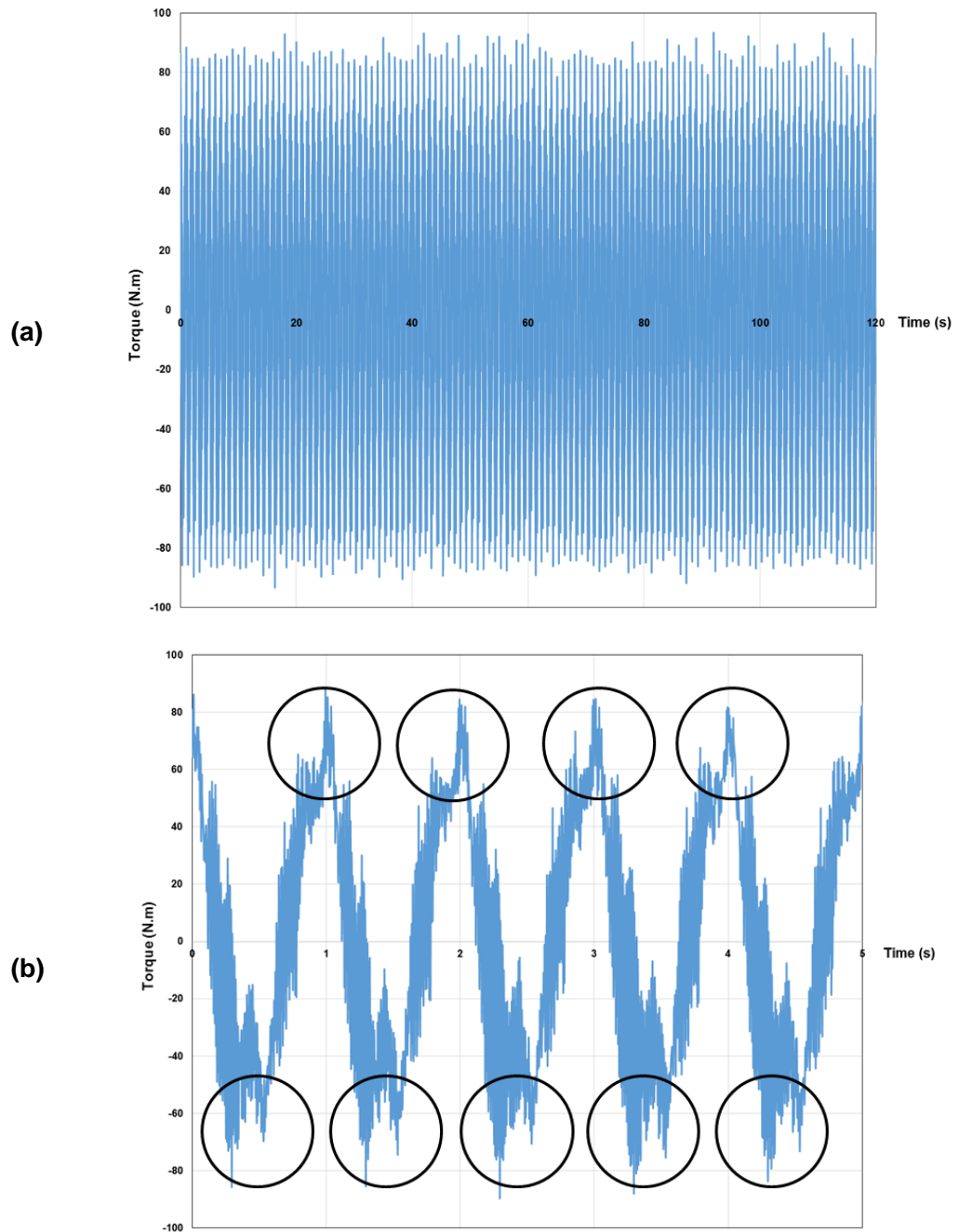
Figure 7-11: Variations in the torque measurement results with test duration for (a) 120 sec (b) 5 sec

The coefficient of friction was calculated using the torque measurement results according to the following equations. There are some assumptions made to simplify the calculation:

- The maximum torque is used to calculate the friction coefficient
- The friction force is directly proportional to the applied load ($f_{friction}=\mu W$)
- The angular velocity is constant
- The membrane is subjected to a uniform distributed load

If we consider a circular element of radius *r* with width of *dr* as shown in Figure 7-12 and consider the fact that friction torque does not change with θ, then:
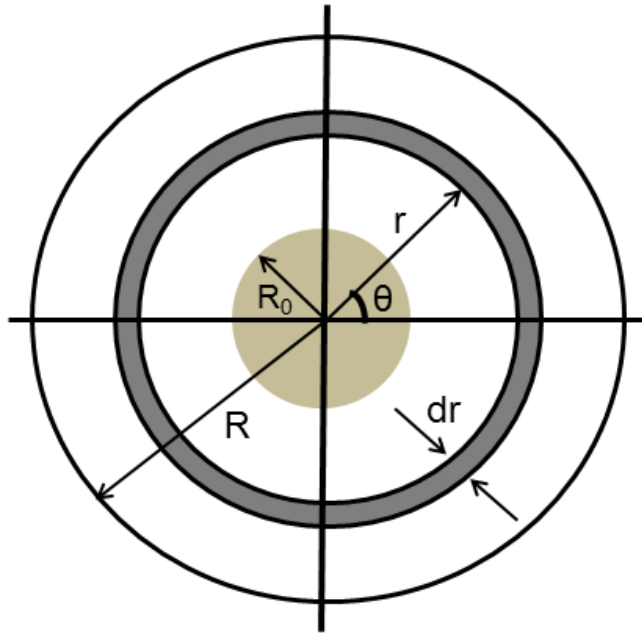
Figure 7-12: Circular element in polar coordinates

$$dT = df_{friction}r = \mu dW.r \tag{7-1}$$

where *T* is the applied torque and *dW* is the load applied to the element from the shaft calculated by the following equation:

$$\frac{dW}{W} = \frac{dA}{A} = \frac{\pi(r+dr)^2 - \pi r^2}{\pi(R^2 - R_0^2)} \tag{7-2}$$

dr² is negligible and can be removed:

$$dW = \frac{2W}{(R^2 - R_0^2)} r dr \tag{7-3}$$

Using the equations (7-1) and (7-3)

$$dT = \frac{2W\mu}{(R^2 - R_0^2)} r^2 dr \tag{7-4}$$

The total torque is obtained by integration of equation (7-4):

$$T = \frac{2W\mu}{(R^2 - R_0^2)} \int_{R_0}^{R} r^2 dr \tag{7-5}$$

gives

$$T = \frac{2W\mu}{3(R^2 - R_0^2)} (R^3 - R_0^3) \tag{7-6}$$

considering the rubbing counterpart geometry and the drilled hole diameter, R and R_0 are 9 and 3.5 mm, respectively. Therefore, the friction coefficient can be calculated using equation 7-7:

$$\mu = 0.15\frac{T}{W} \qquad (7\text{-}7)$$

The friction coefficient for the torque results presented in Figure 7-11 is calculated using equation (7-7) and shown in Figure 7-13.
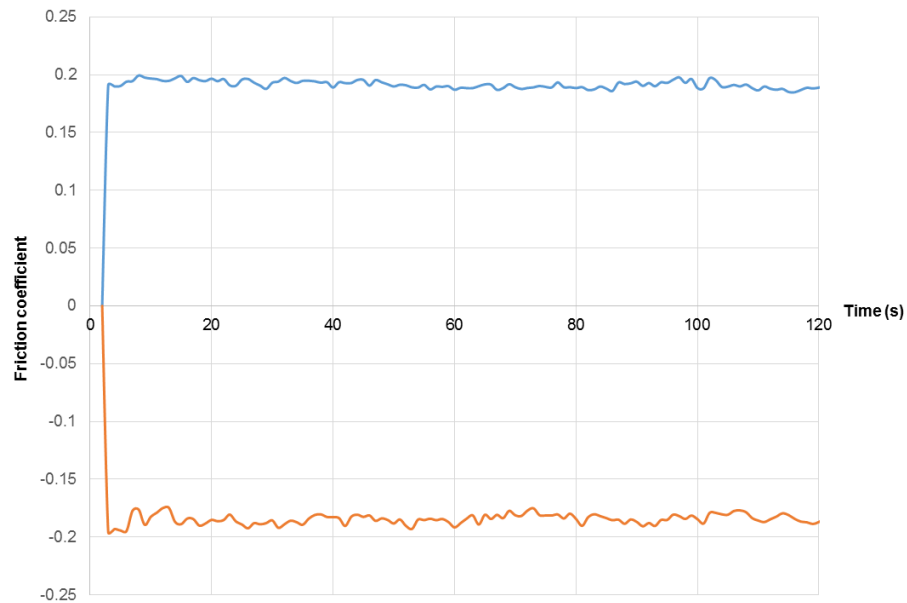
Figure 7-13: Variations in the friction coefficient with time for the steel pair lubricated with PAO

7.5 Effect of rubbing on hydrogen evolution

The effect of rubbing on hydrogen permeation rate was assessed by running experiment in static conditions and comparing the results with the hydrogen measurements during surface-rubbing. The results in Figure 7-14 indicate the contribution of chemical/corrosion reactions on hydrogen permeation through the steel compared to the tribochemical reactions effect. The corrosion products formed and covered the surface and clearly observed as rust (iron oxide) in static conditions, especially in presence of water contamination in the lubricant. However, no increase in permeation current was observed in absence of sliding on the charging side of the membrane. The same behaviour was seen for other lubricants. The formation of corrosion products, red colour rust, is shown in Figure 7-15 in case of having PAO+water in the oil bath.

On the other hand, the increased permeation current during surface-rubbing with PAO lubricant indicates that hydrogen can be generated from PAO under shear stress. In this experiment, hydrogen is produced on the rubbing side of

the specimen and its concentration becomes stable in a short time while the concentration of hydrogen atoms on the detection side of the specimen remains negligible throughout the experiment due to applying oxidizing conditions. Therefore, an unknown proportion of the generated hydrogen is expected to permeate through the sample as a result of the hydrogen concentration gradient between two sides of the steel sample.
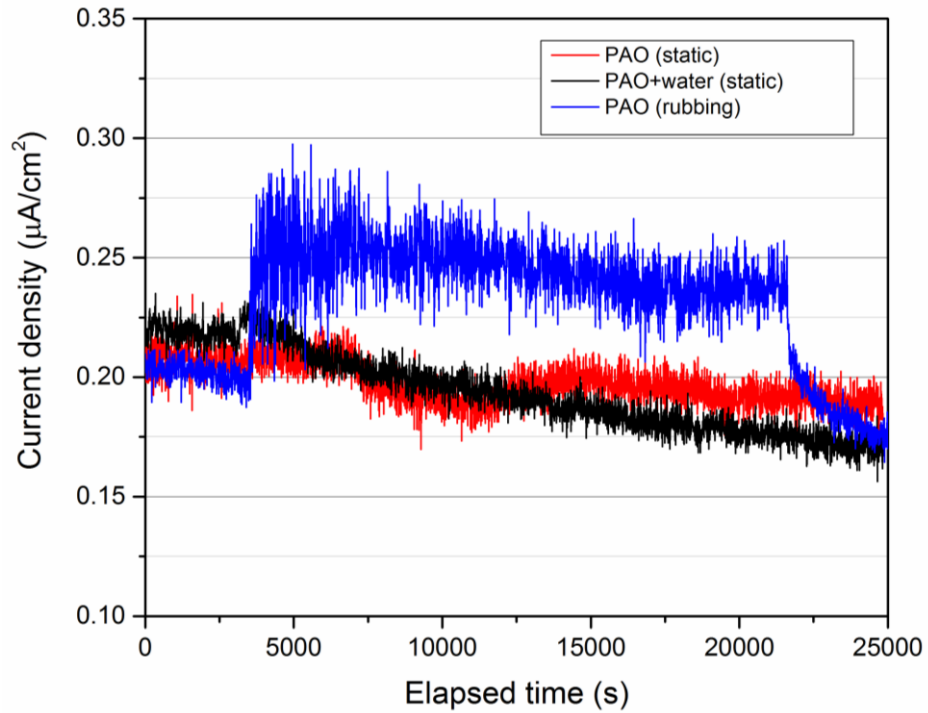
Figure 7-14: The effect of rubbing on hydrogen permeation rate

Figure 7-15: Optical image of the charging side of the membrane immersing in PAO+water in static condition

Figure 7-16 and Figure 7-17 illustrate Raman spectra obtained from the unworn and wear scar region of the membrane, respectively, after the test using PAO lubricant.
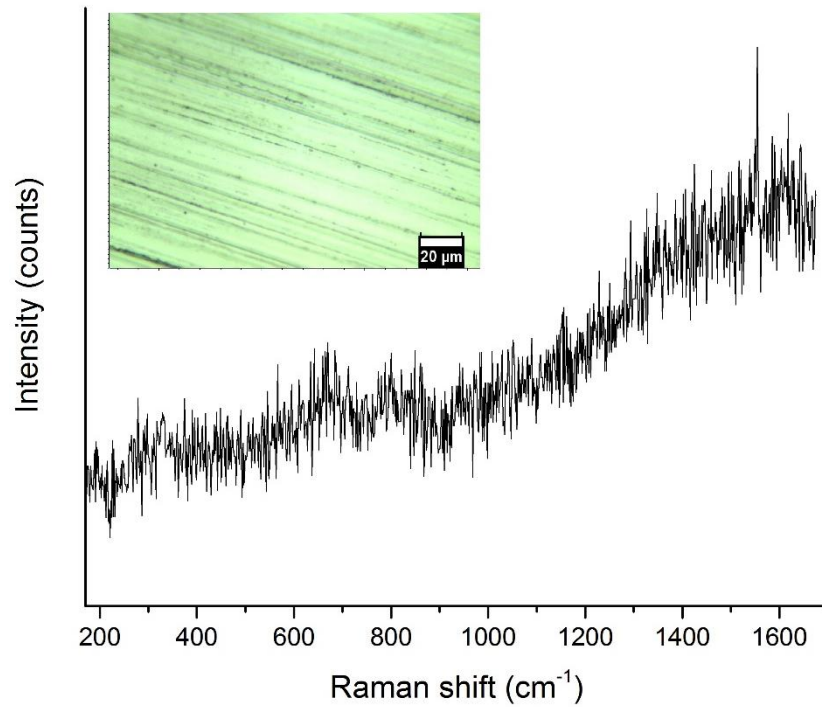
Figure 7-16: Raman spectrum obtained from out of the wear scar as shown in the inset after 5 h experiment with PAO lubricant[1]
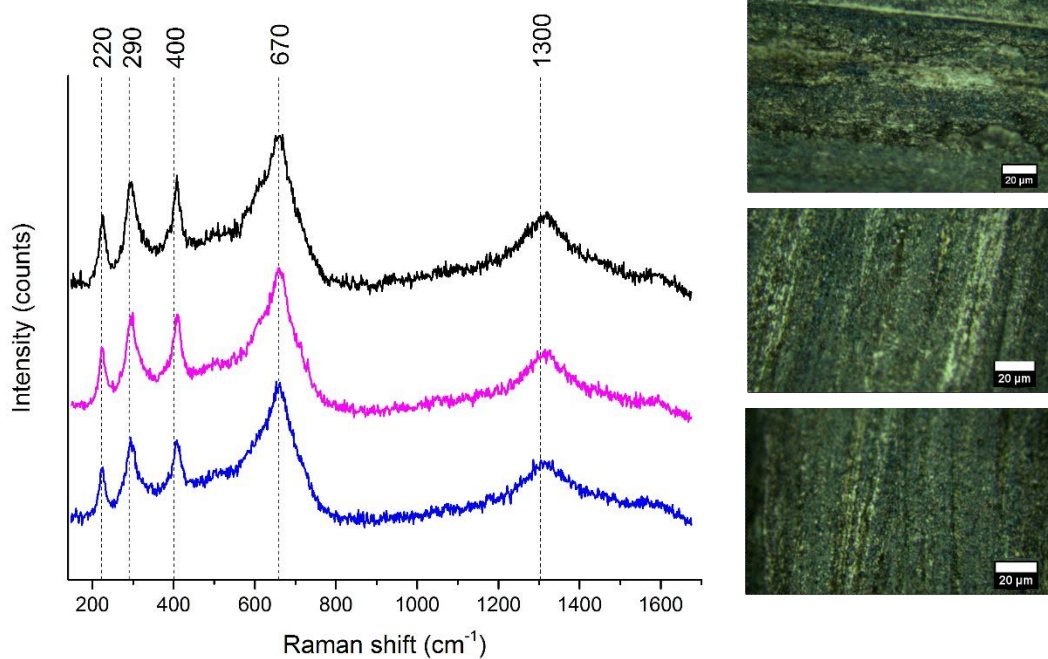
Figure 7-17: Raman spectra obtained from wear scars on tribopair after the test using PAO base oil. The analysed areas are shown in the insets

---

[1] Raman spectroscopy is a semi-quantitative technique and the intensity value in Raman spectra is more of an instrumental data rather than a physical data. It is dependent on many factors such as fluctuations in laser intensity, the orientation of the sample relative to the laser beam and focus. The material properties such as molecular vibration are also have a strong effect on Raman intensity.

97

The Raman spectrum obtained from out of the wear scar of the sample tested by PAO lubricant, Figure 7-16, does not show any distinguishable compound formed on the surface. However, the Raman spectra and EDX results from the wear scar show the formation of the iron oxide, mainly haematite (Fe_2O_3) and magnetite (Fe_3O_4), within the wear scar [137]. The SEM/EDX micrographs and mapping of the wear track for the sample tested by PAO lubricant are shown in Figure 7-18.

Element	Wt%
C	7.32
O	3.23
Si	0.05
P	0.01
S	0.00
Cr	1.68
Mn	0.42
Fe	87.27
Mo	0.02
Total:	100.00
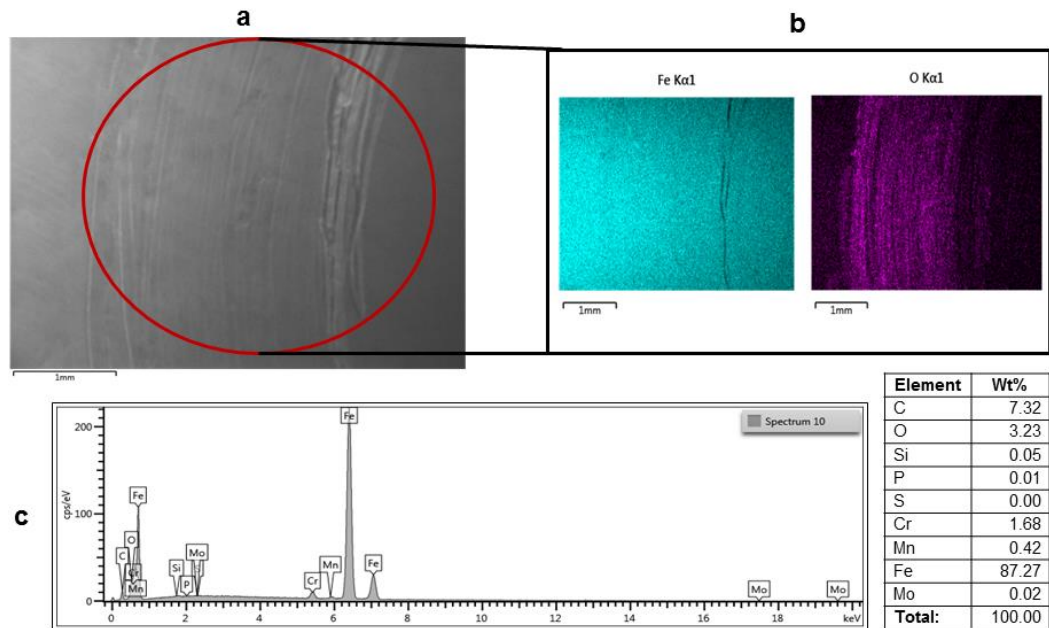
Figure 7-18: (a) SEM micrograph, (b) EDX mapping and (c) spectra from the wear track of the sample tested by PAO lubricant at room temperature

7.6 The effect of water contamination in lubricant on hydrogen permeation rate

The new technique has this ability to measure the amount of hydrogen diffusion through the steel in presence of certain concentration of water contamination in the lubricant. Figure 7-19 demonstrate the changes in current density caused by hydrogen permeation during surface-rubbing using PAO, PAO+water and PAO+salt water. PAO+water contains 5 volumetric percent water in lubricant base oil while PAO+salt water has 3.5% NaCl in solution to water. The water concentration exceeded its saturation level in the lubricant and so was suspended as microscopic droplets. To assure the homogenous distribution of water in lubricant, the water-oil emulsified mixture was prepared by injection of water into the lubricant and placing the container in an ultrasonic bath for 15 minutes. For these tests, there was a visible cloud or haze in the lubricant.
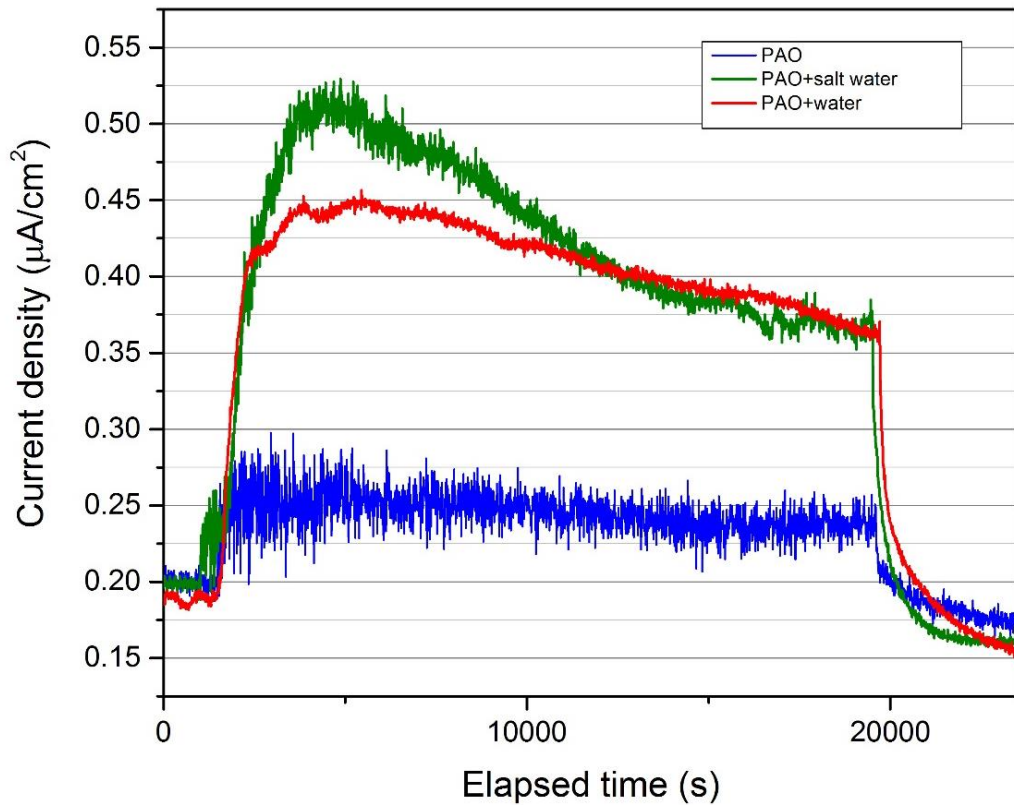
Figure 7-19: Effect of water contamination in lubricant on hydrogen permeation rate

Hydrogen permeation curves obtained from water-contaminated lubricant in Figure 7-19 show that the hydrogen oxidation current incrementally increases after a certain time lag corresponding to the hydrogen travelling time across the steel since the sliding started. The higher oxidation current density compares to PAO lubricant indicates that hydrogen diffusion rate increases as a result of more severe chemical reactions at the interface in presence of water contamination. Figure 7-19 shows that once the sliding process was terminated, the permeation current returned gradually to the initial value showing that rubbing is crucial to remove the surface oxides and promoting hydrogen evolution.

The surface of the samples after the experiment is depicted in Figure 7-20. Surface oxide is visible on the surface of the samples when the lubricant was contaminated with water or salt water. However, less visible corrosion products were seen on the surface of the membrane when PAO was used as lubricant.

(a)   (b)   (c)
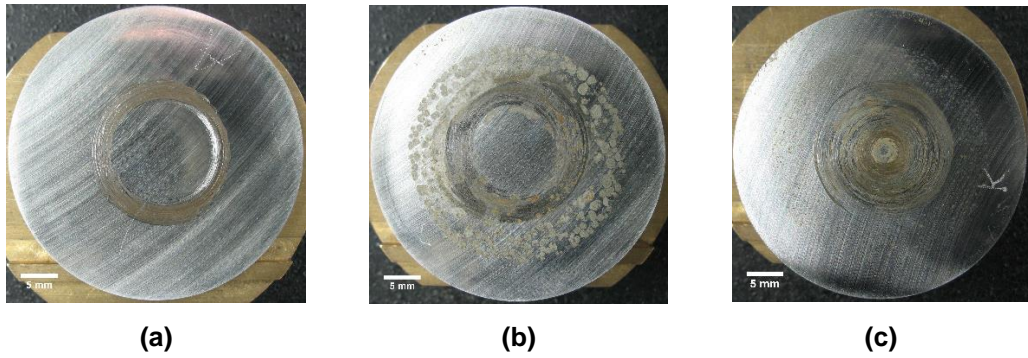
Figure 7-20: Optical images and SEM micrographs of the worn surface after the experiment with (a) PAO, (b) PAO+water, (c) PAO+salt water

EDX analysis was employed to assess the elemental composition of the wear scar. Unique colours were utilised to indicate the positions of specific elements emitting characteristic x-rays within an inspection field. The SEM/EDX micrographs and mapping of the wear track (see Figure 7-21 and Figure 7-22) show significant presence of oxygen within the wear scar. This indicates high oxidation rate of the nascent surfaces formed under shear stress.
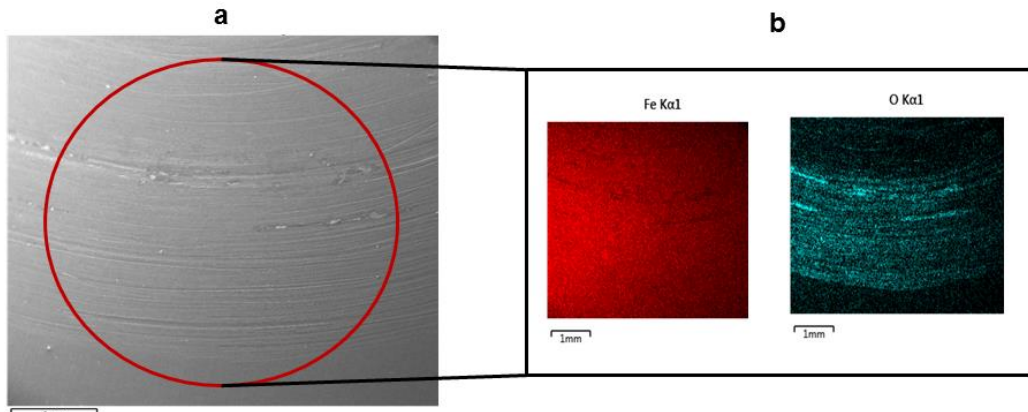
Figure 7-21: (a) SEM micrograph and (b) EDX mapping image of the wear track lubricated with PAO+ salt water after 5 h experiment
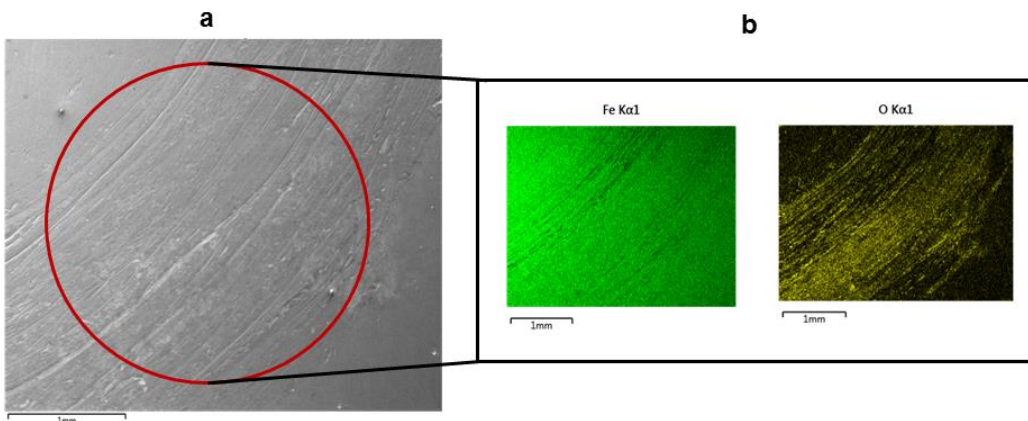
Figure 7-22: (a) SEM micrograph and (b) EDX mapping of the wear track lubricated with PAO+ water after 5 h experiment

100

Raman spectroscopy was used to acquire spectra from unworn region and wear scar region of the samples tested by PAO+water and PAO+salt water and the results are presented in Figure 7-23, Figure 7-24 and Figure 7-25, respectively. The Raman spectrum from unworn region of the sample does not show any Raman sensitive chemical compounds on the surface. Iron oxide was mainly identified within the wear track. Changes in the peak intensities and shift in their positions are indicative of formation of complex compounds, including hydroxides, in presence of water showing the interaction of water with other species in surface reactions. The Raman spectra of the sample tested by salt water contaminated PAO show the formation of Fe_3O_4.
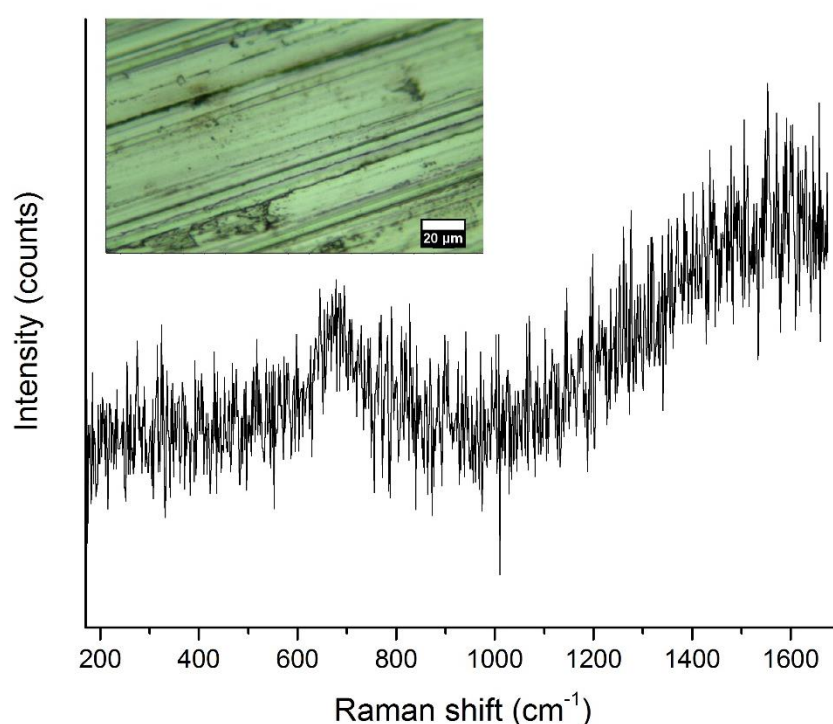
Figure 7-23: Raman spectrum obtained from out of the wear scar, as shown in the inset, after 5 hours experiment

7.7 The effect of lubricant additives on hydrogen permeation rate

The influence of two commonly used lubricant additives, ZDDP and MoDTC, on hydrogen transfer into the steel was assessed using the hydrogen uptake rig. It is seen in Figure 7-26 that hydrogen permeation current is promoted by having ZDDP as an additive in the lubricant as compared to PAO lubricant (hydrogen permeation rate with having PAO as lubricant was shown in Figure 7-19). This behaviour does not meet the expectation that the anti-wear

additive reduces hydrogen generation by decreasing wear. The reason for this discrepancy will be discussed in section 10.4. On the other hand, MoDTC additive reduces the measured permeation current. The influence of these lubricant additives on hydrogen permeation rate is more distinguishable in Figure 7-35 that compares total amount of hydrogen uptake during 5 hours of the experiment.
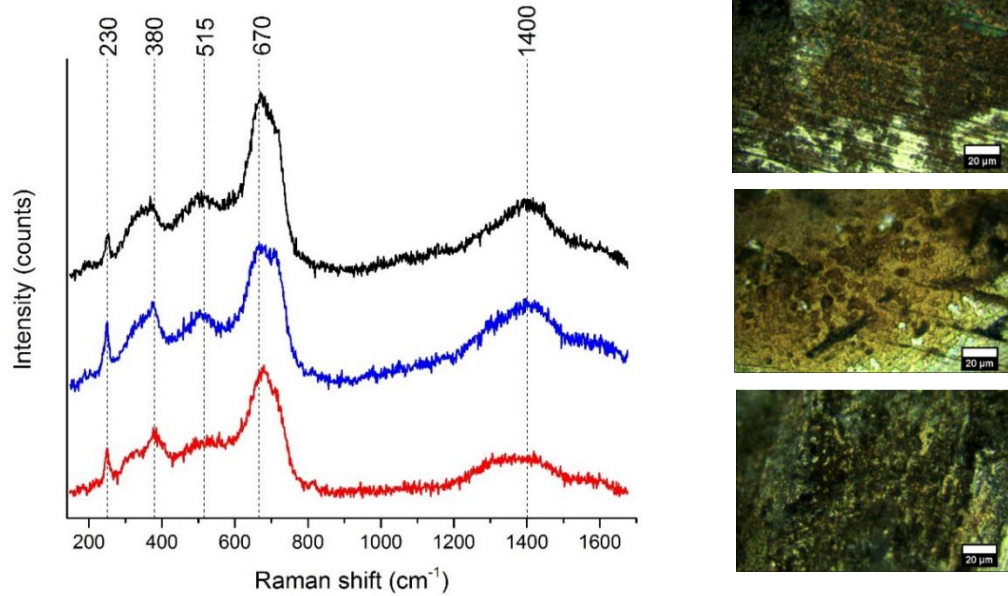
Figure 7-24: Raman spectra obtained from wear scar region of the membrane tested by water contaminated PAO lubricant. The analysed areas are shown in the insets
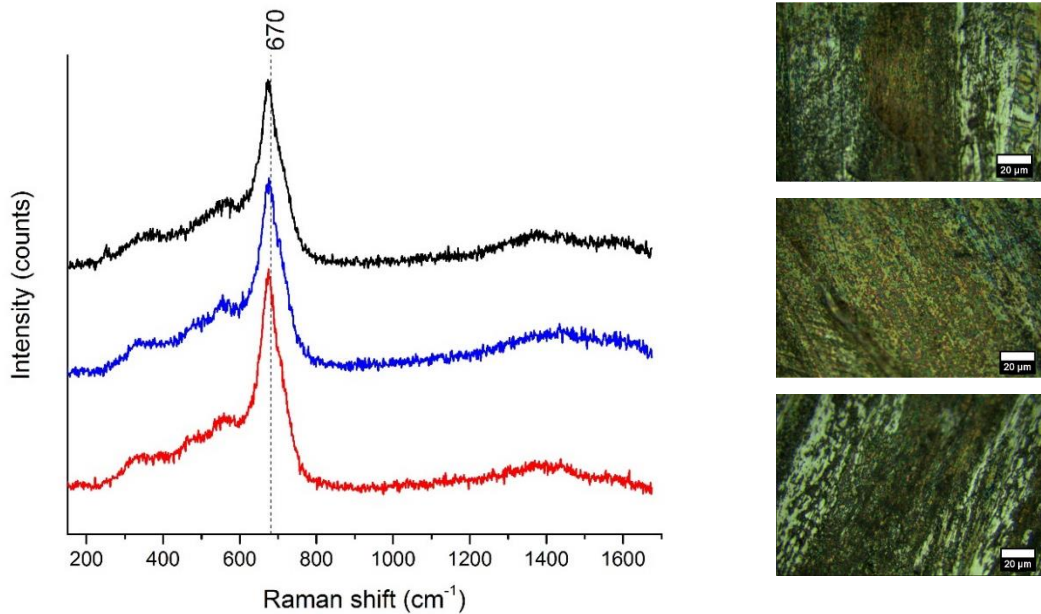
Figure 7-25: Raman spectra obtained from wear scar region of the membrane tested by salt water contaminated PAO lubricant. The analysed areas are shown in the insets
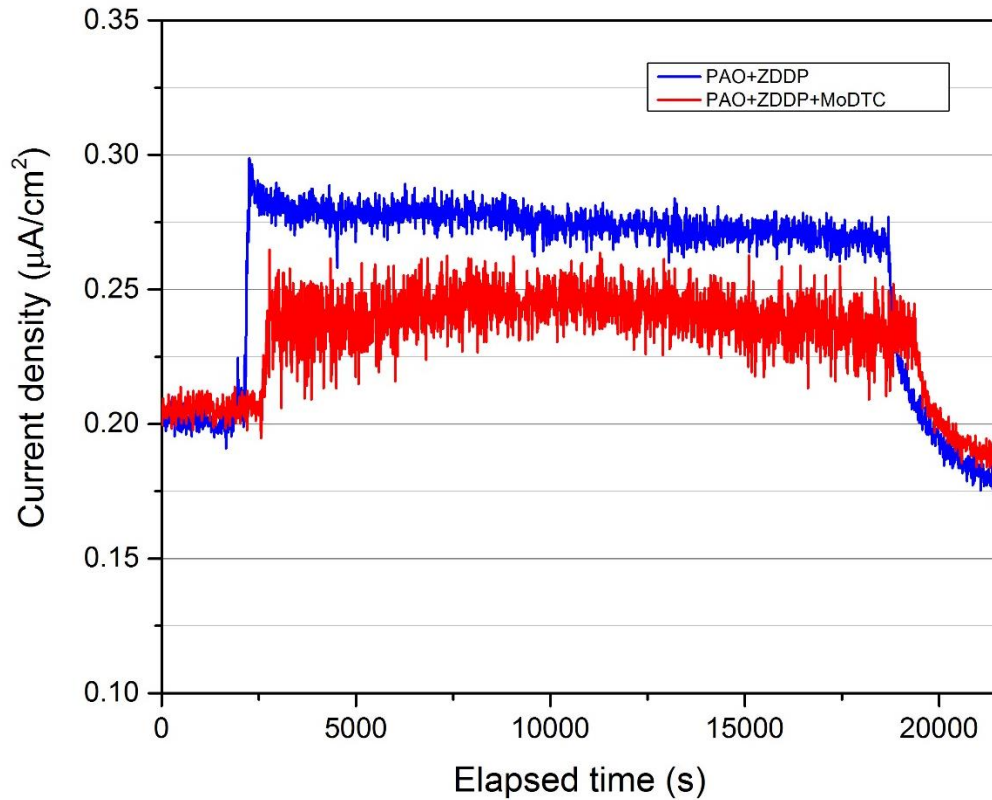
Figure 7-26: Effect of lubricant additives on hydrogen permeation rate

The surfaces of the samples after the experiment, Figure 7-27, showed no visible oxide formation on the samples. The wear volume is clearly less when MoDTC additive was used in the lubricant formulation.

PAO+ZDDP   PAO+ZDDP+MoDTC
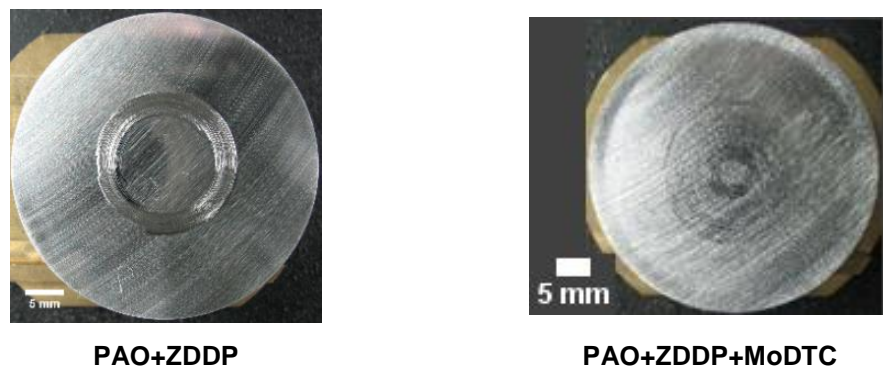
Figure 7-27: Optical images of the worn surface after the experiment

The SEM micrograph and EDX mapping and spectrum of the wear track after 5 hours of experiment by PAO+ZDDP are shown in Figure 7-28. The EDX maps reveal higher concentration of sulphur, zinc and phosphorous within the wear scar. The existence of these elements is attributed to the ZDDP decomposition under shear stress. Similar to these findings, Loeser et al. [138] found zinc, phosphorous and sulphur in high pressure areas of the trio-contact.
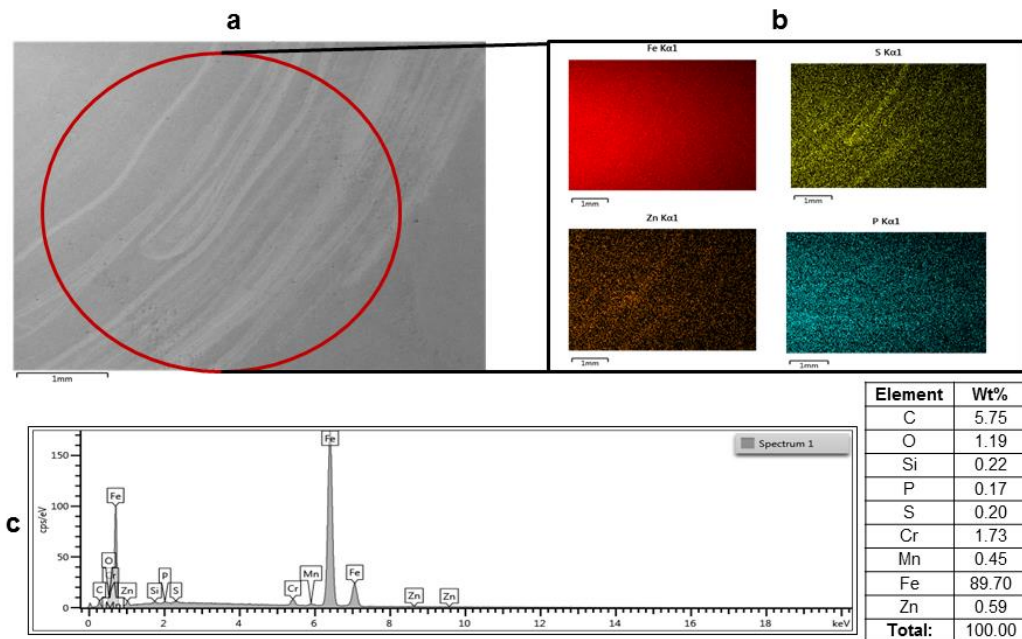
Figure 7-28: (a) SEM micrograph, (b) EDX mapping image and (c) spectrum from the wear track with PAO+ZDDP lubricant after 5 h experiment

The SEM micrograph and EDX mapping and spectrum of the wear track with key additive elements after 5 hours of experiment by PAO+ZDDP+MoDTC are depicted in Figure 7-29. This information reveal high concentration (wt%) of sulphur and molybdenum within the wear track showing that lubricant additives were present in tribo-contact.
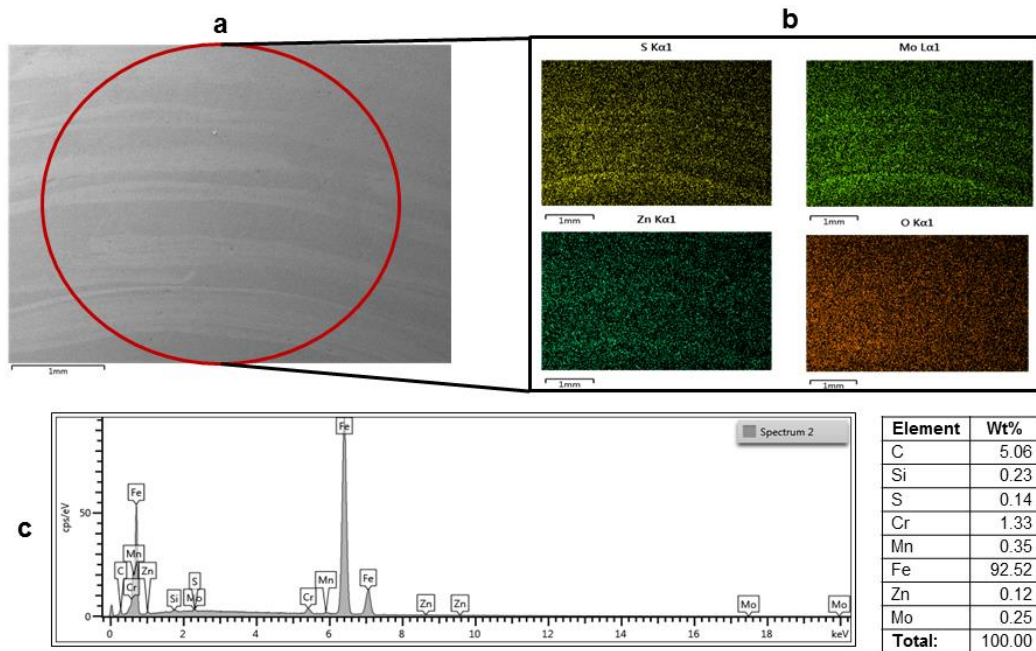
Figure 7-29: (a) SEM micrograph, (b) EDX mapping image and (c) spectrum from the wear track of the sample tested by PAO+ZDDP+MoDTC lubricant after 5 h experiment

Figure 7-30, Figure 7-31 and Figure 7-32 show Raman spectra obtained from unworn region and wear scar region of the sample after 5 hours experiments by PAO+ZDDP and PAO+ZDDP+MoDTC lubricants.
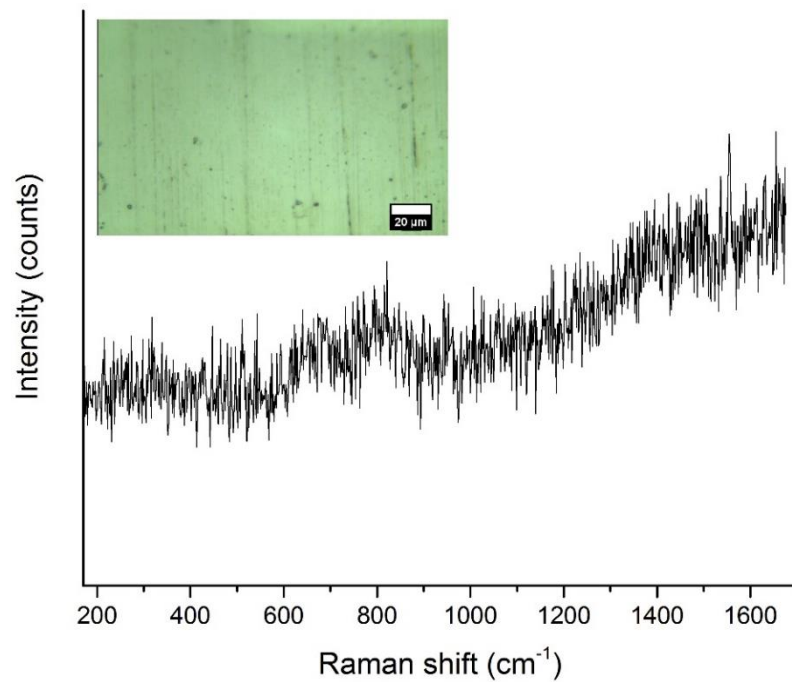
Figure 7-30: Raman spectrum obtained from out of the wear scar, as shown in the inset, after 5 hours experiment
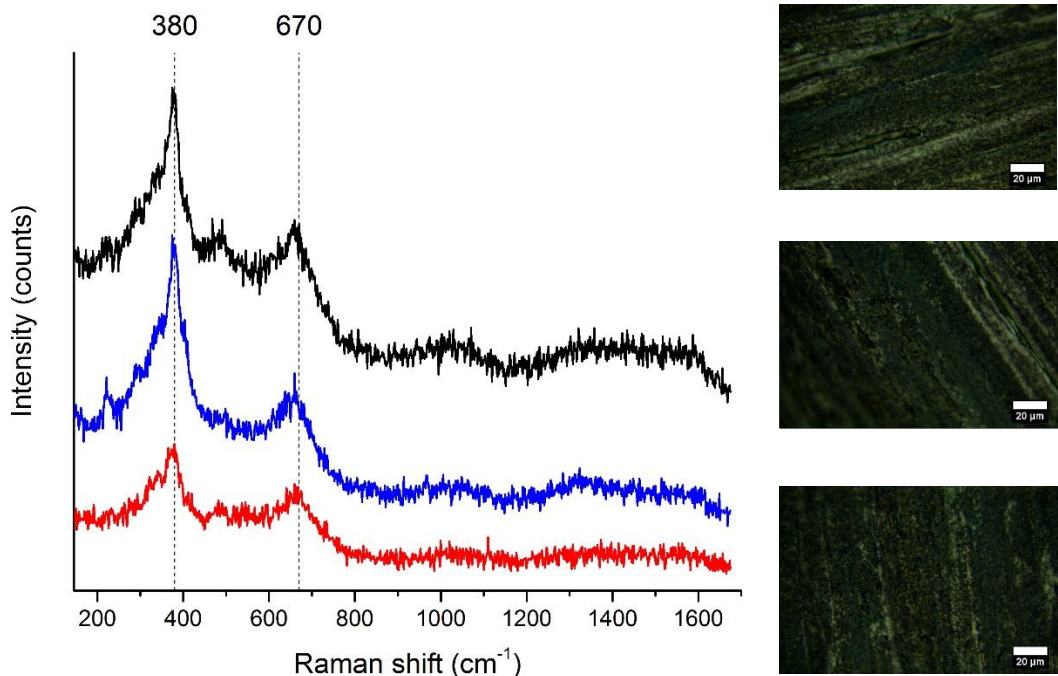
Figure 7-31: Raman spectra obtained from the wear scar on the membrane surface, showed in the insets, after testing with PAO+ZDDP lubricant at room temperature
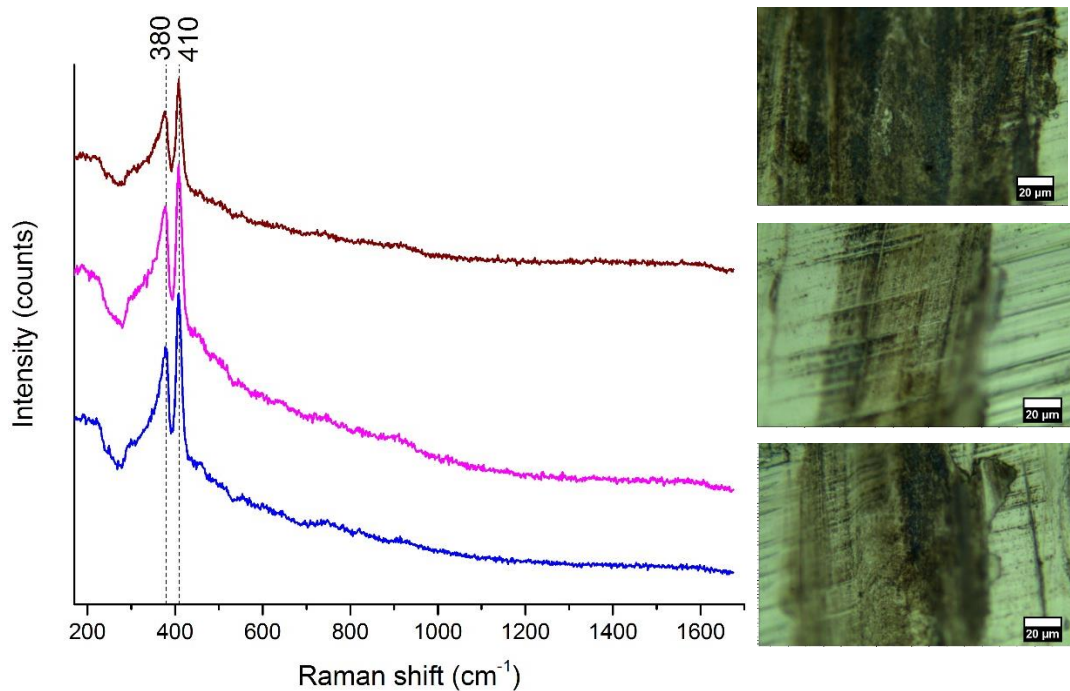
Figure 7-32: Raman spectra obtained from wear scars on tribopair after the test by PAO+ZDDP+MoDTC lubricant. The analysed areas are shown in the insets

The Raman spectrum from unworn surface does not reveal any Raman sensitive compound. However, the Raman spectra obtained from the samples tested by PAO+ZDDP, presented in Figure 7-31, show the formation of magnetite and sulphide without any indication of continuous phosphate tribofilm formation within the wear track. On the other hand, Raman spectra in Figure 7-32 confirm formation of MoS_2 in the wear scar region in presence of MoDTC additive. Raman spectroscopy technique is suited for the study of the molybdenum additive films as MoS_2 is highly Raman active [139]. The peaks observed at 380 and 410 cm^{-1} of the Raman spectra belong to MoS_2 structure. These two peaks are considered as very well-defined peaks for MoS_2 identification [140].

7.8 Friction torque measurement

Figure 7-33 exhibits comparison of variation of maximum friction torque as a function of time (as described in section 7.4) when 70 N load was applied and different lubricants were used. Maximum friction torque appeared constant during the rubbing process.

Friction coefficients were calculated using equation 7-7 and presented in Figure 7-34. The friction coefficient value is almost the same for PAO, PAO+water and PAO+salt water and did not change much during the sliding

106

process. Thus, the generated frictional heat during surface-rubbing by these lubricants is almost the same. The slight changes between the friction coefficient values are mainly due to the different oxide layers formed on the steel surface. The lowest friction value obtained in presence of MoDTC additive due to the MoS_2 formation in asperity contact. The formation of MoS_2 in the worn area was verified in Raman spectra shown in Figure 7-32 even though the experiments were done at room temperature.
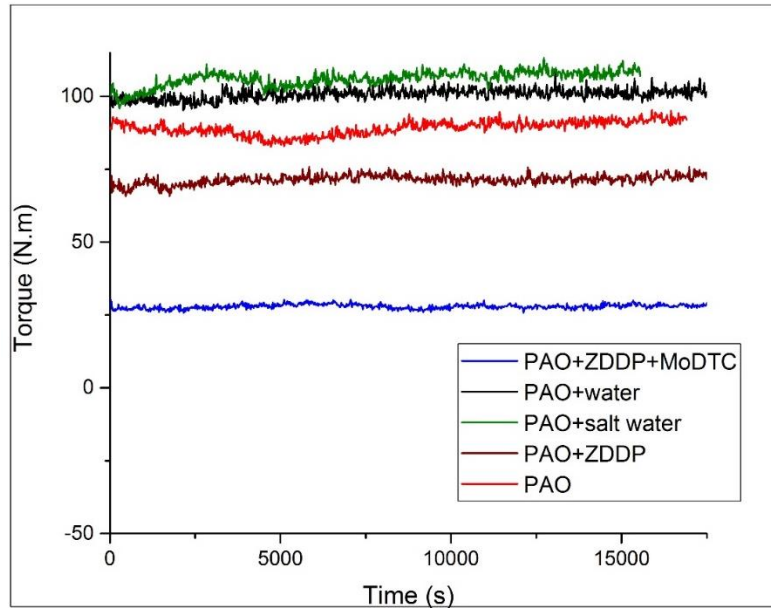
Figure 7-33: Comparison of variation of maximum friction torques as a function of time at 350 kPa contact pressure
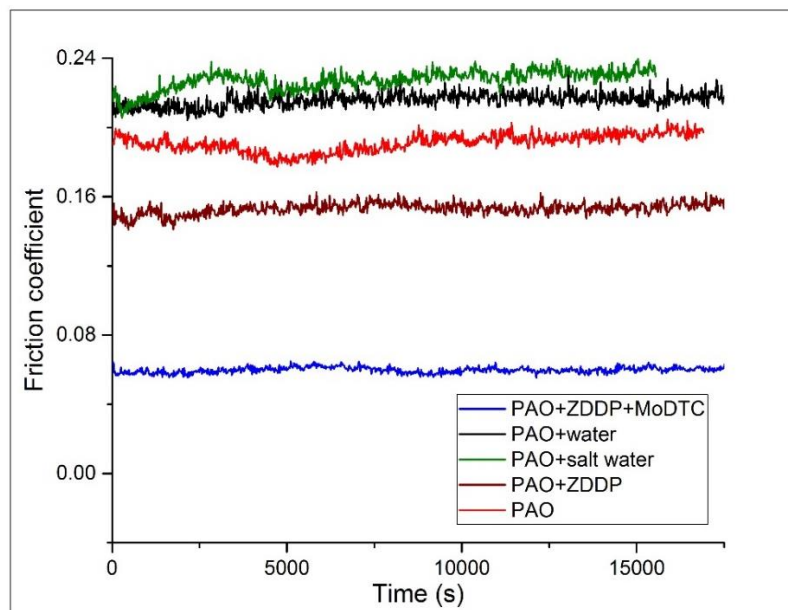
Figure 7-34: Variations in the friction coefficient with time for the steel pair lubricated with different lubricants at 350 kPa contact pressure

7.9 Total amount of permeated hydrogen through the steel

Total amount of permeated hydrogen through the steel membrane calculated by equation 6-4 is plotted in Figure 7-35 for different lubricants. As can be seen, the total amount of permeated hydrogen through the steel in presence of water is almost four times higher than its value for the lubricant without water contamination. This is an important observation as it shows how significant is the effect of water contamination as a contributing factor on hydrogen evolution from a lubricated tribo-contact. In the MoDTC containing lubricant the total absorbed hydrogen was slightly lower than that in PAO base oil; however in the lubricant which contains ZDDP the total permeated hydrogen is higher than the base oil. Almost no hydrogen permeation was measured in static conditions.
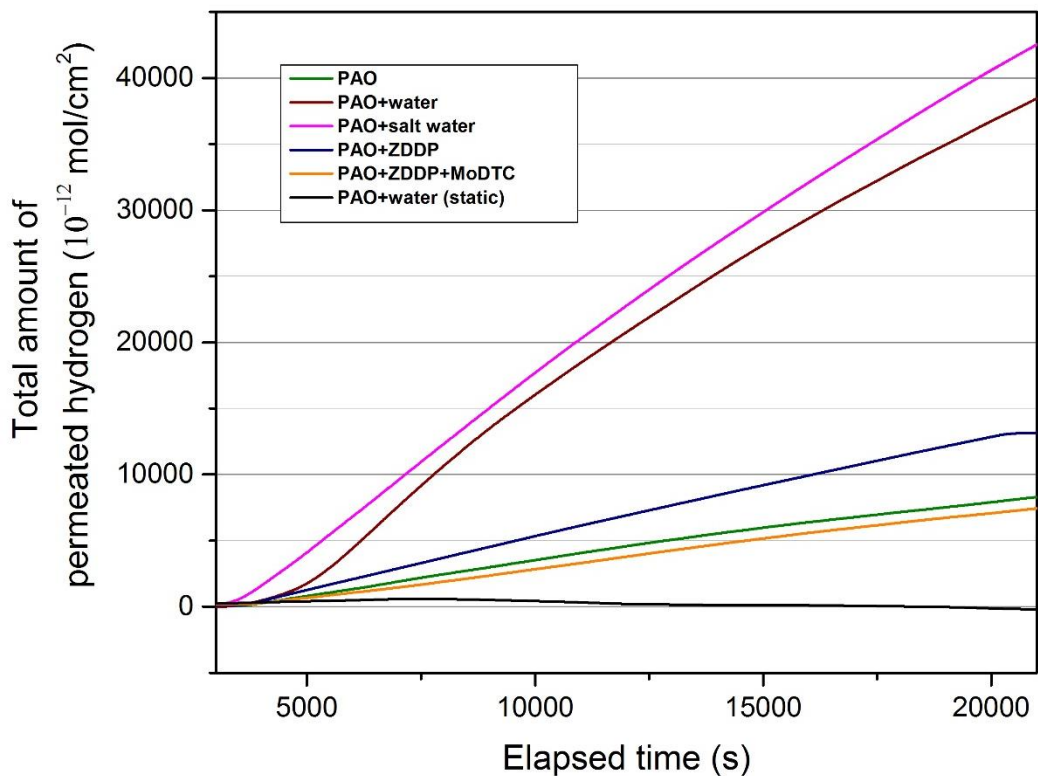
Figure 7-35: Total amount of permeated hydrogen through the steel membrane during 5 h rubbing with various lubricants

The friction coefficient results in Figure 7-34 show that the friction coefficient values are slightly higher when the lubricants contain water and salt water contamination. However, the comparison of the total hydrogen permeation results with the friction coefficient values reveals that friction coefficient changes are very small compared to the effect of water contamination on hydrogen intrusion into the steel.

7.10 Wear measurement

Total wear volume of the membranes after each experiment was calculated by using the white light interferometry and the procedure described in section 6.6. Comparison of the wear measurement results for different lubricants are presented in Figure 7-36. The wear volume increased in water-contaminated lubricants due to the higher oxidation rate of lubricant. Water also tends to increase the adhesion leading to higher wear. On the other hand, lubricant additives reduced the wear by formation of protective surface film. The total wear was higher for PFPE compared to PAO. The only unexpected observation from this graph is the slightly lower wear in presence of ZDDP although no tribofilm formation was observed in the Raman spectra. It can be explained by the fact that the tribofilm might have formed very locally in the asperity contacts where the temperature and pressure is high. However, the tribofilm formed in this condition is in very small regions and patchy that cannot be identified by the Raman spectra.
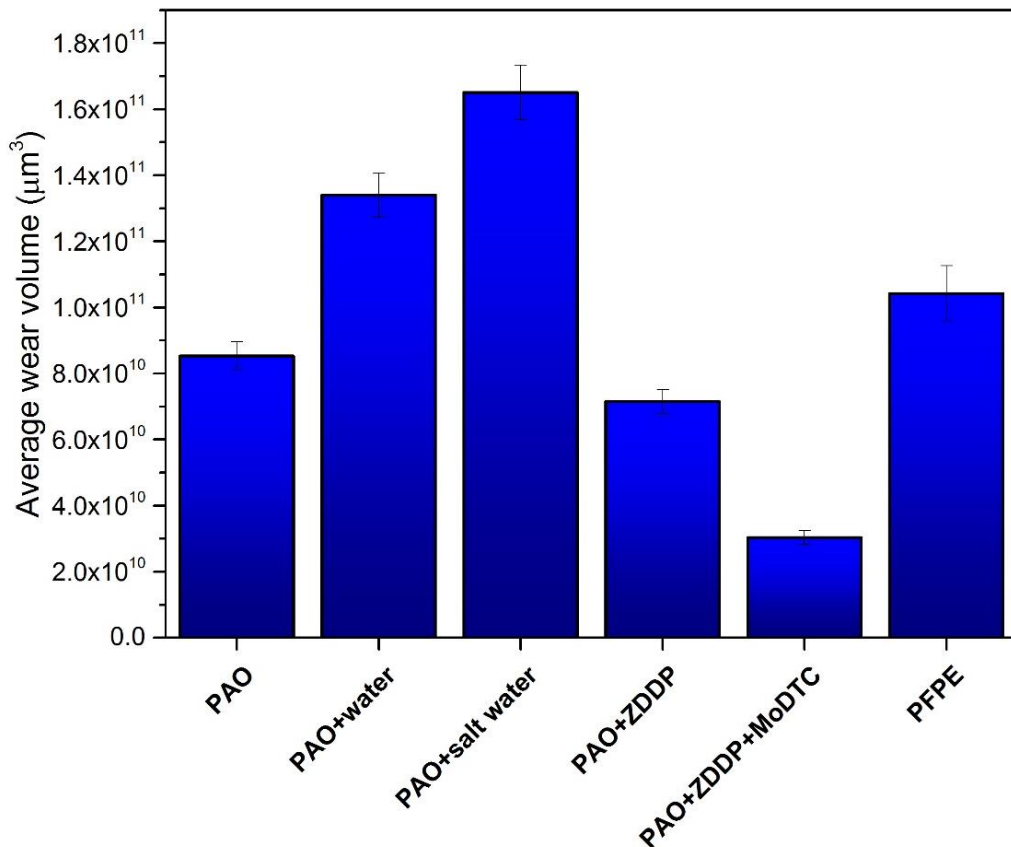
Figure 7-36: The wear volume measurement for different lubricants after 5 h of experiment at room temperature

7.11 Effect of contact pressure on hydrogen uptake at room temperature

In order to investigate the effect of tribological parameters on hydrogen permeation through the steel, the hydrogen uptake measurement was carried out with two different loads, 70 and 30 N, using PAO as lubricant. 70 N load was high enough to generate hydrogen on the surface without bending the thin steel membrane. The equivalent apparent pressures under 70 and 30 N loads are around 350 and 140 kPa, respectively, although the real contact pressure is much higher at asperity levels. The results are presented in Figure 7-37 in comparison with static conditions where no load was applied.
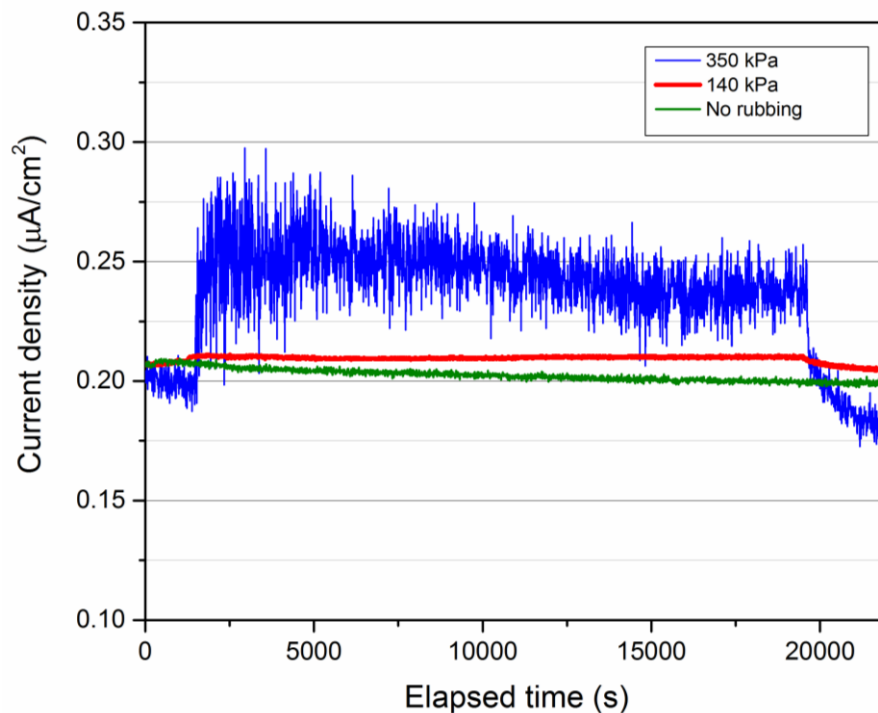
Figure 7-37: Effect of pressure on hydrogen uptake into the steel when PAO is used as lubricant at room temperature

The total amount of permeated hydrogen through the steel membrane is plotted in Figure 7-38. This shows almost no hydrogen permeation through the steel when either no pressure is applied or 140 kPa pressure is applied. However, hydrogen permeation was promoted when the pressure was increased to 350 kPa.

Figure 7-39 shows Raman spectra obtained from the wear scar region on the membrane surface after 5 hours experiment by PAO base oil at room temperature under 140 kPa pressure. When comparing with Raman spectra for the 350 kPa contact pressure (Figure 7-17) it can be seen that the pressure affects the type of iron oxides formed on the membrane. Only magnetite is

formed when 140 kPa pressure is applied, no haematite was detected. The broad peaks at 1370 and 1590 cm^{-1} were assigned to the amorphous carbon.
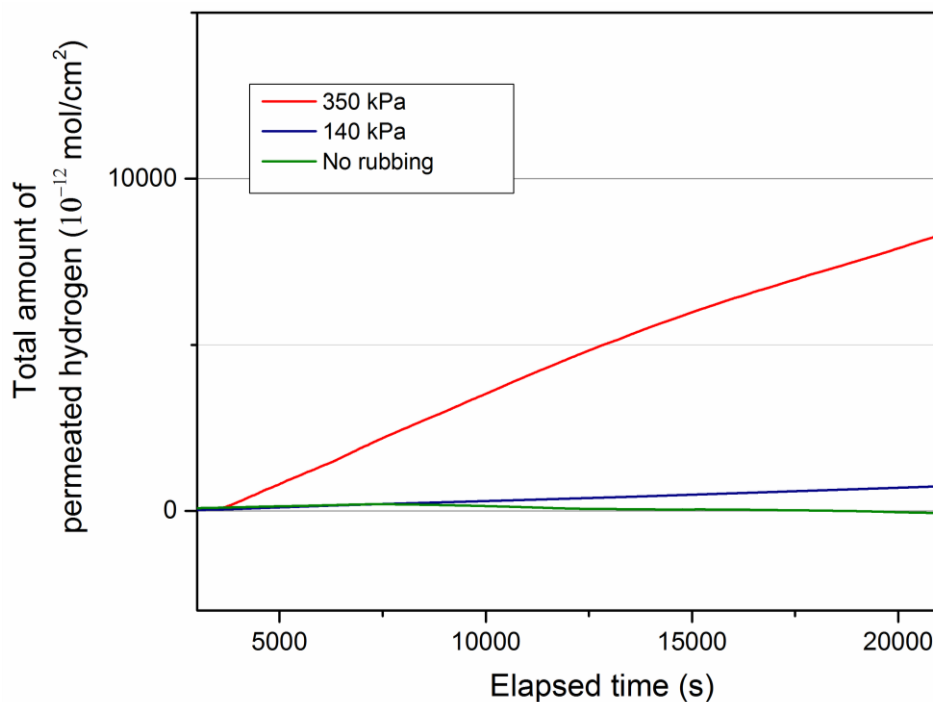
Figure 7-38: Effect of pressure on total amount of permeated hydrogen through the membrane during 5 h experiment at room temperature
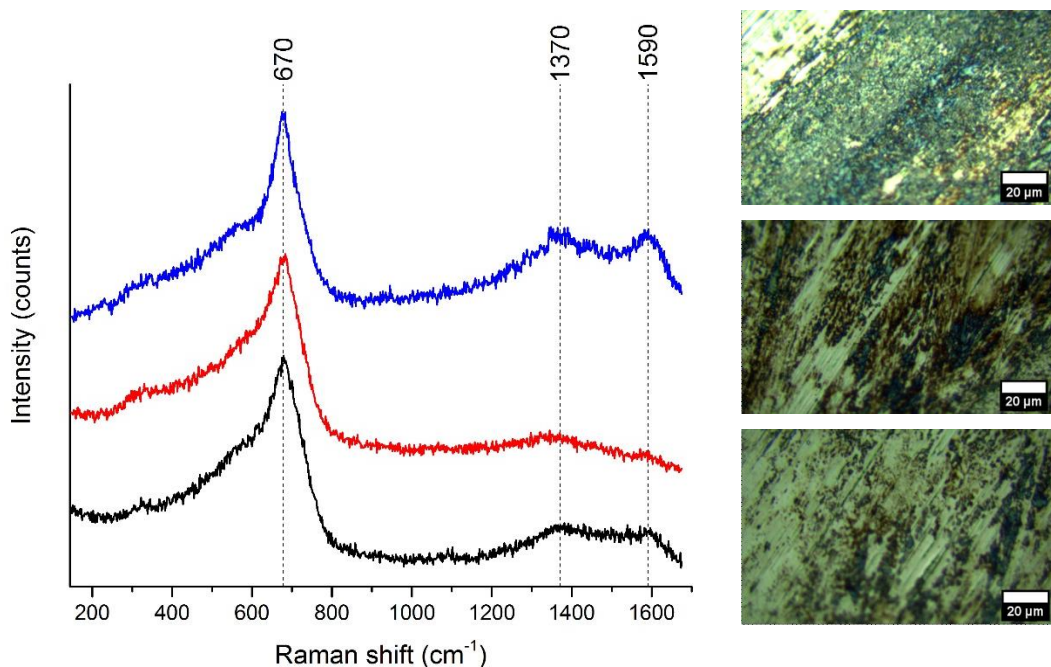
Figure 7-39: Raman spectra obtained from wear scars on tribopair after the test using PAO lubricant under 140 kPa pressure. The analysed areas are shown in the insets

111

The effect of contact pressure on the friction coefficient of pair steel lubricated with PAO lubricant is shown in Figure 7-40. Friction coefficient was calculated using equation 7-7. The wear volume of the samples was also measured using the white light interferometry and the results are presented in Figure 7-41. These results show that both friction coefficient and wear volume significantly reduce by decreasing contact pressure. The higher friction coefficient observed for the experiment under 350 kPa contact pressure can be explained by to the Stribeck curve shown in Figure 2-12. The higher contact pressure causes more asperity contacts and therefore more severe contact conditions leading to the transition of lubrication regime from boundary towards dry condition (or from mixed towards boundary). This will cause an increase in friction values observed at higher contact pressure. Different types of oxides formed on the surfaces may also affect friction coefficient values under different applied contact pressures.
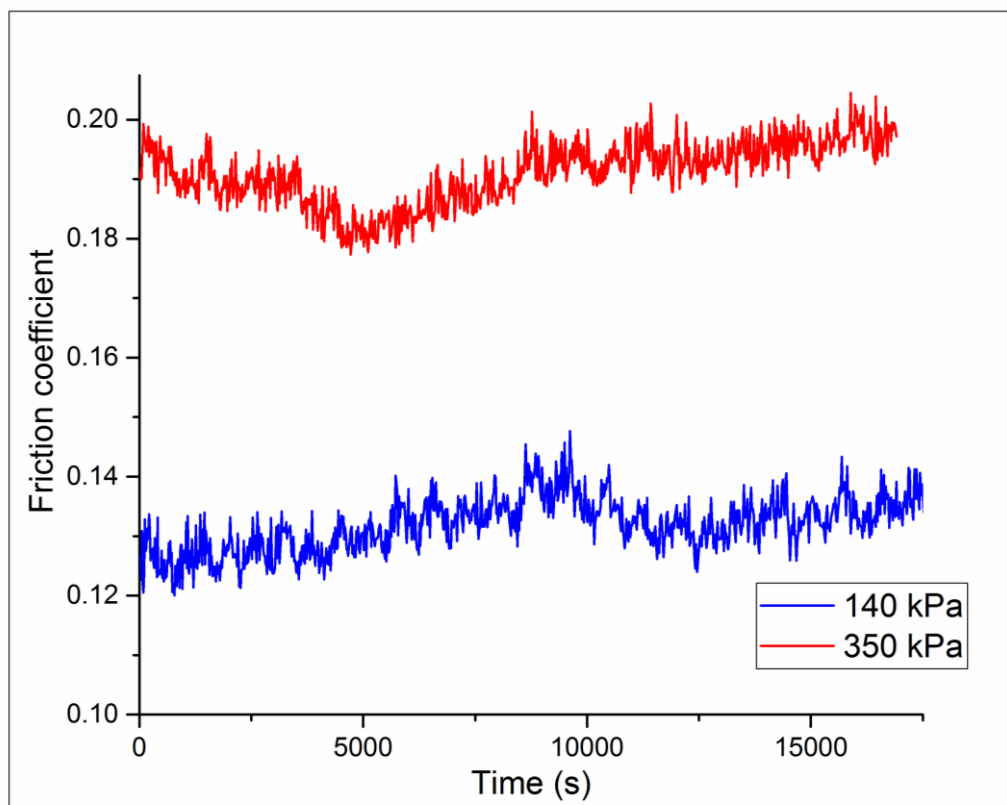
Figure 7-40: The effect of contact pressure on friction coefficient for the steel pair lubricated with PAO
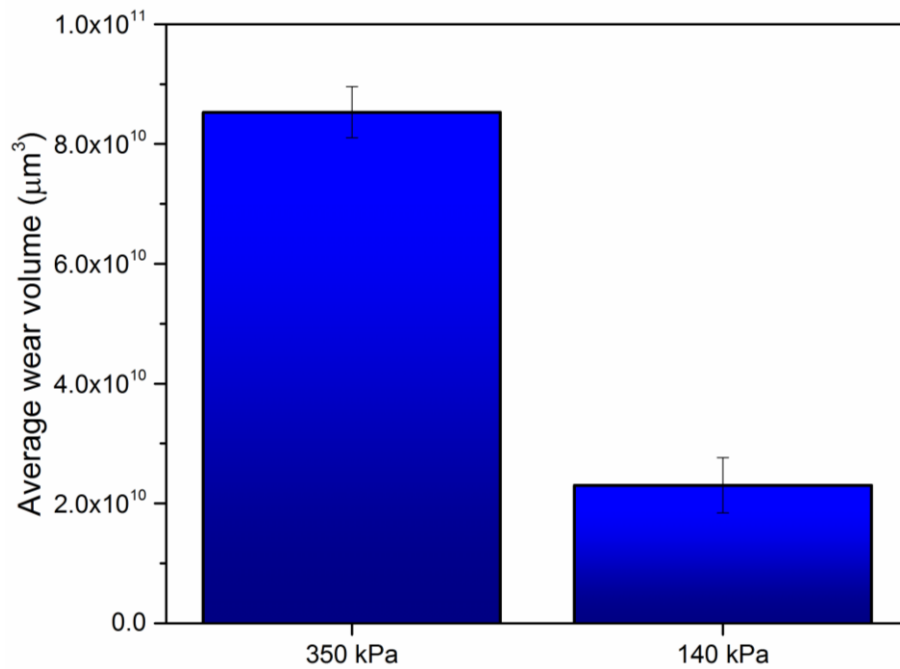
Figure 7-41: The wear volume measurement for PAO lubricant at room temperature after 5 h of experiment under 350 and 140 kPa pressure

7.12 Summary

- Hydrogen permeation was detected when hydrocarbon base oil is used to lubricate the tribo-contact
- No hydrogen permeation was observed in static conditions
- Hydrogen uptake was significantly promoted when the lubricant was contaminated with water
- PAO+ZDDP lubricant caused higher hydrogen permeation into the steel than PAO+ZDDP+MoDTC
- Higher hydrogen permeation rate was observed when 350 kPa pressure was applied compared to the experiments conducted under 140 kPa contact pressure

Chapter 8 Hydrogen uptake into the steel from a lubricated contact at high temperature

8.1 Introduction

Temperature has a potent effect on the kinetics of the surface reactions. Temperature also appeared to influence the synergism between water contamination and lubricant additives. In this chapter, results from tests at higher temperature of around 80-85°C are presented. The method described in section 6.4 was used to circulate and heat lubricants during the experiment. This chapter presents the effect of contact pressure, sliding speed, lubricant additives and water contamination using the hydrogen uptake rig at higher temperature.

8.2 Effect of contact pressure

Hydrogen uptake rig was utilised to investigate the effect of contact pressure on hydrogen permeation through the steel when PAO is used as lubricant at high temperature. The hydrogen permeation curves obtained for two different loads, 70 and 30 N, are depicted in Figure 8-1. The equivalent apparent pressures are around 350 and 140 kPa, respectively, although the real contact pressure is much higher at asperity levels.
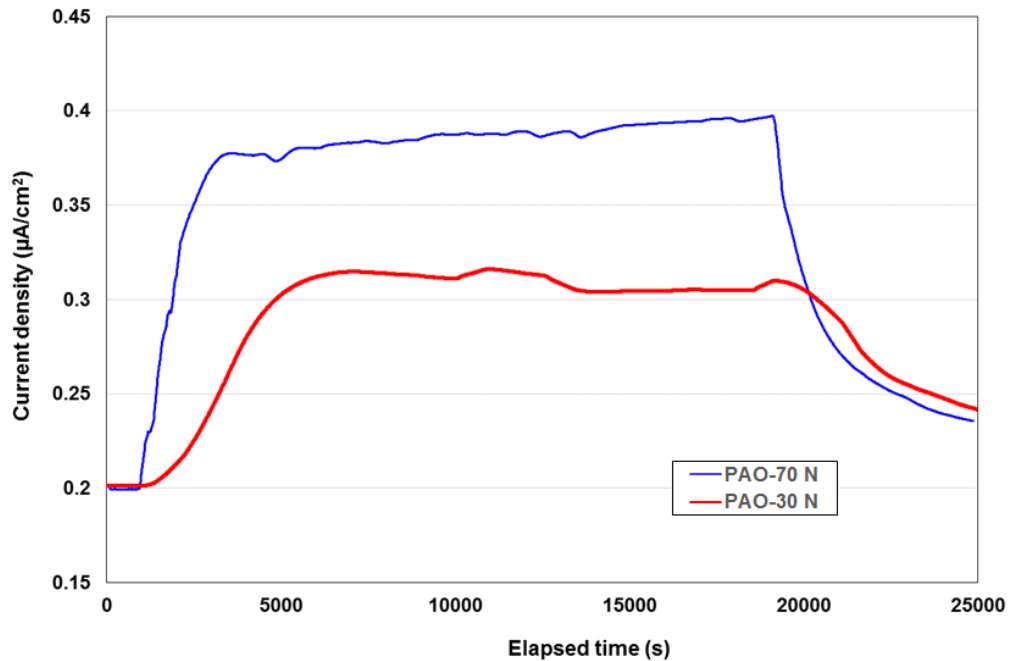
Figure 8-1: Effect of contact pressure on hydrogen uptake into the steel when PAO is used as lubricant at 85°C

114

The total amount of permeated hydrogen through the steel membrane during 5 hours of experiment is plotted in Figure 8-2. It was found that hydrogen permeation through the steel is reduced by decreasing the contact pressure at this temperature.
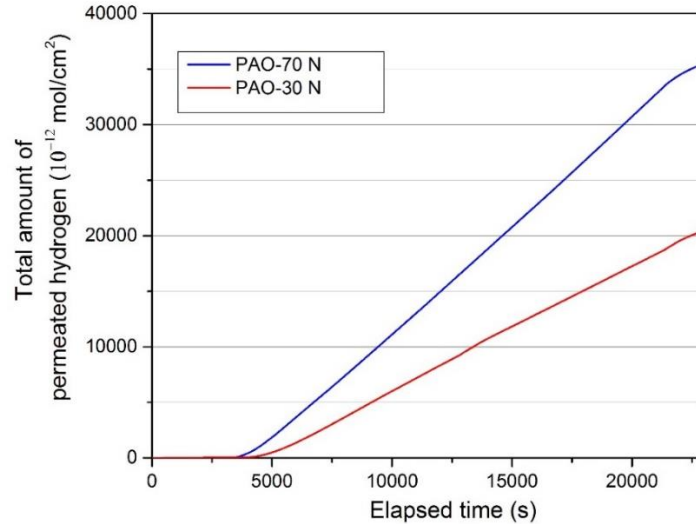
Figure 8-2: The effect of contact pressure on total amount of permeated hydrogen through the steel membrane during surface-rubbing at high temperature

The SEM/EDX micrograph, EDX spectra and mapping of the wear track with key additive elements after 5 h of experiment by PAO lubricant are shown in Figure 8-3 and Figure 8-4 when the contact pressures are 350 kPa and 140 kPa, respectively. EDX analyse was employed to assess the oxygen concentration within the wear track.

Element	Wt%
C	7.39
O	6.81
P	0.04
S	0.06
Cr	1.77
Mn	0.39
Fe	83.52
Zn	0.00
Mo	0.02
Total:	100.00
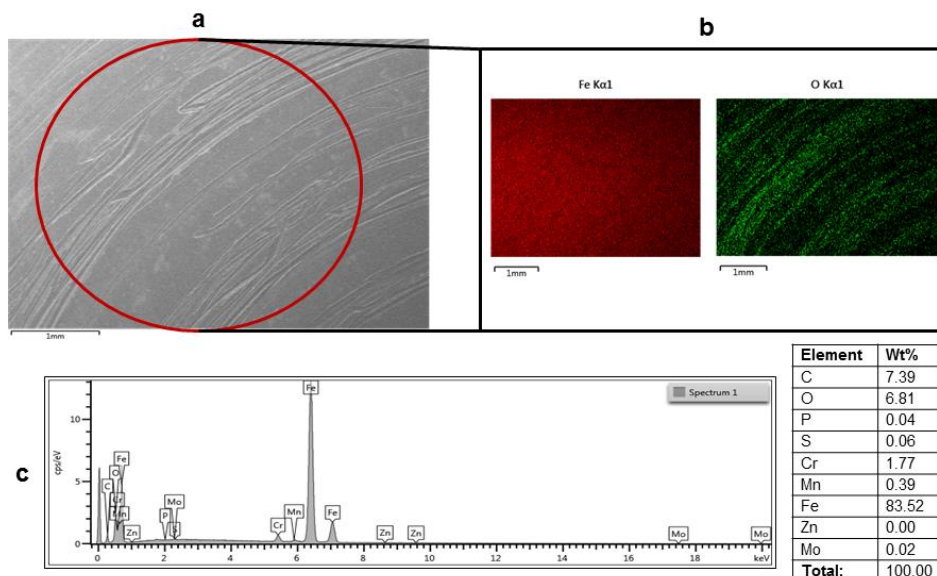
Figure 8-3: (a) SEM micrograph, (b) EDX mapping image and (c) spectra from the wear track of the sample tested by PAO lubricant after 5 h experiment under 350 kPa contact pressure at high temperature

Element	Wt%
C	5.47
O	1.97
Si	0.20
P	0.25
S	0.38
Cr	1.39
Mn	0.27
Fe	89.11
Ni	0.33
Zn	0.63
Total:	100.00
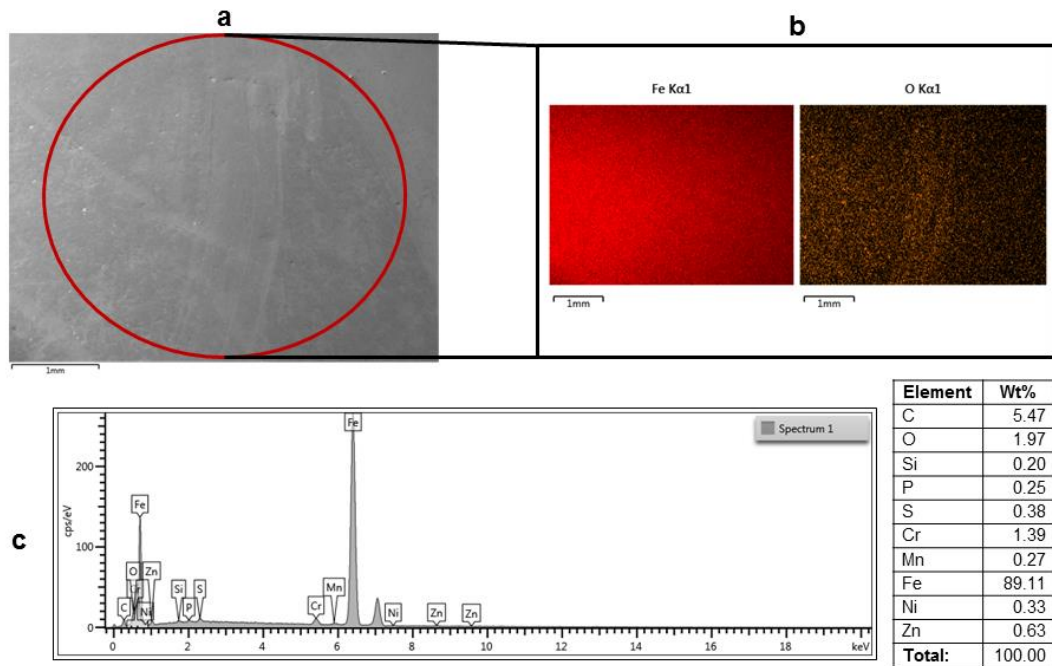
Figure 8-4: (a) SEM micrograph, (b) EDX mapping image and (c) spectra from the wear track of the sample tested by PAO lubricant after 5 h experiment under 140 kPa contact pressure at high temperature

Comparison of the wear measurement results for different contact pressures is presented in Figure 8-5. The wear volume has significantly reduced by decreasing contact pressure.
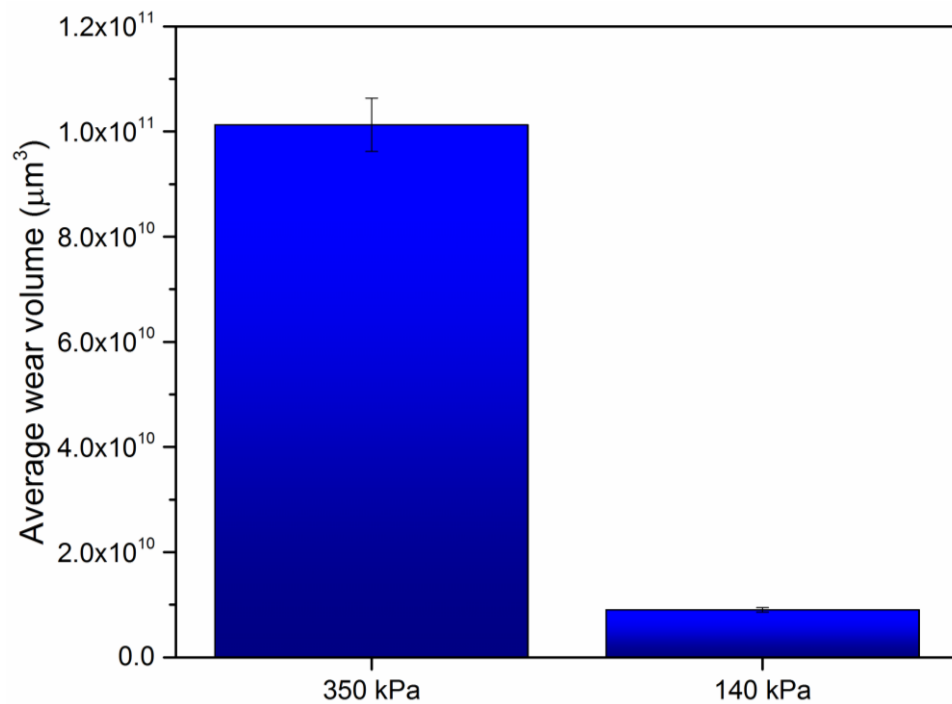
Figure 8-5: The wear volume of the samples tested by PAO lubricant at high temperature under different contact pressures

The optical images taken from the surface of the membranes are shown in Figure 8-6 confirming the significant difference of the wear volumes.

(a)   (b)
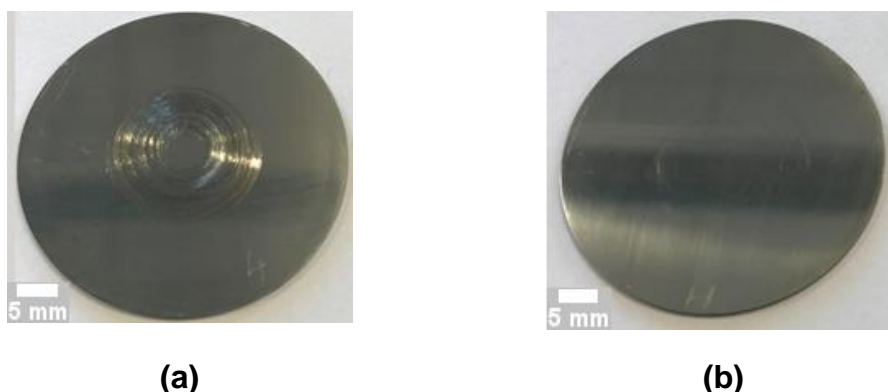
Figure 8-6: Optical images from the surface of the membranes after 5 hours experiment using PAO lubricant at high temperature under (a) 350 kPa (b) 140 kPa contact pressure

Figure 8-7, Figure 8-8 and Figure 8-9 show Raman spectra obtained from the unworn region and wear scar region of the membrane after testing by PAO lubricant under 350 kPa and 140 kPa contact pressure, respectively. No Raman sensitive chemical compounds was identified in unworn region of the sample. Raman spectra revealed iron oxides formation within the wear track. Magnetite and hematite (in some regions) were identified on the surface of the sample tested at 350 kPa contact pressure. Magnetite, less than sample tested at 350 kPa, is also identified on the surface of the sample tested at 140 kPa. Amorphous carbon was also formed on the surface.
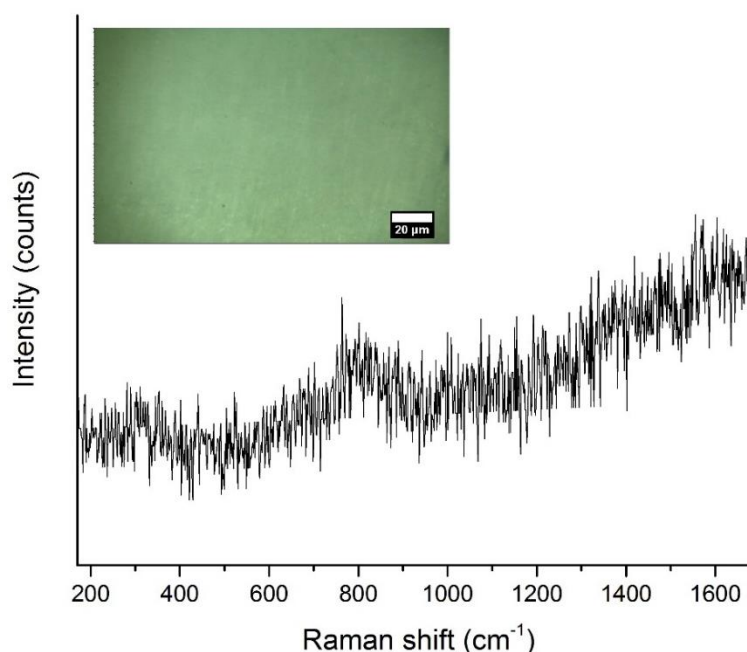
Figure 8-7: Raman spectrum obtained from out of the wear scar after 5 hours experiment by PAO lubricant at high temperature
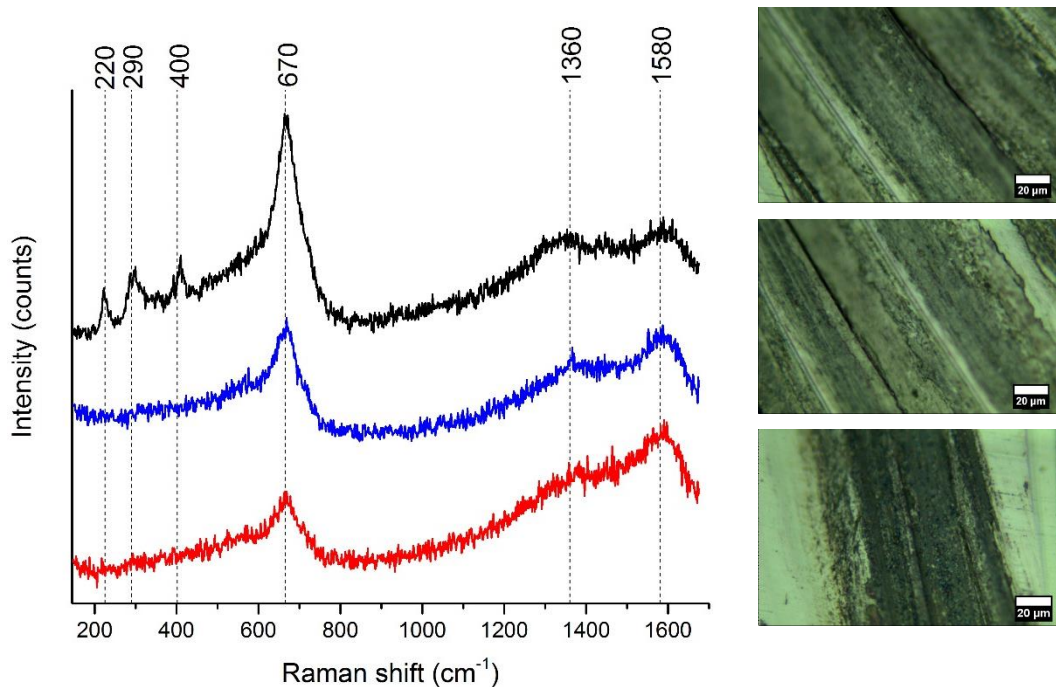
Figure 8-8: Raman spectra obtained from wear scars after testing by PAO lubricant at high temperature and 350 kPa. The analysed areas are shown in the insets
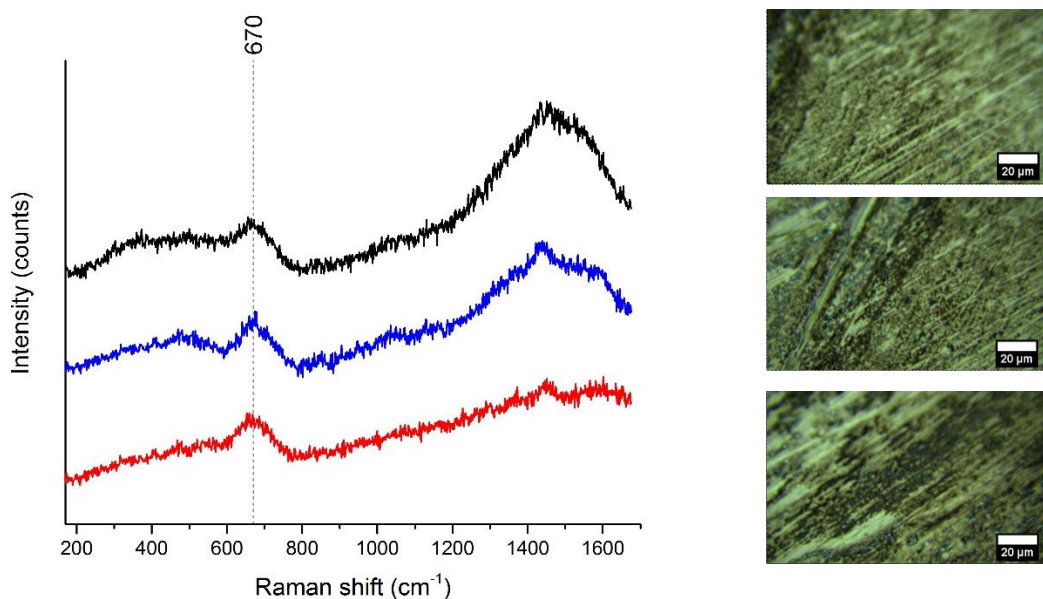
Figure 8-9: Raman spectra obtained from wear scars after experiment at 140 kPa when PAO was used as lubricant at high temperature. The analysed areas are shown in the insets

8.3 Effect of sliding speed

The effect of external energy on hydrogen entry was investigated by changing the sliding speed. The sliding speed has been decreased by reducing the frequency of oscillating motion when PAO was used as lubricant at high

temperature. The frequency of oscillatory motion is directly related to the sliding speed. The hydrogen permeation curve was measured for the frequency of 0.5 Hz and the results are compared with the frequency of 1 Hz in Figure 8-10.
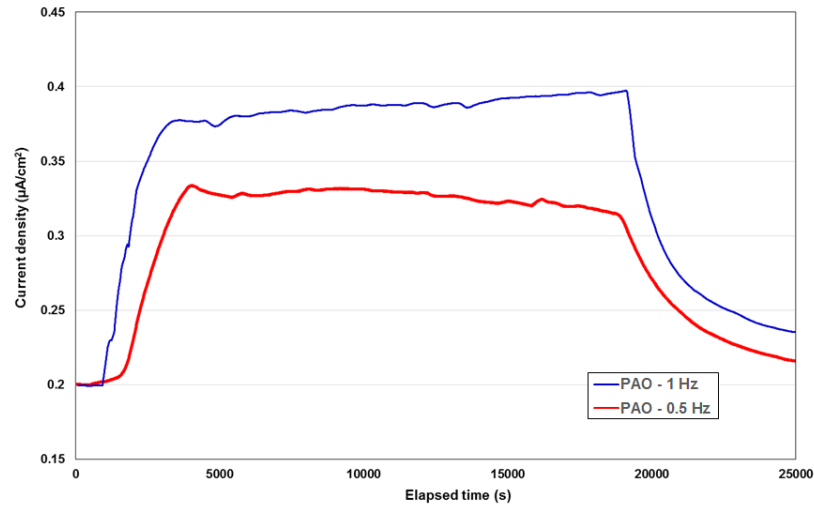
Figure 8-10: Effect of sliding speed on hydrogen uptake into the steel when PAO is used as lubricant at 85°C and 350 kPa

The total amount of permeated hydrogen into the steel membrane during 5 hours of experiment for different frequencies of the oscillatory motion are plotted in Figure 8-11. The results show lower hydrogen permeation through the steel when the sliding speed is decreased by one-half at 350 kPa contact pressure.
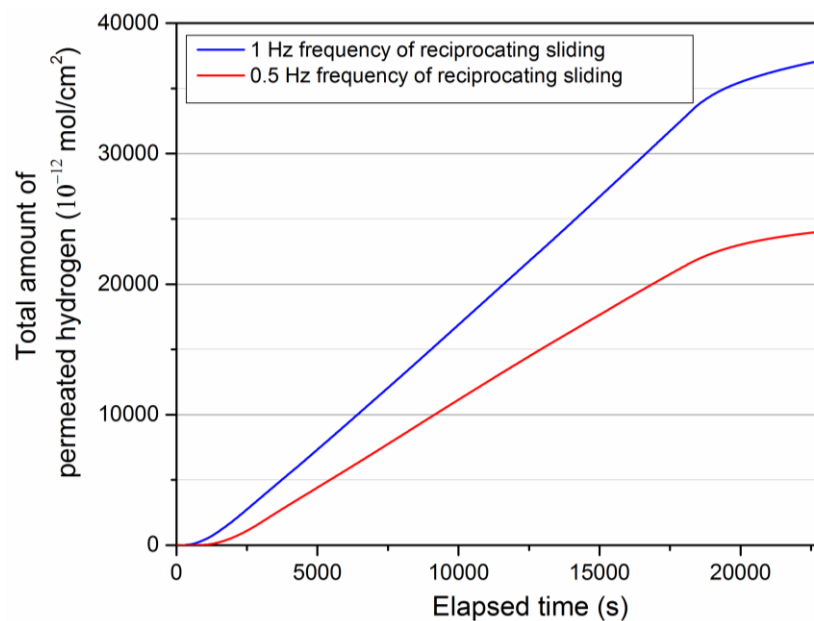
Figure 8-11: The effect of sliding speed on total amount of permeated hydrogen through the steel membrane during surface-rubbing at high temperature

119

The SEM/EDX micrograph, EDX spectra and mapping of the wear track with key additive elements after 5 h of experiment by PAO lubricant at 350 kPa contact pressure are shown in Figure 8-3 and Figure 8-12 when the frequency of oscillating motion were 1 Hz and 0.5 Hz, respectively. The concentration of oxygen was much lower in the latter showing lower oxidation rate in lower sliding speed.

Element	Wt%
C	5.41
O	1.75
Si	0.17
P	0.00
S	0.00
Cr	1.28
Mn	0.32
Fe	90.41
Mo	0.67
Total:	100.00
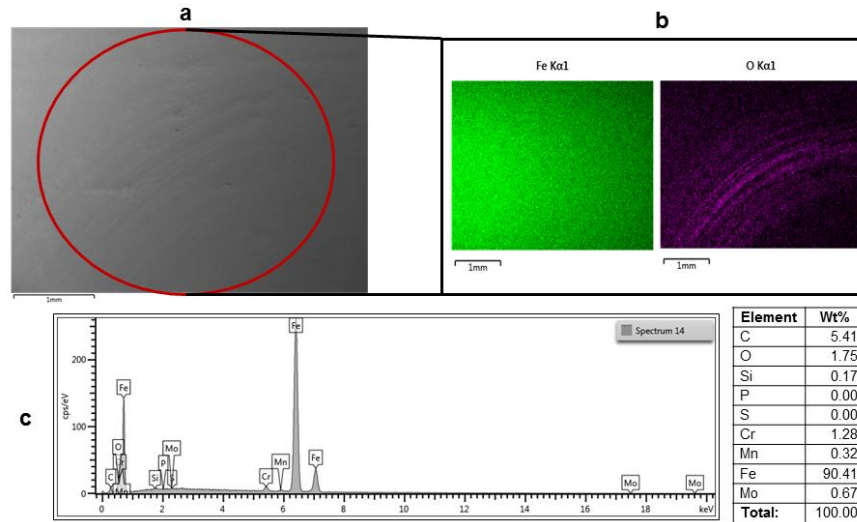
Figure 8-12: (a) SEM micrograph, (b) EDX mapping image and (c) spectra from the wear track after experiment with PAO lubricant at high temperature and 0.5 Hz frequency of oscillatory motion

Comparison of the wear measurement results for different sliding speeds are presented in Figure 8-13. The results show that decreasing the sliding speed to 0.5 Hz reduces the wear volume to less than half. This is due to the lower sliding distance after 5 h experiment with 0.5 Hz.
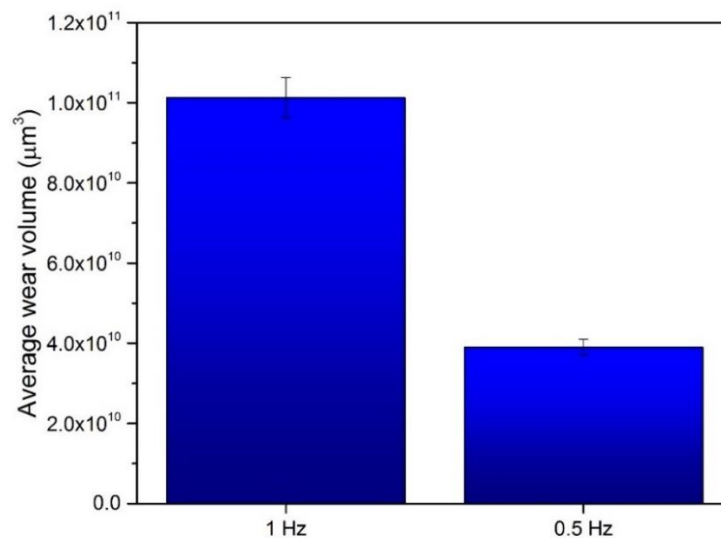
Figure 8-13: The wear volume of the samples tested by PAO lubricant at high temperature with different sliding speeds

The optical photo from the surface of the membrane after 5 hours experiment under 350 kPa contact pressure and 0.5 Hz of the frequency of oscillating motion is shown in Figure 8-14. This can be compared with the one for 1 Hz of frequency of oscillating motion shown in Figure 8-6.
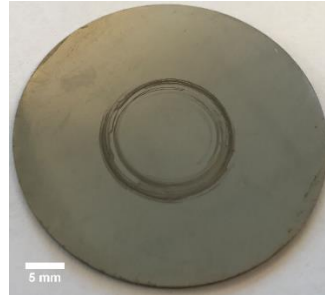
Figure 8-14: Optical photo from the surface of the membrane after 5 hours experiment using PAO lubricant at high temperature and 0.5 Hz oscillatory motion frequency

Figure 8-15 shows Raman spectra obtained from the wear scar region of the membrane surface after 5 hours experiment by PAO lubricant at high temperature under 70 N load when the oscillatory motion frequency was reduced to 0.5 Hz. The results for the 1 Hz have already been presented in Figure 8-8 and the iron oxide formed in some regions are similar. The Raman spectra obtained from different positions of the wear track confirmed formation of both haematite and magnetite as well as amorphous carbon on the surface of the sample tested under 70 N load and 0.5 Hz oscillatory motion.
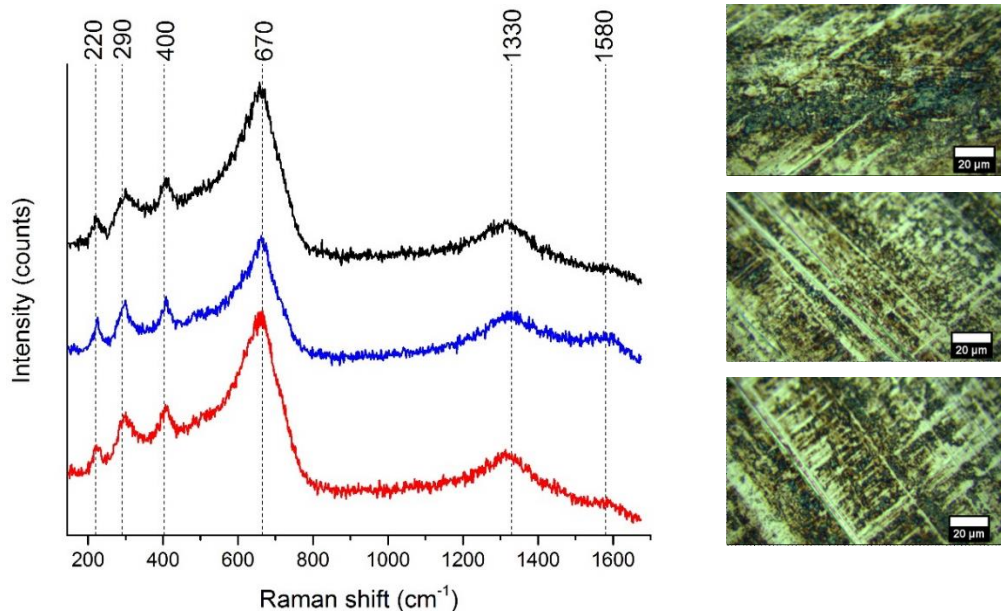
Figure 8-15: Raman spectra obtained from wear track of the membrane tested by PAO lubricant at high temperature and the oscillatory motion frequency of 0.5 Hz. The analysed areas are shown in the insets

8.4 Effect of lubricant additives

The new developed technique in this study enables the study of the effect of lubricant composition on hydrogen transfer into the steel from a lubricated tribocontact. This investigation aims to reveal some of the complex interplay between the composition of the lubricant on one hand and the effect of the tribofilm on hydrogen permeation rate on the other hand. Therefore, the effect of lubricant additives on hydrogen flux into the steel has been assessed at 85°C and the results are presented in this section.

Figure 8-16 compares the changes in hydrogen permeation current during surface-rubbing with PAO lubricant containing ZDDP and MoDTC. The observed trend at this temperature is different from what was observed at room temperature in section 7.7. Both ZDDP and MoDTC are reducing hydrogen permeation rate through the steel at high temperature.
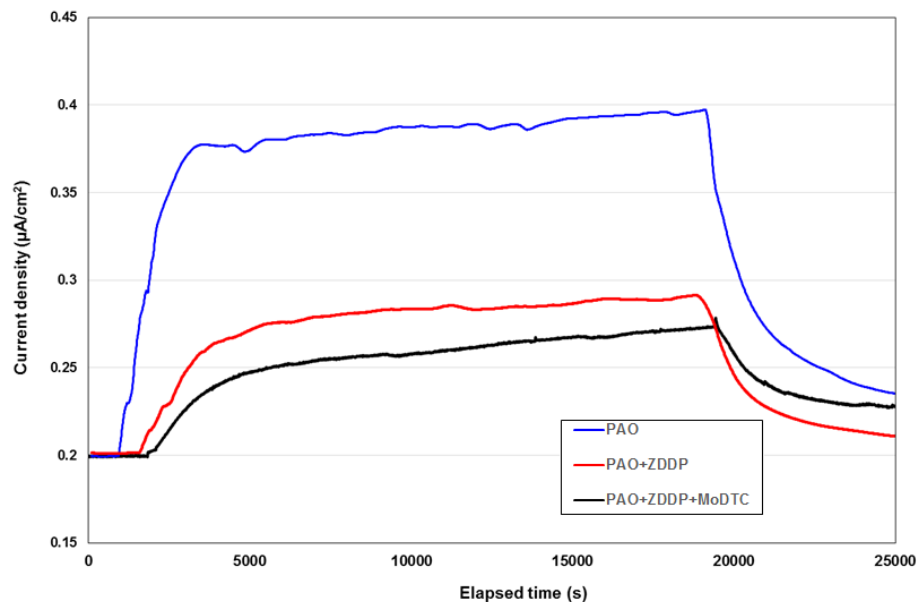
Figure 8-16: Effect of lubricant additives on hydrogen uptake into the steel at 85°C

The total amount of permeated hydrogen through the steel membrane is compared for PAO, PAO+ZDDP and PAO+ZDDP+MoDTC in Figure 8-17. The results in Figure 8-17 show that ZDDP additive decreases the hydrogen flux into the steel compared to the permeation rate measured for PAO lubricant. The permeation current further reduced in presence of MoDTC as an additive in the lubricant. This trend is different from what we observed from the hydrogen uptake measurement results at room temperature that have already been presented in Chapter 7, section 7.7. Surface analyses were employed to understand the main reason of this behaviour.

122
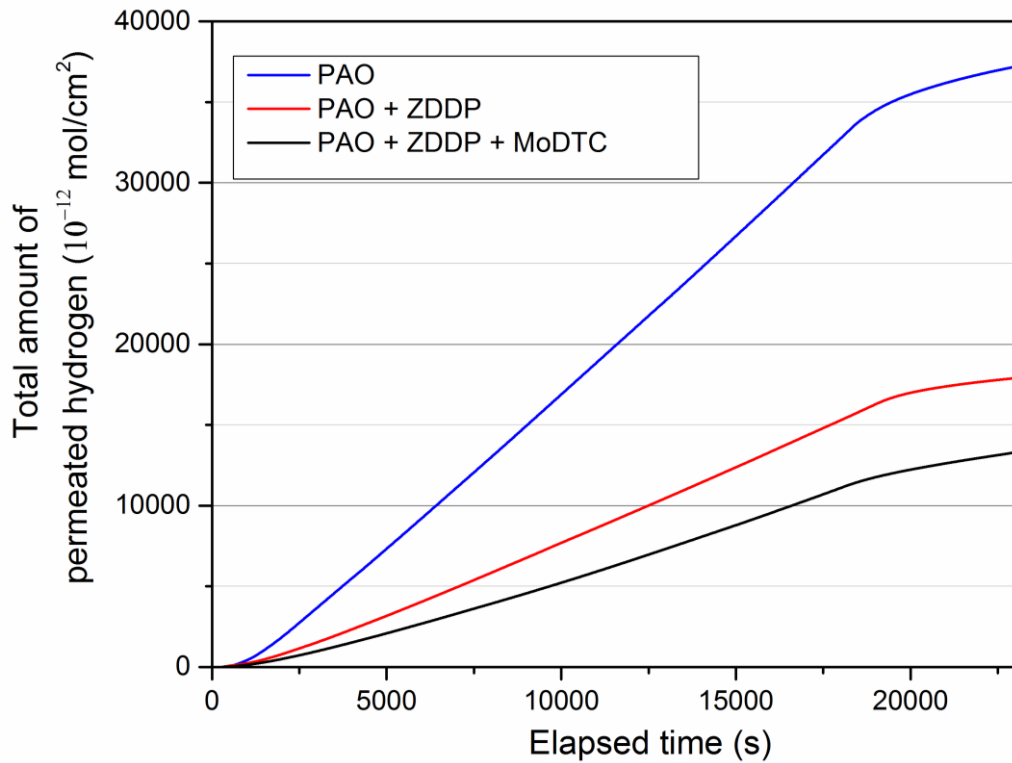
Figure 8-17: The effect of lubricant additives on total amount of permeated hydrogen through the membrane during rubbing at high temperature

The SEM/EDX micrograph and EDX mapping of the wear track with key additive elements after 5 h of the experiment under 350 kPa contact pressure are shown in Figure 8-18 and Figure 8-19 when PAO+ZDDP and PAO+ZDDP+MoDTC are used as lubricant, respectively.
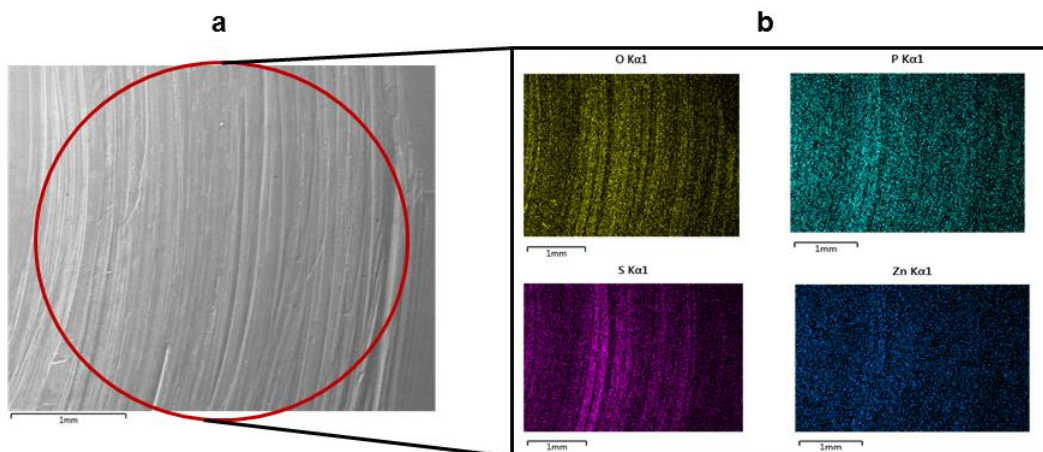
Figure 8-18: (a) SEM micrograph and (b) EDX mapping image of the wear track after 5 h experiment with PAO+ZDP lubricant at high temperature under 350 kPa contact pressure
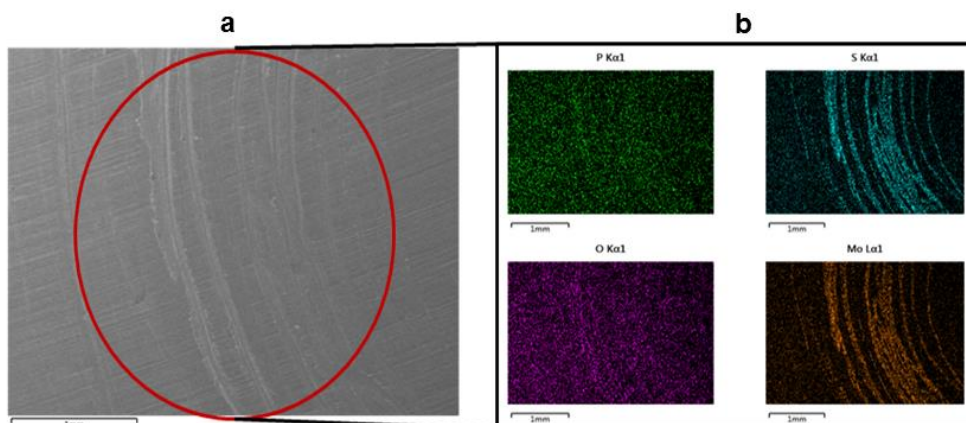
Figure 8-19: (a) SEM micrograph and (b) EDX mapping image of the wear track after 5 h experiment using PAO+ZDDP+MoDTC lubricant at high temperature under 350 kPa contact pressure

Raman spectra of the tribofilm formed in wear scar region of the samples tested by PAO+ZDDP and PAO+ZDDP+MoDTC lubricants are shown in Figure 8-20 and Figure 8-21, respectively.
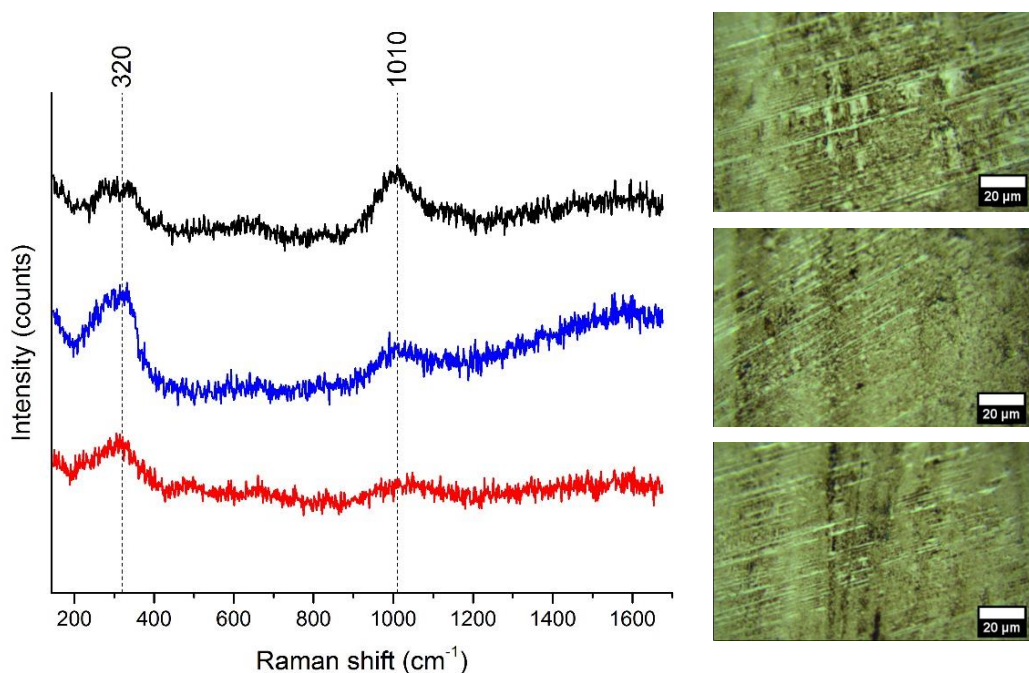
Figure 8-20: Raman spectra obtained from wear track of the membrane tested using PAO+ZDDP lubricant at high temperature. The analysed areas are shown in the insets

These Raman studies show very interesting surface characteristics. The Raman spectra identify the tribofilm formation within the wear track of the membrane tested at high temperature. The broad peak in the region of 900-1100 cm^{-1} of the Raman spectra in Figure 8-20 indicates that the wear scar was composed of the phosphates [141]. The broad peak observed at 200-400

cm^{-1} of the Raman spectra also show the formation of iron sulphide (FeS) on the surface. The formation of iron salt on the surface deactivate the nascent surface and consequently reduce decomposition rate of lubricant [9]. In agreement with these results, Glaeser et al. [142] found FeS formed only in the wear track showing that contact pressure conditions are required for the boundary film reactions. They reported that this thin sulphide film (6-10 nm) plays an important role in inhibiting adhesive wear by preventing direct asperity-asperity contact. This is in agreement with other reports that found higher sulphur amount in asperities due to the higher local pressure [138]. Bell et al. [143] suggested that FeS forms due to the reaction of sulphide products from the frictional and thermal induced decomposition of ZDDP with the metal surface. It is also reported that the metal sulphide improves adhesion between the phosphate layer on top and the metal substrate [143]. Based on these observations, the tribofilm was formed within the wear track at high temperature despite the experiments conducted at room temperature. According to previous studies, elevated temperature accelerates ZDDP decomposition and this is the main reason for this observation [144-146].
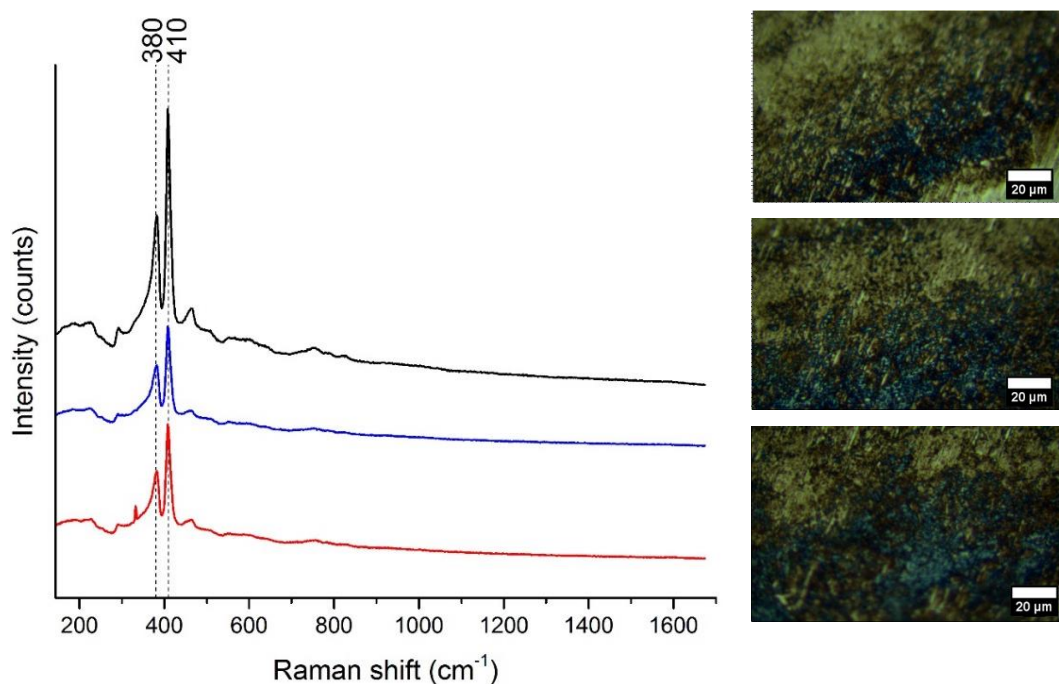
Figure 8-21: Raman spectra obtained from wear scar of the membrane surface after 5 h experiment using PAO+ZDDP+MoDTC lubricant at high temperature. The analysed areas are shown in the insets

The MoS$_2$ formation was confirmed within the wear scar of the membrane tested by PAO+ZDDP+MoDTC lubricant. The peaks observed at 380 and 410 cm^{-1} of the Raman spectra in Figure 8-21 belong to MoS$_2$. A broad peak is also observed around 200 cm^{-1}. This is proposed to be due to the stress-

induced crystalline disorder in MoS_2 structure of the tribofilm occurring under tribological conditions [140].

Total wear volume of the membranes, Figure 8-22, show significant effect of the lubricant additives on decreasing the wear volume. This was expected considering the nature of additives used in this study.
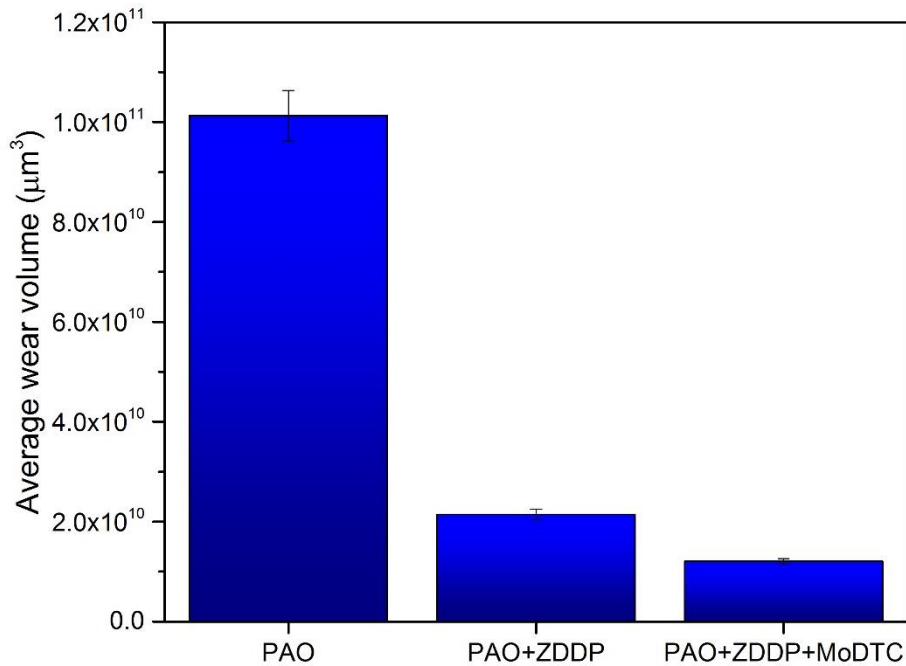
Figure 8-22: The wear volume of the samples tested by different lubricants at high temperature

The optical images from the surface of the membranes after 5 hours experiment using PAO+ZDDP and PAO+ZDDP+MoDTC lubricants are shown in Figure 8-23. The optical photo from the surface of the sample tested by PAO lubricant was presented in Figure 8-6.

(a)   (b)
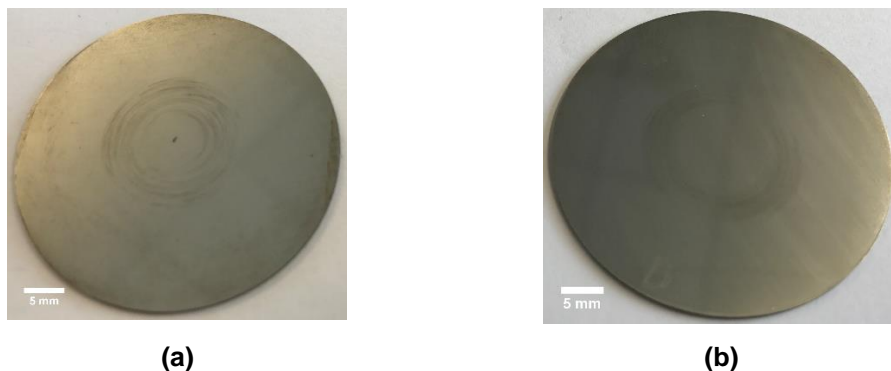
Figure 8-23: Optical photos from the surface of the membranes after 5 hours experiment using (a) PAO+ZDDP and (b) PAO+ZDDP+MoDTC as lubricant at high temperature

8.5 Synergistic effect of water contamination and ZDDP additive

The synergistic effect of water and anti-wear additive on hydrogen entry was studied using solutions of PAO and ZDDP with and without water. This helps to understand the mechanism of hydrogen permeation in presence of the water as we already know from the literature that water contamination affects additives behaviour in tribo-contact [59]. The water-oil blends was prepared by injection of water into the oil and putting the container in an ultrasonic bath for 15 minutes to prepare the emulsified mixture.

The effect of water contamination in both PAO lubricant and PAO+ZDDP were examined by the hydrogen uptake rig and the results are compared with the hydrogen permeation rate of PAO and PAO+ZDDP in Figure 8-24. The increase of current density very soon after starting the rubbing in case of having PAO+ZDDP+water means that hydrogen was evolved as soon as friction was commenced.
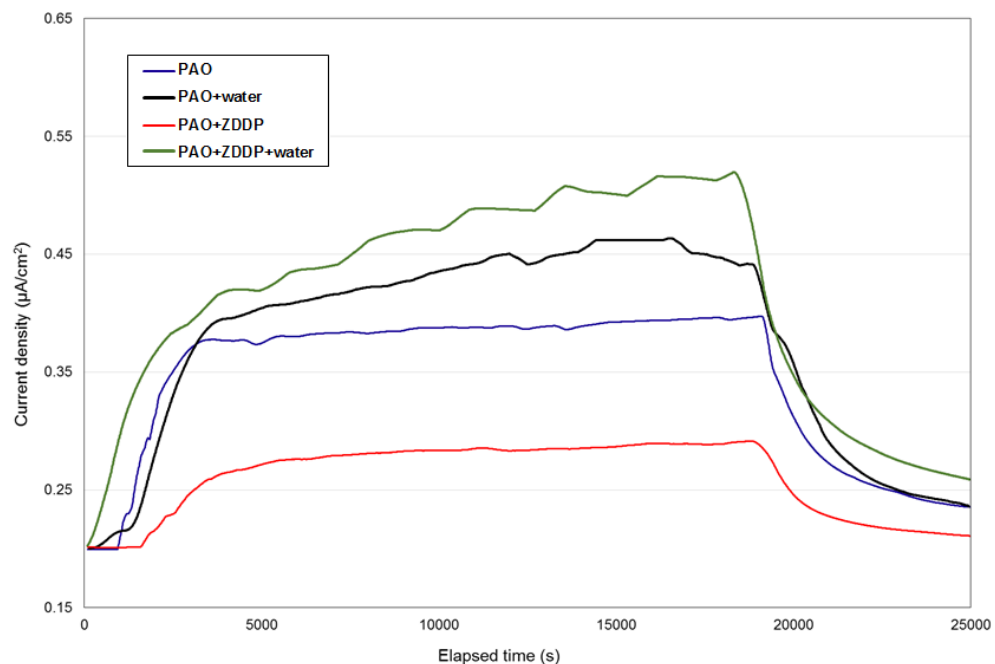
Figure 8-24: Synergistic effect of water and ZDDP additive on hydrogen uptake into the steel at 85°C

The total amount of permeated hydrogen through the steel membrane during 5 hours of the experiment is illustrated in Figure 8-25 based on the curves in Figure 8-24. This reveals the synergistic effect of water contamination and ZDDP additive on total amount of hydrogen permeation through the steel. The results indicate that the effect of water on hydrogen permeation is more detrimental in presence of ZDDP additive in the lubricant compared to PAO.

127
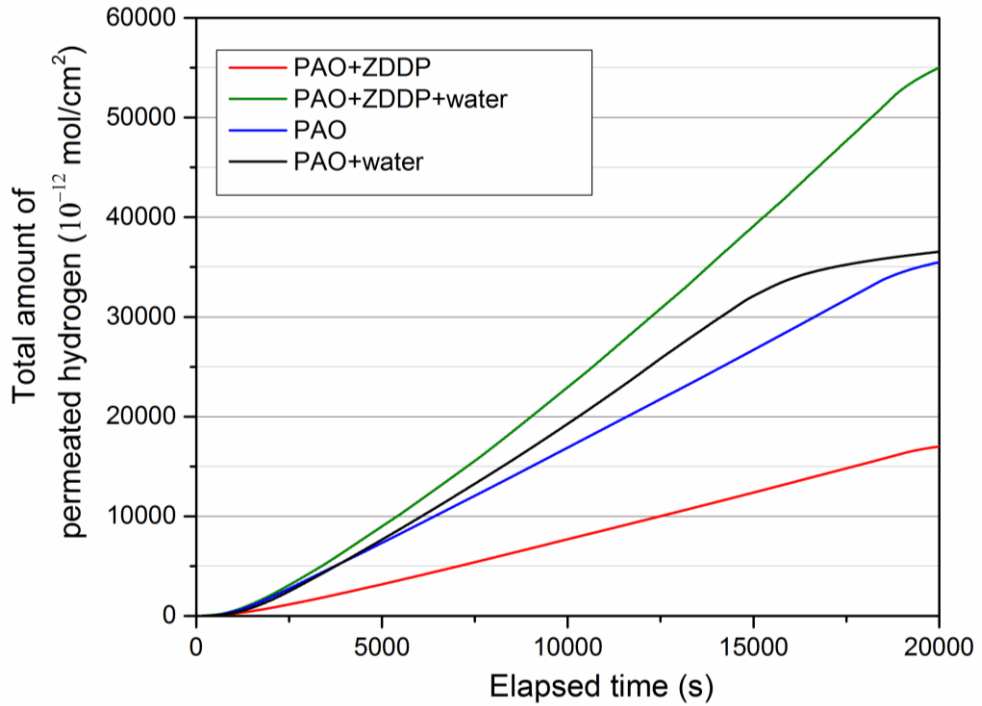
Figure 8-25: The synergistic effect of water contamination and ZDDP anti-wear additive on total amount of permeated hydrogen through the membrane during surface-rubbing at high temperature

The hydrogen uptake increase ratio was calculated for water contaminated PAO to PAO lubricant and also for PAO-ZDDP contaminated lubricant with water to PAO-ZDDP additive blend. Figure 8-26 reveals that hydrogen permeation rate significantly increases when ZDDP and water are both present in the lubricant.
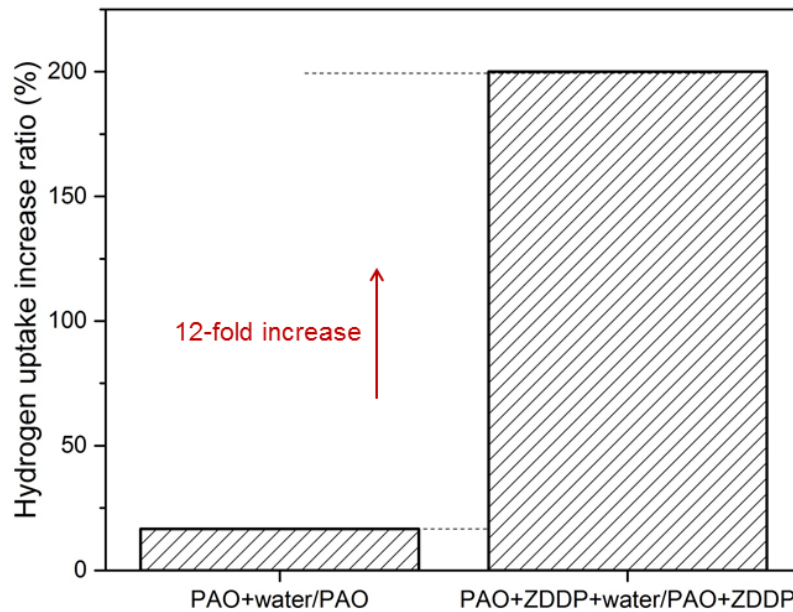
Figure 8-26: Hydrogen uptake increase ratio upon switching from PAO to PAO+water and PAO+ZDDP to PAO+ZDDP+water

The SEM/EDX micrograph and EDX mapping of the wear track with key additive elements after 5 h of the experiment at 350 kPa are shown in Figure 8-27 and Figure 8-28 when PAO+water and PAO+ZDDP+water, respectively, are used as lubricant at high temperature.
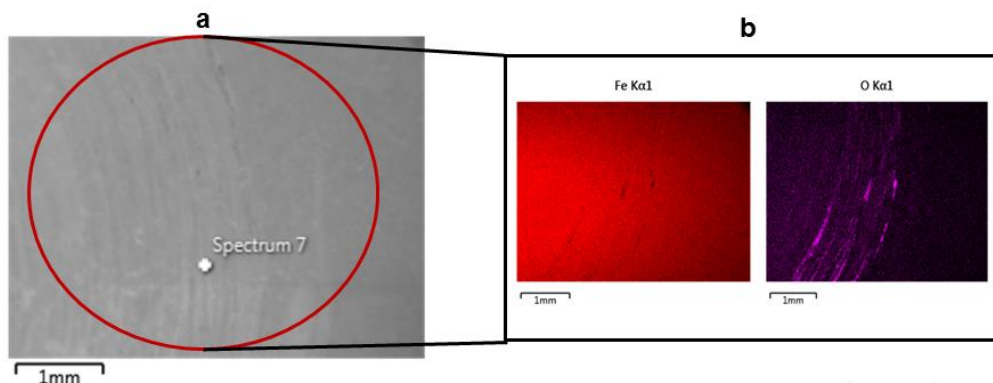
Figure 8-27: (a) SEM micrograph and (b) EDX mapping image of the wear track of the membrane tested by PAO+water lubricant at high temperature
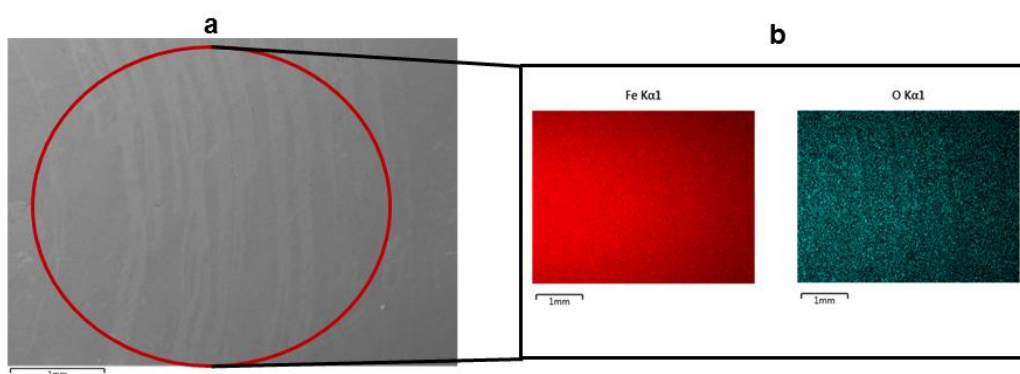
Figure 8-28: (a) SEM micrograph and (b) EDX mapping image of the wear track after 5 h experiment with PAO+ZDDP+water lubricant at high temperature

Figure 8-29 and Figure 8-30 present Raman spectra obtained from out of the wear scar region and the wear scar region, respectively, of the membrane surface after 5 hours experiments by using PAO+water lubricant at high temperature. The results for the PAO lubricant was reported in Figure 8-8. No chemical compound was identified out of the wear scar. However, hematite and magnetite were identified within the wear track although the concentration of these oxides are less than the sample tested by PAO due to the formation of hydroxides and complex compounds in presence of water contamination. Amorphous carbon was also formed within the wear track.
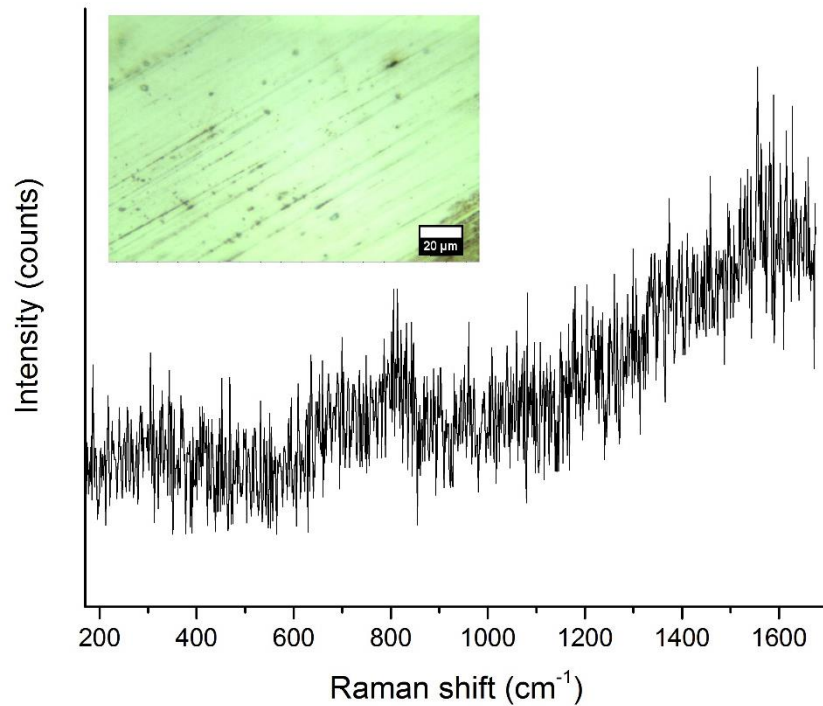
Figure 8-29: Raman spectrum obtained from out of the wear scar as shown in the inset after 5 hours experiment with PAO+ZDDP+water at high temperature
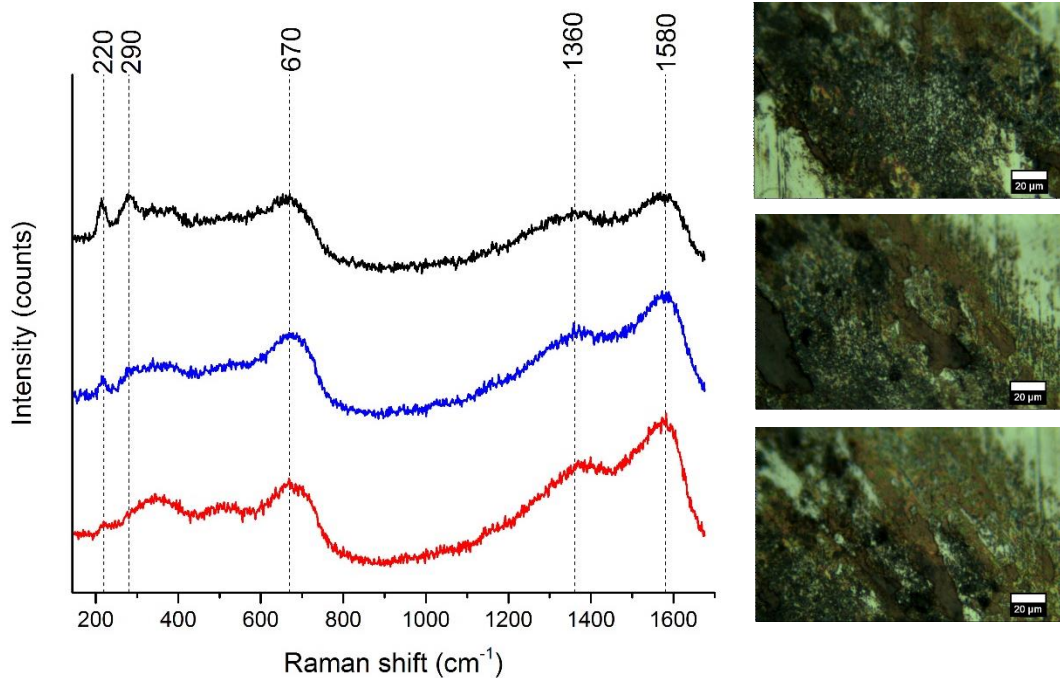
Figure 8-30: Raman spectra obtained from wear scars on tribopair after tests by PAO+water lubricant at high temperature. The analysed areas are shown in the insets

Figure 8-31 presents Raman spectra obtained from the wear scar region of the membrane surface after 5 hours experiment by PAO+ZDDP+water lubricant at high temperature. The results for the PAO+ZDDP lubricant was

reported in Figure 8-20. The most important observation is that Raman spectra obtained from the sample tested by PAO+ZDDP+water shows no indication of phosphate tribofilm. This means that water in the lubricant either damage the tribofilm or does not allow the tribofilm to be formed. Amorphous carbon was also identified on the surface.
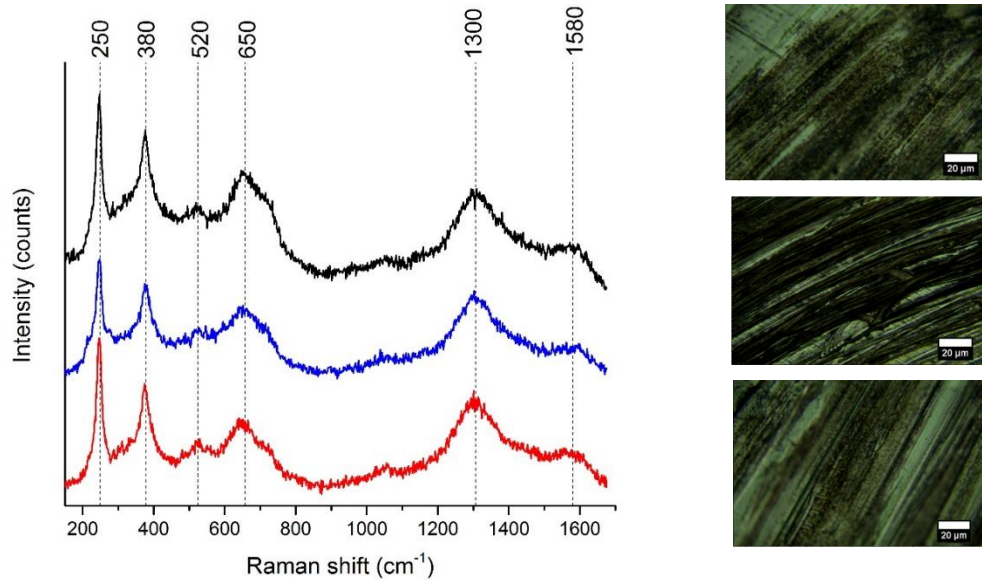
Figure 8-31: Raman spectra obtained from wear scars after tests using PAO+ZDDP+water lubricant at high temperature. The analysed areas are shown in the insets

Total wear volume of the membranes after the experiments was calculated by using the white light interferometry and the results in Figure 8-32 can be compared to the results in Figure 8-22 for PAO and PAO+ZDDP lubricants in absence of water contamination. The water contamination increases wear volume in both presence and absence of ZDDP additive.
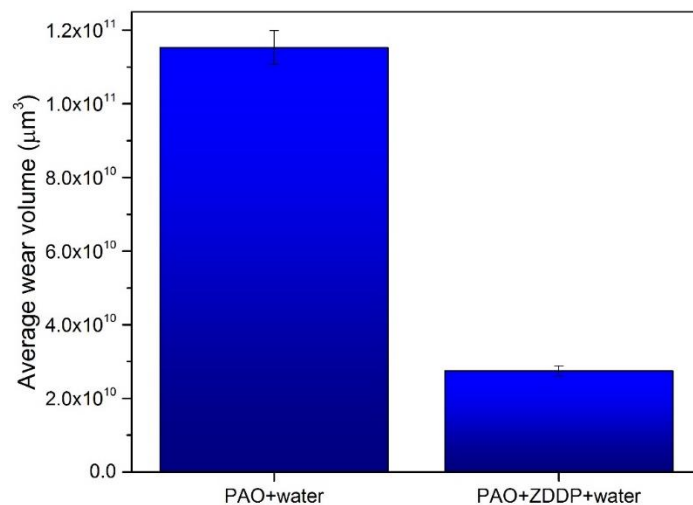
Figure 8-32: The wear volume of the samples tested by PAO+water and PAO+ZDDP+water lubricants at high temperature after 5 h experiments

The optical photos from the surface of the membranes after 5 hours experiment using PAO+water and PAO+ZDDP+water lubricants at high temperature are shown in Figure 8-33. The optical photos from the surface of the samples tested by PAO and PAO+ZDDP lubricants were presented in Figure 8-6 and Figure 8-23, respectively.

(a)   (b)
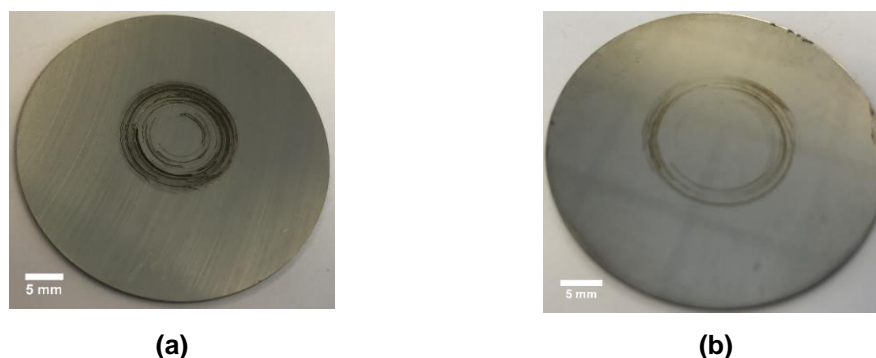
Figure 8-33: Optical images from the surface of the membranes tested by (a) PAO+water and (b) PAO+ZDDP+water as lubricant at high temperature

8.6 Friction coefficient

Monitoring friction coefficient as a function of time showed that the friction rapidly reached its steady value. The steady state friction coefficients of steel/steel couples when different lubricants were used are presented in Figure 8-34. Similar to the experiments conducted at room temperature, no correlation is observed between the friction coefficient and the hydrogen uptake values. It should be noted that friction coefficient slightly increased for the PAO+ZDDP lubricant compared to pure PAO. Many reports have suggested that ZDDP tribofilm increases friction by inhibiting the entrainment of the lubricating film within the tribo-contact [147, 148]. This confirms the Raman spectroscopy results (Figure 8-20) that tribofilm was formed within the tribo-contact. The formation of MoS_2 on the surface of the steel that was tested by MoDTC containing lubricant significantly reduced the friction coefficient value during surface-rubbing.

8.7 Summary

- Higher hydrogen permeation rate was observed when higher contact pressure and higher sliding speed were applied during surface-rubbing
- Lower hydrogen permeation was observed for the experiments with PAO+ZDDP and PAO+ZDDP+MoDTC compared to the experiments with PAO base oil

- The effect of water contamination on hydrogen permeation is more detrimental in presence of ZDDP additive in PAO base oil compare to the pure PAO
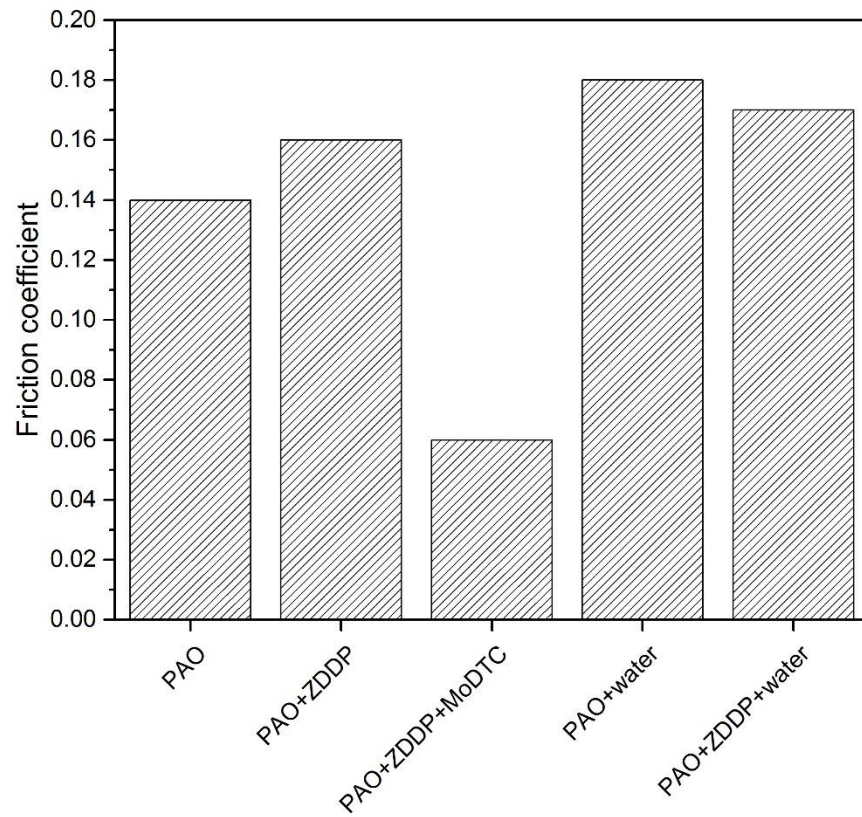
Figure 8-34: Steady state friction coefficient of the steel pair lubricated with different lubricants

Chapter 9 AC measurements in lubricant media

9.1 Introduction

Electrochemical techniques are relatively quick, simple and inexpensive *in-situ* methods. The AC impedance technique can be used to evaluate the electrical properties of the bulk region of the lubricant and of the lubricant-metal interface. Since electrical properties of a hydrocarbon lubricant, in general, are extremely low, the electrochemical measurements in such media are more difficult than in aqueous solutions. This chapter describes the method that has been used in this study to replicate previous EIS measurements in high electric resistance media. The application of AC measurements in understanding the tribochemical reactions and evaluating impedance value of the tribo-contact on hydrogen permeation rate is discussed.

9.2 Electrochemical measurements in high resistance media

Lubricant condition monitoring has usually been done by taking samples and performing *ex-situ* physical and chemical tests. These tests are regularly performed providing information for maintenance plans. There are a number of lab analysis techniques generally employing for oil condition monitoring such as viscosity measurement, infrared spectrometers, debris analysis techniques and EIS. The electrochemical information obtained by EIS can be used to interpret oil condition and is widely used for the analysis of complex electrochemical systems such as oil-steel interface [149-151]. The EIS is compatible with the harsh, high resistance, complex chemistry of the lubricants, polymers and colloids. The main difficulty in measuring electrochemical parameters in lubricant is the poor electrical conductivity of the lubricant, especially fresh lubricants. However, EIS technique has been employed to measure the conductivity of some high resistance media such as industrial polymers, lubricants and colloids [152, 153]. The EIS measurement was also useful in industrial lubricants for detecting water contamination and soot contamination [154-156].

Oil degradation affects physical and chemical properties of the base oil. Oil oxidation process increases its conductivity mainly due to the increase of the conductive species concentration in the oil. The conductive species include oxidation by-products such as nitiric acid and contaminants such as metallic debris and water. A large amount of effort has been invested over the years

to develop reliable on-line monitoring techniques to assess the oil quality. Monitoring changes in the electrical properties of the oil provides a potentially powerful means to inspect the oil performance.

9.3 **Initial AC impedance measurements**

Initial experiments were done to assess the applicability and the strength of the EIS technique for future implementation into the hydrogen uptake rig developed in this study. The EIS measurement is a relatively quick, versatile and inexpensive *in-situ* technique that can be used on the oil side of the developed rig. It can provide useful information on oil condition and the chemical reactions occurring at the lubricant-metal interface. This can increase the understanding of the complex water-additive interactions taking place on the nascent steel surface generating hydrogen.

The initial experiments were performed in a two-electrode configuration set-up in a static condition as described in section 6.10. This set-up was chosen due to the inapplicability of using an aqueous-based reference electrode in non-aqueous media [149]. The two-electrode arrangement is commonly used to investigate the electrolyte properties rather than the electrochemical reactions occurring on the surface. In two-electrode electrochemical cells, one electrode serves as a combined working and reference electrode, and the other one serves as both counter and reference electrode. The total impedance is measured between two reference electrodes in this type of electrode arrangement. The two electrodes have to be very close to each other in order to minimize the IR drop in the electrolyte solution, lubricant, by reducing the resistance to current flow.

The EIS results are generally reported in two forms, namely Bode and Nyquist plots. In Nyquist curves, the imaginary impedance component is plotted against the real impedance component. On the other hand, the Bode plots show the logarithmic absolute impedance $|Z|$ as a function of the logarithm of frequency. The obtained results for PAO lubricant at room temperature with a typical small AC voltage amplitude (10 mV) show a very low signal-to-noise ratio especially at frequencies below 100 Hz. Figure 9-1 illustrates the obtained results for PAO lubricant at room temperature with a small AC voltage amplitude (10 mV). In low resistance media such as typical aqueous systems that corrosion experiments are generally carried out, the voltage amplitude is limited to ~5-10 mV to minimize non-linear electrochemical responses [110]. However, using such small voltage in highly resistive system

is not giving much current through and the output will be very noisy due to the low conductivity and low concentration of electroactive species in the oil samples used in this study.

(a) (b)
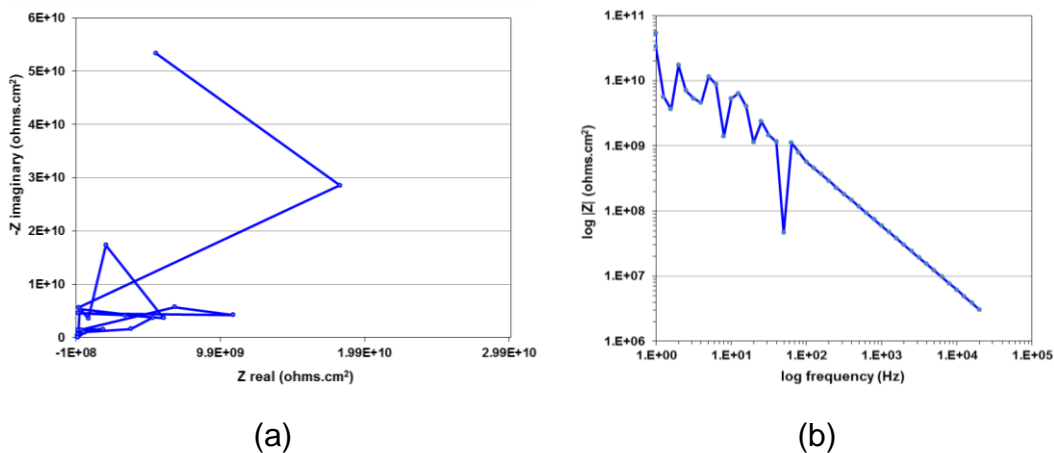
Figure 9-1: (a) Nyquist and (b) Bode plot of the PAO lubricant at room temperature with 10 mV overpotential

9.4 EIS measurement using a high voltage amplitude

The improvement of signal-to-noise ratio was studied by increasing the AC voltage amplitude up to 2 V varied about the open circuit potential. The lubricant temperature was also increased to improve the measurement. Figure 9-2 shows the results obtained for 100 mV overpotential at 50°C.

(a) (b)
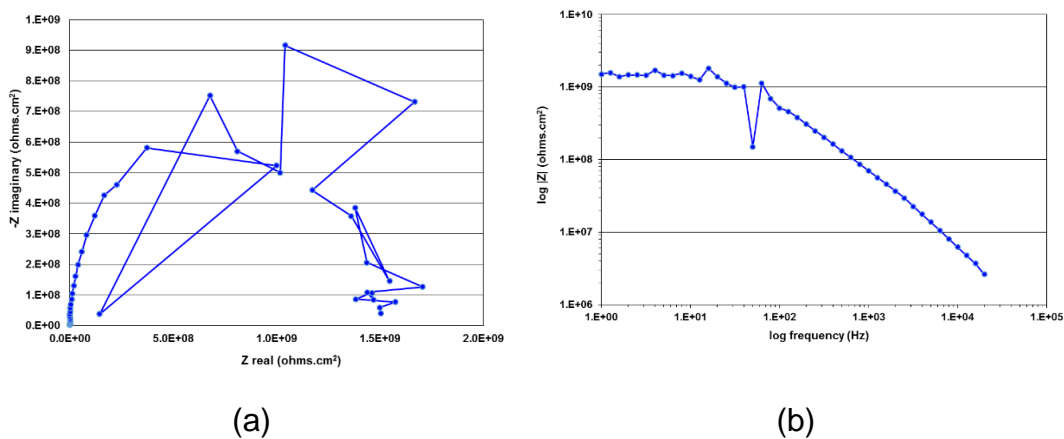
Figure 9-2: (a) Nyquist and (b) Bode plot of the PAO lubricant at 50°C with 100 mV overpotential

Eventually, 500 mV was chosen as it gave a good signal-to-noise ratio and also negligible differences were observed between the obtained results from 500 mV, 1000 mV and 2000 mV. The Nyquist and Bode plots of the PAO lubricant at 50°C using 500 mV AC amplitude showed a good signal-to-noise ratio (Figure 9-3).

136
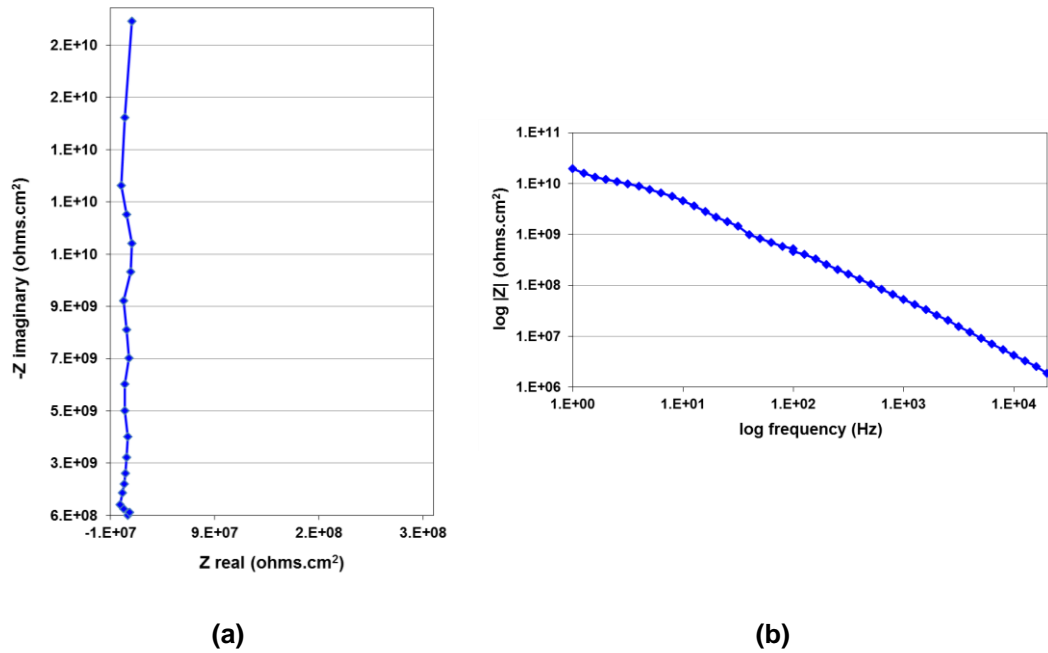
Figure 9-3: (a) Nyquist and (b) Bode plot of the PAO lubricant at 50°C

The EIS results measure the impedance of the lubricant. Impedance defines as the opposition to the flow of electrons in an AC circuit. Impedance is defined as a complex number (equation 9-1) where the resistance is the real component and the sum of capacitance and inductance is the imaginary component of the complex number. The absolute magnitude of the impedance can be calculated using equation 9-2 and is used in the Bode plot.

$$Z = Z_{real} + Z_{img} \tag{9-1}$$

$$|Z| = \sqrt{Z_{real}^2 + Z_{img}^2} \tag{9-2}$$

The obtained results are similar to what reported by Soleimani et al. [157] for fresh lubricant using 100 mV overpotential.

9.5 Base oil ageing detection using EIS

PAO lubricant was aged for 16 hours using the method explained in section 6.5. Figure 9-4 shows the images of aged oils. The dark colour of aged oil indicates some level of degradation of the oil due to ageing process.

FTIR was employed to assess the changes of oil chemistry due to ageing process. FTIR spectra of both fresh and aged oil are shown in Figure 9-5. The R_3C-H stretching band is found in broad region of 2850-3000 cm^{-1} when the CH is adjacent to a non-carbon atom. The IR bands between 1385-1500 cm^{-1} are attributed to alkyl C-H bending. The peak at 722 cm^{-1} belongs to alkyl

137

chains [135]. The exposure of the base oil to the high temperature and oxygen during ageing process results in oxidation products. The peak at 1720 cm^{-1} is attributed to oxidation and is appeared after 16 h of ageing process. The observation of this peak and the dark colour of aged oil showed in Figure 9-4 indicate that the oil has gone through a degradation process.

(a)   (b)
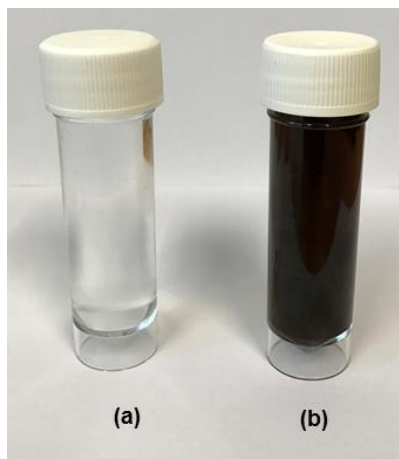
Figure 9-4: Visual inspection of (a) fresh base oil and (b) oil after 16 h oxidation time
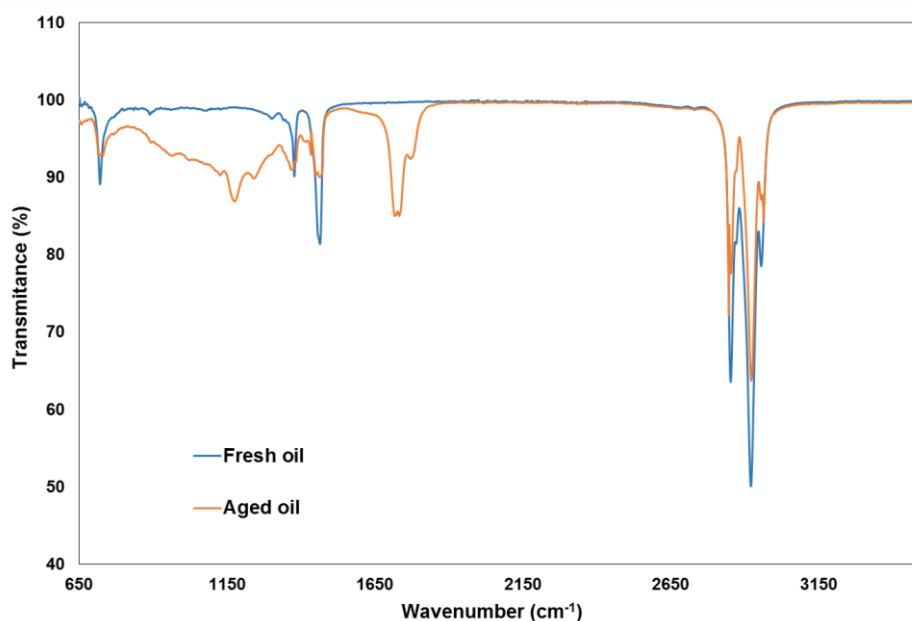
Figure 9-5: FTIR spectra of fresh base oil and after 16 h of ageing

The changes in EIS spectra were employed to identify its response to the lubricant's ageing. Figure 9-6 presents the Nyquist plots of the aged oil when the measurement is done at 50°C. The real and imaginary parts of the impedance of the aged oils are plotted on the x-axis and the y-axis, respectively. Each point on the plot shows the measured impedance value at different frequencies.
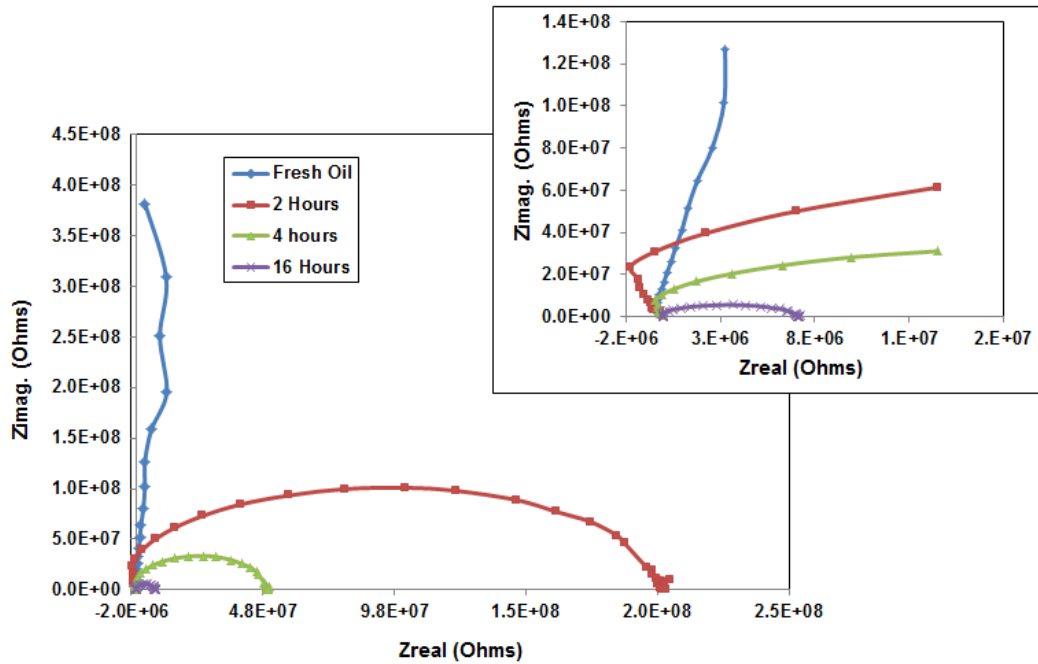
Figure 9-6: Nyquist plots of the oxidised oil samples

As can be seen in Figure 9-6, semicircles are formed (except for the fresh oil) and the diameter of the semicircles become smaller with the level of oxidation time. This shows that the impedance is reduced by increasing the oxidation time due to the fact that the diameter corresponds to the resistance revealing that the lubricant conductivity and ion mobility both increased. Regarding the fresh oil result, the impedance is very high for the fresh oil resisting against the passing current calling capacitive behaviour. The fresh oil results are part of a very large semicircle that only part of it is seen in the Nyquist plot.

9.6 Potential implementation of EIS electrodes into the hydrogen uptake rig

These results have demonstrated that EIS is evidently a viable technique to monitor oil quality and specifically the effect of oxidation process on the oil electrical properties. This capability can be used on the oil side of the developed hydrogen uptake rig in this research. The simultaneous recording of the electrochemical impedance on hydrogen entry side and hydrogen permeation monitoring during surface-rubbing can be employed to ascertain the correlation between the oil properties and the electrons/ions exchange rate on the metal-electrolyte interface and the various hydrogen permeation rate through the steel membrane. This measurement could also be used to monitor the effect of tribofilm on impeding electron/ion exchange rate and correlate its effect on hydrogen generation and permeation through the steel.

139

The combination of EIS measurement and conventional Devanathan double cell has already developed by Gabrielli et al. [131, 158] to study the interaction between the permeation process and the surface reactions on the hydrogen input side. A schematic view of the proposed configuration for the EIS measurement on the oil side of the hydrogen uptake rig is shown in Figure 9-7. The two-electrode system is implemented on the oil side in a way that the steel membrane is employed as one of the electrodes giving electrochemical information from steel-lubricant interface. The other steel plate has to be fixed close to the steel membrane. This information can be used to monitor the impedance and interpret the chemical reactions occurring on the surface. Combination of the impedance measurement on the hydrogen entry side with the electrochemical *in-situ* monitoring of the hydrogen permeation will provide detailed information on the mechanism of hydrogen generation and the effect of surface condition on hydrogen diffusion rate.
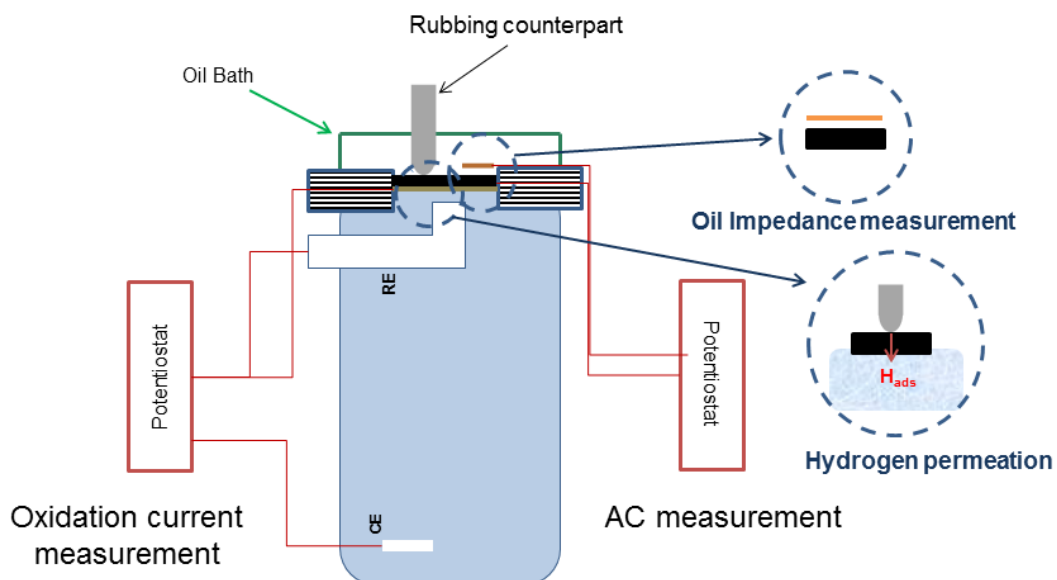
Figure 9-7: Schematic view of the combination of EIS and hydrogen uptake measurement

9.7 Summary

- The surface impedance measurement in a high electrical resistance media was replicated
- The idea of the combination of EIS measurement and hydrogen uptake rig was suggested. This will help to correlate the impedance entry with the hydrogen permeation rate

Chapter 10 Discussion and future work

10.1 Introduction

The monitoring techniques for tribological hydrogen generation have been discussed in Chapter 4. Those techniques, generally, measure the amount of hydrogen that escapes from the contact, not the absorbed hydrogen by tribopairs. However, results in Chapter 7 and Chapter 8 showed that the developed rig in the current study, described in Chapter 5, enables real-time monitoring of hydrogen permeation through the steel from a metal-metal tribological contact and indeed what matters most in terms of HE is hydrogen uptake into the steel rather than hydrogen gas evolution rate. While the focus of this research endeavour was to develop an *in-situ* technique to monitor hydrogen permeation from a tribological contact that is capable of ranking hydrocarbon lubricants in terms of hydrogen generation, it was equally important to understand the mechanism of hydrogen evolution from a tribo-contact. Thus, the new hydrogen uptake rig was utilised to explore the source of hydrogen and the effect of various parameters such as lubricant additives, water contamination, contact pressure and sliding speed on hydrogen permeation rate at both room temperature and high temperature. Surface analysis techniques such as Raman spectrometry and SEM/EDX were utilised to describe the mechanisms.

Failure analysis of rolling bearings in wind turbines have suggested 80°C and 65°C as the highest temperature of bearings in the summer and winter, respectively [159]. So, the experiments in this research were conducted at both 80-85°C as well as room temperature. The atomic hydrogens in this set-up were generated from two flat rubbing surfaces which is not an exact representation of a common tribology regime in rolling bearings. Therefore, the results from this methodology are not suggested to be used for fatigue failure prediction in bearings. However, the sliding contact between two metal surfaces provides shear stress and wear which enables study of the hydrogen generation from a lubricated contact. In this chapter, the following topics will be discussed:

- Diffusion coefficient of hydrogen in the steel
- What are the sources of hydrogen?
- How can water contamination and lubricant additives affect hydrogen permeation rate through the steel at different temperatures?
- The effect of tribofilm on hydrogen entry

- The correlation between mechanical wear and hydrogen permeation rate
- The influence of operating conditions such as contact pressure and sliding speed on hydrogen permeation rate
- Synergistic effect of water contamination and ZDDP additive on hydrogen permeation rate

10.2 **Diffusion coefficient of hydrogen**

The effective hydrogen diffusivity is determined by the time-lag method using the hydrogen permeation transients as well as the sample thickness (800 µm). Figure 10-1 presents the D_{eff} values calculated from the hydrogen permeation tests carried out with different lubricants at different temperatures. The diffusion coefficient values are almost the same with that reported elsewhere [136, 160]. Diffusion coefficient is assumed to be constant at a given temperature. However, a degree of uncertainty is expected due to the changes of the membrane thickness during sample preparation procedure. The slightly lower diffusion coefficient of hydrogen in presence of the lubricants additives can be attributed to the barrier effect of tribofilm forms on the surface. It will be discussed in more details in section 10.4. The oxide layers formed in presence of the water contamination in the lubricant also decreases the diffusion rate at room temperature. However, that value is almost the same for the water contaminated PAO compared to the pure PAO at high temperature since most of the water evaporates at early stage of the experiment.

Another interesting observation is that the diffusion rate has decreased at higher temperature. It can be explained by the fact that hydrogen solubility limit of the steel increases by temperature. Therefore, more hydrogen atoms dissolve in the steel before emerging on the detection side leading to lower hydrogen permeation through the membrane.

10.3 **The mechanism of hydrogen generation from hydrocarbon molecules**

The hydrogen permeation process through the membrane includes its entry at the tribological side, transport through the metal and exit at the detection side. We can assume that hydrogen permeation rate in our study depends only on the process of entry, because all the membranes are from the same material and the hydrogen transportation inside the metal proceeds

undisturbed. Moreover, the oxidation of hydrogen atoms at the exit side occurs instantaneously in presence of palladium. Therefore, the observed changes in total hydrogen permeation, hydrogen flux and hydrogen permeation decay rate after stopping the rubbing are entirely ascribed to the intensity of hydrogen entry.
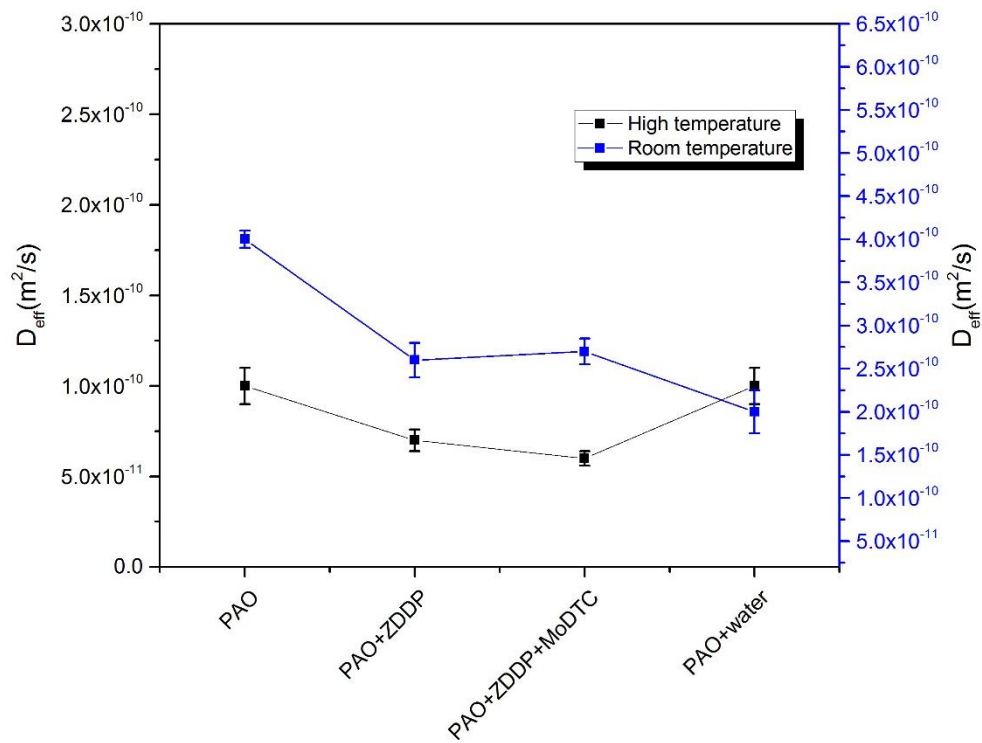
Figure 10-1: Effective diffusivity of hydrogen into the steel when different lubricants were used at different temperatures

In order to verify the origin of hydrogen, a control test was carried out using PFPE lubricant. PFPE is a nontoxic, long-chain polymer consisting carbon, oxygen and fluorine atoms in its structure. Its structure could be in form of linear, branched, or a combination of both. A typical structure of PFPE molecule is shown in Figure 10-2. The carbon atoms have very strong bonds with fluorine and oxygen atoms making PFPE extremely inert. Being inert provides a very good performance at high temperature conditions and makes PFPE a good lubricant to work in presence of corrosive species, acids and liquids containing oxygen. The PFPE mechanism of lubricating is mainly related to its outer layer of non-reactive fluorine atoms. This causes the adjacent molecules to easily slip by each other allowing the formation of a PFPE film layer formation on the surface. This film is very efficient in reducing wear and minimising friction. However, the main reason which make it ideal for control test in this study is the fact that it does not have any hydrogen in its

structure, unlike hydrocarbon lubricants. Therefore, no hydrogen permeation increase is expected using PFPE as lubricant.
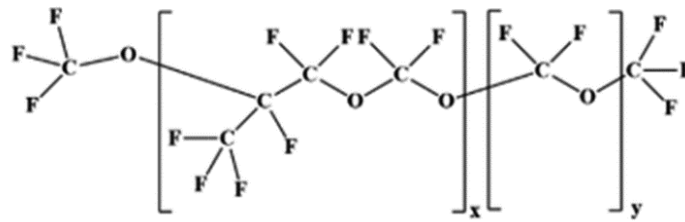
Figure 10-2: Molecular structure of PFPE [161]

The hydrogen uptake experiment results for the PFPE lubricated contact, Figure 7-10, did not show any hydrogen permeation. The curve shape is different from hydrogen permeation curve for PAO lubricant that gradually increases and reaches a steady state. Based on these observations, the hydrogen evolution from the PAO lubricated contact is speculated to originate from hydrocarbon molecules. Other researchers have already reported the hydrogen generation from decomposition of the hydrocarbon molecules too [9, 11, 71]. It has been suggested that lubricants composed of hydrocarbons decompose under repeated stress and heat caused by rubbing contact generating hydrogen. This hydrogen diffuses into the steel and exceeds the critical value causing shorter RCF life of lubricated parts [13]. Thermal decomposition of chemisorbed water and surface contaminants participating in the tribochemical processes occurring at the interface are the other possible sources of hydrogen evolution [5, 9, 11].

Furthermore, the hydrogen permeation measurements in static conditions highlighted the role of tribological processes on hydrogen evolution. No evidence of hydrogen diffusion was observed in static tests showing that either it is not large enough to be detected or the oxide layer on the surface prevents its penetration. This also suggests that hydrogen entry is only expected from inside wear track in tribo-tests. In the static conditions, hydrogen could be generated by corrosion reactions occurring on the surface. Corrosion products were seen on the surface of the samples after being exposed to the lubricant, especially for water containing lubricant (Figure 7-15).

On the other hand, the permeation results during surface-rubbing show that the current rise and fall are linked to the starting and stopping of the rubbing. This reveals that the permeation of hydrogen is tied to the rubbing process. Steel surface is usually covered by a thin air-formed oxide layer and the friction removes this film as well as other surface contaminants. As a result,

metal-hydrogen bonds form on the fresh metal surface. It is also assumed that the nascent steel surface formed under mechanical stimulation condition catalyses decomposition reaction of organic molecules leading to higher rate of hydrogen generation. The material defects act as active sites on the fresh steel surface. They extremely promote the decomposition of the lubricant. This observation is in line with previous *in-situ* measurements that showed hydrogen is being emitted only when sliding occurs in a tribological contact [11, 12]. Molecular dynamics simulations [7] have shown that if a hydrocarbon lubricant film is subjected to shearing between two sliding surfaces, both hydrogen diffusion and hydrogen adsorption on the metal surfaces will be induced.

The lubricant film in the asperity contact is subjected to high temperature, pressure, and friction. These are accelerating lubricant decomposition and hydrogen generation [17, 162]. There is a proposed mechanism describing lubricant decomposition and tribochemical reactions in a trib-ocontact [11, 17]. According to this scenario, hydrocarbon lubricant is initially adsorbed by the nascent surface which was generated by mechanical contact. This is followed by C-C bond rupture leading to production of lighter hydrocarbon by unzipping of the molecular chain. These reactions are thermodynamically favoured on the catalytic nascent surfaces. As a result of this process, hydrogen is formed and the metal surface is covered by C_xH_x species which are adsorbed by iron-carbon bonds. These organic deposits will be removed later by friction forces and the whole process repeats again.

Another possible mechanism to consider is the formation of lighter hydrocarbon molecules through the shear-induced breakdown of the long hydrocarbon chain [11, 12, 17]. Shear stress promotes decomposition of hydrocarbon long chain molecules by rupturing bonds leading to higher hydrogen evolution rate [12, 17]. Decomposition of lubricant molecules under frictional shear stress accelerates by different parameters such as high activity of fresh metal surface, high local temperature, shear stresses on sliding surface and pressure at the contact area [8, 9, 11-13, 71, 163]. Figure 10-3 shows the proposed reaction pathway for decomposition of hydrocarbon lubricant initiated by nascent steel surface formation and the absorption of the hydrocarbon molecules to the active sites generated on the metal surface. Moreover, when the surface is loaded, hydrogen transportation into the subsurface material is enhanced under compressive stresses [162]. It should also be noted that some of the generated hydrogen diffuses into the rubbing counterpart.
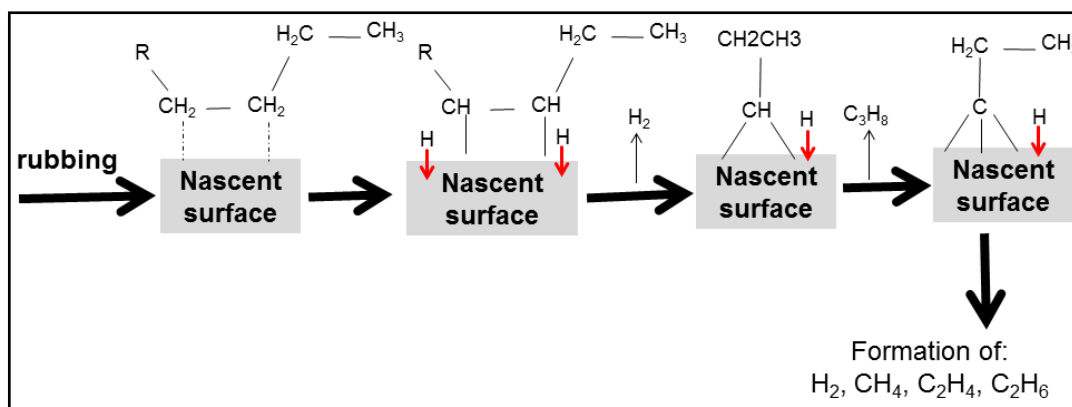
Figure 10-3: Proposed reaction pathway for decomposition of hydrocarbon oil within tribocontacts [11, 17]

The comparison of Raman spectra obtained from the worn area of the sample tested by PAO, Figure 7-17, with the unworn area, Figure 7-16, clearly shows the effect of rubbing on the tribochemical reactions. The rubbing provides enough energy for stimulation of tribochemical reactions occurring on the surface. The by-products of these reactions are formed in the worn area and identified in both Raman and EDX results (Figure 7-18). However, no Raman sensitive chemical compounds were identified on unworn area of the surface.

There is always a trace of hydrogen trapped within the steel from the manufacturing process. This hydrogen is released during surface-rubbing from the worn steel volume, and therefore some of the hydrogen diffusion into the membrane might be due to the hydrogen liberation from the worn steel. The influence of this amount of hydrogen considered negligible in comparison to the hydrogen released from decomposition of the hydrocarbon lubricant and water contamination given the fact that the experiments with PFPE do not show significant hydrogen permeation into the steel although the wear was higher compared to the PAO. The maximum hydrogen amount that can be released from the worn steel volume in the experiment with PAO lubricant (~ 8.5×10^{-8} mole considering 1 ppm hydrogen content in the steel) is almost three times higher than the value for the experiment with PAO+ZDDP+MoDTC. However, the hydrogen permeation rate during 5 h experiment is almost the same in these two experiment showing that the effect of hydrogen liberation from the worn steel volume is not significant on hydrogen permeation rate.

10.4 **The effect of tribofilm on hydrogen permeation rate**

The effect of lubricant additives on hydrogen permeation rate has been assessed by using the hydrogen uptake rig. As discussed in section 10.2,

catalytic effect of nascent surface is crucial for lubricant decomposition. This is where lubricant additives can interfere. Two commonly used additives, ZDDP and MoDTC, have been tested and the results were presented in Figure 7-26 and Figure 8-16 for the experiments conducted at room temperature and high temperature, respectively. The results show contradictory effect of ZDDP additive on hydrogen permeation rate depending on the temperature. Total hydrogen permeation results in Figure 8-17 reveal that hydrogen uptake reduces in case of ZDDP and MoDTC containing lubricants compared to pure PAO whereas the opposite was observed for the ZDDP containing PAO lubricant when the experiment carried out at room temperature (Figure 7-35). This observation highlights the importance of temperature on hydrogen entry into the steel in presence of lubricant additives.

Although less fresh metal formation is anticipated in presence of ZDDP, Figure 7-26 shows higher hydrogen flux for ZDDP containing lubricant compared to PAO base oil, Figure 7-14. This behaviour is observed more clearly in Figure 7-35 plotting the total amount of permeated hydrogen during surface-rubbing. The wear measurement results in Figure 7-36 shows lower wear volume in presence of ZDDP, although frictional hydrogen uptake has slightly increased. Based on these results, reducing the fresh metal surface area by decreasing wear is not merely enough to prevent hydrogen entry. This is consistent with previous experimental results that showed hydrogen diffusion into the steel is not reduced in presence of anti-wear additives [127].

The higher permeation of hydrogen in presence of anti-wear additive is attributed to ZDDP decomposition products acting as poisoning agents to inhibit the recombination of atomic hydrogen to hydrogen gas [127]. This is leading to an increase in the concentration of atomic hydrogen at the metal surface. The presence of the poisoning agents on the wear track of the samples tested by PAO+ZDDP, especially sulphur, has been confirmed in EDX measurements (Figure 7-28) conducted on the surface. A study conducted by Barcroft et al. [164] suggested that the tribofilm formation starts with a sulphur-rich thiophosphate formed on the metal surface at low temperatures. The reaction between this deposited compound and the rubbing surface occurs when the temperature of the oil is raised. There are also some reports proposing that H_2S gas liberates during ZDDP decomposition [165, 166]. It is very well known that HE failures considerably increase in presence of H_2S in oil and gas industry [167-170]. H_2S plays a multiple role in promoting hydrogen uptake into the steel. On the one hand, it increases the corrosion rate and poisons the hydrogen atoms recombination

on the other hand. Consequently, the hydrogen atoms surface coverage increases so that concentration gradient of hydrogen between two sides of the membrane will increase. As a result, hydrogen has more probability to diffuse into the steel before desorption from the surface as hydrogen gas. In addition, the Raman spectra in Figure 7-31 did not show the formation of a uniform tribofilm within the wear track. The patchy tribofilm structure has already been reported for the tribofilms formed at room temperature. Barcroft et al. [164] report highlighted the effect of temperature on tribofilm formation by showing that tribofilm forms only at the asperity-asperity contacts where temperature is high. They found that in the regions with lower temperature such as between the asperities, a heterogeneous amorphous thiophosphate deposits.

On the other hand, ZDDP additive decreased hydrogen permeation rate through the membrane at high temperature (Figure 8-16). The lower hydrogen uptake in presence of ZDDP can be attributed to the lower wear volume (Figure 8-22). As a result, the degradation of hydrocarbon molecules is inhibited by deactivating catalytic effect of fresh metal. However, the lower wear volume did not decrease the hydrogen permeation rate when the tribofilm was patchy. Hence, there should be another mechanism involved in preventing hydrogen entry.

The Raman spectra from the tested sample by PAO+ZDDP lubricant at high temperature show very different compounds formed on the surface compared to the spectra obtained from the tested sample at room temperature. The Raman spectra shown in Figure 8-20 reveal formation of phosphate tribofilm within the wear track. Previous studies also suggested that ZDDP chemisorption starts only from temperatures above 50°C [171]. As discussed, phosphate film and metal sulphides were identified in Raman spectra. The obtained spectra from different positions of the wear scar show a uniform film formed within the wear scar. The presence of phosphate film is due to the decomposition of ZDDP additive. The formation of the ZDDP tribofilm composed of the phosphate has been reported as a reason for wear protection [172]. Lubricant additives that form iron salts such as iron phosphate and iron sulphide on the surface decrease decomposition rate of lubricant by deactivating the nascent surface leading to lower hydrogen evolution. Higher critical load is required to generate hydrogen when these additives are present in the lubricant [9].

A homogeneous tribofilm deactivates the catalytic action of nascent surfaces. The formation of this tribofilm is believed here to be the main reason of lower hydrogen flux. The strong interaction between sulphur and phosphate layer with the metal surface allow fewer active sites to be generated and less metal-metal asperity contact. This layer may also act as barrier to hydrogen permeation particularly when one considers the multilayer structure of the tribofilm with having a glassy polyphosphate layer on top [143]. This top layer seems to be very effective in reducing the hydrogen access to the bottom sulphide layer and metal nascent surface. Bec et al. [173] proposed the most likely multilayer structure of ZDDP tribofilm as depicted in Figure 10-4. This structure suggests that the layer close to the ferrous substrate is solid with strong adhesion to the metal. However, the semi-solid outer layer adheres weakly to the lower layer. The concentration of iron, iron oxide and iron sulphide increases with the depth of the tribofilm towards the substrate. These observations led to the conclusion that apart from the lower nascent surface formation in presence of a uniform tribofilm, the tribofilm itself plays a role in controlling hydrogen permeation into the contacting surfaces.
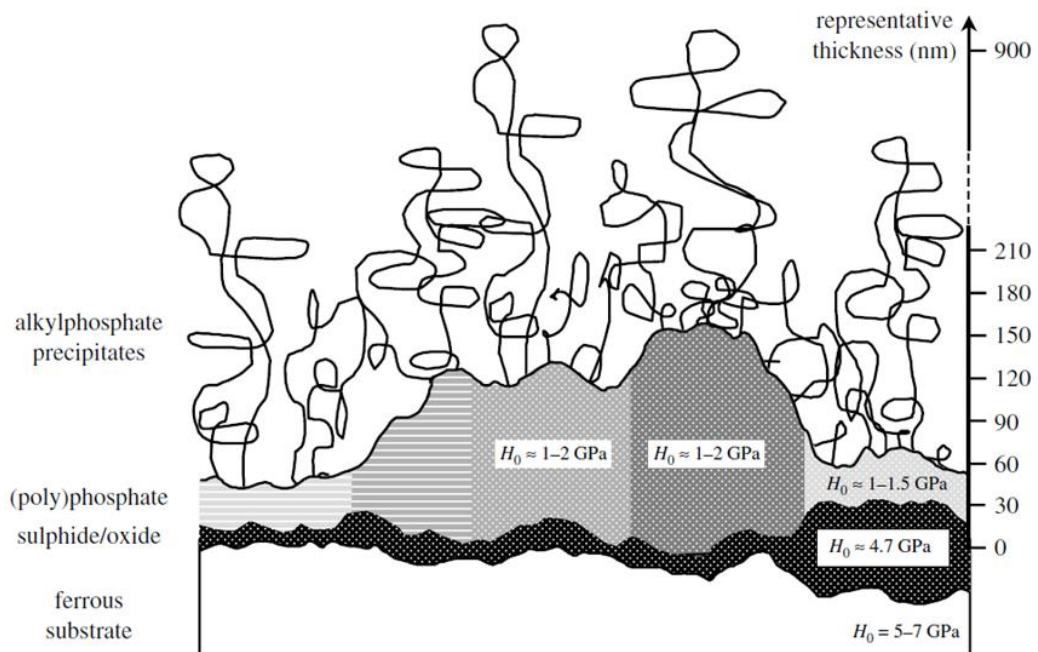
Figure 10-4: Schematic picture of ZDDP multilayer tribofilm [173]

The influence of tribofilm on mitigating hydrogen permeation has also been reported by other researchers [39]. They reported that both ZDDP and trioctylphosphate (TOP) anti-wear additives reduce hydrogen permeation into

the steel (Figure 10-5). ZDDP containing lubricant reduced hydrogen permeation amount in the disc to around 50% less compared to PAO base oil in 10 hours test [39]. This is almost the same value we observed in our measurements for the total hydrogen uptake in the steel (Figure 8-17).
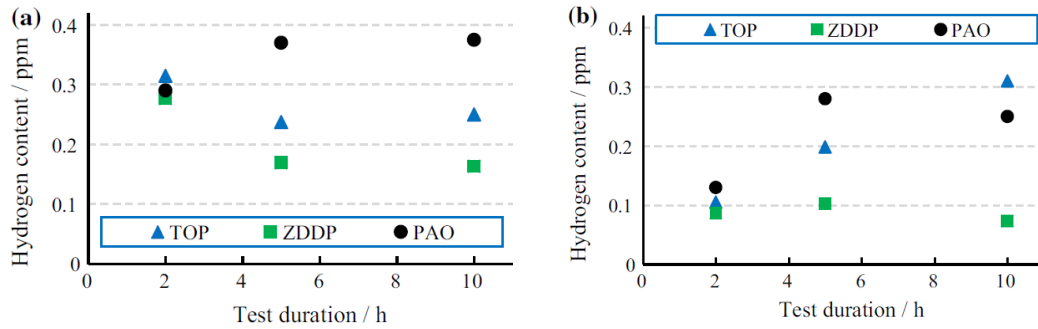
Figure 10-5: Hydrogen content in (a) disc and (b) ball specimens after the tribotest measured by thermal desorption spectrometry [39]

The hydrogen permeation results for PAO+ZDDP+MoDTC lubricant in Figure 7-26 and Figure 8-16 showed the positive effect of friction modifier additive (MoDTC) on reducing hydrogen permeation through the steel at both high temperature and room temperature. One mechanism is related to the less wear in presence of MoDTC. The beneficial effect of MoDTC is also postulated to be due to the reduced friction at asperity levels. The lower friction value in presence of MoDTC additive is due to the MoS_2 deposition in asperity contact [174]. The MoS_2 formation is attributed to the MoDTC tribofilm formed within the wear scar according to previous studies [175]. Decomposition of MoDTC enhances tribofilm growth within the tribo-contact. Both molybdenum and sulphur have been identified in EDX results in Figure 7-29. The formation of MoS_2 was confirmed by Raman spectra obtained from the wear track of the tested sample at room temperature and high temperature as shown in Figure 7-32 and Figure 8-21, respectively. Decomposition of MoDTC within a tribo-contact occurs, even at room temperature, due to the shear stress. The reduced friction torque is anticipated mainly due to the formation of MoS_2 in the contact. MoS_2 is a crystal with hexagonal lattice structure composed of separate layers weakly bonded together via coulombic forces. The layers consist of molybdenum atoms sandwiched between sulphur atoms are the main reason for reducing friction [176].

The hydrogen entry into the membrane is determined by the hydrogen evolution rate and its adsorption to the surface. The former depends on the kinetics of the tribochemical reactions on the surface and the latter depends on the oxides that form on the surface. Figure 10-6 and Figure 10-7 were

extracted from the transient current curves and can be used to compare the effect of lubricant additives on hydrogen flux at the steady state period and the decay rate after stopping rubbing at both room and high temperature. The half-life time ($t_{1/2}$) is reported for the decay process since it shows an exponential behaviour.

This shows the influence of lubricant's composition on the hydrogen permeation and decay rate. The higher hydrogen entry can be correlated to the increasing adsorbed hydrogen atoms (H_{ads}) coverage (θ_H) of the surface and/or to the higher transfer rate into the absorbed state (H_{abs}) in the subsurface layer of the membrane. The higher θ_H is mainly due to the strengthening of the metal-hydrogen bonds and the exposure of nascent metal. This happens when a large area of the surface was freed from air-formed oxide layer. Therefore, the higher hydrogen flux mostly can be explained by the higher wear rate with the exception of PAO+ZDDP compared to PAO at room temperature that the mechanism has already been described. On the other hand, the hydrogen decay rate generally depends on the exposure of the nascent surface. Thus, the type of oxides formed on the surface and the rate of their formation are important. The exponential behaviour of the decay process shows the significant rate of oxide formation within the wear track. Consequently, the hydrogen-metal bonding would not be possible anymore.
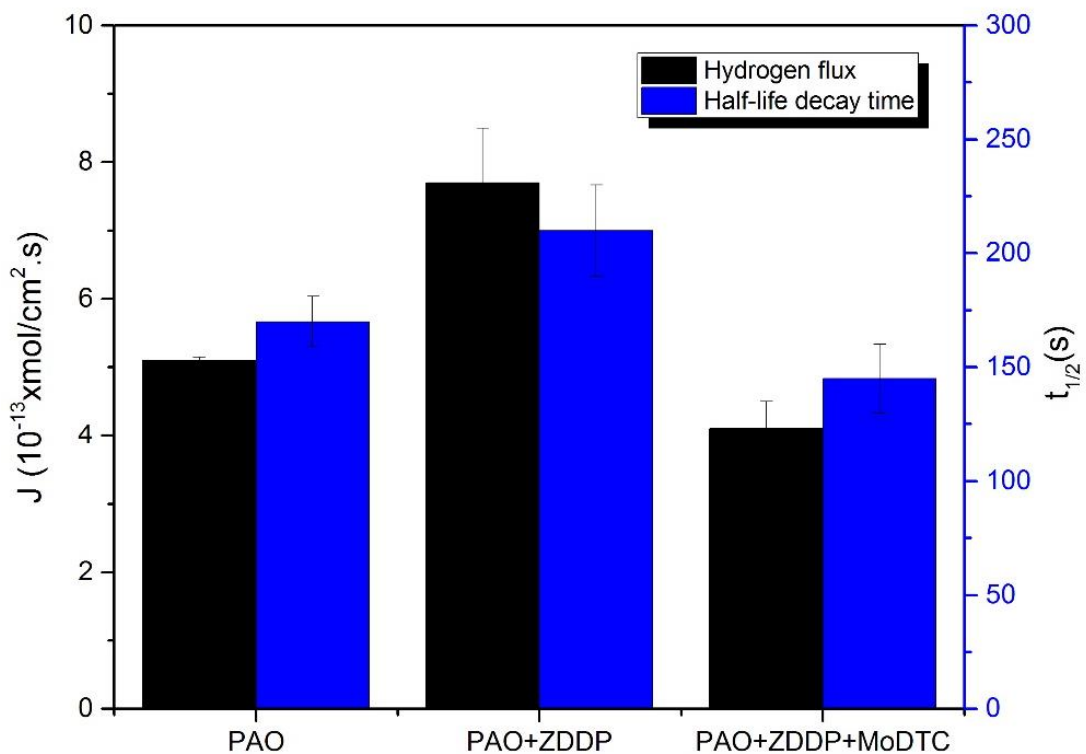
Figure 10-6: The effect of lubricant additives on hydrogen flux and half-life decay time at room temperature

151
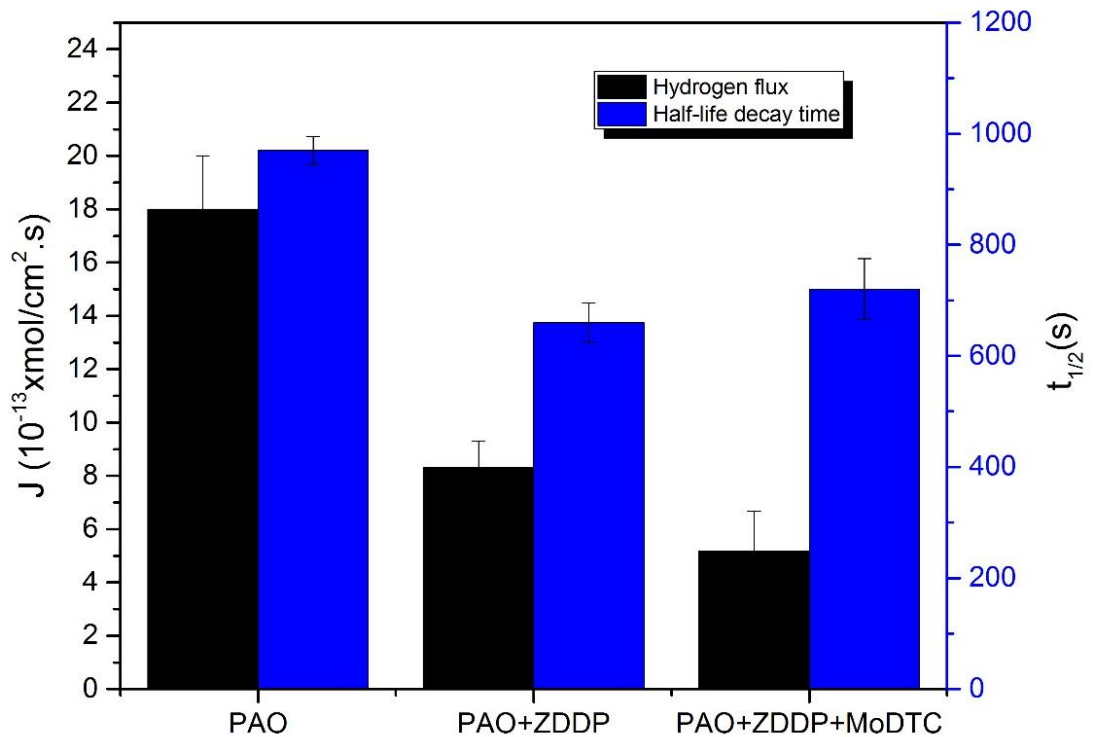
Figure 10-7: The effect of lubricant additives on hydrogen flux and half-life decay time at high temperature

Overall, the results suggested that ZDDP additive mitigates hydrogen permeation when it forms a continuous tribofilm on the surface. Nonetheless, the ZDDP decomposition products such as sulphur and phosphorus seems to promote hydrogen permeation where the tribofilm is patchy. On the other hand, the formation of MoS_2 in presence of MoDTC reduces the friction coefficient and wear leading to lower hydrogen uptake.

10.5 The effect of water contamination in lubricant on hydrogen permeation

Tribo-contact is very complex; on the one hand, there are tribofilm and oxide layer protecting the substrate from further degradation. On the other hand, wear-induced corrosion and corrosion-induced wear accelerate material failure. This will be more complicated when tribochemistry and tribocorrosion processes are taking into account through the effect of water. Water contamination in lubricant is considered as another source of hydrogen in lubricated tribosystems. Water enters the lubricating liquid throughout operation of the bearing either from humid air in contact with the lubricant or condensation of the water in the system. Deleterious effects of water contamination on the bearing fatigue life have been widely investigated so far [71, 85, 98, 99, 177, 178]. Cantley [85] has shown that presence of water in

lubricant significantly lowers bearing fatigue life and this effect increases in higher water concentration. Referring to his results, water absorbing capacity of lubricant varies according to chemical composition and additives of the lubricant as well as the working temperature. Later study by Gao et al. [179] showed that the presence of water alters the mechanism of RCF failure from spall-related failure into crack-related failure.

The effect of water contamination in lubricant on hydrogen permeation rate was assessed using the hydrogen uptake rig. Figure 10-8 shows that the hydrogen flux in the presence of water in lubricant is significantly higher compared to the experiments conducted by PAO base oil. The calculation of total amount of permeated hydrogen through the steel (Figure 7-35) reveals that hydrogen permeation in presence of the water contamination in the lubricant is fourfold higher than the total hydrogen permeation in PAO base oil after 5 hours of the experiment. The higher hydrogen entry rate in the water contaminated lubricants is correlated to the increasing θ_H due to the higher hydrogen evolution rate in presence of water contamination. This can be related to the reduction of water molecules on the fresh metal surface. Another possibility can be related to the effect of water on accelerating oxidative decomposition of the lubricant [71]. Other studies suggested that the water contamination promotes hydrogen permeation rate due to the generation of hydrogen as a product of surface corrosion reactions occurring on the metal surface [98, 99]. Hydrolysis of corrosion products as shown in equations (10-1) and (10-2) are suggested reaction paths to produce hydrogen.

$$3Fe^{2+} + 4H_2O = Fe_3O_4 + 8H^+ + 2e^- \qquad (10\text{-}1)$$

$$2H^+ + 2e^- = 2H_{ads} \qquad (10\text{-}2)$$

Hydrogen can also be generated in absence of oxygen by water molecule reduction according to reaction (10-3):

$$2H_2O + 2e^- = 2OH^- + 2H^+ \qquad (10\text{-}3)$$
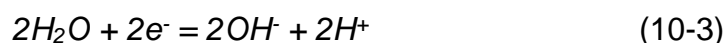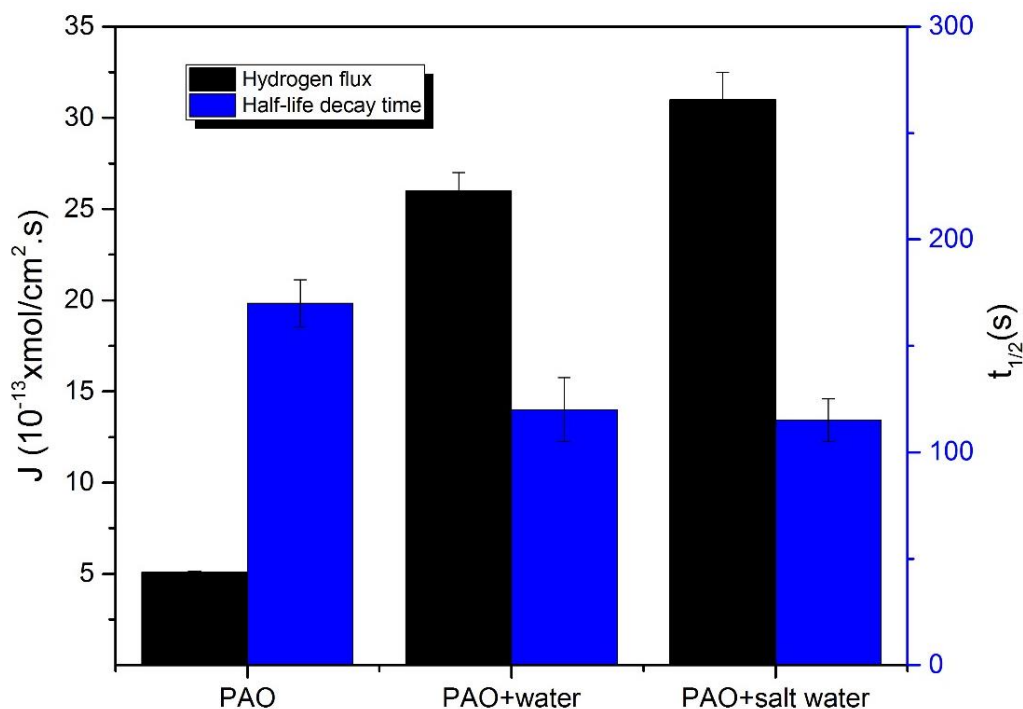
Figure 10-8: The effect of water/salt water contamination on hydrogen flux and half-life decay time at room temperature

The higher decay rate observed in Figure 10-8 also correlates to the faster oxidation rate of the surface after stopping the rubbing in presence of water. The strength of the hydrogen bonds with the oxide layers is less than its bonds with the nascent surface. EDX mapping results from the surface of the samples tested by water contaminated lubricants were presented in Figure 7-21 and Figure 7-22. These results show substantial presence of oxygen in the wear track showing severe oxidation reactions happening in tribo-contact compared to the unworn area. The fresh metal generated by wear was rapidly oxidised by water contamination in the lubricant. Schatzberg and Felsen [98, 99] have already proposed occurrence of corrosive wear in a lubricated rubbing interface with having water as contamination. The Raman technique was also employed to identify the oxide compounds formed on the surface and it was seen in Figure 7-24 and Figure 7-25 that iron oxides are mainly formed in presence of the water in tribo-contact. The difference between these spectra and the spectra obtained from samples tested by PAO (Figure 7-17) is due to the formation of other hydroxides in the worn area revealing that water participated in the reactions occurring on the nascent surface.

Another interesting observation is that the current transient curve of the water/salt water containing lubricants do not reach steady state. The permeation currents for water contaminated and salt water contaminated PAO show a maximum around 1 h and 1.5 h, respectively, after the start of rubbing,

and then it starts to decay. This appears to be a result of non-uniform generation of hydrogen over the charging surface due to the highly corrosive system. It also seems to happen due to the covering of the metal surface by corrosion products hindering further permeation of the hydrogen atoms through the steel [131, 180]. The accumulation of the corrosion products on the surface are visible on the surface of the samples examined in lubricants with water mixture as shown in optical photos in Figure 7-20. Progressive accumulation of corrosion products and deactivation of the surface is leading to the lower hydrogen evolution from the tribological interface. In other words, the constant permeation current was not reached due to the fact that the nascent surface formation rate which is proportional to the sliding velocity did not balance with the diminishing rate of active sites when corrosion products covering the surface.

According to the suggested mechanism associated with the effect of water on fatigue life of the bearing, water accelerates fatigue failure in two ways. Firstly, water causes corrosion on the metal surface. As a result, additional surface defects such as micropits are formed. Surface cracks originate from these defects at lower stresses and propagate until material failure. Gao et al. [179] have revealed that cracks are formed more readily and in greater numbers in water-lubricated contacts compared to oil-lubricated contacts. Secondly, once cracks have formed, water squeezes into the crack by the passing load and forced ahead of the microcrack. It has been suggested that the water reacts with the fresh metal surface at the crack tip. It can be expected, therefore, that water breaks down and generates hydrogen. This hydrogen reduces mechanical strength of the steel as a result of HE and causes higher crack growth rate [98, 99, 178]. It is hard to obtain continuous observation of crack initiation and propagation. However, the significant higher hydrogen flux in presence of water recorded in our measurements confirms the latter hypothesis that hydrogen diffusion involves in failure mechanism of the steel when water is present in the contact.

It needs to be considered that the magnitude of water effects depends on various factors such as contact pressure and operating temperature. Therefore, the presented results for the hydrogen permeation rate in our measurement should be restricted to the conditions similar to the one employed in obtaining the test data.

10.6 **Synergistic effect of water contamination and ZDDP additive**

The influence of water contamination in PAO base oil was tested both in presence and absence of anti-wear additive and the results were plotted in Figure 8-24. Before discussing the synergistic effect of water and ZDDP, the effect of water on hydrogen permeation rate is assessed at different temperatures by calculating the percentage increase of total permeated hydrogen during the 5 h experiment. The percentage increases of permeated hydrogen were 375% and 16% for experiments conducted at room temperature and high temperature, respectively. This can be related to the evaporation of water from the lubricant in early stages of the experiments conducted at high temperature [88].

Furthermore, the hydrogen uptake increase ratio results presented in Figure 8-26 show that hydrogen flux significantly promotes when water and ZDDP both present in the lubricant. The results reveal that the hydrogen uptake increase ratio is 200% when ZDDP and water are present in PAO base oil, whereas this is less than 20% in absence of ZDDP in the lubricant. These results clearly demonstrate that the effect of water is much more detrimental in presence of ZDDP additive. This detrimental effect can also be seen in Figure 10-9 comparing the hydrogen flux for different lubricants. These results show that the hydrogen atoms coverage of the surface and its absorption to the membrane is higher when both water and ZDDP are in the lubricant. Considering that the experiments were done at high temperature, this implies that water affects hydrogen permeation rate even if exists in PAO+ZDDP lubricant for a brief period of time before escaping the lubricant by evaporation. This is suggested to be due to the fact that even a small amount of water contamination in the lubricant accelerates ZDDP decomposition rate [46, 89]. The higher decomposition rate of ZDDP in presence of water increases the concentration of poisonous agents on the metal surface. These agents inhibit the recombination of atomic hydrogens to hydrogen gas leading to an increase in the hydrogen permeation rate. Spedding et al. [46] postulated that water catalyses ZDDP decomposition through the following reaction:

$$RO - P \xrightarrow{H_2O} R' = CH_2 + H^{+-}O - P - \qquad (10\text{-}4)$$
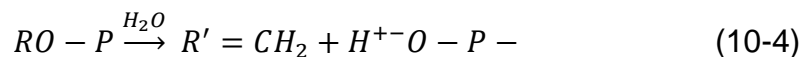
They also pointed out that water reacts with sulphur species resulting in H_2S formation according to reaction (10-5) and accelerating HE:

$$-P = S + H_2O \rightarrow -P = O + H_2S \qquad (10\text{-}5)$$

156
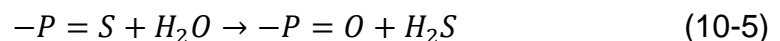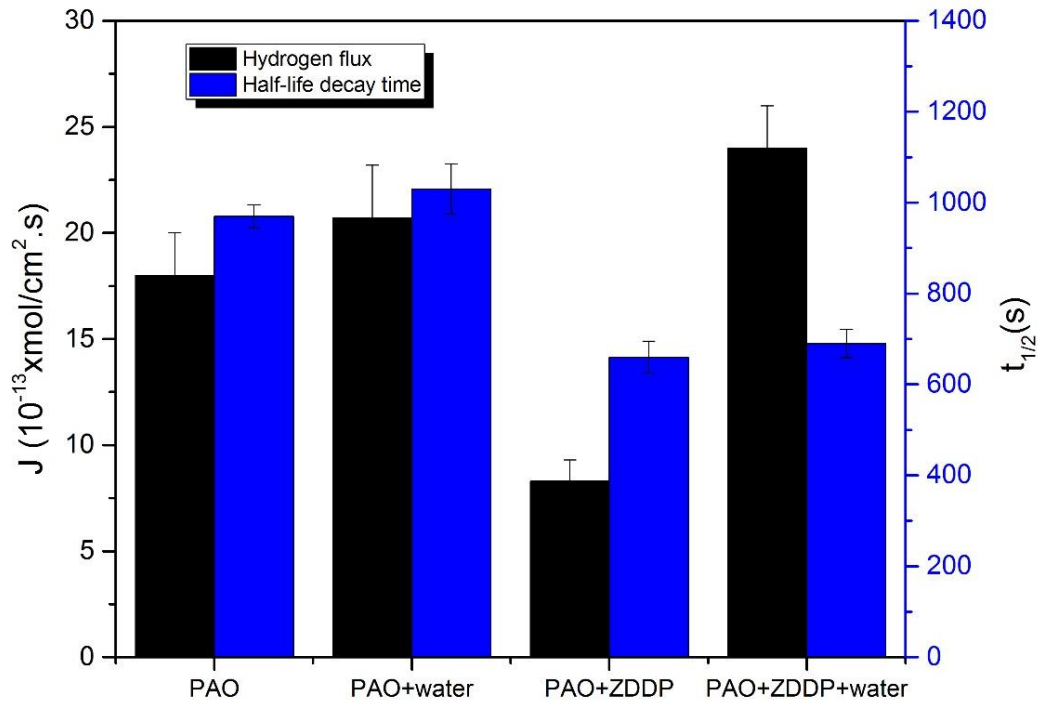
Figure 10-9: The synergistic effect of water contamination and ZDDP additive on hydrogen flux and half-life decay time

The Raman spectra obtained from the surface of the sample tested by PAO+ZDDP+water, shown in Figure 8-31, reveal that tribofilm has not formed on the surface of the sample. The tribofilm formation has already confirmed for the samples tested by PAO+ZDDP, Figure 8-20. This indicates that the presence of water disturbs the mechanism of ZDDP additive in blocking hydrogen permeation. In agreement with this observation, the experiments of Nedelcu et al. [59] showed that tribochemical reactions are affected in presence of water due to its interference with the additives on the contacting surface. This is reducing the formation rate of the tribofilm.

The Raman spectrum in Figure 8-29 was obtained from the un-worn area of the sample tested by PAO+water at high temperature reveals that no detectable oxide layer was formed on the surface of the membrane where there is no friction. This means that water was not capable of forming a uniform oxide layer in absence of rubbing. On the other hand, iron oxides were formed within the wear track as shown in Raman spectra presented in Figure 8-30.

10.7 Correlation between wear and total hydrogen uptake

The higher hydrogen entry is associated mainly to the increasing θ_H and the disintegration of the surface by wear removal which promotes ingress of hydrogen. Kohara et al. [12] noticed that the hydrogen generation rate is

proportional to the wear width where no lubricant additive is used. Their measurement results (Figure 10-10) using mass spectrometry technique have shown that the amount of hydrogen generated from lubricants is influenced by wear rate.
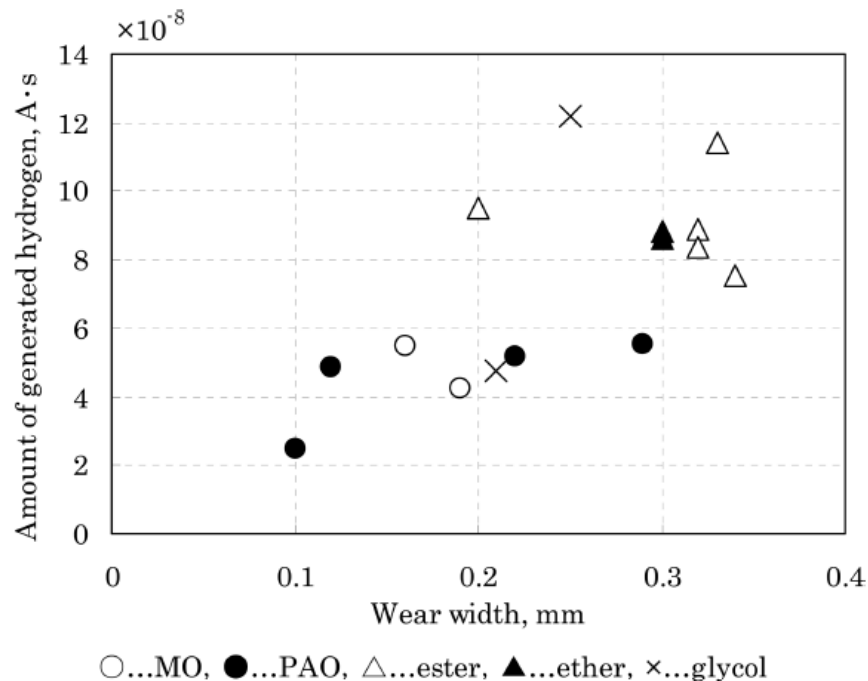
Figure 10-10: Amount of hydrogen generated from test oils and wear width on disc [12]

Similarly, the results in Figure 10-11 illustrating the total amount of hydrogen permeation after 5 hours of the experiment with PAO and water contaminated PAO versus the average wear volume confirm that hydrogen permeation is promoted by increasing wear. The reason behind this could be traced back to the higher generation of hydrogen due to the larger nascent surface formation. The more generation of nascent metal surface catalyses tribochemical reactions on the surface leading to production of more hydrogen.

The severe contact is also considered as the main reason for higher hydrogen uptake when DP sprayed polishing paper is used. Although the operational parameters were same, comparison of the results presented in Figure 7-5 with the results in Figure 7-14 and Figure 7-26 reveals that the hydrogen permeation rate is significantly higher for both PAO and PAO+ZDDP lubricants when DP sprayed polishing paper is used as rubbing counterpart. This is mainly due to the higher wear rate when the DP sprayed polishing paper is rubbing against the steel surface (see Figure 7-7) compared with the wear rate of steel-steel contact (see Figure 7-36). The higher wear rate is due to the very high abrasive wear in presence of diamond powder.
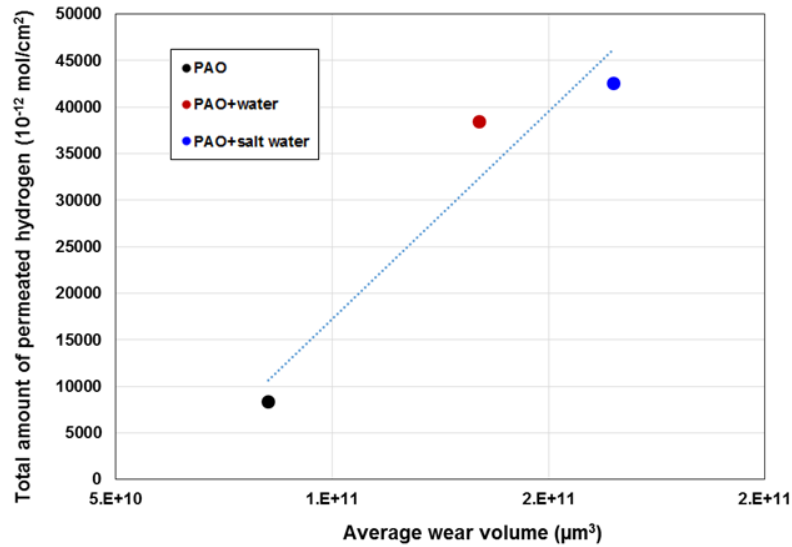
Figure 10-11: Wear volume in comparison with total permeated hydrogen for PAO, PAO+water and PAO+salt water

On the other hand, such correlation between wear and hydrogen uptake is not seen when lubricant additives are used. Figure 10-12 and Figure 10-13 present compilation of total hydrogen uptake results and the wear volume results for the experiments carried out at room temperature and high temperature, respectively. Operating conditions were identical for all the experiments, while the lubricants used for the experiments were different. It can be concluded from Figure 10-12 and Figure 10-13 that there is co-existence of chemical and physical mechanisms involved in promoting hydrogen uptake. The surface protection effect of lubricant additives is influential in this behaviour.
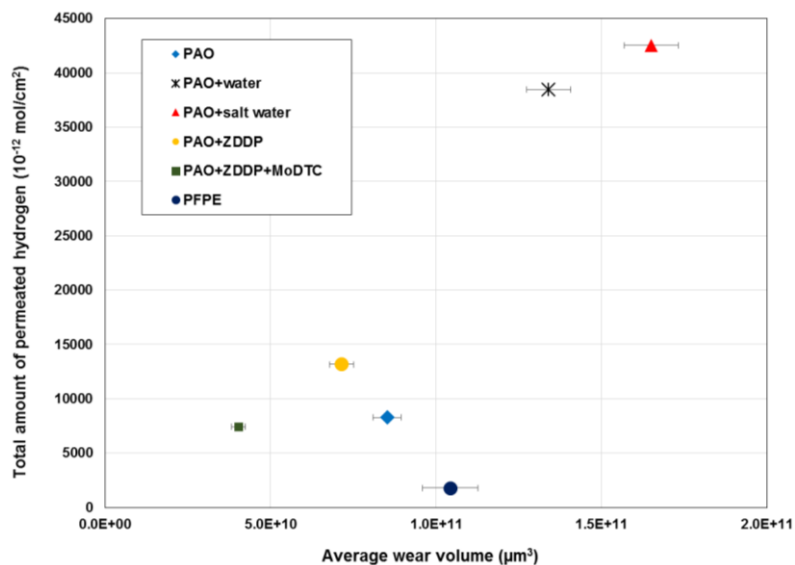
Figure 10-12: Wear volume in comparison with total permeated hydrogen through steel for the experiments carried out at room temperature

159
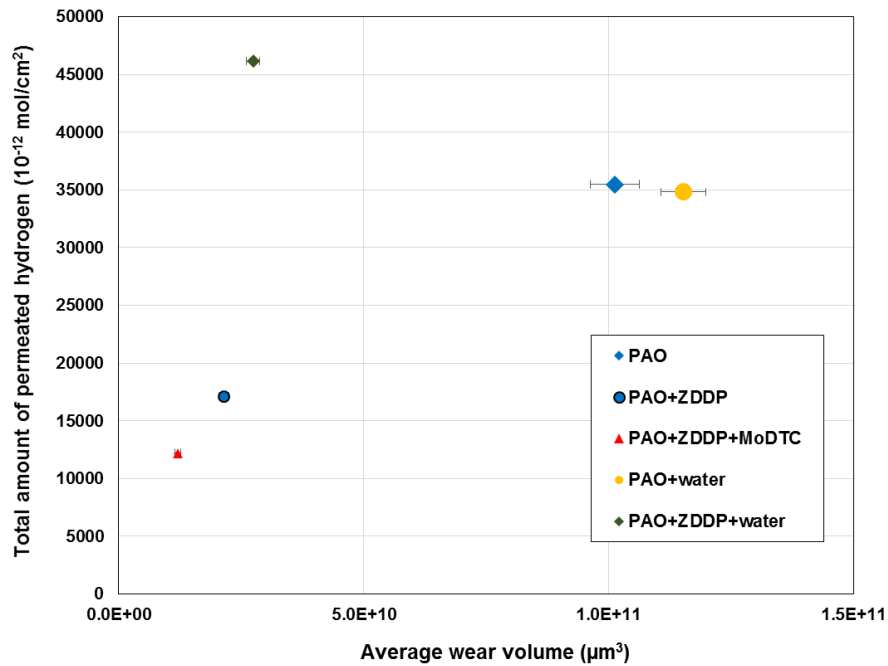
Figure 10-13: Wear volume in comparison with total permeated hydrogen through steel for the experiments carried out at high temperature

The link between the wear/tribological conditions and the hydrogen permeation rate when lubricant additives are used still needs more experimental data to be substantiated. Especially running experiments with lubricants containing different concentrations of additives would be useful to find the correlation between the mechanical removal of the surface in presence of additives and hydrogen permeation rate.

10.8 Effect of tribological parameters on hydrogen permeation rate

Figure 7-37 indicates that hydrogen is generated as a result of tribological contact at room temperature. It was noticed almost no hydrogen permeation detects when load is not applied. The total hydrogen is also negligible at 140 kPa contact pressure, as shown in Figure 7-38, compared to the hydrogen permeation at 350 kPa. This is an important observation as it shows that a critical pressure is required for hydrogen permeation in a lubricated tribo-contact. This confirms previous findings that a critical load is necessary for hydrogen generation from lubricated contacts [11]. This critical load is required to remove the oxide layer and form nascent steel surface. More experiment results are required with the load swiped between 30 N and 70 N to identify the critical load. These experiments will show the correlation between the contact pressure and the induction time for hydrogen intrusion into the steel.

160

The contact pressure also affects hydrogen flux and decay rate according to Figure 10-14. The higher hydrogen entry is correlated to the higher θ_H mainly due to the strengthening of the metal-hydrogen bonds and the exposure of nascent surface. This is due to the larger wear volume and the larger surface area that was freed from air-formed oxide layer when the higher load is applied. The higher friction coefficient at 350 kPa compared to the friction at 140 kPa, shown in Figure 7-40, also increases the energy input into the contact accelerating tribochemical reactions.
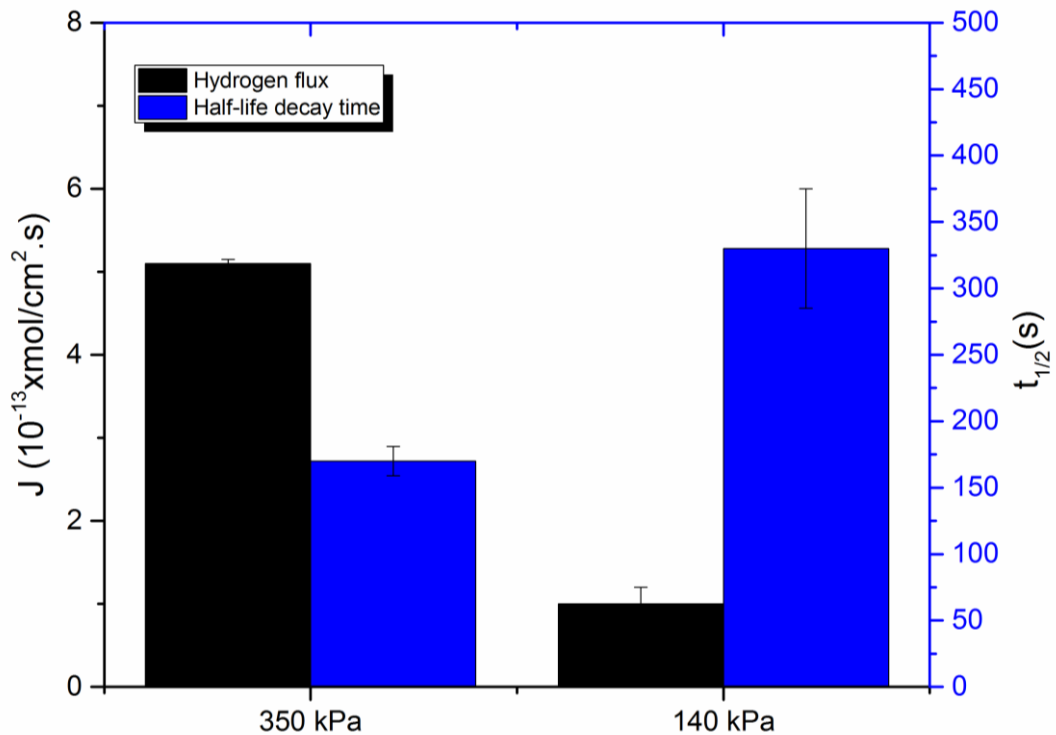
Figure 10-14: The effect of contact pressure on hydrogen flux and half-life decay time at room temperature

The effect of contact pressure at high temperature was also investigated and the results presented in Figure 8-1 show that the hydrogen flux is increasing at higher contact pressure. One of the reasons is the higher wear volume at 350 kPa compared to the wear at 140 kPa as shown in Figure 8-5 and Figure 8-6. SEM/EDS analysis reveal that the concentration of oxygen on the wear track of the sample tested at 350 kPa is almost 3 times higher than that of the sample tested at 140 kPa. The higher oxidation rate at higher contact pressure is another reason for the higher hydrogen permeation rate. The higher contact pressure and frictional heat causes different surface oxides formed compared to the lower contact pressure as seen in Raman spectra obtained from the worn area. The 140 kPa critical contact pressure for hydrogen permeation was

not seen for the hydrogen generation maybe due to the higher tribochemical reaction rates at high temperature.

The effect of sliding speed as another important tribological parameter on hydrogen evolution was investigated by running experiments in two different frequencies, 1 and 0.5 Hz, using PAO lubricant. The hydrogen uptake results were illustrated in Figure 8-10 and the corresponding total permeated hydrogen during 5 hours of the experiment were presented in Figure 8-11. The hydrogen permeation rate was reduced by lowering the sliding speed due to the smaller wear volume as shown in Figure 8-13. It is due to the lower decomposition rate of the lubricant as it has already been revealed that lubricant decomposition rate is directly proportional to sliding velocity and the applied load [8, 9, 11].

The EDX results for 0.5 Hz presented in Figure 8-12 have shown lower oxygen concentration on the wear track compared to the oxygen concentration measured for the sample tested with higher sliding speed at the same contact pressure, Figure 8-3. The higher oxidation rate for higher sliding speed causes higher hydrogen generation due to the higher energy input although the Raman spectra obtained from the surface showed that the type of oxide formed on the surface is not changed by sliding speed.

Figure 10-15 compares the effect of operational parameters on hydrogen flux and the decay rate at high temperature. The higher hydrogen entry rate can be correlated to the higher kinetics of reactions and higher adsorption rate of hydrogen atoms to the surface. The higher contact pressure and sliding speed increase the energy input into the contact and the wear. The former promotes surface reactions and the latter forms the nascent surface that is accelerating hydrogen evolution reactions. The different decay rates ($t_{1/2}$) can be correlated to the different types of oxides formed within the wear track. The formation of these oxides were observed in Raman spectra acquired after the tribo-tests. Magnetite and hematite were identified within the wear scar of the sample tested under 0.5 Hz. However, magnetite was mainly formed on the surface of the samples tested with higher sliding speed.
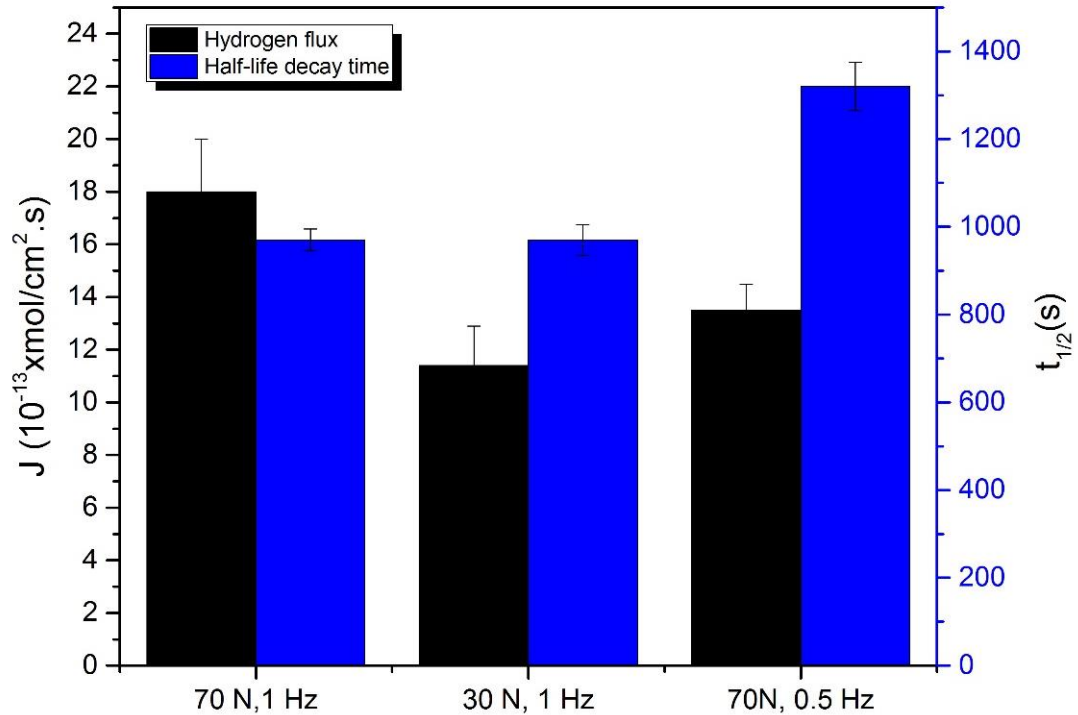
Figure 10-15: The effect of operational parameters on hydrogen flux and half-life decay time at high temperature

10.9 Recommendations for future work

Thus far, the capability of this *in-situ* hydrogen uptake measurement rig was verified for different lubricants and the results were promising. The following recommendations could help further development of the rig for more detailed studies.

10.9.1 Development of the tribological interface for rolling/sliding contacts

Ultimately, the rig has to be able to monitor hydrogen permeation as a function of more realistic tribological conditions for boundary lubricated contacts. Thus, the interface from which the hydrogen permeation is measured has to be modified to a rolling/sliding contact enables to generates severe shear stress and high enough wear rates to generate hydrogen.

10.9.2 Coupling of production and permeation results

The developed *in-situ* technique in this study has been able to provide a measure of the permeation of hydrogen. Other techniques based on mass spectrometry have been able to determine the production of hydrogen but have given no information of the permeation. These two different approaches

can be coupled to build a methodology being able to capture the entire process.

10.9.3 Implementation of AC impedance measurement electrodes to the tribological side of the rig

As discussed in Chapter 9, EIS measurement gives useful information regarding reactions and mechanisms involved within a lubricated interface. Coupling such technique with the hydrogen uptake rig will help understanding the mechanism and the rate of responsible reactions for hydrogen generation. This will also help to investigate the effect of surface oxide layer and tribofilm on preventing hydrogen uptake into the substrate.

10.9.4 The mechanism of hydrogen generation from lubricated contacts

Although the hydrogen intrusion into the steel was measured by the new developed technique in this study, the mechanism by which this hydrogen was generated is not clear since no direct observation is currently possible at the rubbing side of the rig. Therefore, AC impedance measurement and mass spectrometry techniques which are already explained in sections 10.9.2 and 10.9.3 are suggested to be employed to investigate the mechanism of hydrogen generation in future work. The combination of the results from hydrogen generation side and total hydrogen diffusion into the steel can be used to propose a comprehensive mechanism for hydrogen generation within a tribo-contact.

Chapter 11 Conclusions

A novel robust method based on the modified Devanathan-Stachurski technique has been developed to experimentally assess hydrogen permeation through the steel from a metal-metal lubricated sliding contact. The new methodology can be employed to assess the origins and permeation rates of hydrogen within a lubricated tribo-contact. Repeatability of the results was acceptable when precautions were taken to avoid contamination of surfaces and keep the palladium coating free from mechanical damage. The results indicate that the hydrogen permeation rate is strongly dependent on the lubrication type and condition. Under the conditions tested, the following conclusions can be drawn.

11.1 Experiments conducted at room temperature

- Hydrogen permeation was not detected in absence of sliding contact. The potential reason for this is the removal of the oxide layer by friction leading to the permeation of hydrogen. The generation of hydrogen is also catalysed by nascent steel surface formation during surface-rubbing.

- Hydrogen uptake was not detected when hydrogen-free lubricant was used showing that the hydrocarbon base oil is one of the sources of hydrogen in a metal-metal lubricated contact.

- It was shown that hydrogen intrusion into the steel was substantially promoted in presence of water contamination in the lubricant. According to the results, hydrogen uptake from the tribological contact increased up to four times in presence of 5% water blended into the PAO. This can be postulated that the unsteady permeation current in presence of the water is due to the formation of oxide layer that makes hydrogen atoms adsorption to the surface more difficult.

- Hydrogen uptake is promoted in presence of AW (ZDDP) in the lubricant. It is supposed to be due to the inhibition effect of ZDDP on the recombination of hydrogen atoms.

- Hydrogen permeation decreases in presence of MoDTC additive in the lubricant. This is likely to be due to the reduced friction at asperity levels and lower rate of nascent surface formation because of lower friction and wear. The formation of MoS_2 identified in Raman study considered as the main reason for lower friction coefficient and wear.

- A minimum critical load is required for hydrogen permeation in a lubricated tribo-contact. This is necessary to remove the oxide layer and form nascent steel surface.
- Both chemical and physical mechanisms are involved in promoting hydrogen uptake
- The trapped hydrogen into the steel from the manufacturing process is liberated during surface-rubbing. This is also a source of hydrogen diffusion although the experiment by hydrogen-free lubricant showed that this source of hydrogen is negligible compared to the amount of hydrogen coming from hydrocarbon molecules and water contamination.

11.2 **Experiments conducted at high temperature**

- Hydrogen permeation rate increases by increasing the contact pressure. The potential reasons for this are the higher oxidation rate and more wear which are responsible for higher generation of hydrogen
- Decreasing sliding speed leads to lower hydrogen permeation rate. This can be due to the lower wear volume.
- ZDDP tribofilm was postulated to have a beneficial effect on hydrogen permeation rate. Formation of a continuous tribofilm in presence of ZDDP additive deactivates the catalytic action of nascent surfaces. This is suggested as the main reason of lower hydrogen flux in presence of anti-wear additive. The strong interaction between sulphur and phosphate layer with the metal surface allow fewer active sites to be generated and less metal-metal asperity contact. This layer may also act as barrier to hydrogen permeation.
- Hydrogen permeation further decreases in presence of MoDTC additive in the lubricant. This is likely to be due to the formation of MoS_2, and therefore less asperity-asperity contact.
- The influence of water contamination in lubricant on hydrogen permeation rate is significantly reduced by increasing temperature. This is due to the evaporation of water molecules and escaping from the lubricant in early stages of the experiments carried out at high temperature.
- Hydrogen uptake results demonstrate that water contamination is much more detrimental in presence of ZDDP additive. This is likely to be due to the fact that water contamination in the lubricant accelerates ZDDP decomposition rate. ZDDP decomposition by-products act as

poisonous agents for recombination of hydrogen atoms. It was also suggested that water facilitates hydrogen permeation by damaging the tribofilm due to its interference with the additives on the contacting surface.

References

1. *Bearings - global strategic business report.* Global Industry Analysts, Inc, January 2015.

2. Bhadeshia, H., *Steels for bearings.* Progress in materials Science, 2012. **57**(2): p. 268-435.

3. Woodtli, J. and R. Kieselbach, *Damage due to hydrogen embrittlement and stress corrosion cracking.* Engineering Failure Analysis, 2000. **7**(6): p. 427-450.

4. Kittel, J., F. Ropital, and J. Pellier. *New insights into hydrogen permeation in steels: measurements through thick membranes*. in *Corrosion 2008*. 2008. NACE International.

5. Mizuhara, K., T. Taki, and K. Yamanaka, *Anomalous cracking of bearing balls under a liquid-butane environment.* Tribology International, 1993. **26**(2): p. 135-142.

6. Tamada, K. and H. Tanaka, *Occurrence of brittle flaking on bearings used for automotive electrical instruments and auxiliary devices.* Wear, 1996. **199**(2): p. 245-252.

7. Okumura, T. and J. Sugimura, *Molecular dynamics simulation of gas molecules dissolved in lubricant under shear.* Tribology Online, 2009. **4**(4): p. 92-95.

8. Karpińska, A., C. Kajdas, and K.i. Hiratsuka, *On hydrogen generation during tribo-degradation of organic compounds.* Tribologia: tarcie, zużycie, smarowanie, 2006(6): p. 21-37.

9. Lu, R., H. Nanao, K. Kobayashi, T. Kubo, and S. Mori, *Effect of lubricant additives on tribochemical decomposition of hydrocarbon oil on nascent steel surfaces.* Journal of the Japan Petroleum Institute, 2010. **53**(1): p. 55-60.

10. Ray, D., L. Vincent, B. Coquillet, P. Guirandenq, J. Chene, and M. Aucouturier, *Hydrogen embrittlement of a stainless ball bearing steel.* Wear, 1980. **65**(1): p. 103-111.

11. Lu, R., I. Minami, H. Nanao, and S. Mori, *Investigation of decomposition of hydrocarbon oil on the nascent surface of steel.* Tribology Letters, 2007. **27**(1): p. 25-30.

12. Kohara, M., T. Kawamura, and M. Egami, *Study on mechanism of hydrogen generation from lubricants.* Tribology Transactions, 2006. **49**(1): p. 53-60.

13. Kino, N. and K. Otani, *The influence of hydrogen on rolling contact fatigue life and its improvement.* JSAE review, 2003. **24**(3): p. 289-294.

14. Uyama, H., H. Yamada, H. Hidaka, and N. Mitamura, *The effects of hydrogen on microstructural change and surface originated flaking in rolling contact fatigue.* Tribology Online, 2011. **6**(2): p. 123-132.

15. Bronshtein, L. and E. Pashkov, *Methods for the investigation of hydrogen uptake in friction and hydrogen-induced wear of metals in lubricating media.* Chemistry and Technology of Fuels and Oils, 1992. **28**(7): p. 423-430.

16. Imran, T., B. Jacobson, and A. Shariff, *Quantifying diffused hydrogen in AISI-52100 bearing steel and in silver steel under tribo-mechanical action: Pure rotating bending, sliding–rotating bending, rolling–rotating bending and uni-axial tensile loading.* Wear, 2006. **261**(1): p. 86-95.

17. John, P., J. Cutler, and J. Sanders, *Tribological behavior of a multialkylated cyclopentane oil under ultrahigh vacuum conditions.* Tribology letters, 2001. **9**(3-4): p. 167-173.

18. Hamrock, B.J. and W.J. Anderson, *Rolling-element bearings.* 1983.

19. Collis, D.J., *A resource‐based analysis of global competition: the case of the bearings industry.* Strategic management journal, 1991. **12**(S1): p. 49-68.

20. Harnoy, A., *Bearing design in machinery: engineering tribology and lubrication.* 2002: CRC press.

21. *The SKF web page 2014. Available from: www.skf.com.*

22. Basu, A., J. Chakraborty, S. Shariff, G. Padmanabham, S. Joshi, G. Sundararajan, J. Dutta Majumdar, and I. Manna, *Laser surface hardening of austempered (bainitic) ball bearing steel.* Scripta Materialia, 2007. **56**(10): p. 887-890.

23. Kobs, K., H. Dimigen, C. Denissen, E. Gerritsen, J. Politiek, L. Van Ijzendoorn, R. Oechsner, A. Kluge, and H. Ryssel, *Friction reduction and zero wear for 52100 bearing steel by high‐dose implantation of carbon.* Applied Physics Letters, 1990. **57**(16): p. 1622-1624.

24. Davis, J., *Surface hardening of steels.* ASM International, Materials Park, OH, 2002. **227**.

25. Stachowiak, G. and A.W. Batchelor, *Engineering tribology.* 2013: Butterworth-Heinemann.

26. Holmberg, K., P. Andersson, and A. Erdemir, *Global energy consumption due to friction in passenger cars.* Tribology International, 2012. **47**: p. 221-234.

27. Pawlak, Z., *Tribochemistry of lubricating oils.* Vol. 45. 2003: Elsevier.

28. Comfort, A., *An introduction to heavy-duty diesel engine frictional losses and lubricant properties affecting fuel economy-Part I.* 2003, SAE Technical Paper.

29. Stachowiak, G.W., *Wear: materials, mechanisms and practice.* 2006: John Wiley & Sons.

30. Priest, M., *Principles of Tribology.* Lecture Notes. 2013: University of Leeds.

31. Hutchings, I., *Tribology: friction and wear of engineering materials.* Mater. Des, 1992. **13**(3): p. 187.

32. Landolt, D., S. Mischler, and M. Stemp, *Electrochemical methods in tribocorrosion: a critical appraisal.* Electrochimica Acta, 2001. **46**(24): p. 3913-3929.

33. Evans, M., L. Wang, and R. Wood, *Formation mechanisms of white etching cracks and white etching area under rolling contact fatigue.* Proceedings of the Institution of Mechanical Engineers, Part J: Journal of Engineering Tribology, 2014. **228**(10): p. 1047-1062.

34. Caines, A.J. and R.F. Haycock, *Automotive lubricants reference book.* Vol. 354. 2004: John Wiley & Sons.

35. Hsu, S.M. and R. Gates, *Boundary lubricating films: formation and lubrication mechanism.* Tribology international, 2005. **38**(3): p. 305-312.

36. Booth, J.E., *The feasibility of using electostatic charge condition monitoring for lubricant additive screening*, in *Faculty of Engineeting, Science and Mathematics.* 2008, University of Southampton.

37. Bhushan, B., *Modern Tribology Handbook, Two Volume Set.* 2010: CRC Press.

38. Lara, J., T. Blunt, P. Kotvis, A. Riga, and W.T. Tysoe, *Surface chemistry and extreme-pressure lubricant properties of dimethyl disulfide.* The Journal of Physical Chemistry B, 1998. **102**(10): p. 1703-1709.

39. Tanaka, H., V.B. Niste, Y. Abe, and J. Sugimura, *The effect of lubricant additives on hydrogen permeation under rolling contact.* Tribology Letters, 2017. **65**(3): p. 94.

40. Gullac, B. and O. Akalin, *Frictional characteristics of IF-WS2 nanoparticles in simulated engine conditions.* Tribology Transactions, 2010. **53**(6): p. 939-947.

41. Lahouij, I., F. Dassenoy, L. De Knoop, J.-M. Martin, and B. Vacher, *In situ TEM observation of the behavior of an individual fullerene-like MoS2 nanoparticle in a dynamic contact.* Tribology Letters, 2011. **42**(2): p. 133-140.

42. Khaemba, D.N., *Raman spectroscopic studies of friction modifier Molybdenum DialkyldiThioCarbamate (MoDTC)*. 2016, University of Leeds.

43. Barnes, A.M., K.D. Bartle, and V.R. Thibon, *A review of zinc dialkyldithiophosphates (ZDDPS): characterisation and role in the lubricating oil.* Tribology International, 2001. **34**(6): p. 389-395.

44. Georges, J.-M., A. Tonck, S. Poletti, E. Yamaguchi, and P. Ryason, *Film thickness and mechanical properties of adsorbed neutral and basic zinc diisobutyl dithiophosphates.* Tribology Transactions, 1998. **41**(4): p. 543-553.

45. Spikes, H., *The history and mechanisms of ZDDP.* Tribology letters, 2004. **17**(3): p. 469-489.

46. Spedding, H. and R. Watkins, *The antiwear mechanism of zddp's. Part I.* Tribology International, 1982. **15**(1): p. 9-12.

47. So, H., Y. Lin, G.G. Huang, and T.S. Chang, *Antiwear mechanism of zinc dialkyl dithiophosphates added to a paraffinic oil in the boundary lubrication condition.* Wear, 1993. **166**(1): p. 17-26.

48. Bancroft, G., M. Kasrai, M. Fuller, Z. Yin, K. Fyfe, and K.H. Tan, *Mechanisms of tribochemical film formation: stabilityof tribo-and thermally-generated ZDDP films.* Tribology Letters, 1997. **3**(1): p. 47-51.

49. Fuller, M.S., L.R. Fernandez, G. Massoumi, W. Lennard, M. Kasrai, and G. Bancroft, *The use of X‐ray absorption spectroscopy for monitoring the thickness of antiwear films from ZDDP.* Tribology Letters, 2000. **8**(4): p. 187.

50. Lainé, E., A. Olver, and T. Beveridge, *Effect of lubricants on micropitting and wear.* Tribology International, 2008. **41**(11): p. 1049-1055.

51. Benyajati, C. and A. Olver, *The effect of a ZnDTP anti-wear additive on micropitting resistance of carburised steel rollers.* 2004: AGMA.

52. Spikes, H.A., A.V. Olver, and P.B. Macpherson, *Wear in rolling contacts.* Wear, 1986. **112**(2): p. 121-144.

53. Laine, E., A. Olver, M. Lekstrom, B. Shollock, T. Beveridge, and D. Hua, *The effect of a friction modifier additive on micropitting.* Tribology Transactions, 2009. **52**(4): p. 526-533.

54. Kabir, M., C.F. Higgs, and M.R. Lovell, *A pin-on-disk experimental study on a green particulate-fluid lubricant.* Journal of Tribology, 2008. **130**(4): p. 041801.

55. Kondo, Y., T. Koyama, and S. Sasaki, *Tribological properties of ionic liquids*, in *Ionic liquids-New aspects for the future*. 2013, InTech.

56. Sadeghi, F., B. Jalalahmadi, T.S. Slack, N. Raje, and N.K. Arakere, *A review of rolling contact fatigue.* Journal of Tribology, 2009. **131**(4): p. 041403-041403.

57. Oila, A. and S. Bull, *Assessment of the factors influencing micropitting in rolling/sliding contacts.* Wear, 2005. **258**(10): p. 1510-1524.

58. Hoeprich, M.R., *Analysis of micropitting of prototype surface fatigue test gears.* Tribotest, 2001. **7**(4): p. 333-347.

59. Nedelcu, I., E. Piras, A. Rossi, and H.R. Pasaribu, *XPS analysis on the influence of water on the evolution of zinc dialkyldithiophosphate–derived reaction layer in lubricated rolling contacts.* Surface and Interface Analysis, 2012. **44**(8): p. 1219-1224.

60. Fast, J.D., *Gases in metals.* MacMillan Publishing Co. 1976, 260 p(Book). 1976.

61. Fukai, Y., *The metal-hydrogen system: basic bulk properties*. Vol. 21. 2006: Springer Science & Business Media.

62. Kiuchi, K. and R. McLellan, *The solubility and diffusivity of hydrogen in well-annealed and deformed iron.* Acta Metallurgica, 1983. **31**(7): p. 961-984.

63. Moroz, L. and T. Mingin, *Hydrogen embrittlement of steel.* Metal Science and Heat Treatment, 1962. **4**(3): p. 135-137.

64. Tiwari, G., A. Bose, J. Chakravartty, S. Wadekar, M. Totlani, R. Arya, and R. Fotedar, *A study of internal hydrogen embrittlement of steels.* Materials Science and Engineering: A, 2000. **286**(2): p. 269-281.

65. Huang, F., J. Liu, Z. Deng, J. Cheng, Z. Lu, and X. Li, *Effect of microstructure and inclusions on hydrogen induced cracking susceptibility and hydrogen trapping efficiency of X120 pipeline steel.* Materials Science and Engineering: A, 2010. **527**(26): p. 6997-7001.

66. Zapffe, C.A. and G.A. Moore, *A micrographic study of the cleavage of hydrogenized ferrite.* Trans. AIME, 1943. **154**: p. 335-359.

67. Troiano, A.R., *The role of hydrogen and other interstitials in the mechanical behavior of metals.* trans. ASM, 1960. **52**(1): p. 54-80.

68. Petch, N. and P. Stables, *Delayed fracture of metals under static load.* Nature, 1952. **169**: p. 842-843.

69. Bastien, P. and P. Azou, *Proceeding of First World Metallurgical Congress.* ASM Cleveland, Ohio, 1951: p. 535.

70. Tabata, T. and H. Birnbaum, *Direct observations of the effect of hydrogen on the behavior of dislocations in iron.* Scripta Metallurgica, 1983. **17**(7): p. 947-950.

71. Ciruna, J. and H. Szieleit, *The effect of hydrogen on the rolling contact fatigue life of AISI 52100 and 440C steel balls.* Wear, 1973. **24**(1): p. 107-118.

72. Farrell, K. and A. Quarrell, *Hydrogen embrittlement of ultra-high-tensile steel.* Journal of the Iron and Steel Institute, 1964. **202**(12): p. 1002-&.

73. Murakami, Y. and S. Matsuoka, *Effect of hydrogen on fatigue crack growth of metals.* Engineering Fracture Mechanics, 2010. **77**(11): p. 1926-1940.

74. Slycke, J. and R. Vegter, *The role of hydrogen on rolling contact fatigue response of rolling element bearings.* Journal of ASTM International, 2009. **7**(2): p. 1-12.

75. Cassagne, T. and F. Embrittlement. *A review on hydrogen embrittlement of duplex stainless steels*. in *CORROSION 2005*. 2005. NACE International.

76. Park, G.T., S.U. Koh, H.G. Jung, and K.Y. Kim, *Effect of microstructure on the hydrogen trapping efficiency and hydrogen induced cracking of linepipe steel.* Corrosion science, 2008. **50**(7): p. 1865-1871.

77. Hirth, J.P., *Effects of hydrogen on the properties of iron and steel.* Metallurgical Transactions A, 1980. **11**(6): p. 861-890.

78. Nanninga, N., J. Grochowsi, L. Heldt, and K. Rundman, *Role of microstructure, composition and hardness in resisting hydrogen embrittlement of fastener grade steels.* Corrosion Science, 2010. **52**(4): p. 1237-1246.

79. Lancaster, J., *A review of the influence of environmental humidity and water on friction, lubrication and wear.* Tribology International, 1990. **23**(6): p. 371-389.

80. Sojka, J., V. Vodárek, I. Schindler, C. Ly, M. Jérôme, P. Váňová, N. Ruscassier, and A. Wenglorzová, *Effect of hydrogen on the properties and fracture characteristics of TRIP 800 steels.* Corrosion Science, 2011. **53**(8): p. 2575-2581.

81. Murakami, Y., T. Kanezaki, Y. Mine, and S. Matsuoka, *Hydrogen embrittlement mechanism in fatigue of austenitic stainless steels.* Metallurgical and materials Transactions A, 2008. **39**(6): p. 1327.

82. Maeda, K., K. Tamada, H. Nakashima, and N. Tsushima, *A new type of microstructural change due to rolling contact fatigue.* Japanese Society of Tribologists, 1990: p. 791-796.

83. Duncanson, M., *Detecting and controlling water in oil.* Practicing Oil Analysis Magazine, 2005: p. 22-24.

84. Fitch, J. and S. Jaggernauth, *Moisture-The second most destructive lubricant contaminate and its effects on bearing life.* P/PM Magazine, 1994.

85. Cantley, R.E., *The effect of water in lubricating oil on bearing fatigue life.* ASLE Transactions, 1977. **20**(3): p. 244-248.

86. Bauer, C. and M. Day, *Water contamination in hydraulic and lube systems.* Practicing Oil Analysis Magazine, 2007. **9**(9-10).

87. Spikes, H. and P. Macpherson. *Water content of helicopter gear oils.* in *International Power Transmissions and Gearing Conf. San Francisco.* 1980.

88. Cen, H., A. Morina, A. Neville, R. Pasaribu, and I. Nedelcu, *Effect of water on ZDDP anti-wear performance and related tribochemistry in lubricated steel/steel pure sliding contacts.* Tribology International, 2012. **56**: p. 47-57.

89. Rounds, F.G., *Some factors affecting the decomposition of three commercial zinc organodithiophosphates.* ASLE Transactions, 1975. **18**(2): p. 79-89.

90. Lamping, G., J. Cuellar Jr, H. Silvus, and H. Barsun, *Guidelines for maintaining steam turbine lubrication systems. Final report.* 1986, Southwest Research Inst., San Antonio, TX (USA).

91. Liu, W., D. Dong, Y. Kimura, and K. Okada, *Elastohydrodynamic lubrication with water-in-oil emulsions.* Wear, 1994. **179**(1): p. 17-21.

92. Faut, O.D. and D.R. Wheeler, *On the mechanism of lubrication by tricresylphosphate (TCP)—the coefficient of friction as a function of temperature for TCP on M-50 steel.* ASLE Transactions, 1983. **26**(3): p. 344-350.

93. Fuller, M.L.S., M. Kasrai, G.M. Bancroft, K. Fyfe, and K.H. Tan, *Solution decomposition of zinc dialkyl dithiophosphate and its effect on antiwear and thermal film formation studied by X-ray absorption spectroscopy.* Tribology International, 1998. **31**(10): p. 627-644.

94. Cen, H., *Effect of water on the performance of lubricants and related tribochemistry in boundary lubricated steel/steel contacts.* 2012, University of Leeds.

95. Nicholls, M.A., T. Do, P.R. Norton, M. Kasrai, and G.M. Bancroft, *Review of the lubrication of metallic surfaces by zinc dialkyl-dithiophosphates.* Tribology International, 2005. **38**(1): p. 15-39.

96. Hollox, G., R. Hobbs, and J. Hampshire, *Lower bainite bearings for adverse environments.* Wear, 1981. **68**(2): p. 229-240.

97. Grunberg, L. and D. Scott, *The acceleration of pitting failure by water in the lubricant.* Journal of the Institute of Petroleum, 1958. **44**(419): p. 406.

98. Schatzberg, P. and I. Felsen, *Effects of water and oxygen during rolling contact lubrication.* Wear, 1968. **12**(5): p. 331-342.

99. Schatzberg, P. and I.M. Felsen, *Influence of water on fatigue-failure location and surface alteration during rolling-contact lubrication.* Journal of Lubrication Technology, 1969. **91**(2): p. 301-307.

100. Grunberg, L., D. Jamieson, and D. Scott, *Hydrogen penetration in water-accelerated fatigue of rolling surfaces.* Philosophical Magazine, 1963. **8**(93): p. 1553-1568.

101. Richardson, A., L. Wang, R. Wood, M. Evans, W. Anderson, and M. Ingram. *Investigation of the role of hydrogen in white structure flaking (WSF) of wind turbine gearbox bearings.* in *STLE annual meeting, Dalas, TX.* 2015.

102. Evans, M.-H., L. Wang, H. Jones, and R. Wood, *White etching crack (WEC) investigation by serial sectioning, focused ion beam and 3-D crack modelling.* Tribology International, 2013. **65**: p. 146-160.

103. Evans, M.-H., A. Richardson, L. Wang, and R. Wood, *Effect of hydrogen on butterfly and white etching crack (WEC) formation under rolling contact fatigue (RCF).* Wear, 2013. **306**(1): p. 226-241.

104. Evans, M.-H., A. Richardson, L. Wang, and R. Wood, *Serial sectioning investigation of butterfly and white etching crack (WEC) formation in wind turbine gearbox bearings.* Wear, 2013. **302**(1): p. 1573-1582.

105. Evans, M., *White structure flaking (WSF) in wind turbine gearbox bearings: effects of 'butterflies' and white etching cracks (WECs).* Materials Science and Technology, 2012. **28**(1): p. 3-22.

106. Mischler, S., *Triboelectrochemical techniques and interpretation methods in tribocorrosion: a comparative evaluation.* Tribology International, 2008. **41**(7): p. 573-583.

107. Wu, P.-Q. and J.P. Celis, *Electrochemical noise measurements on stainless steel during corrosion–wear in sliding contacts.* Wear, 2004. **256**(5): p. 480-490.

108. Serre, I., R.M. Pradeilles-Duval, and N. Celati, *Tribological and corrosion experiments of graphite ring against Ti–6Al–4V disk: Influence of electrochemical and mechanical parameters.* Wear, 2006. **260**(9–10): p. 1129-1135.

109. Ponthiaux, P., F. Wenger, D. Drees, and J.-P. Celis, *Electrochemical techniques for studying tribocorrosion processes.* Wear, 2004. **256**(5): p. 459-468.

110. Abedi Esfahani, E., H. Salimijazi, M. Golozar, J. Mostaghimi, and L. Pershin, *Study of corrosion behavior of arc sprayed aluminum coating on mild steel.* Journal of Thermal Spray Technology, 2012. **21**(6): p. 1195-1202.

111. Enomoto, M., D. Hirakami, and T. Tarui, *Thermal desorption analysis of hydrogen in high strength martensitic steels.* Metallurgical and Materials Transactions A, 2012. **43**(2): p. 572-581.

112. Godai, T., T. Sugiyama, M. Sugino, M. Kondo, and T. Ogawa, *Process and apparatus for measurement of diffusible hydrogen*. 1980, Google Patents.

113. Ichitani, K., S. Kuramoto, and M. Kanno, *Quantitative evaluation of detection efficiency of the hydrogen microprint technique applied to steel.* Corrosion Science, 2003. **45**(6): p. 1227-1241.

114. Kim, C., J. Lee, Y. Lee, N. Cho, D. Kim, and W. Kang, *Hydrogen sensing characteristics of Pd-SiC Schottky diode operating at high temperature.* Journal of Electronic Materials, 1999. **28**(3): p. 202-205.

115. Okuyama, S., Y. Ito, T. Sugawara, K. Okuyama, K. Matsushita, and J. Kido, *Hydrogen-induced light emission from an organic electroluminescent device.* Applied physics letters, 1997. **71**: p. 2877-2879.

116. Kula, P., R. Pietrasik, B. Wendler, and K. Jakubowski, *The effect of hydrogen in lubricated frictional couples.* Wear, 1997. **212**(2): p. 199-205.

117. Murayama, Y., T. Satoh, S. Uchida, Y. Satoh, S. Nagata, T. Satoh, Y. Wada, and M. Tachibana, *Effects of hydrogen peroxide on intergranular stress corrosion cracking of stainless steel in high temperature water,(V) Characterization of oxide film on stainless steel by multilateral surface analyses.* Journal of Nuclear Science and Technology, 2002. **39**(11): p. 1199-1206.

118. Ichitani, K. and M. Kanno, *Visualization of hydrogen diffusion in steels by high sensitivity hydrogen microprint technique.* Science and Technology of Advanced Materials, 2003. **4**(6): p. 545-551.

119. Devanathan, M. and Z. Stachurski. *The adsorption and diffusion of electrolytic hydrogen in palladium.* in *Proceedings of the Royal Society of London A: Mathematical, Physical and Engineering Sciences*. 1962. The Royal Society.

120. Newman, J. and L. Shreir, *Role of hydrides in hydrogen entry into steel from solutions containing promoters.* Corrosion Science, 1969. **9**(8): p. 631-641.

121. Gelder, K.V., M.S. Thomas, and C. Kroese, *Hydrogen-induced cracking: determination of maximum allowed H_2S partial pressures.* Corrosion, 1986. **42**(1): p. 36-43.

122. Turnbull, A., M.S. de Santa Maria, and N. Thomas, *The effect of H_2S concentration and pH on hydrogen permeation in AISI 410 stainless steel in 5% NaCl.* Corrosion Science, 1989. **29**(1): p. 89-104.

123. Tsuru, T., Y. Huang, M.R. Ali, and A. Nishikata, *Hydrogen entry into steel during atmospheric corrosion process.* Corrosion science, 2005. **47**(10): p. 2431-2440.

124. Ootsuka, S., S. Fujita, E. Tada, A. Nishikata, and T. Tsuru, *Evaluation of hydrogen absorption into steel in automobile moving environments.* Corrosion Science, 2015. **98**: p. 430-437.

125. Huang, Y., A. Nakajima, A. Nishikata, and T. Tsuru, *Effect of mechanical deformation on permeation of hydrogen in iron.* ISIJ International, 2003. **43**(4): p. 548-554.

126. 17081:2014, I., *Method of measurement of hydrogen permeation and determination of hydrogen uptake and transport in metals by an electrochemical technique.* 2014.

127. Han, B., J. Binns, and I. Nedelcu, *In-situ detection of hydrogen uptake from lubricated rubbing contacts.* Tribology Online, 2016. **11**(2): p. 450-454.

128. Fielding, L., E.J. Song, D.-K. Han, H. Bhadeshia, and D.-W. Suh. *Hydrogen diffusion and the percolation of austenite in nanostructured bainitic steel.* in *Proceedings of the Royal Society of London A: Mathematical, Physical and Engineering Sciences.* 2014. The Royal Society.

129. Svoboda, J., G. Mori, A. Prethaler, and F. Fischer, *Determination of trapping parameters and the chemical diffusion coefficient from hydrogen permeation experiments.* Corrosion Science, 2014. **82**: p. 93-100.

130. Manolatos, P., M. Jerome, and J. Galland, *Necessity of a palladium coating to ensure hydrogen oxidation during electrochemical permeation measurements on iron.* Electrochimica Acta, 1995. **40**(7): p. 867-871.

131. Gabrielli, C., G. Maurin, L. Mirkova, and H. Perrot, *Transfer function analysis of hydrogen permeation through a metallic membrane in a Devanathan cell: Part II: Experimental investigation on iron membrane.* Journal of Electroanalytical chemistry, 2006. **590**(1): p. 15-25.

132. Devanathan, M., Z. Stachurski, and W. Beck, *A technique for the evaluation of hydrogen embrittlement characteristics of electroplating baths.* Journal of the Electrochemical Society, 1963. **110**(8): p. 886-890.

133. *Standard Test Method for Corrosiveness and Oxidation Stability of Hydraulic Oils, Aircraft Turbine Engine Lubricants, and Other Highly Refined Oils.* ASTM D4636-99, 2010.

134. Topolovec-Miklozic, K., T.R. Forbus, and H.A. Spikes, *Film thickness and roughness of ZDDP antiwear films.* Tribology Letters, 2007. **26**(2): p. 161-171.

135. Griffiths, P.R., *The handbook of infrared and Raman characteristic frequencies of organic molecules.* Vibrational Spectroscopy, 1992. **4**(1): p. 121.

136. Addach, H., P. Bercot, M. Rezrazi, and M. Wery, *Hydrogen permeation in iron at different temperatures.* Materials Letters, 2005. **59**(11): p. 1347-1351.

137. Colomban, P., S. Cherifi, and G. Despert, *Raman identification of corrosion products on automotive galvanized steel sheets.* Journal of Raman Spectroscopy, 2008. **39**(7): p. 881-886.

138. Loeser, E., R. Wiquist, and S. Twiss, *Cam and tappet lubrication. IV–radioactive study of sulfur in the EP film.* ASLE Transactions, 1959. **2**(2): p. 199-207.

139. Windom, B.C., W. Sawyer, and D.W. Hahn, *A Raman spectroscopic study of MoS2 and MoO3: applications to tribological systems.* Tribology Letters, 2011. **42**(3): p. 301-310.

140. Khaemba, D.N., A. Neville, and A. Morina, *A methodology for Raman characterisation of MoDTC tribofilms and its application in investigating the influence of surface chemistry on friction performance of MoDTC lubricants.* Tribology Letters, 2015. **59**(3): p. 38.

141. Berkani, S., F. Dassenoy, C. Minfray, J.-M. Martin, H. Cardon, G. Montagnac, and B. Reynard, *Structural changes in tribo-stressed zinc polyphosphates.* Tribology Letters, 2013. **51**(3): p. 489-498.

142. Glaeser, W., D. Baer, and M. Engelhardt, *In situ wear experiments in the scanning Auger spectrometer.* Wear, 1993. **162**: p. 132-138.

143. Bell, J., K. Delargy, and A. Seeney, *Paper IX (ii) the removal of substrate material through thick zinc dithiophosphate anti-wear films.* Tribology series, 1992. **21**: p. 387-396.

144. Coy, R. and R. Jones, *The thermal degradation and EP performance of zinc dialkyldithiophosphate additives in white oil.* ASLE transactions, 1981. **24**(1): p. 77-90.

145. Choa, S.-H., K.C. Ludema, G.E. Potter, B.M. Dekoven, T.A. Morgan, and K.K. Kar, *A model of the dynamics of boundary film formation.* Wear, 1994. **177**(1): p. 33-45.

146. Bird, R. and G. Galvin, *The application of photoelectron spectroscopy to the study of EP films on lubricated surfaces.* Wear, 1976. **37**(1): p. 143-167.

147. Taylor, L., A. Dratva, and H. Spikes, *Friction and wear behavior of zinc dialkyldithiophosphate additive.* Tribology transactions, 2000. **43**(3): p. 469-479.

148. Taylor, L. and H. Spikes, *Friction-enhancing properties of ZDDP antiwear additive: part I—friction and morphology of ZDDP reaction films.* Tribology transactions, 2003. **46**(3): p. 303-309.

149. Allahar, K.N., D.P. Butt, M.E. Orazem, H.A. Chin, G. Danko, W. Ogden, and R.E. Yungk, *Impedance of steels in new and degraded ester based lubricating oil.* Electrochimica Acta, 2006. **51**(8): p. 1497-1504.

150. Wang, S.S. and H.-S. Lee, *The application of ac impedance technique for detecting glycol contamination in engine oil.* Sensors and Actuators B: Chemical, 1997. **40**(2): p. 193-197.

151. Lvovich, V.F. and M.F. Smiechowski, *AC impedance investigation of conductivity of automotive lubricants using two-and four-electrode electrochemical cells.* Journal of Applied Electrochemistry, 2009. **39**(12): p. 2439.

152. Lvovich, V.F. and M.F. Smiechowski, *Impedance characterization of industrial lubricants.* Electrochimica Acta, 2006. **51**(8): p. 1487-1496.

153. Wang, S.S., S.P. Maheswari, and S.C. Tung, *AC impedance measurements of the resistance and capacitance of lubricants.* ASLE Transactions, 1986. **30**(4): p. 436-443.

154. Smiechowski, M.F. and V.F. Lvovich, *Electrochemical monitoring of water–surfactant interactions in industrial lubricants.* Journal of Electroanalytical Chemistry, 2002. **534**(2): p. 171-180.

155. Ulrich, C., H. Petersson, H. Sundgren, F. Björefors, and C. Krantz-Rülcker, *Simultaneous estimation of soot and diesel contamination in engine oil using electrochemical impedance spectroscopy.* Sensors and Actuators B: Chemical, 2007. **127**(2): p. 613-618.

156. Smiechowski, M.F. and V.F. Lvovich, *Characterization of non-aqueous dispersions of carbon black nanoparticles by electrochemical impedance spectroscopy.* Journal of Electroanalytical Chemistry, 2005. **577**(1): p. 67-78.

157. Soleimani, M., M. Sophocleous, L. Wang, J. Atkinson, I.L. Hosier, A.S. Vaughan, R.I. Taylor, and R.J. Wood, *Base oil oxidation detection*

using novel chemical sensors and impedance spectroscopy measurements. Sensors and Actuators B: Chemical, 2014. **199**: p. 247-258.

158. Gabrielli, C., G. Maurin, L. Mirkova, H. Perrot, and B. Tribollet, *Transfer function analysis of hydrogen permeation through a metallic membrane in a Devanathan cell. I. Theory.* Journal of Electroanalytical Chemistry, 2006. **590**(1): p. 1-14.

159. Tallian, T., *Failure atlas for rolling bearings in wind turbines.* 2006, National Renewable Energy Laboratory (NREL), Golden, CO.

160. Solano-Alvarez, W., E.J. Song, D.K. Han, D.-W. Suh, and H. Bhadeshia, *Cracks in martensite plates as hydrogen traps in a bearing steel.* Metallurgical and Materials Transactions A, 2015. **46**(2): p. 665-673.

161. Ganesh, V.A., S.S. Dinachali, S. Jayaraman, R. Sridhar, H.K. Raut, A. Góra, A. Baji, A.S. Nair, and S. Ramakrishna, *One-step fabrication of robust and optically transparent slippery coatings.* RSC Advances, 2014. **4**(98): p. 55263-55270.

162. Kadin, Y., *Modeling of hydrogen transport in static and rolling contact.* Tribology Transactions, 2015. **58**(2): p. 260-273.

163. Mori, S., *Adsorption of benzene on the fresh steel surface formed by cutting under high vacuum.* Applied surface science, 1987. **27**(4): p. 401-410.

164. Barcroft, F., R. Bird, J. Hutton, and D. Park, *The mechanism of action of zinc thiophosphates as extreme pressure agents.* Wear, 1982. **77**(3): p. 355-384.

165. Feng, I.-M., W.L. Perilstein, and M.R. Adams, *Solid film deposition and non-sacrificial boundary lubrication.* ASLE TRANSACTIONS, 1963. **6**(1): p. 60-66.

166. Feng, I., *Pyrolysis of zinc dialkyl phosphorodithioate and boundary lubrication.* Wear, 1960. **3**(4): p. 309-311.

167. Tsay, L., M. Chi, Y. Wu, J. Wu, and D.-Y. Lin, *Hydrogen embrittlement susceptibility and permeability of two ultra-high strength steels.* Corrosion science, 2006. **48**(8): p. 1926-1938.

168. Tsay, L., M. Chi, H. Chen, and C. Chen, *Investigation of hydrogen sulfide stress corrosion cracking of PH 13-8 Mo stainless steel.* Materials Science and Engineering: A, 2006. **416**(1): p. 155-160.

169. Berkowitz, B. and H. Horowitz, *The role of H_2S in the corrosion and hydrogen embrittlement of steel.* Journal of the Electrochemical Society, 1982. **129**(3): p. 468-474.

170. Townsend Jr, H., *Hydrogen sulfide stress corrosion cracking of high strength steel wire.* Corrosion, 1972. **28**(2): p. 39-46.

171. Plaza, S., *The adsorption of zinc dibutyldithiophosphates on iron and iron oxide powders.* ASLE transactions, 1987. **30**(2): p. 233-240.

172. Morina, A., A. Neville, M. Priest, and J. Green, *ZDDP and MoDTC interactions and their effect on tribological performance–tribofilm characteristics and its evolution.* Tribology Letters, 2006. **24**(3): p. 243-256.

173. Bec, S., A. Tonck, J.-M. Georges, R. Coy, J. Bell, and G. Roper. *Relationship between mechanical properties and structures of zinc dithiophosphate anti–wear films.* in *Proceedings of the Royal Society of London A: Mathematical, Physical and Engineering Sciences.* 1999. The Royal Society.

174. Lansdown, A.R., *Molybdenum disulphide lubrication.* Vol. 35. 1999: Elsevier.

175. Miklozic, K.T., J. Graham, and H. Spikes, *Chemical and physical analysis of reaction films formed by molybdenum dialkyl-dithiocarbamate friction modifier additive using Raman and atomic force microscopy.* Tribology Letters, 2001. **11**(2): p. 71-81.

176. Onodera, T., Y. Morita, A. Suzuki, M. Koyama, H. Tsuboi, N. Hatakeyama, A. Endou, H. Takaba, M. Kubo, and F. Dassenoy, *A computational chemistry study on friction of h-MoS$_2$. Part I. mechanism of single sheet lubrication.* The Journal of Physical Chemistry B, 2009. **113**(52): p. 16526-16536.

177. Polk, C. and C. Rowe, *Crack growth rate: Its measurement and a controlling factor in rolling contact fatigue.* ASLE Transactions, 1976. **19**(1): p. 23-32.

178. Polk, C., W. Murphy, and C. Rowe, *Determining fatigue crack propagation rates in lubricating environments through the application of a fracture mechanics technique.* ASLE Transactions, 1975. **18**(4): p. 290-298.

179. Gao, N. and R. Dwyer-Joyce, *The effects of surface defects on the fatigue of water-and oil-lubricated contacts.* Proceedings of the Institution of Mechanical Engineers, Part J: Journal of Engineering Tribology, 2000. **214**(6): p. 611-626.

180. Flis, J., T. Zakroczymski, V. Kleshnya, T. Kobiela, and R. Duś, *Changes in hydrogen entry rate and in surface of iron during cathodic polarisation in alkaline solutions.* Electrochimica acta, 1999. **44**(23): p. 3989-3997.

Annex

Countersunk, Holes M6
8 off on a 134mm P.C.D.

Ø20

Ø33.60

D&T M6x12mm deep
8 holes on a 48mm P.C.D.

Ø150

10

55

B

B

Ø114

15

Ø84

Ø40 +0.20 0

50

5

2.20

6.80

1.50

1.80

9.50

8

SECTION B-B
SCALE 1 : 1

183

DO NOT SCALE IF IN DOUBT ASK

UNLESS OTHERWISE STATED
1) MACHINE AT ∀ TO 3.2 μm Ra MAX
2) TOLERANCE ON MACHINED DIMENSIONS AS FOLLOWS: 0-500 ±0.2; 500-1000 ±0.4

DATE

SCALE

TITLE
Electrochemical cell

DRAWN BY E. A.E.

DRG No

Ø150 +0.20 / 0
Ø114 +0.20 / 0
Ø120
Ø126.40

260
130
130
260
20

A
A

M6 x 1.0 tapped hole
8 off equi. spaced.

10
7.50
150
113.99
3.20
3
2.80
4
9.15

M6 x 1.0 tapped
hole, 8 deep

SECTION A-A

LUMED
THE UNIVERSITY OF LEEDS
SCHOOL OF MECHANICAL ENGINEERING

DATE
SCALE

TITLE
Mount Plate

DRAWN BY E. A.E.
DRG No

185

260

260

A

A

φ200

20

SECTION A-A
SCALE 1 : 2

3

LUMED
THE UNIVERSITY OF LEEDS
SCHOOL OF MECHANICAL ENGINEERING

DATE

SCALE

TITLE   Base Plate

DRAWN
BY   E. A.E

DRG
No

186

260

196

18.50

35

7

100

M6tapped
holes 8 off.

244

212

48

16

80

65

15

LUMED
THE UNIVERSITY OF LEEDS
SCHOOL OF MECHANICAL ENGINEERING

DATE

SCALE

TITLE
Rear Stabilizer Block

DRAWN
BY   E. A.E.

DRG
No

Ø64

Ø28

Countersunk Holes M6
8 off equi. spaced

10

SECTION A-A
SCALE 1 : 5

190